5-2019

Application of Remote Sensing Technology in Water Resources Management

Mahesh Pun
University of Nebraska-Lincoln, maheshpoon@hotmail.com

APPLICATION OF REMOTE SENSING TECHNOLOGY IN WATER RESOURCES MANAGEMENT

by

Mahesh Pun

A DISSERTATION

Presented to the Faculty of

The Graduate College at the University of Nebraska

In Partial Fulfillment of Requirements

For the Degree of Doctor of Philosophy

Major: Civil Engineering

(Water Resources)

Under the Supervision of Professors David M. Admiraal and Trenton E. Franz

Lincoln, Nebraska

May, 2019

APPLICATION OF REMOTE SENSING TECHNOLOGY IN WATER RESOURCES MANAGEMENT

Mahesh Pun, Ph.D.

University of Nebraska, 2019

Advisors: David M. Admiraal and Trenton E. Franz

The primary goal of this dissertation was to leverage the capabilities of remote sensing technology for capturing detailed spatial information at different spatial resolutions to monitor agricultural crops and generate accurate input datasets for water resources models. This dissertation is divided into three different research studies. In the first study, a remote sensing classification method was developed for classifying irrigated and non-irrigated fields that integrates Vegetation indices with surface energy balance fluxes. The method was applied in the COHYST2010 hydrological model region with wide climate variation and to multiple growing seasons with results that were 92.1% accurate and explained 97% variation in National Agricultural Statistics Service (NASS) county irrigation statistics. In the second study, a new method was developed (referred to as "footprint method") of re-projecting Moderate Resolution Imaging Spectroradiometer (MODIS) satellite images that preserves the geometric orientation and size of satellite sensor pixels. It properly represents satellite sensor pixel orientations in fields, and eliminates artifacts introduced by conventional processing methods. Statistical results of field comparison in AmeriFlux experimental fields US-Ne1 and US-Ne2 based on Leaf Area Index (LAI) equation of Myneni eat al. showed improvement in LAI estimation when the footprint method was applied with reduced RMSE by 16.05%, ubRMSE by 26.25%,

and nRMSE by 16.1% in average. On the contrary, the results of statistical analysis of MODIS Green LAI estimates based on Green LAI equation of Viña et al. does not support this conclusion. A third study explored the potential opportunities and benefits of utilizing gridded precipitation data, which is the combination of remotely sensed and weather stations precipitation data with more detailed spatial variability in water resources models. This study explored differences in spatial patterns between precipitation and recharge maps generated by interpolating data from weather stations and maps generated by gridded method. The percentage difference in annual average precipitation volume over 16 million acres of the Republican River basin area was around 14%. In a sensitivity analysis of precipitation in the watershed model, the effects of same rates of precipitation were found to be different for different types of soils, crops, and irrigation settings.

ACKNOWLEDGEMENTS

First and foremost, I would like to express my deep and sincere gratitude to my advisors, Dr. David M. Admiraal and Dr. Trenton E. Franz for their support and invaluable guidance during the research and preparation of this dissertation. Their wisdom, knowledge, and commitment to the highest standards inspired and motivated me. I have been fortunate and truly thankful that I had this opportunity to work with them.

I want to express a sincere appreciation to my dissertation committee members Dr. Elizabeth Walter-Shea, Dr. Yusong Li, and Dr. Xu Li for their support and review of my research work which helped this dissertation to take a definite shape and form. I am grateful to Dr. Denis Mutiibwa who later joined in my dissertation committee, advised and helped me to publish a scientific journal paper related to the research of this dissertation. I am truly grateful to receive technical assistance from Dr. Gengxin Ou (Michael Ou) in simulating water resources models, Doruk Ozturk, who was a graduate student in laying out the foundation and de-bugging complex programming script for handling MODIS satellite image data. Furthermore, I am grateful to Isaac Mortensen and Marc Groff from Flatwater Group for providing technical assistance during sensitivity analysis of soil water balance model to precipitation data. All their support has made this dissertation possible.

A debt of gratitude is owned to all the nice people I have met during my 15 years of stay in Lincoln, Nebraska; the place I consider my second home town. Memories made in this town, and friendships built with folks from around here have a lot of influence in my life. I would also like to remember the cubicle I worked from at Hardin Hall, Adele Hall Learning Commons near Love Library at the university, and coffee shops of Lincoln

(Meadowlark Coffee & Espresso and Starbucks) where I would spend endless hours working on my research and drafting this dissertation.

Last but not least, my final and most heartfelt acknowledgement must go to my family, to whom this dissertation is dedicated. My family has been a constant source of love, concern, support, and strength to me.

TABLE OF CONTENTS

APPLICATION OF REMOTE SENSING TECHNOLOGY IN WATER RESOURCES MANAGEMENT i

ACKNOWLEDGEMENTS iii

CHAPTER 1: INTRODUCTION 1

1.1 Problem Statement 1

1.2 Research Objectives and Outline of Dissertation 5

1.3 References 7

CHAPTER 2: LAND USE CLASSIFICATION – A SURFACE ENERGY BALANCE AND VEGETATION INDEX APPLICATION TO MAP AND MONITOR IRRIGATED LANDS 9

2.1 Abstract 9

2.2 Introduction 10

2.3 Materials and Methods 13

2.3.1 Study Area 13

2.3.2 Datasets 14

2.3.3 Calibration Growing Season 16

2.3.4 Normal Difference Vegetation Index and Green Index 18

2.3.5 Surface Energy Balance System (SEBS) 19

2.3.6 Irrigation Indices Development 20

2.3.7 Thresholding 24

2.3.8 Performance Assessment 26

2.4 Results 28

2.4.1 NEG Classification Method and Ground Truth 28

2.4.2 Spatial Distribution of Irrigation 29

2.4.3 NEG Classification Method and NASS Statistics 33

2.5 Discussion 34

2.5.1 Dual Indices and Single Index Classification Systems 34

2.5.2 Seasonal Development of NGI and EGI 36

2.5.3 Application in Humid to Arid Climate Regimes and Wet to Dry Growing Seasons 37

2.6 Conclusions 40

2.7 References 41

CHAPTER 3: APPLICATION OF MODIS DATA FOR FIELD SCALE ANALYSIS …….. 45

3.1 Abstract 45

3.2 Introduction 46

3.3 Implications of Existing MODIS Data Handling Method for Field Scale Analysis 51

3.3.1 Sensor Pixels and Fixed Grids in Agricultural Fields..... 51

3.3.2 Problems with the Existing Methodology of MODIS Data Reprojection in Field Scale Analysis..... 54

3.4 Footprint Methodology: Re-projecting MODIS Data in Native Sensor Pixel Orientation..... 58

3.5 Field Scale Accuracy Assessment of Footprint Methodology and Gridded Methodology 64

3.5.1 Study Area 64

3.5.2 Accuracy Assessment of Results 69

3.5.3 Paired T-Test Analysis..... 80

3.6 Potential Use of MODIS Data in Irrigation Water Management..... 83

3.7 Conclusions 86

3.8 References 88

CHAPTER 4: POTENTIAL APPLICATION OF REMOTELY SENSED GRIDDED PRECIPITATION DATA IN WATER RESOURCES MANAGEMENT 90

4.1 Abstract 90

4.2 Introduction 91

4.3 Comparison of Gridded and Weather Station Interpolated Precipitation Data..... 97

4.3.1 Methods..... 97

4.3.2 Results..... 101

4.3.2.1 Precipitation Analysis 101

4.3.2.2 Recharge Analysis 107

4.4 Sensitivity Analysis of the Soil Water Balance Model to Precipitation Data..... 114

4.4.1 Methods..... 114

4.4.2 Results..... 117

4.4.2.1 Effects of Precipitation Rates in an Irrigation Setting 117

4.4.2.2 Effects of Precipitation Rates on Different Crop Types 120

4.4.2.3 Effects of Precipitation Rates in Different Soil Types..... 123

4.4.3 Summary of Sensitivity Analysis of the Soil Water Balance Model to Precipitation 126
4.5 Sensitivity Analysis of Precipitation to Baseflow of a River System 129
4.5.1 Methods 129
4.5.2 Results 130
4.6 Summary and Conclusions 134
4.7 References 136

CHAPTER 5: SUMMARY AND CONCLUSIONS 138
5.1 Overall Conclusion 138
5.2 Recommendations for Future Research 141
5.3 References 142

APPENDIX A: LIST OF SATELLITE IMAGES USED IN ANALYSIS 143

APPENDIX B: MODIS BACKGROUND INFORMATION 145
B.1 MODIS Satellite and Sensor Description 145
B.2 Sensor Pixel Orientation 147
B.3 Triangular Point Spread Function 149
B.4 View Zenith Angle 152
B.5 Bowtie Effect 153
B.6 MODIS Data Products 155
B.6.1 MODIS Swath Data 156
B.6.2 MODIS Gridded Data 160
B.7 References 164

APPENDIX C: MODIS ESTIMATED AND GROUND TRUTH DATA 167

APPENDIX D: FIXED GRID CELLS WITH PIXEL CONTAMINATION IN MODIS IMAGES DURING FIELD SCALE ANALYSIS 171

APPENDIX E: PYTHON SCRIPT (v 2.7) FOR REPROJECTING MODIS IMAGES WITH THE FOOTPRINT METHOD 191

APPENDIX F: RESULTS OF FULL RANGE SENSITIVITY OF THE SOIL WATER BALANCE MODEL TO PRECIPITATION DATA 194

APPENDIX G: RESULTS OF FULL RANGE SENSITIVITY OF BASEFLOW OF RIVER SYSTEM TO PRECIPITATION DATA 201

TABLE OF FIGURES

Figure 2.1: *Map of Nebraska showing the Cooperative Hydrology Study (COHYST) hydrological model region, rivers, and Natural Resources Districts (NRDs)* 14

Figure 2.2: *Sampled irrigated (355) and non-irrigated (464) ground truth fields across the COHYST region during the 2014 growing season* 16

Figure 2.3: *Nebraska precipitation average for the months of June, July, and August from 1980 to 2017; 1901–2000 mean precip (μ: 239.3 mm); and the standard deviations (σ: 2.11 mm) about the mean.* 17

Figure 2.4: *Empirical distributions of NGI and EGI indices for all fields combined (Irrigated and non-irrigated areas), irrigated, and non-irrigated areas. Blue lines indicate the threshold values of NGI and EGI*.....22

Figure 2.5: *Empirical distributions of NGI index for irrigated and non-irrigated areas after the classification method has been applied*.....25

Figure 2.6: *NDVI-Evaporation Fraction-Green Index (NEG) Irrigation classification method flow diagram. Thd = Threshold*.....27

Figure 2.7: *Spatial distribution of NEG derived irrigated fields in the COHYST model region during the growing season of 2010 (A) and 2015 (B). Crop types derived from NASS CDL* 31

Figure 2.8: *Normal rainfall distribution across the COHYST region during the growing season (June, July and August). Base period: 1981–2010.*.....32

Figure 2.9: *Regression between NASS and NEG irrigated area by county for 2010 and 2015* 34

Figure 2.10: *Seasonal profile of NGI (**A**) and EGI (**B**) for irrigated and non-irrigated soybean and maize during the 2014 growing season. Each data point is an average of nine contiguous pixels of a square. DOY denotes Day of Year*.....38

Figure 3.1*: Spatial distribution of irrigated and non-irrigated maize fields*.....48

Figure 3.2*: Different shape and sizes of fields (Earth Observatory, 2006)*.....49

Figure 3.3*: Spatial orientation of fixed grid cells (left) and satellite sensor pixels (right) overlaid on a center pivot field (green)* 51

Figure 3.4*: Overlapping of fixed grid cells and satellite sensor pixels overlaid on a center pivot field (green)* 52

Figure 3.5*: Value assignment to grid cells using Nearest Neighbor resampling technique* 53

Figure 3.6*: Value assignment to grid cells using Bilinear and Cubic Convolution resampling techniques* 54

Figure 3.7*: Problem of pixel value contamination in a grid cell well within a field*.....55

Figure 3.8*: Pixel contamination problem in Nearest Neighbor resampling technique*....57

***Figure 3.9**: Problem of re-projecting MODIS data in finer resolution using MODIS swath tool*.....59

***Figure 3.10**: Step by step refinement of grid cell resampling resolution*.....61

***Figure 3.11**: 10 m grid cells within a sensor footprint pixel*.....63

***Figure 3.12**: Increase in mismatch area with increase in pixel spatial resolution*.....64

***Figure 3.13**: Location of the study site in Nebraska* 65

***Figure 3.14**: Field analysis study area location* 66

***Figure 3.15**: Ground truth locations within center pivot fields* 66

***Figure 3.16**: Grid cells and sensor pixels representing center pivot maize fields. (a) gridded data, and (b) footprint data* 68

***Figure3.17**: LAI values estimated using the footprint and gridded methods, and ground truth measurements for field US-Ne1, using LAI equation of Myneni et al.* 70

***Figure 3.18**: LAI values estimated using the footprint and gridded method, and ground truth measurements for field US-Ne2, using LAI equation of Myneni et al.* 70

***Figure 3.19**: LAI (equation of Myneni et al.) as a function of growing degree days using the MODIS footprint and gridded methods and ground truth measurements (Field US-Ne1)* 73

***Figure 3.20**: LAI (equation of Myneni et al.) as a function of growing degree days using the MODIS footprint and gridded methods and ground truth measurements (Field US-Ne2)* 73

***Figure 3.21**: Green LAI values estimated (equation of Viña et al.) using the footprint and gridded methods, and ground truth measurements for field US-Ne1*.....75

***Figure 3.22**: Green LAI values estimated (equation of Viña et al.) using the footprint and gridded method, and ground truth measurements for field US-Ne2* 76

***Figure 3.23**: Green LAI (equation of Viña et al.) as a function of growing degree days using the MODIS footprint and gridded methods and ground truth measurements (Field US-Ne1)*.....78

***Figure 3.24**: Green LAI (equation of Viña et al.) as a function of growing degree days using the MODIS footprint and gridded methods and ground truth measurements (Field US-Ne2)*.....79

***Figure 3.25:** SAVI curve of irrigated maize for different growing seasons derived from Landsat images (2002 – 2012). (modified figure from Campos et. al., 2017, figure 1)* 84

***Figure 3.26:** Refined crop characteristic curve of irrigated maize after combining multiple years of Landsat images. (modified figure from Campos et. al., 2017, figure 2)*.....85

***Figure 3.27:** SAVI curve of irrigated maize field US-Ne2 for a single growing season of year 2012 derived from MODIS images using footprint method* 86

Figure 4.1: *Effect of a local storm event near the Ogallala weather station caused by the interpolation process* 93

Figure 4.2: *Percent difference in NIR in COHYST2010 model area of year 2002*.....93

Figure 4.3*: Spatial coverage of Republican River groundwater model in Colorado, Nebraska, and Kansas* 98

Figure 4.4*: Spatial distribution of soil types in the Republican River model area (RRCA Ground Water Model, 2003, Appendix E)* 99

Figure 4.5*: Precipitation-Recharge curves for different soil types used in Republican River model (RRCA Ground Water Model, 2003, Appendix F)* 100

Figure 4.6*: Spatial distribution of yearly precipitation rate from WSI and gridded Data of year 2005* 102

Figure 4.7*: Spatial distribution of yearly precipitation rate from WSI and gridded Data of year 2006* 103

Figure 4.8*: Spatial distribution of yearly precipitation rate from WSI and gridded Data of year 2007* 104

Figure 4.9*: Spatial distribution of difference in precipitation between WSI and gridded method for year 2005*.....105

Figure 4.10*: Spatial distribution of difference in precipitation between WSI and gridded method for year 2006*.....105

Figure 4.11*: Spatial distribution of difference in precipitation between WSI and gridded method for year 2007*.....106

Figure 4.12*: Spatial distribution of yearly recharge rate as determined from WSI and gridded precipitation of year 2005* 108

Figure 4.13*: Spatial distribution of yearly recharge rate as determined from WSI and gridded precipitation of year 2006* 109

Figure 4.14*: Spatial distribution of difference in recharge between WSI and gridded method for year 2005*.....110

Figure 4.15*: Spatial distribution of difference in recharge between WSI and gridded method for year 2005*.....111

Figure 4.16*: Spatial distribution of difference in recharge between WSI and gridded method for year 2006*.....112

Figure 4.17*: Spatial distribution of difference in recharge between WSI and gridded method for year 2007*.....112

Figure 4.18*: Annual baseline precipitation rate and multiplier rates from 1950 to 2013 for the Gothenburg weather station data*.....116

Figure 4.19*: Average annual precipitation of baseline run and runs with multipliers applied* 116

***Figure 4.20**: Response of DP to a range of precipitation multipliers for irrigated and non-irrigated maize* 118

***Figure 4.21**: Response of ET to precipitation multipliers for irrigated and non-irrigated maize* 119

***Figure 4.22**: Response of DP to precipitation multipliers for different crop types* 121

***Figure 4.23**: Responses of RO to precipitation multipliers for different crop types* 122

***Figure 4.24**: Response of NIR to precipitation multipliers for different crop types* 123

***Figure 4.25**: Response of DP to changes in precipitation multipliers for soil types* 124

***Figure 4.26**: Responses of RO to variations in the Precipitation multipliers for different soil types* 125

***Figure 4.27**: Response of DP to varying multipliers of precipitation for soils with different Water Holding Capacity* 126

***Figure 4.28**: Spatial coverage of COHYST2010 model in Nebraska state* 130

***Figure 4.29**: Baseflow comparison at the Cozad gaging station. (a) monthly baseflow and (b) cumulative annual baseflow* 131

***Figure B.1**: Path of satellite and sensor scanning orientation of MODIS (modified from Wolfe et al., 2002, fig.1)* 146

***Figure B.2**: Orientation of 500 m band pixels and 1 km band pixels in MODIS sensor along the scan direction* 147

***Figure B.3**: Orientation of 500 m band pixels and 1 km band pixels in MODIS sensor along the scan direction* 148

***Figure B.4**: Orientation of 250m band pixels and 1 km band pixels in MODIS sensor along the scan direction* 148

***Figure B.5**: Detector along-scan triangular point spread function and the peak-to-peak alignment of the three MODIS spatial resolutions* 149

***Figure B.6**: Sensor triangular PSF (example at 500 m resolution) which better models that of MODIS, in which nominal observation area contributes 75% of the actual observation (Nishihama et al., 1997, Figure 2-6)* 150

***Figure B.7**: Registration of 250 m, 500 m, and 1 km MODIS observations showing the PSFs of various resolutions of MODIS data observation (B. Tan et al., 2006 fig.4a)* 151

***Figure B.8**: Satellite sensor pixels covering more earth surface area with increasing view zenith angle (θv) (Peng et al, 2015, Figure 4)* 153

***Figure B.9**: Pixel observation dimension as a function of view zenith angle (θv) (Wolfe et al., 1998, Figure 2a)* 154

***Figure B.10**: Three consecutive MODIS scans showing the "bowtie" effect (scan 2 is shaded) (Wolfe, 1998, Figure 2b)* 154

***Figure B.11**: Relationship between irregular observation space and fixed-pixel projected grid space (Montano, 2015, Figure 1.1)*.....155

***Figure B.12**: ModisSwath Tool Graphic User Interface*.....158

***Figure B.13**: Step of selecting bands for re-projection*.....158

***Figure B.14**: Steps for spatial subsetting*.....159

***Figure B.15**: Step for selecting resampling option*.....159

***Figure B.16**: Geometric orientation of satellite sensor grid and re-projected output image grid*.....162

***Figure B.17**: MODIS gridded tiles covering the earth's surface*.....162

***Figure B.18**: Overlapping of an observation in a fixed grid cell (Wolfe et al., 1998, Figure 5)*.....163

***Figure D.1**: Grid cells with contaminated pixels for MODIS image (fields US-Ne1 in left and US-Ne2 in right) from 05/05/12*.....171

***Figure D.2**: Grid cells with contaminated pixels for MODIS image (fields US-Ne1 in left and US-Ne2 in right) from 05/10/12*.....172

***Figure D.3**: Grid cells with contaminated pixels for MODIS image (fields US-Ne1 in left and US-Ne2 in right) from 05/14/12*.....172

***Figure D.4**: Grid cells with contaminated pixels for MODIS image (fields US-Ne1 in left and US-Ne2 in right) from 05/16/12*.....173

***Figure D.5**: Grid cells with contaminated pixels for MODIS image (fields US-Ne1 in left and US-Ne2 in right) from 05/21/12*.....173

***Figure D.6**: Grid cells with contaminated pixels for MODIS image (fields US-Ne1 in left and US-Ne2 in right) from 06/02/12*.....174

***Figure D.7**: Grid cells with contaminated pixels for MODIS image (fields US-Ne1 in left and US-Ne2 in right) from 06/04/12*.....174

***Figure D.8**: Grid cells with contaminated pixels for MODIS image (fields US-Ne1 in left and US-Ne2 in right) from 06/11/12*.....175

***Figure D.9**: Grid cells with contaminated pixels for MODIS image (fields US-Ne1 in left and US-Ne2 in right) from 06/18/12*.....175

***Figure D.10**: Grid cells with contaminated pixels for MODIS image (fields US-Ne1 in left and US-Ne2 in right) from 06/22/12*.....176

***Figure D.11**: Grid cells with contaminated pixels for MODIS image (fields US-Ne1 in left and US-Ne2 in right) from 06/24/12*.....176

***Figure D.12**: Grid cells with contaminated pixels for MODIS image (fields US-Ne1 in left and US-Ne2 in right) from 06/27/12*.....177

***Figure D.13**: Grid cells with contaminated pixels for MODIS image (fields US-Ne1 in left and US-Ne2 in right) from 07/03/12*.....177

***Figure D.14**: Grid cells with contaminated pixels for MODIS image (fields US-Ne1 in left and US-Ne2 in right) from 07/04/12*.....178

***Figure D.15**: Grid cells with contaminated pixels for MODIS image (fields US-Ne1 in left and US-Ne2 in right) from 07/06/12*.....178

***Figure D.16**: Grid cells with contaminated pixels for MODIS image (fields US-Ne1 in left and US-Ne2 in right) from 07/10/12*.....179

***Figure D.17**: Grid cells with contaminated pixels for MODIS image (fields US-Ne1 in left and US-Ne2 in right) from 07/13/12*.....179

***Figure D.18**: Grid cells with contaminated pixels for MODIS image (fields US-Ne1 in left and US-Ne2 in right) from 07/17/12*.....180

***Figure D.19**: Grid cells with contaminated pixels for MODIS image (fields US-Ne1 in left and US-Ne2 in right) from 07/19/12*.....180

***Figure D.20**: Grid cells with contaminated pixels for MODIS image (fields US-Ne1 in left and US-Ne2 in right) from 07/20/12*.....181

***Figure D.21**: Grid cells with contaminated pixels for MODIS image (fields US-Ne1 in left and US-Ne2 in right) from 07/22/12*.....181

***Figure D.22**: Grid cells with contaminated pixels for MODIS image (fields US-Ne1 in left and US-Ne2 in right) from 07/24/12*.....182

***Figure D.23**: Grid cells with contaminated pixels for MODIS image (fields US-Ne1 in left and US-Ne2 in right) from 07/26/12*.....182

***Figure D.24**: Grid cells with contaminated pixels for MODIS image (fields US-Ne1 in left and US-Ne2 in right) from 07/29/12*.....183

***Figure D.25**: Grid cells with contaminated pixels for MODIS image (fields US-Ne1 in left and US-Ne2 in right) from 08/02/12*.....183

***Figure D.26**: Grid cells with contaminated pixels for MODIS image (fields US-Ne1 in left and US-Ne2 in right) from 08/04/12*.....184

***Figure D.27**: Grid cells with contaminated pixels for MODIS image (fields US-Ne1 in left and US-Ne2 in right) from 08/05/12*.....184

***Figure D.28**: Grid cells with contaminated pixels for MODIS image (fields US-Ne1 in left and US-Ne2 in right) from 08/09/12*.....185

***Figure D.29**: Grid cells with contaminated pixels for MODIS image (fields US-Ne1 in left and US-Ne2 in right) from 08/20/12*.....185

***Figure D.30**: Grid cells with contaminated pixels for MODIS image (fields US-Ne1 in left and US-Ne2 in right) from 08/21/12*.....186

***Figure D.31**: Grid cells with contaminated pixels for MODIS image (fields US-Ne1 in left and US-Ne2 in right) from 08/27/12*.....186

***Figure D.32**: Grid cells with contaminated pixels for MODIS image (fields US-Ne1 in left and US-Ne2 in right) from 08/30/12*.....187

***Figure D.33**: Grid cells with contaminated pixels for MODIS image (fields US-Ne1 in left and US-Ne2 in right) from 09/05/12*.....187

***Figure D.34**: Grid cells with contaminated pixels for MODIS image (fields US-Ne1 in left and US-Ne2 in right) from 09/06/12*.....188

***Figure D.35**: Grid cells with contaminated pixels for MODIS image (fields US-Ne1 in left and US-Ne2 in right) from 09/08/12*.....188

***Figure D.36**: Grid cells with contaminated pixels for MODIS image (fields US-Ne1 in left and US-Ne2 in right) from 09/10/12*.....189

***Figure D.37**: Grid cells with contaminated pixels for MODIS image (fields US-Ne1 in left and US-Ne2 in right) from 09/15/12*.....189

***Figure D.38**: Grid cells with contaminated pixels for MODIS image (fields US-Ne1 in left and US-Ne2 in right) from 09/22/12*.....190

***Figure D.39**: Grid cells with contaminated pixels for MODIS image (fields US-Ne1 in left and US-Ne2 in right) from 10/21/12*.....190

Figure F.1: *Annual baseline precipitation rate and multiplier rates from 1950 to 2013 for the Gothenburg weather station data*.....194

***Figure F.2**: Average annual precipitation of baseline run and runs with multipliers applied* 194

***Figure F.3**: Response of DP to a range of precipitation multipliers for irrigated and non-irrigated maize*.....195

***Figure F.4**: Response of ET to precipitation multipliers for irrigated and non-irrigated maize* 195

***Figure F.5**: Response of DP to precipitation multipliers for different crop types*.....196

***Figure F.6**: Responses of RO to precipitation multipliers for different crop types* 196

***Figure F.7**: Response of NIR to precipitation multipliers for different crop types*.....197

***Figure F.8**: Response of DP to changes in precipitation multipliers for soil types*.....197

***Figure F.9**: Responses of RO to variations in the Precipitation multipliers for different soil types* 198

***Figure F.10**: Response of DP to varying multipliers of precipitation for soils with different Water Holding Capacity* 198

***Figure G.1**: Baseflow comparison at the North Platte gaging station. (a) monthly baseflow and (b) cumulative annual baseflow*.....201

***Figure G.2**: Baseflow comparison at the Brady gaging station (a) monthly baseflow and (b) cumulative annual baseflow*.....202

***Figure G.3**: Baseflow Comparison at the Cozad Gaging Station (a) monthly baseflow and (b) cumulative annual baseflow*.....203

***Figure G.4**: Baseflow comparison at the Overton gaging station (a) monthly baseflow and (b) cumulative annual baseflow*.....204

***Figure G.5**: Baseflow comparison at the Odessa gaging station (a) monthly baseflow and (b) cumulative annual baseflow*.....205

***Figure G.6**: Baseflow Comparison at the Grand Island Gaging Station (a) monthly baseflow and (b) cumulative annual baseflow*.....206

***Figure G.7**: Baseflow comparison at the Duncan gaging station (a) monthly baseflow and (b) cumulative annual baseflow*.....207

TABLE OF TABLES

***Table 2.1**: Results of error matrix and Kappa analysis between NEG method and ground truth data from the 2010, 2014, and 2015 growing seasons* 29

***Table 2.2**: NEG COHYST estimated irrigated acreages (ha) and percentage from total irrigated acreages for the main crops grown in COHYST model region in the 2015 growing season* 32

***Table 2.3**: Coefficient of determination (R^2), MAPE and RMSE between NASS and NEG estimated county irrigated area for 2015 and 2010* 33

***Table 3.1**: MODIS estimated and field ground truth LAI values for field US-Ne1* 71

***Table 3.2**: MODIS estimated and field ground truth LAI values for field US-Ne2* 71

***Table 3.3**: Statistical comparison of LAI estimates from footprint and gridded data for field US-Ne1 and US-Ne2 (LAI equation of Myneni et al.)* 72

***Table 3.4**: Statistical comparison of fields with gap filled LAI data* 74

***Table 3.5**: MODIS estimated (equation of Viña et al.) and field ground truth Green LAI values for field US-Ne1* 76

***Table 3.6**: MODIS estimated (equation of Viña et al.) and field ground truth Green LAI values for field US-Ne2* 77

***Table 3.7**: Statistical comparison of Green LAI estimates from footprint and gridded data for field US-Ne1 and US-Ne2* 77

***Table 3.8**: Statistical comparison of fields with gap filled Green LAI data* 79

***Table 3.9**: Statistical parameters and final p-value computed for MODIS LAI estimated using Myneni et al. LAI equation* 82

***Table 3.10**: Statistical parameters and final p-value computed for MODIS LAI estimated using Viña et al. LAI equation* 83

***Table 4.1**: Yearly precipitation volume of WSI and gridded Data in groundwater model area* 106

***Table 4.2**: Annual groundwater recharge volume determined from WSI and gridded precipitation data for the model coverage area* 113

***Table 4.3**: Response of hydrologic components in flux rates to variable precipitation multipliers* 127

***Table 4.4**: Response of hydrologic components in percent change of flux rates to variable precipitation multipliers* 128

***Table 4.5**: Response of model baseflow in annual average volume to variable precipitation multipliers at different gage locations* 132

***Table 4.6**: Response of model baseflow in percent change to variable precipitation multipliers at different gage locations* 132

***Table A.1**: Landsat scene identification (ID), acquisition spacecraft and date, and path and row of images used for the project* 143

***Table C.1**: LAI values for center pivot maize field US-Ne1 determined from MODIS data and field samples.* 167

***Table C.2**: LAI values for center pivot maize field US-Ne2 determined from MODIS data and field samples.* 168

***Table C.3**: LAI values for center pivot maize field US-Ne1 determined from MODIS data and field samples* 169

***Table C.4**: LAI values for center pivot maize field US-Ne2 determined from MODIS data and field samples* 170

***Table F.1**: Response of hydrologic components in flux rates to variable precipitation multipliers* 199

***Table F.2**: Response of hydrologic components in percent change of flux rates to variable precipitation multipliers* 200

***Table G.1**: Response of model baseflow in annual average volume to variable precipitation multipliers at different gage locations* 208

***Table G.2**: Response of model baseflow in percent change to variable precipitation multipliers at different gage locations* 208

CHAPTER 1: INTRODUCTION

1.1 Problem Statement

Although 71% of the earth's surface is covered with water, only 2.5% is fresh water. Since 1.7% is in the form of glaciers and polar ice caps, only 0.8% is readily available for use [1]. As the population of the world is rapidly growing and is projected to reach over nine billion by the year 2050, there is a need to efficiently manage water resources so that there is a sustainable balance between fresh water demands and water availability. However, water resources assessments of the last two decades have made it clear that the challenges that we face in the field of water resources are ever increasing. Due to natural and human induced stresses in the environment, there is a risk of depletion of the water resources on which humans are highly dependent.

The projected impact of climate change on agriculture is diverse and may cause substantial economic damage. The redistribution of rainfall events is expected to have a major impact on agriculture as storms become shorter and more intense [2]. There already exist conflicts related to water resources, both locally and internationally. For example, countries in the Nile River basin are wrangling over water consumption, and the sharing of water from the Jordan River in the Middle East is getting acrimonious. In the United States of America, the states situated above the High Plains Aquifer are involved in water lawsuits related to over consumption of surface and groundwater for agriculture. Litigation between downstream and upstream users has placed restrictions on the amount of water available to growers in the Republican and Platte River Basins. The Kansas vs. Nebraska suit, Pumpkin Creek conflict, Platte River Cooperative Agreement, South Platte River Compact and the

Republican River Compact are examples of water conflicts between upstream and downstream users [3,4].

Nebraska is predominately an agricultural state and the state's economy relies heavily on agricultural productivity. The majority of land use in the state is for the purpose of agriculture, and irrigation demands account for about 71% of the total water use. The value of the land in this area is strongly dependent on the water rights associated with the land. Due to increasing industrial and municipal usage and environmental regulations, the availability of water for agriculture is declining [5].

In recent years there has been increasing concern about water availability and water sharing in Nebraska, and water supplies and use have come under increased scrutiny. The sustainability of water resources in the long-term is threatened by many years of consecutive drought and overexploitation of groundwater [6]. The drought of 2002, the third driest year in a 108-year record [7], is estimated to have caused losses of up to eleven billion dollars [5]. The long-term viability of water resources is even more threatened by the combination of several years of drought and unsustainable pumping of groundwater supplies. For instance, litigation between "downstream" and "upstream" users has resulted in restrictions on the amount of water available to growers. Recently, some growers are being limited to pumping only 50% to 70% of the full-water requirement for maximum yield, forcing adoption of deficit irrigation strategies in response to limited water resources [6].

Sustainable agriculture and development in the region will depend upon the development of the framework for resolving these water resources issues. State and federal water regulatory agencies are searching for reliable and robust techniques to determine

hydrologic balances in major basins in the state. An efficient and accurate determination of the water balance in major watersheds is needed for better planning and for quantifying the current water supply, availability, consumption and future allocation [6]. For this we need to develop better analysis tools and better models; we also need to secure better data to model and bring major benefits in the long run [8].

The scientific and engineering community is compelled to research and develop methods that reliably and accurately predict environmentally sustainable water consumptive use by agriculture, power generation, industrial sector municipalities and ecological conservation. Of these conjunctive users, irrigated agriculture consumes the largest share of available fresh water resources. Therefore, application rates and spatial distribution of irrigation is paramount information for successful modeling and management of water resources. Long term monitoring and classification of irrigated and non-irrigated fields at refined spatial scales are needed to generate land use data with more accuracy and for better estimation of crop water consumptive use. More refined and accurate land use data when used as inputs can produce a highly robust and well calibrated water resources model for water balance study and analysis.

There is a need to develop an irrigation classification method which can be applied to remotely sensed satellite images with refined spatial resolution, generate phenological contrast over irrigated and non-irrigated surfaces, and produce maps of irrigated and non-irrigated classified fields in high spatial resolution. Such a method should be applicable in many regions for a wide range of climates and growing season variabilities.

Whether at the scale of monitoring global agricultural production or maximizing yield for an individual field, Landsat imagery has played an important role in informing

management decisions [9]. The disadvantage of Landsat satellite images is their temporal resolution with time intervals between replicate images of around two weeks. Therefore, in a given month only two images can be retrieved for any particular location. If weather conditions are not ideal during the satellite overpass (e.g., cloudy conditions) images will not be as useful for analysis. Monitoring of agricultural fields on a more frequent basis is needed to study and analyze the response of crops to environmental stress. Terra and Aqua MODIS satellites provide frequent images (daily) for an area coverage. With coarse spatial resolution of 250m, 500m, and 1000m for different bands, they are used for studying land cover characteristics at regional, continental, and global scales. The opportunity to take advantage of the higher temporal resolution of MODIS satellite images for more frequent and long-term monitoring and analysis of agricultural fields needs to be explored. The possibility of applying MODIS satellite images for field scale analysis needs to be tested.

Traditionally, precipitation maps have been generated by interpolating precipitation data between weather stations. The quality of these maps depends on the density of proximate weather stations. The spatial patterns of precipitation in these maps are simplistic, and any variations in precipitation that occur between weather stations are not captured in the maps. Data from the maps are used as inputs in water resources models. Precipitation maps generated with remote sensing methods such as Radar Doppler technology are widely available. These maps capture spatial patterns of precipitation in much greater detail. There is an opportunity of using these remotely sensed gridded precipitation data in the field of water resources modeling. Before applying data from precipitation maps generated from remote sensing methods in water resources models, quality and quantity comparison of maps generated from weather station interpolation and

remote sensing methods is needed. Similarly, the sensitivity of water resources model outputs to precipitation rates needs to be understood.

1.2 Research Objectives and Outline of Dissertation

Remote sensing technology has the ability to capture and preserve hydrologic data at different spatial and temporal resolutions. The overall goal of this dissertation is to investigate hydrologic applications of remote sensing technology and to apply them in the field of water resources management.

To meet this goal, the following research objectives were identified:

1. Develop and test a method which is able to utilize Landsat Satellite images to classify irrigated and non-irrigated fields at field scales;
2. Explore the use of coarse resolution MODIS satellite images in field scale analysis, and develop a methodology to handle MODIS images for field scale analysis; and
3. Analyze the sensitivity of precipitation in water resources models to precipitation estimation methods, and explore the benefits and limitations of applying remotely sensed gridded precipitation data to water resources models

In Chapter 2, a remote sensing classification method was developed to classify and map the spatial distribution of irrigated and non-irrigated croplands. The research of this chapter was published in Remote Sensing Journal on December of 2017 [10]. The method integrates surface energy balance (SEB) partitioning and vegetation indices to classify irrigated and non-irrigated cropland at high spatial resolution. The phenological

characteristics of crop and soil moisture conditions are evaluated using the classification method. The objective of this study is to develop an irrigation classification method that

i. is applicable across a large region or multiple regions with climate patterns varying from humid to arid; and
ii. is adaptable to growing seasonal precipitation variation (dry, normal, and wet) without recalibration

The research in Chapter 3 explores the use of MODIS data (which have daily temporal resolution as compared to the 16-day coverage of Landsat data) for field scale studies. The MODIS data projected in gridded format do not preserve the geometric orientation of satellite sensor pixels spatially and are not suitable for field scale analysis due to the coarse spatial resolution of the MODIS bands (250m, 500m, and 1000m). In this chapter, a methodology was developed to project MODIS data in its original higher resolution format, which improves the usefulness of MODIS data for field scale analysis. The objectives of this research chapter are

i. to develop a methodology (referred to as the footprint method) that can project MODIS data while preserving the geometric orientation of satellite pixel data;
ii. to perform field scale accuracy assessment on MODIS data projected with the footprint method and conventional gridded data; and
iii. to explore the usefulness of MODIS data for agricultural water management at field scales

The research in chapter 4 explores the potential opportunities of using remotely sensed gridded precipitation data in water resources models. Precipitation is a major water budget

component in water resources models, and more accurate precipitation maps are in demand. Before replacing precipitation maps generated by interpolating data from weather stations (WSI) with maps generated by a combination of radar data and weather station data (gridded data) in water resources models, there needs to be a qualitative and quantitative comparison between them (WSI and gridded data). The limitations of WSI and the advantages of gridded data need to be explored. The objectives of this research chapters are to

i. Analyze the differences in spatial precipitation patterns and volumes of precipitation resulting from the application of WSI and gridded data precipitation maps
ii. Analyze the sensitivity of precipitation in a soil water balance model in relation to irrigation settings, crop types, and soil types
iii. Analyze the sensitivity of baseflow of a river system to the different precipitation models based on the output of a water resources model, and
iv. Analyze the WSI generated precipitation maps

1.3 References

1. Williams, M. What percent of Earth is water? PHYS.ORG, 2 December **2014**. Available online: https://phys.org/news/2014-12-percent-earth.html (accessed on Nov 23, 2019).
2. Mutiibwa, D. Identifying a 'Fingerprint' for Discriminating the Anthropogenic Components of Land Use/Land Cover Change on Climate Change. *Ph.D. proposal-University of Nebraska at Lincoln*. **2010**. Web. 30 May 2012.
3. Nebraska Department of Natural Resources (NDNR). Annual Report and Plan of Work for the Nebraska State Water Planning and Review Process. Nebraska Department of Natural Resources, 15 September **2007**. Available online:

http://govdocs.nebraska.gov/epubs/N1500/A004-2007.pdf (accessed on Nov 28, 2017).

4. Aiken, J.D. The Republican River: Negotiation, arbitration, and a federal water master. *Cornhusker Econ.* **2008,** 382. Available online: http://digitalcommons.unl.edu/agecon_cornhusker/382/
5. Hutson, S.S.; Barber, N.L.; Kenny, J.F.; Linsey, K.S.; Lumia, D.S.; Maupin, M.A. Estimated use of water in United States in 2000: Reston, Va. *U.S. Geological Survey Circular 1268*. **2004**, 46.
6. Singh, R. K. *Geospatial Approach for Estimating land Surface Evapotranspiration*. Diss. University of Nebraska, **2009**. Web. 24 June 2012.
7. National Climatic Data Center (NCDC). **2003**. Climate of 2002: Annual review, US. drought. http://lwf.ncdc.noaa.gov/oa/climate/research!2002/ann/droughtsummary.html (accessed April 15, 2013).
8. Kirchner, J.W. Getting the Right Answers for the Right Reasons: Linking Measurements, Analyses, and Models to Advance the Science of Hydrology. *Water resources Research.* **2006**, 42 (W03S04).
9. Leslie, C.R.; Serbina, L.O.; Miller, H.M. Landsat and agriculture—Case studies on the uses and benefits of Landsat imagery in agricultural monitoring and production. *U.S. Geological Survey Open-File Report 2017–1034*. **2017**, 27 https://doi.org/10.3133/ofr20171034.
10. Pun, M.; Mutiibwa, D.; Li, R. Land Use Classification: A Surface Energy Balance and Vegetation Index Application to Map and Monitor Irrigated Lands. *Remote Sens.* **2017**, 9, 1256. https://doi.org/10.3390/rs9121256.

CHAPTER 2: LAND USE CLASSIFICATION – A SURFACE ENERGY BALANCE AND VEGETATION INDEX APPLICATION TO MAP AND MONITOR IRRIGATED LANDS

2.1 Abstract

Irrigated agriculture consumes the largest share of available fresh water, and awareness of the spatial distribution and application rates is paramount to functional and sustainable communal consumptive water use. This remote sensing study leverages surface energy balance fluxes and vegetation indices to classify and map the spatial distribution of irrigated and non-irrigated croplands. The purpose is to introduce a classification method applicable across a wide variation in regional climate and inter-growing seasonal precipitation. The rationale for climate and inter-growing seasonal adaptability is founded in the derivation and calibration of the method based on the wettest growing season. Therefore, the method becomes a more efficient classifier during normal and dry growing seasons. Using empirical distribution functions, two indices are derived from evapotranspiration fluxes and vegetation indices to contrast and classify irrigated croplands from non-irrigated. The synergy of the two indices increases the classification proficiency by adding another classifying layer which re-characterizes misclassified croplands by the base index. The method was applied to a region with wide climate variation and to multiple years of growing seasons. The results presented, in cross validation with ground truth, show an accurate and consistent approach to classify irrigation with overall accuracy of 92.1%, applicable from humid to semi-arid climate, and from dry to normal and wet growing seasons.

2.2 Introduction

Water shortage is a growing major global concern due to increasing droughts, decreasing snow packs, and expanding municipalities, among other factors [1]. A renown hot-spot of potential conflict instigated by water shortage is the Nile basin hydro-political contention between the upper and lower riparian countries, driven by increasing population, environmental degradation, and decreasing river flow [2]. In the United States of America (USA), states that share the High Plains aquifer have filed litigations over surface water and groundwater consumption [3, 4]. These are just two of many international and regional contentions that highlight the urgency for informed solutions, planning, and policy making for sustainable management of water resources. The scientific and engineering community is therefore compelled to research and develop methods that reliably and accurately predict environmentally sustainable water consumptive use by agriculture, power generation, industrial sector, municipalities and ecological conservation. Of these conjunctive users, irrigated agriculture consumes the largest share of available fresh water resources. Therefore, application rates and spatial distribution of irrigation is paramount information for successful modeling and management of water resources.

Remote sensing, as a widely regarded methodology of resolving land use and land cover patterns over expansive areas, has been commended for mapping irrigated croplands [5]. Alexandris et al. [6] synoptically assessed several remote sensing indices, such as Normalized Difference Vegetation Index (NDVI), Normalized Difference Water Index (NDWI), and methods of determining irrigation status, including Principal Component Analysis (PCA), and supervised and unsupervised classification. The methods showed

good accuracy although they were constrained to arid or semi-arid regions where irrigated and non-irrigated areas exhibited high spectral contrast. Wardlow and Egbert [7] devised a decision tree classification technique on a time-series of MODIS NDVI, however the method was inadequate during above normal wet growing seasons. In an effort to avoid empirical thresholding in supervised classification, Jin et al. [8] used machine learning (Support Vector Machine) on maximum NDVI and Time Integrated NDVI to successfully classify irrigated wheat in a semi-arid region of China. And, in a multi-year study, Ambika et al. [9] classified irrigation using a hierarchal decision model on seasonal peak MODIS NDVI producing relatively accurate results across India. Other studies [10-12] have also taken advantage of MODIS NDVI's high temporal resolution and seamlessness to map irrigation status in several regions but with constrained seasonal and agro-regional climate applicability.

This study develops a remote sensing classification method that integrates surface energy balance (SEB) partitioning and vegetation indices to classify irrigated and non-irrigated croplands at high spatial resolution. The study exploits NDVI, a vegetation index that has been widely investigated as a diagnostic indicator of phenological development and health, and Green Index (GI) [13], a vegetation index described as the most sensitive index to phenological development [14]. Integration with SEB fluxes enables the classification method to account for soil moisture stress, and energy and mass exchange between the vegetation surface and the atmosphere over irrigated and non-irrigated surfaces. Because soil moisture is the mass exchanged, evaporative fluxes derived from SEB partitioning provide a synoptic assessment of soil moisture availability to meet the atmospheric evaporative demand over a vegetation surface. Soil moisture deficiency or

sufficiency of non-irrigated or irrigated surfaces, respectively, cause thermal and vegetative stresses that are distinctive in spectral and thermal signatures. Therefore, the phenological contrasts and variation in SEB fluxes over non-irrigated and irrigated surfaces are synergistically evaluated in this study to classify the two crop water management practices.

The Surface Energy Balance System (SEBS) algorithm [15] is used to partition SEB components from which an evaporative fraction index is derived and integrated with the NDVI and GI to derive two highly contrasting indices of irrigated and non-irrigated surfaces. The objective of this study is to develop an irrigation classification method that; (i) is applicable across a large region or multiple regions with climate patterns varying from humid to arid, and (ii) adaptable to inter-growing seasonal precipitation variation (dry, normal, and wet) without recalibration. The elimination of the need for recalibration is the vital uniqueness of the classification method developed by this study. The rationale for the seasonal adaptability of the method is that the thresholds calibrated during the wettest growing season, which spectrally is the most difficult growing season in which to distinguish between irrigated and non-irrigation surfaces, become more accurate classifiers during normal and dry growing seasons. Therefore, the method is a new approach expected to classify irrigated and non-irrigated croplands in a wide range of climate and growing season variability.

2.3 Materials and Methods

2.3.1 Study Area

The Cooperative Hydrology Study (COHYST) region is a hydrological model region located between the Loup River and the Republican River in the Platte River basin, upstream of Columbus, Nebraska, USA (Figure 2.1). Three watershed basins constitute the largest part of the COHYST region: the Platte River, Republican River, and Blue River basins. The region is a confluence of water conflicts from different water resources stakeholders with vying interests, including power generation, irrigation water distribution, municipal use, and conservation of endangered wildlife. Some of the endangered wildlife species in the region include the Whooping Crane, Least Tern, Piping Plover, and the Pallid Sturgeon. The region consists of about 5,007,677.3 ha, in 35 counties (Figure 2.1), and contains the most irrigated cropland in Nebraska. Much of the water for irrigation is drawn from the High Plains aquifer or diverted from the Platte River. Maize and soybeans are the most cultivated crops in the region, along with winter wheat, and grass/pasture for ranching (predominately in the northwest). The regional climate is characterized as humid to semi-arid continental climate along the east to west gradient of the interior midlatitude USA. Temperatures across the region vary widely. From an average winter minimum of −2.2 °C recorded at the Grand Island weather station, to an average summer maximum of 28 °C recorded at the York weather station [16]. Based on the 2000 to 2009 period, the average annual precipitation increases from 406 mm in the west to 711 mm in the east [17] with annual recorded amounts as low as 271 mm (2002).

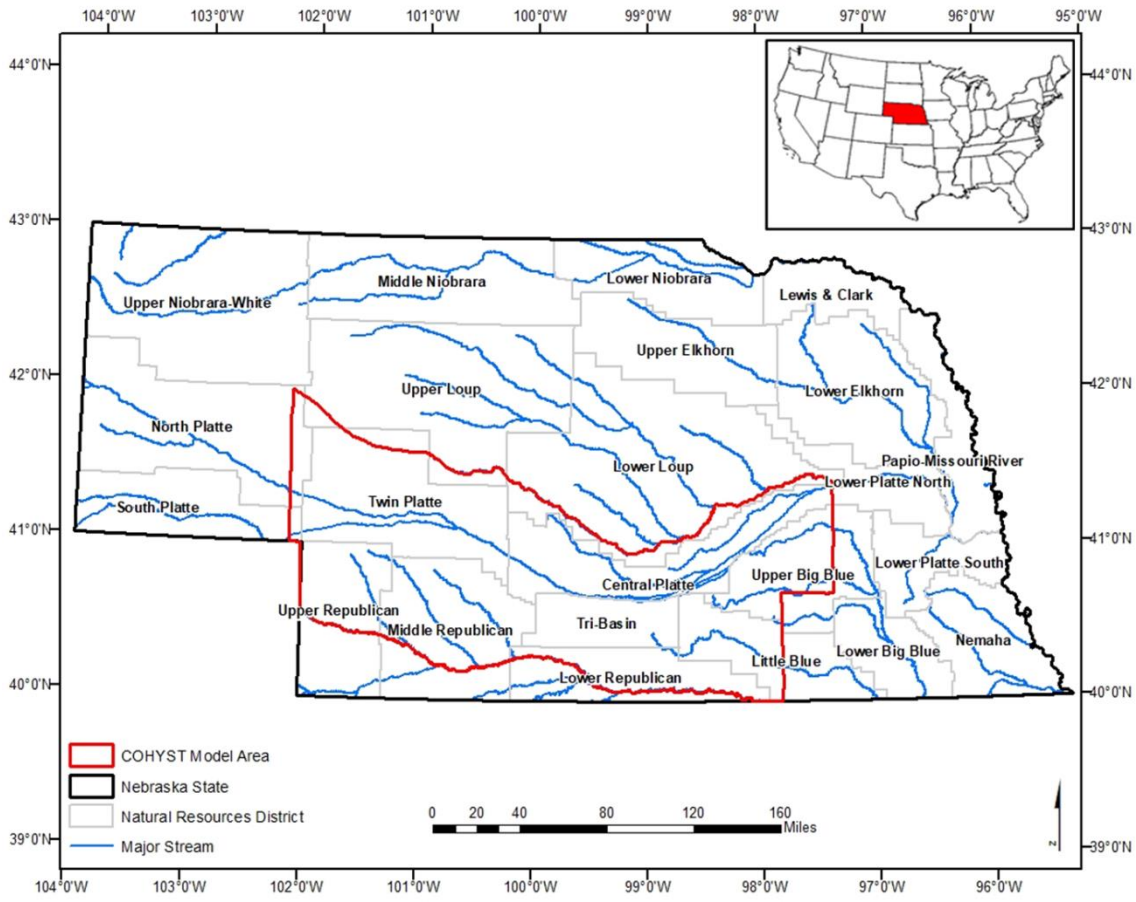

Figure 2.1: *Map of Nebraska showing the Cooperative Hydrology Study (COHYST) hydrological model region, rivers, and Natural Resources Districts (NRDs)*

2.3.2 Datasets

The hourly weather data used in SEBS were obtained from automated weather stations across the region (Figure 2.2) and downloaded from the High Plains Regional Climate Center (HPRCC) website (http://www.hprcc.unl.edu/). The instrumentation specifications for the measurement of air temperature, soil temperature, relative humidity, wind speed, wind direction, precipitation, and solar radiation are available on the HPRCC website (http://www.hprcc.unl.edu/awdn/ instruments/ manual.pdf). A Digital Elevation Dataset (DEM) at 10-m resolution was downloaded from the Nebraska Department of Natural

Resources website (http://www.dnr.ne.gov/elevation-data). The DEM data used in this study were resampled to a 30-m resolution using bilinear interpolation. Cropland Data Layer (CDL) [18] datasets available at 30-m resolution were retrieved from http://nassgeodata.gmu.edu/CropScape/. National Agricultural Statistics Service (NASS) county irrigation statistics were obtained from the USDA Farm Service Agency and were used as cross reference and verification of results on county aggregated irrigated croplands. Ground truth data were collected across the COHYST region during the growing seasons of 2010, 2014 (Figure 2.2), and 2015. A sampling team methodologically traversed the region surveying land cover and land use data which included date, location, irrigation status, irrigation type, and crop type. Sampled fields were identified based on pre-determined data needs and for accuracy assessment of irrigation classification. The data were logged directly into ArcGIS allowing quick geo-referencing in the field (Riverside Technology Inc., Fort Collins, CO, USA, [19]). In the 2010 growing season, 1103 locations (782 for irrigated and 321 for non-irrigated) were sampled. In the 2014 growing season, 464 irrigated and 355 non-irrigated were sampled, and in the 2015 growing season, 2246 locations were sampled, of which 611 were irrigated and 1635 were non-irrigated.

Landsat data were downloaded from the United States Geological Survey Global Visualization Viewer website (http://glovis.usgs.gov). The COHYST region is covered by an array of 8 Landsat scenes. For each scene two or three high quality images with the least cloud cover were downloaded to supplement each other in case of cloud contamination, and data striping. A total of 46 images were downloaded and processed for the study. Because the irrigation season in the region typically starts in mid-June and lasts until the end of August or early September (year 2010, 2014, and 2015), all images used in this

study were acquired during the same period. Priority for image selection was given to the least cloudy images acquired after a long period without rainfall. The path, row, acquisition date, scene and satellite identification (ID) are presented in Appendix, Table A1.

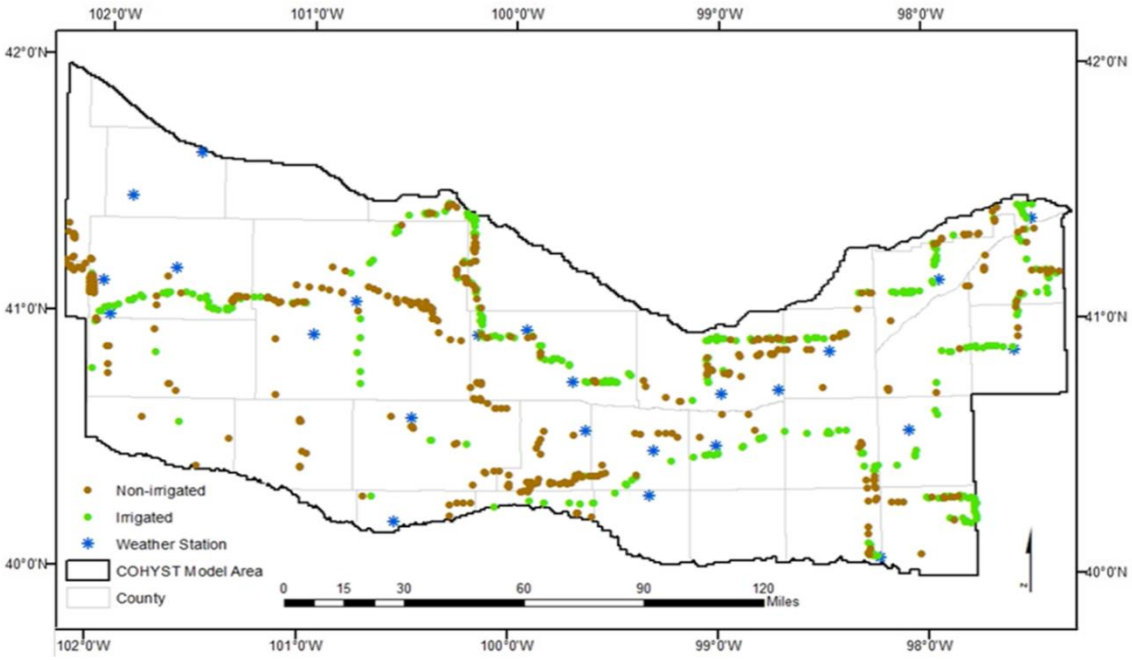

Figure 2.2: *Sampled irrigated (355) and non-irrigated (464) ground truth fields across the COHYST region during the 2014 growing season*

2.3.3 Calibration Growing Season

The purpose of this study was to develop a classification method that is reliable in most growing season wetness regimes. Recent wet, normal, and dry growing seasons in the COHYST region were identified using the National Oceanic and Atmospheric Administration (NOAA)—National Climatic Data Center (NCDC) climate monitoring portal (http://www.ncdc.noaa.gov/cag/). The time series of the regional average precipitation of June, July, and August from 1980 to 2017 was plotted (Figure 2.3) along with the long-term average of 1901–2000 (239.3 mm) and one and two standard deviations

about the mean. From the time series, 2015 was a normal growing season of 276.6 mm of rainfall, and 2012 was a dry year with 95 mm of rainfall during the growing season. The most recent wettest growing season with ground truth data was 2010 (362.7 mm), closely followed by 2014 (346.7 mm) (Figure 2.3). Both the 2010 and 2014 growing season rainfall were more than two standard deviations above the long term mean precipitation. For the derivation and calibration of the method, 2014 was selected as the wettest season over 2010, because, Landsat 8 imagery available for 2014 was of higher quality than Landsat 7 and 5 imagery available for 2010. In addition, the 2014 growing season had more sampled irrigated (464) and non-irrigated (355) fields than the 2010 growing season. A total of 213 irrigated fields and 280 non-irrigated fields across the region (Figure 2.2) were used for the development and calibration of the classification method. The remaining 142 (irrigated) and 184 (non-irrigated) fields were used for the validation of the classification method.

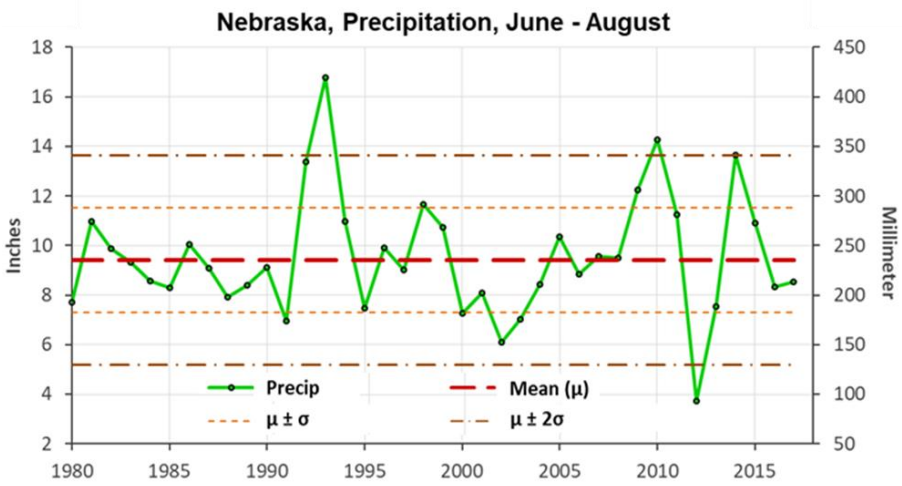

Figure 2.3: *Nebraska precipitation average for the months of June, July, and August from 1980 to 2017; 1901–2000 mean precip (μ: 239.3 mm); and the standard deviations (σ: 2.11 mm) about the mean. Data source: http://www.ncdc.noaa.gov/cag/time-series/us*

2.3.4 Normal Difference Vegetation Index and Green Index

NDVI and GI indices were computed from the top of the atmosphere (TOA) reflectance of green, red and near infrared spectral bands as shown below:

$$NDVI = \frac{\rho_{nir} - \rho_{red}}{\rho_{nir} + \rho_{red}} \quad (1)$$

$$GI = \frac{\rho_{nir}}{\rho_{green}} \quad (2)$$

where ρ_{green}, ρ_{red} and ρ_{nir} are TOA reflectance from band 2, band 3, and band 4, respectively, of Landsat 5 and 7, and band 3, band 4, and band 5, respectively, of Landsat 8. NDVI has been widely used as an important vegetation and irrigation monitoring tool [8, 11, 12, 20, 21, 22]. GI on the other hand, has been a less exploited vegetation index, yet studies [23, 24] have found the index more sensitive to chlorophyll than NDVI, Enhanced Vegetation Index (EVI) [25], and Wide Dynamic Range Vegetation Index (WDRVI) [26].

The high sensitivity of GI is due to the green leaves high absorption (more than 80%) in the green spectrum (e.g., [27-29]), and a much lower penetration (four to six times) of blue and red spectrum in the leaf canopy (e.g., [30]). Therefore, in the green spectrum, the absorption of light is adequately high to generate a highly sensitive GI to chlorophyll content but the absorption is much lower in the blue and red spectrum, thus preventing index saturation [13, 27].

2.3.5 Surface Energy Balance System (SEBS)

SEBS [15] is a physical model that uses the principle of conservation of energy (Equation (3)) to partition net available energy from the sun, (net radiation (Rn)) into the major surface energy components; soil heat (G), sensible heat (H) and latent heat (λE) flux.

$$Rn = \lambda E + H + G \tag{3}$$

Net radiation (Wm^{-2}) was calculated as the radiation balance of net shortwave and net long wave radiation [31-33]. Soil heat flux (Wm^{-2}) was estimated as a fraction of net radiation by an empirical function derived by Choudhury et al. [34], and the constants were calibrated by Monteith [35] and Kustas et al. [36]. Sensible heat flux (Wm^{-2}) was estimated using the similarity theory and solving a system of non-linear equations using the Broyden method [37]. The non-linear equations are similarity relationships for the profiles of friction velocity, Monin Obukhuv length, aerodynamic resistance, and mean temperature (i.e., the difference between surface temperature and air temperature). The procedure to derive sensible heat flux is methodically described in [15] and requires only wind speed, temperature at a reference height and surface temperature as inputs.

SEBS estimates latent heat flux (evapotranspiration) by interpolating the relative evaporation between the dry-limit and wet-limit [15]. Under the dry-limit, latent heat flux becomes zero due to the limitation of soil moisture, and sensible heat flux is assumed to be at a maximum. Under the wet-limit, latent heat flux is at potential rate limited only by the available energy under the given surface and atmospheric conditions, and sensible heat flux is assumed to be at a minimum. The SEBS evaporative fraction (ETRF) used to derive the irrigation classification index in this study was estimated using Equation (4). SEBS

estimates ETRF in the range of 0 to 1 [15]. The normalization of λE by $Rn - G$ serves to reduce the impact of drivers of the evaporative flux that are less directly related to soil moisture stress (e.g., insolation load and atmospheric demand), [38].

$$ETRF = \frac{\lambda E}{Rn - G} \quad (4)$$

The SEBS model inputs are surface emissivity, albedo, surface temperature, and NDVI. These inputs were processed from spectral reflectance and radiance of Landsat optical and thermal bands. The other inputs include weather station variables, air temperature, air pressure, relative humidity, wind speed, and measurement height, and day-of-year and time of (Landsat) overpass.

2.3.6 Irrigation Indices Development

In this procedure several indices were evaluated, some from the literature and some new composites. The procedure was to statistically evaluate the probability distributions of the indices and select the most effective classifiers. They were evaluated as the most effective classifiers of irrigation croplands in the region by assessing their sensitivity to irrigation.

An ideal index in this study was expected to generate a bimodal distribution function that separated irrigated from non-irrigated pixels during the growing season of year 2014. Two compound indices EGI and NGI were derived from GI, ETRF, and NDVI as shown in Equation (5) and Equation (6), respectively.

$$EGI = \frac{ETRF}{GI} \quad (5)$$

$$NGI = NDVI * GI \quad (6)$$

Other vegetation indices and combinations that were tested during the procedure were:

Vegetation indices: NDVI, EVI, GI, ETRF, Surface Temperature (Temp.), Albedo, maximum NDVI, cumulative NDVI, cumulative ETRF, maximum daily λE, and cumulative daily λE

Combinations of vegetation indices: [ETRF $*$ NDVI $*$ GI], [$Temp.*$ ETRF] , [Temp.$*$ NDVI], $\left[\frac{ETRF}{NDVI}\right]$, and $\left[\frac{Temp.}{ET*NDVI*Albedo}\right]$

Non-agricultural areas such as cities, forests, conservation ecological areas, and water features were masked from the indices using CDL data from the 2014 growing season. Using ground truth data from the 2014 growing season, irrigated and non-irrigated pixels of an index were extracted, and distribution functions were then fit to the irrigated pixels, non-irrigated pixels, and all pixels combined as shown in Figure 2.4.

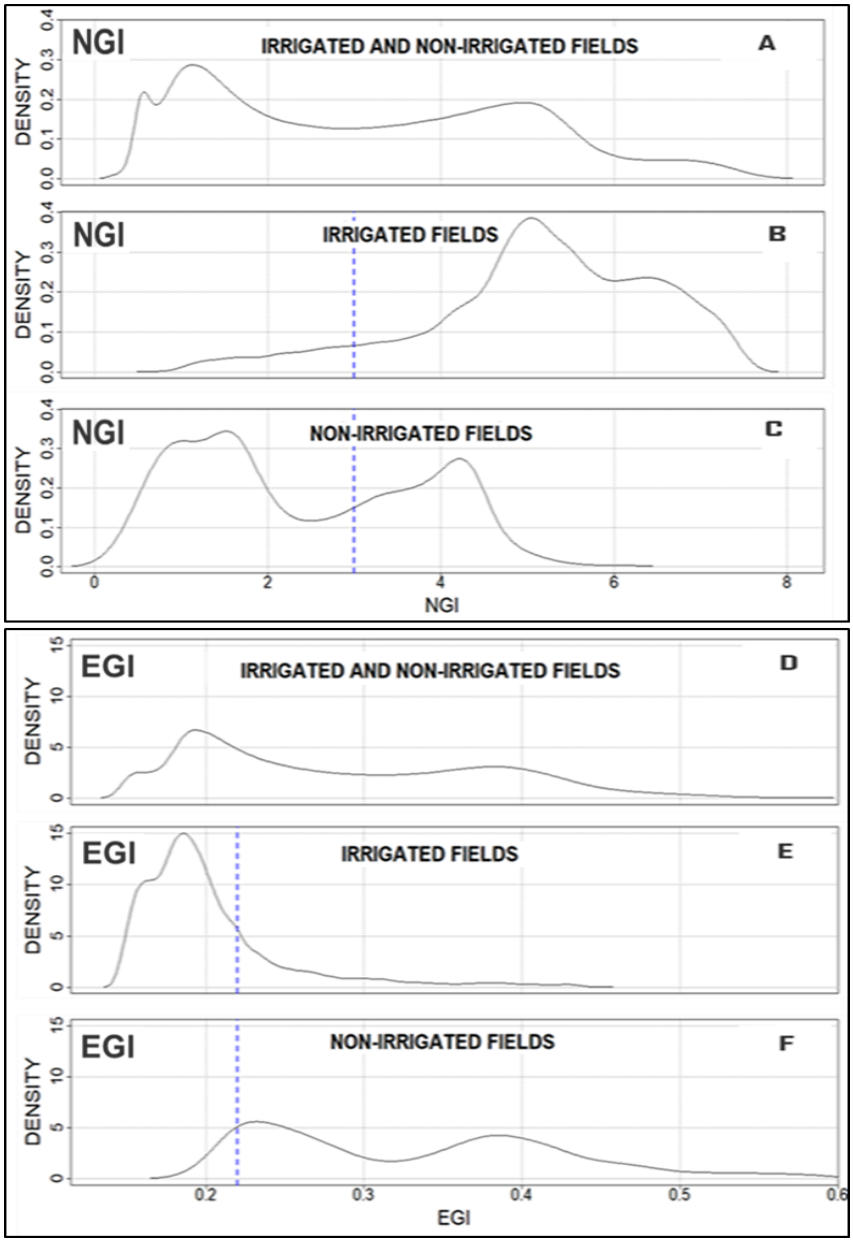

Figure 2.4: *Empirical distributions of NGI and EGI indices for all fields combined (Irrigated and non-irrigated areas), irrigated, and non-irrigated areas. Blue lines indicate the threshold values of NGI and EGI*

Most derived indices formed an empirical bimodal distribution (as shown in Figure 2.4-A and D) on a mixture of irrigated and non-irrigated croplands, however distance between the two modes varied with precipitation amounts. The thickness of the middle section of

the distribution is a variable of water stress difference between irrigated and non-irrigated crops. In the wet season, the two peaks of distribution overlap more, since the difference in vegetation covers of irrigated and non-irrigated croplands is insignificant. In the wet season or humid areas, the middle section is much thicker since the vegetation canopy of non-irrigated crops is usually insignificantly different from irrigated crops, though the yield may differ at the end of the growing season. During the dry season or arid climate, there is less overlap between the two peaks since the vegetation cover of non-irrigated and irrigated cropland is usually significantly different. The middle section is thin since the vegetation canopy of non-irrigated crops is significantly different from irrigated crops. Most of the vegetation indices and their combination tested produced the same fashion of distribution, but the middle section which is key to the methodology were thicker compared to NGI and EGI, especially in the wet season.

NGI and EGI indices discriminated irrigation from non-irrigation better than the standard indices. They generated the widest distribution contrast between irrigated and non-irrigated conditions in 2014, and were ultimately selected for the classification method. Figure 2.4-A shows the bimodal distribution of NGI for both irrigated and non-irrigated pixels combined. The NGI distribution function isolated irrigated pixels to the right with a long tail to the left (Figure 2.4-B). The NGI distribution function isolated most of the non-irrigated pixels to the left, with a bimodal function and short tail to the right. By comparing the *x*-axes of Figure 2.4-B and C, it is clear that most non-irrigated pixels were isolated to the long tail section of the irrigated distribution. Similarly, Figure 2.4-D shows the bimodal distribution of EGI for both irrigated and non-irrigated pixels combined.

However, in a reverse fashion, this distribution isolated irrigated pixels to the left and non-irrigated to the right (Figure 2.4-E and F).

2.3.7 Thresholding

Although both indices showed contrast between irrigated and non-irrigated pixels, there was still some overlap of irrigated and non-irrigated pixels in the middle of the distributions. For the NGI distribution, most of the irrigated pixels had values of greater than 4 (Figure 2.4-B), and most non-irrigated pixels had values of less than 5 (Figure 2.4-C), with significant overlap between index values 2 and 5, which is the mid-section of the bimodal distribution (Figure 2.4-C). For the EGI distribution, most of the irrigated pixels had values of less than 0.25 (Figure 2.4-E), and most non-irrigated pixels had values of greater than 0.20 (Figure 2.4-F), with significant overlap between index values 0.2 and 0.28. Therefore, to improve the identification of irrigated pixels, the two indices were combined to take advantage of their distribution properties of contrasting irrigation from non-irrigation status.

The distinguishing characteristics of the two indices were combined by first applying a preliminary first threshold of NGI < 3 to exclude non-irrigated pixels (Figure 2.4-C). Then the remaining non-irrigated pixels were eliminated by applying a second threshold of EGI > 0.22 (Figure 2.4-F). The two thresholds (NGI = 3 and EGI = 0.22) were calibrated by iterating in the middle of the bimodal distribution, where the irrigated and non-irrigated pixels overlapped, using a computer program (in Python) until the combination of the two thresholds accurately classified all irrigated and non-irrigated fields in the ground truth data. Figures 2.5 show the

distribution of NGI for irrigated (Figure 2.5-A) and non-irrigated (Figure 2.5-B) pixels after the calibrated thresholds were applied to all fields in the region.

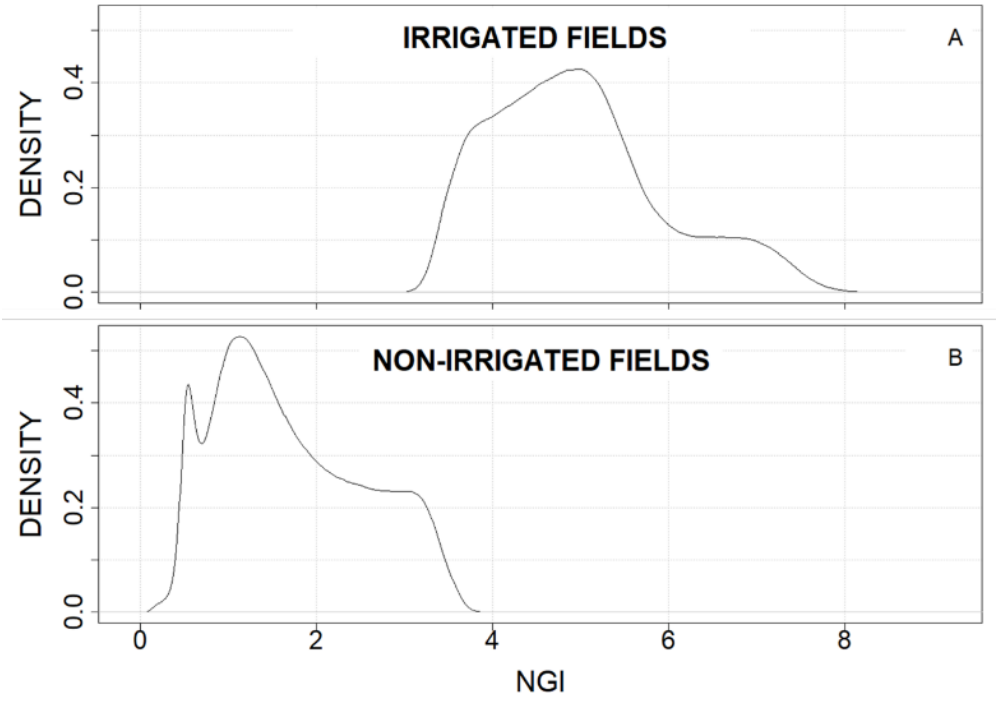

Figure 2.5: *Empirical distributions of NGI index for irrigated and non-irrigated areas after the classification method has been applied*

A conceptual flow diagram (Figure 2.6) describes the implementation of the method, including the data inputs, derivation of the indices, and thresholding of indices. Methodically, ETRF from SEBS, NDVI, and GI, are derived separately, and are formulated into EGI and NGI. A crop mask from CDL for the growing season is applied on the two indices to remove non-agricultural areas. The NGI as the base index, cycles through the first threshold, NGI threshold to remove non-irrigated pixels. The remaining non-irrigated pixels in NGI are then removed, conditioned with the EGI threshold. As shown in Figure 2.6, the pixels which are not selected as irrigated areas from the two threshold cycles are

combined to identify the non-irrigated fields. The entirety of the method in Figure 2.6 is also referred to hereafter as the NDVI-Evaporation Fraction-Green Index (NEG) classification method.

2.3.8 Performance Assessment

The derived classification method was validated and evaluated for the growing seasons of 2010, 2014, and 2015, which had ground truth data on irrigation status in the COHYST region. The performance of the classification method was evaluated using Kappa analysis, confusion (error) matrix referenced to ground truth data, the coefficient of determination (R^2) as a measure of goodness of fit (i.e., the measure of variance in NASS county data accounted for by NEG county aggregated estimates), Root Mean Square Deviation (RMSD) as a measure of the absolute difference between NASS and NEG, and Mean Absolute Percent Error (MAPE) as a measure of NEG accuracy in percentage terms (Equation (7)), where N is the number of counties. Note, the counties partitioned by the COHYST boundary were excluded from the NASS-NEG county performance assessment.

$$MAPE = \frac{1}{N}\sum\left(\frac{|NASS - NEG|}{NASS}\right) * 100 \quad (7)$$

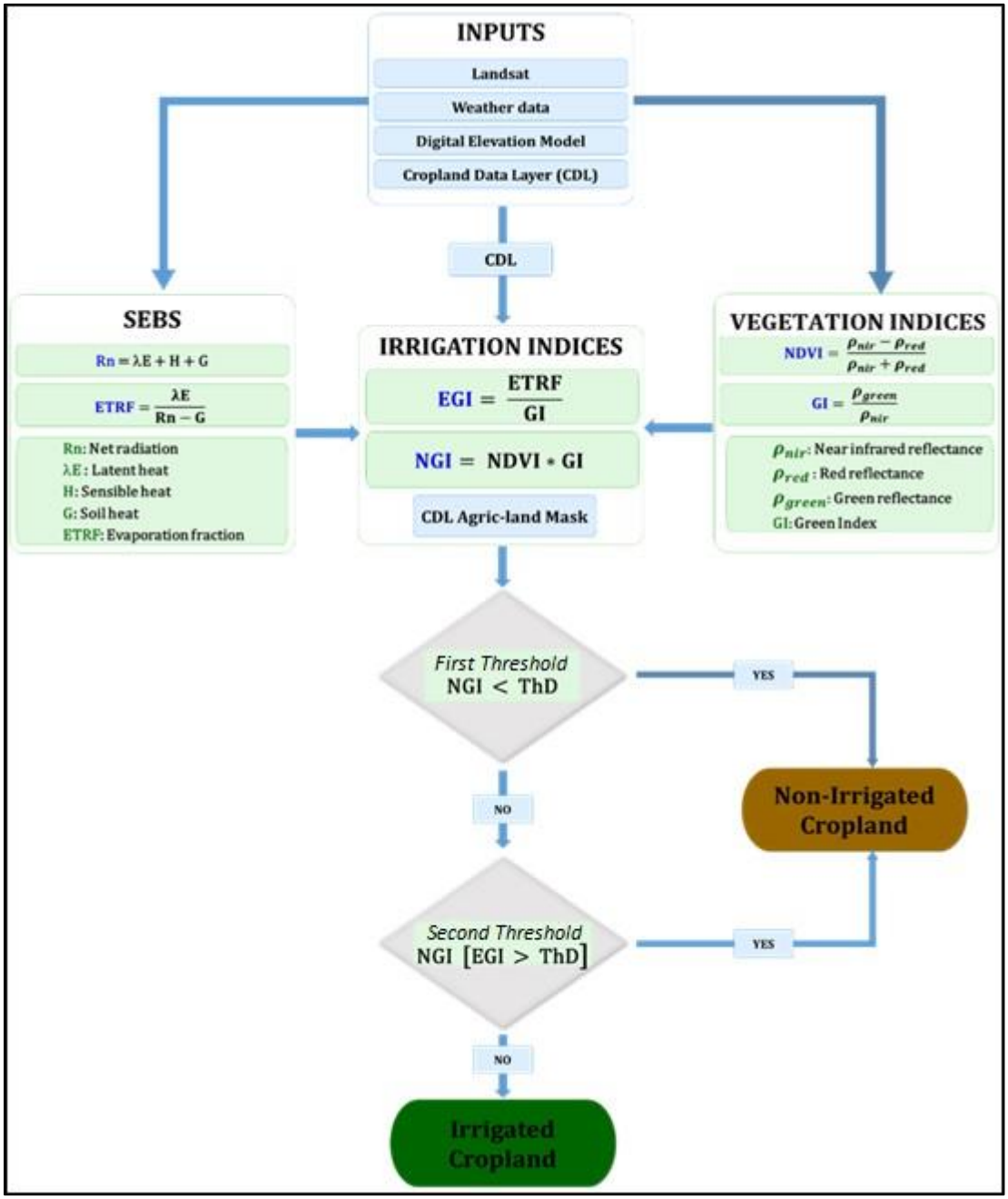

Figure 2.6: *NDVI-Evaporation Fraction-Green Index (NEG) Irrigation classification method flow diagram. Thd = Threshold*

2.4 Results

2.4.1 NEG Classification Method and Ground Truth

The NEG classification method was validated with ground truth data available from the growing seasons of 2010, 2014, and 2015. The year 2014 was a calibration year where half of data was used for calibration and other half used for validation. The results from the error matrix analysis in reference to ground truth for the three years area presented in Table 2.1. Producer's Accuracy in Table 2.1 represents how often real features on the ground are correctly shown on the classified map. It is the number of reference sites classified accurately divided by the total number of reference sites for that class. User's Accuracy represents how often the class on the map will actually be present on the ground. It is calculated by taking the total number of correct classifications for a particular class and dividing it by the row total [39].

In 2015, a normal year of precipitation during the growing season, 93% (i.e., 567 of 611) of NEG irrigated fields and 86% (i.e., 1402 of 1635) of non-irrigated fields matched ground truth data. In 2014, a wet year, the method had a performance of 98% (i.e., 453 of 464) of NEG irrigation fields and 83% (i.e., 294 of 355) of non-irrigated fields matching ground truth data. In 2010, also a wet year during the growing season, 90% (i.e., 704 of 782) of NEG irrigated fields and 81% (i.e., 260 of 321) of non-irrigated fields matched ground truth data. The overall accuracy of classifying irrigation for the three years combined was 92.1%. The lower producer accuracy for the non-irrigated croplands in Table 2.1 was because some of the non-irrigated ground truth locations were sampled from the corners of center pivot fields. If these points were within 60m of a pivot circle, they were sometimes misclassified as irrigated.

Table 2.1: *Results of error matrix and Kappa analysis between NEG method and ground truth data from the 2010, 2014, and 2015 growing seasons*

Year	Irrigation Status	Producer's Accuracy (%)	User's Accuracy (%)	Overall Accuracy (%)	Kappa Value
2010	Irrigated	90	92	87	0.70
	Non-irrigated	81	77		
2014	Irrigated	98	88	91	0.82
	Non-irrigated	83	96		
2015	Irrigated	93	71	88	0.72
	Non-irrigated	86	97		

2.4.2 Spatial Distribution of Irrigation

NEG method was applied in the COHYST region and agricultural fields were classified irrigated and non-irrigated for year 2010, 2014, and 2015. As shown in Figure 2.7, the COHYST region has extensive irrigation in the east that diminishes in the western part of the region (Figure 2.7). York and Hamilton counties, both in the east, were the most irrigated counties with more than 70% of county area classified as irrigated cropland. In the northwest of the region a few scattered fields were classified as irrigated. The most irrigated crop in the northwest was alfalfa; for instance, in Arthur and Garden counties, 58.3% and 60.6% of irrigated cropland was alfalfa during the 2015 growing season. In McPherson County, however, pasture was the most irrigated crop at 42%. Across the region, a total of 1,606,008 ha in 2015 and 1,462,004 ha in 2010 were classified as irrigated, many of which were maize and soybean.

The extent and intensity of irrigation in a region depends on four key factors: rainfall, water accessibility, topography, and soil type. The northwest, as part of the Nebraska Sandhills, is mostly sandy soils and semi-arid conditions. During the three months (June, July, and August) of intensive irrigation in the region, rainfall distribution across the region decreases from east to west by 89 mm (239 to 328mm), Figure 2.8. The difference in

rainfall across the state is significant given that the average seasonal evapotranspiration for irrigated maize is 548 mm and 452 mm for soybeans [40]. Precipitation is a constraining factor, but aside from water availability the main limiting factor of irrigation expansion in the west is the nutrient-deficiency and low water holding capacity of the sandy soils that dominate the region. Consequently, the region is dominated by grass and pasture for ranching, winter wheat, and alfalfa. Nonetheless, close to the river basin in Keith, Perkins, and Lincoln counties, irrigation of major crops such as maize and soybeans is widespread. The contrast in the intensity of irrigation between the east and west of the region means that there is higher groundwater and surface water consumption in the east than in the west.

By far, the most widely grown and irrigated crops across the region were maize and soybeans (Figure 2.7-A and B). In 2015 sixty eight percent (68%) of the region was irrigated maize and 28% was irrigated soybeans. In 2010, 67% of the region was irrigated maize and about 31% was irrigated soybeans (Table 2.2). Note that, because the classification method was applied during the intensive irrigation months of July and August, irrigated winter wheat, which is typically harvested in late June, may be fittingly classified as non-irrigated or as other short season crops. Therefore, despite winter wheat being a major crop in the region, the further classification of irrigated croplands into crop-types excluded winter wheat.

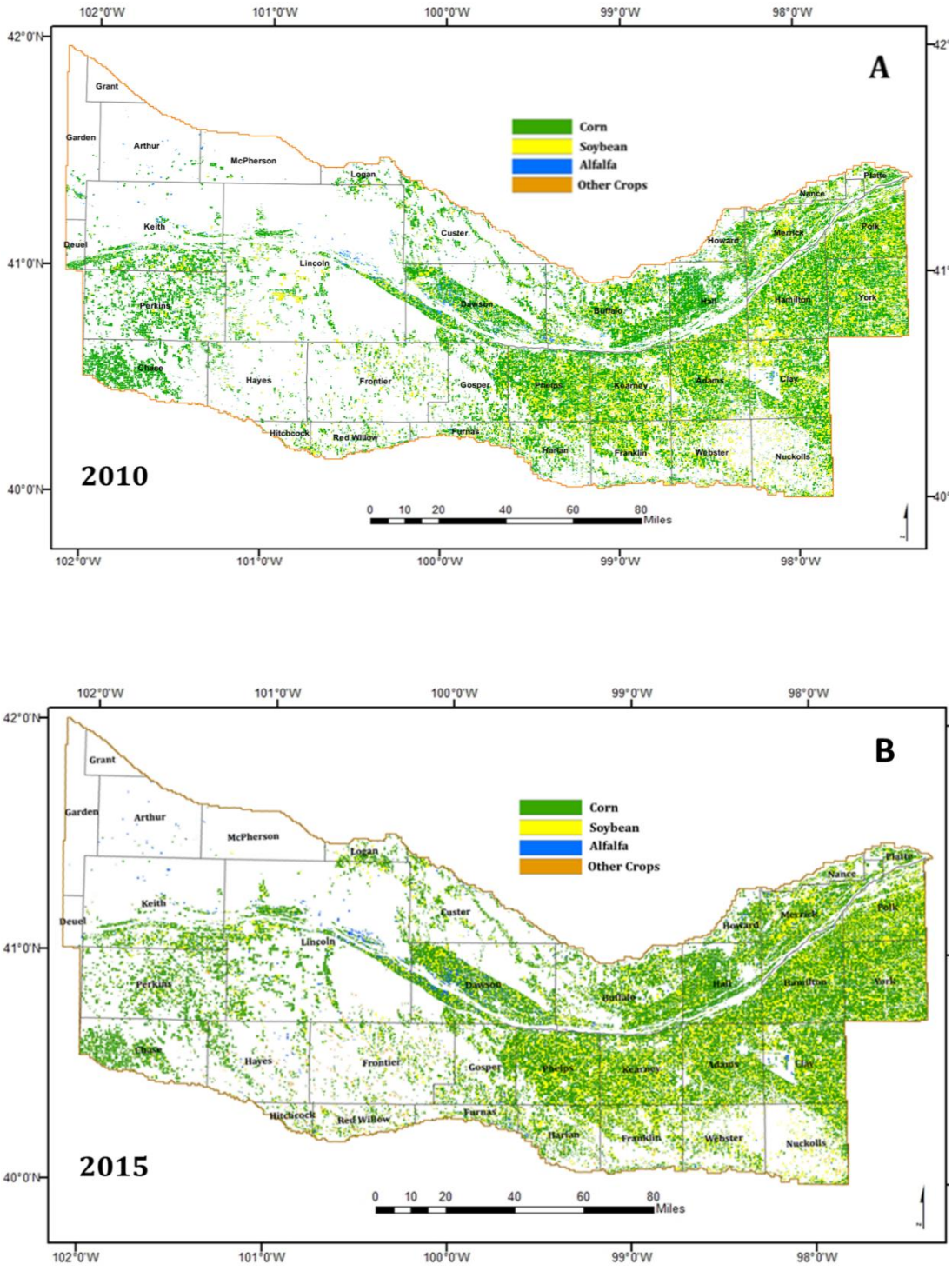

Figure 2.7: *Spatial distribution of NEG derived irrigated fields in the COHYST model region during the growing season of 2010 (A) and 2015 (B). Crop types derived from NASS CDL*

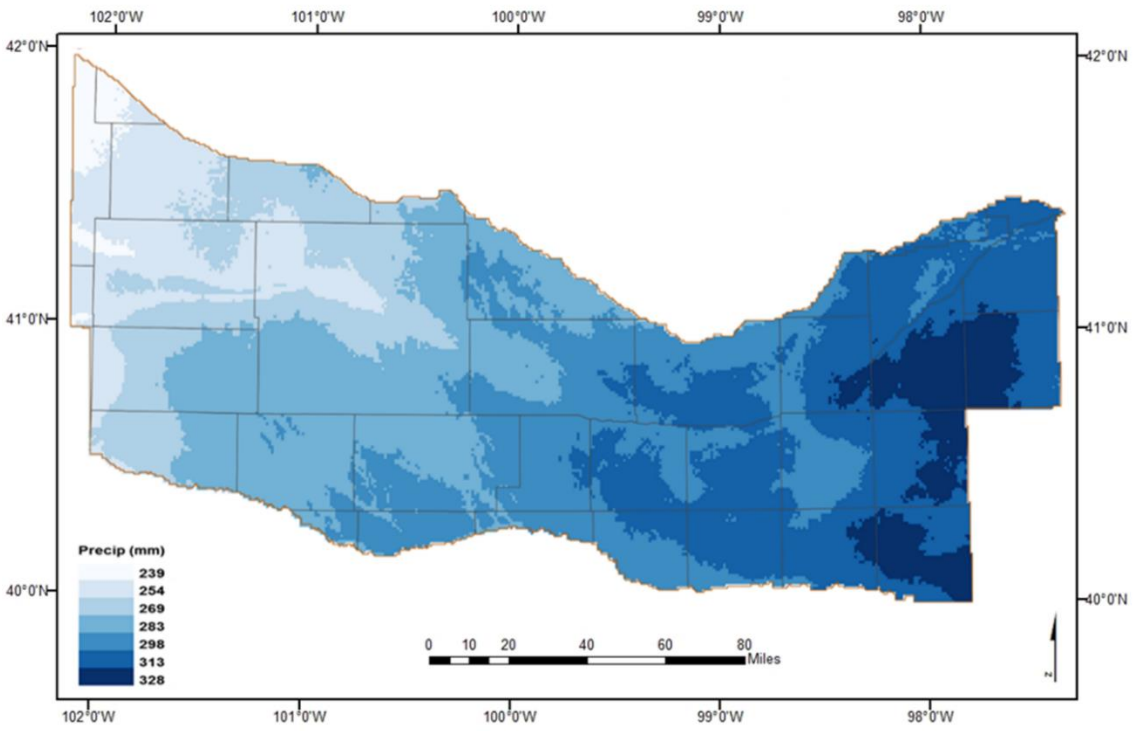

Figure 2.8: *Normal rainfall distribution across the COHYST region during the growing season (June, July and August). Base period: 1981–2010. Data source: Prism [41]*

Table 2.2: *NEG COHYST estimated irrigated acreages (ha) and percentage from total irrigated acreages for the main crops grown in COHYST model region in the 2015 growing season*

Crop	2010		2015	
	Area (ha)	% Area	Area (ha)	% Area
Corn	979,246	67.0	1,093,569	68.0
Soybean	446,856	30.6	456,255	28.0
Alfalfa	35,902	2.5	34,665	2.1

2.4.3 NEG Classification Method and NASS Statistics

As the official estimates of national agricultural statistics, NASS county irrigated acreages were used for cross reference, rather than as measures of accuracy, to assess the performance of the NEG classification method at the county aggregated level. The regression results (R^2) showed that NEG county aggregates explained 98% and 99% variation in NASS county data (Table 2.3, Figure 2.9) for the 2010 and 2015 growing seasons, respectively. The MAPE statistics had comparable overestimation values of 6.3% to 7.48% for the two growing seasons (Table 2.3). The overestimation is possibly because NASS statistics are compiled from the top most grown crops in the region; maize, soybean, Alfalfa, etc. The irrigation acreages of other crops such as sorghum, small grains, potatoes, among others, are assumed to be negligible.

Table 2.3: *Coefficient of determination (R^2), MAPE and RMSE between NASS and NEG estimated county irrigated area for 2015 and 2010*

STATS	2015	2010
R^2	0.99	0.98
MAPE (%)	7.48	6.30
RMSE (ha)	6829.40	4625.00

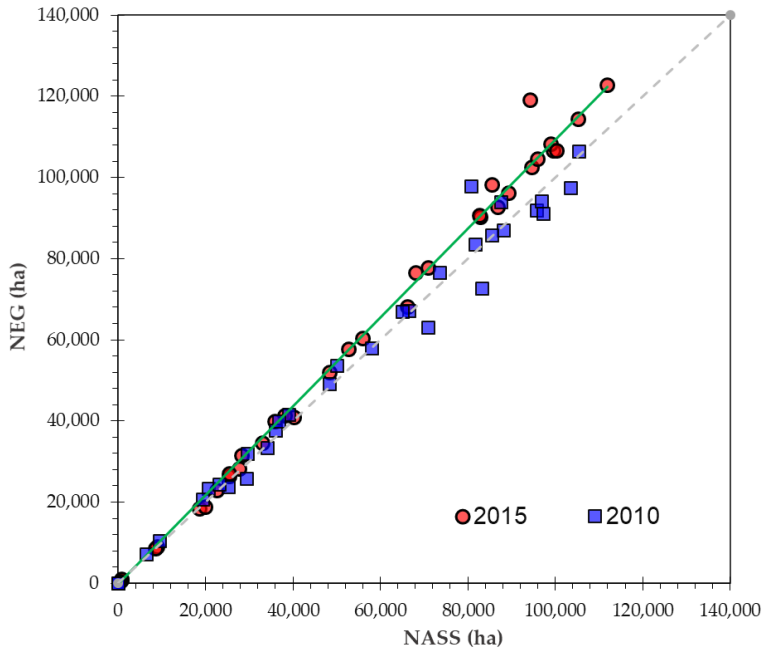

Figure 2.9: *Regression between NASS and NEG irrigated area by county for 2010 and 2015*

2.5 Discussion

2.5.1 Dual Indices and Single Index Classification Systems

Single-index methods have been successfully used in several studies (e.g., [10, 42, 43]) to classify irrigated croplands. Peak NDVI and differential NDVI have been the most commonly studied indices to classify irrigated croplands [11, 44, 45]. These methods, however, may be subject to misclassification due to NDVI saturation [46] and disparity in crop development as a result of crop management practices, such as planting dates and cultivar varieties. Indeed, the variability in land use patterns increases the difficulty of classifying crop water management practices (irrigation and non-irrigated) as opposed to classifying land cover patterns. For successful classification of land use patterns such as irrigation status, knowledge of crop- and land-management, or some understanding of

when and where farmers plant, fertilize and supply other supplements to enhance crop development is essential [5].

Pervez and Brown [10] considered peak NDVI as a proxy for the peak level of photosynthetic activity and biomass. And at the peak NDVI, irrigated and non-irrigated crops exhibited the highest NDVI differential. However, the effectiveness of peak NDVI differential is constrained by index saturation and sensitivity to crop variety. Indeed, it is only possible to classify irrigation using a single index if the area contains only a few crop types [5]. And, in the case of wet growing seasons, the peak NDVI differential is marginal for successful irrigation classification.

The synergy of two functionally different indices presented in this study increases the classification proficiency by adding another classifying layer which re-characterizes misclassified croplands by the base index. The two NEG indices are functionally different because NGI is purely a phenological index, and EGI is both a phenological and soil water stress index. Therefore, for EGI, in addition to classifying irrigation based on long term cumulative vegetation development difference as NGI, also classifies irrigation based on short term soil water stress difference between irrigated and non-irrigated crops. The short term ability based on soil water stress enhances the implementation of the NEG method in humid climates and wet growing seasons. EGI is a function of scaled evaporative fraction (ETRF) which is the water stress index for both short term and long term. ERTF has been used as water stress index in different studies [47,48].

A dynamic thresholding method derived by Wardlow and Egbert [7] calibrated NDVI thresholds on NASS statistics to estimate county irrigation acreages. The results correlated with NASS estimates, but the thresholds required calibration for every county and different

growing season, thus subjecting the method to the availability and accuracy of NASS statistics. Our results show that the NEG classification method was not only viable for wet and normal growing seasons, but also that the fixed thresholds were reliable across the different counties in the region. Although the NEG classification method was applied to a region with a relatively wide variation in climate, and it was applied for all growing seasons (dry, normal, and wet years), more validation is necessary to evaluate the suitability of the method in distinctively different agro-climate regions. A number of factors can potentially impact the performance of the NEG classification method in agro-climate regions that are different from the COHYST region. The COHYST region is dominated by two crops (maize and soybeans); therefore, increase in crop variability in a different region may impact classification performance. Furthermore, the crops in the COHYST region are typically narrow row crops, thus NEG performance may also differ for wide row crops such as vineyards and orchards.

2.5.2 Seasonal Development of NGI and EGI

The development of NGI during the growing season shows that during the initial growth stage, the index values for irrigated and non-irrigated maize and soybean were comparable (Figure 2.10-A). In the study region, evapotranspiration during the initial growth stage is primarily soil evaporation [49] driven by soil moisture from the previous winter snow melt and spring rains. As the crop matures, the NGI of irrigated and non-irrigated crops diverged owing to soil moisture availability. The cumulative vegetation growth differential peaks during the mid-season of crop development, and declines during late-season as the crop undergoes senescence. In addition, non-irrigated crops have a

reduced growth rate relative to irrigated crops which further augment the vegetative growth differential during the mid-season crop stage. Therefore, during the mid-season of crop development, NGI was highly different for the two crop water management practices for both maize and soybeans (Figure 2.10-A). The peak NGI value for irrigated maize was about 7, while non-irrigated maize only reached a peak of about 4. The growth sensitivity coefficient, calculated as the difference between mid-stage (highest) value and initial value of irrigated crop divided by the difference between mid-stage (highest) value and initial value of non-irrigated crop, for maize and soybeans was 1.75 and 2.70, respectively, during the mid-season of crop development. The EGI growth sensitivity coefficient between irrigated and non-irrigated crops was about 1.0 for both types of crops (Figure 2.10-B). Likewise, EGI had a higher difference between irrigated and non-irrigated soybeans than maize during the mid-season stage. Since both indices generated maximum contrast between irrigated and non-irrigated conditions during mid-season stage, for optimal classification results, the classification method was (and should in principle be) implemented during the mid-season of crop development (which normally lasts between mid-July and mid-August in the COHYST region).

2.5.3 Application in Humid to Arid Climate Regimes and Wet to Dry Growing Seasons

Irrigation application in wet and semi-wet climate regions or during wet growing seasons is a supplementary crop water management practice. In these agro-climate and seasonal scenarios, the vegetation canopy of non-irrigated crops is usually insignificantly different from irrigated crops, though the yield may differ at the end of the growing season [50]. For

that reason, irrigation classification is an arduous procedure since the phenological difference in vegetation canopy is subtle for classification methods to reliably detect the

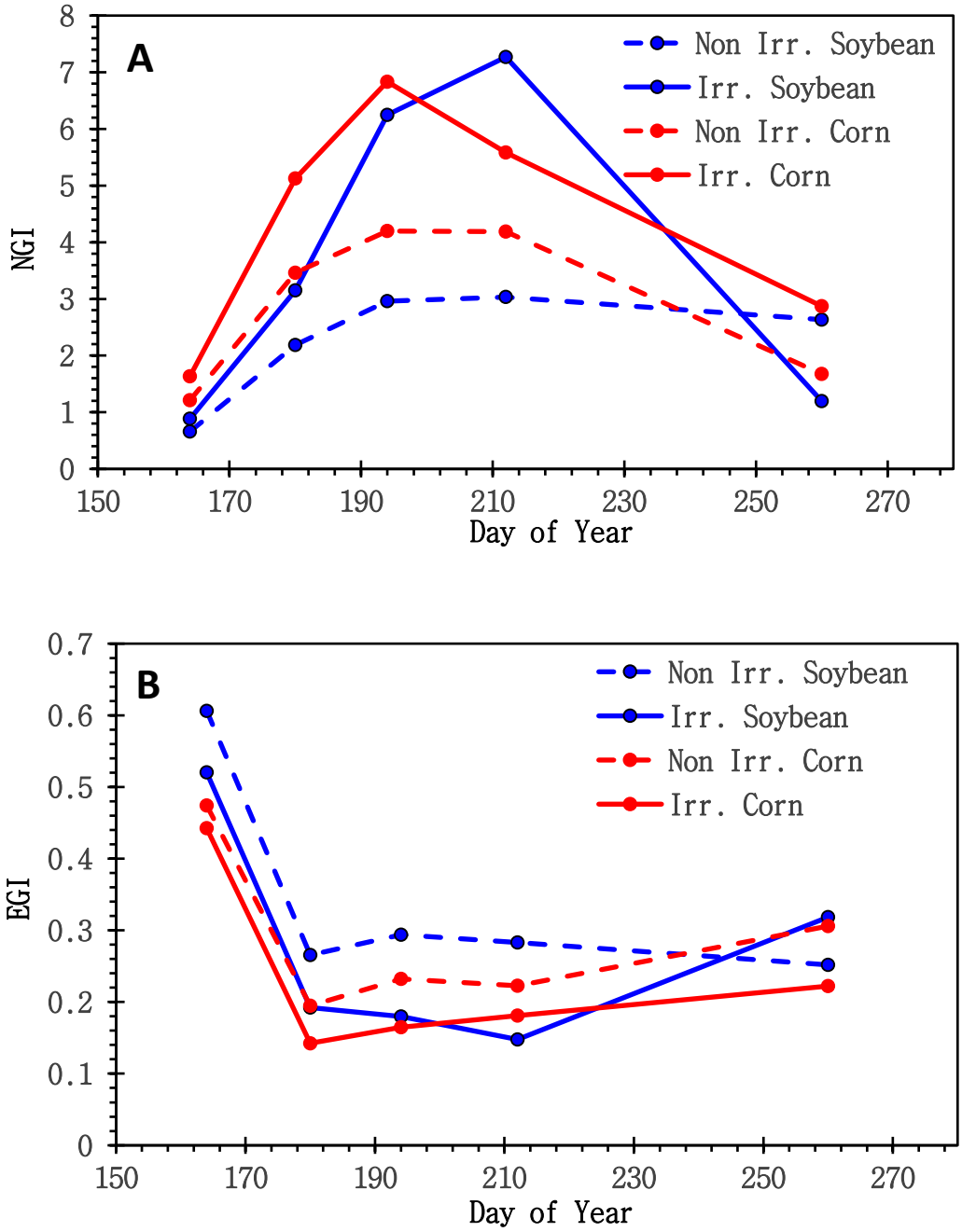

Figure 2.10: *Seasonal profile of NGI (**A**) and EGI (**B**) for irrigated and non-irrigated soybean and maize during the 2014 growing season. Each data point is an average of nine contiguous pixels of a square. DOY denotes Day of Year*

spectral difference between irrigated and non-irrigated surfaces. Several studies (e.g., [10, 12, 21]) have determined that the most widely used classification methods are based on vegetation indices that are only spectrally sensitive to phenological variation under severe conditions such as droughts or desert climate.

In this study, the proposed dual index method assimilates ETRF (scaled by GI), a phenological and soil water stress index [51] that is sensitive to short and long term water sufficiency or deficiency. Therefore, the cumulative vegetative difference due to long term water availability is the principal factor for detecting irrigated surfaces from a non-irrigated in humid climate and wet growing seasons. Such conditions took effect in the eastern part of COYHST region in 2014 and 2010; that is, a humid agro-climate region in a wet growing season. Since EGI is a proxy soil water stress index, prioritizing Landsat images that are available after a long period without rainfall is an important caveat in the NEG classification method to enhance irrigation classification in wet seasons or wet climate regions. Management practices such as tillage, planting density etc. may have confounding effects which may require research studies to understand. Additional analysis is needed for different field management practice settings.

In arid climates and dry growing seasons, irrigated and non-irrigated cropland distinction is a clear-cut classification due to wide spectral differences between the two surfaces and likely crop failure for non-irrigated croplands [10] during periods of drought. Dry conditions cause leaf cells to shrink, consequently shriveling or rolling the leaves of the canopy. Concomitant with the structural change of the canopy is the reduced production of chlorophyll. These changes, phenology and bioprocesses, result in less scattering in near infrared and less absorption of visible red light [52]. Thus far, none of the years considered

that have ground truth data (2010, 2014, and 2015) were dry years in the region. Therefore, to evaluate the performance of the NEG classification method in a dry year, the method was implemented on the 2012 growing season, and on a smaller area of twelve counties in the middle of the COYHST region and wrapped in two adjacent Landsat scenes (P30/R32 and P29/R32). The 2012 growing season was an extraordinary drought in intensity and extent across the United States. During the growing season, the U.S. Department of Agriculture declared 1692 counties, about 63% of the conterminous United States, as disaster areas [53]. Without ground truth, the performance of the NEG method was only evaluated with respect to NASS irrigation statistics, and the performance was comparable to other years with R^2 of 97% and MAPE of 8.49%. The semi-arid western part of the region in a dry year and the humid eastern part of the region in a wet year were considered in this study as the two extremes of a climate spectrum which many other regional climate patterns fall between, and in which the NEG method is inferred to perform capably.

2.6 Conclusions

An irrigation classification method applicable across a wide range of regional climates and inter-growing seasonal precipitation is derived from the SEB partitioning and vegetation indices, and calibrated during the wettest growing season. The method referred to as NEG, is a combination of two indices, NGI and EGI, with distribution functions that highly contrast irrigated and non-irrigated croplands. The two indices are functionally different because NGI is a phenological index and EGI is both a phenological and soil water stress index. For optimal classification, the method should, in principle, be implemented using satellite imagery acquired after a long dry period without precipitation

and during the mid-season stage of crop growth. The method was applied to a region with wide climate variation and to multiple growing seasons. The results revealed that across multiple growing seasons, the classification method was 92.1% accurate and explained 97% variation in NASS county irrigation statistics. Although further tests would be valuable, the performance demonstrates that the NEG irrigation classification method is an accurate and consistent approach to classify and estimate irrigated acreage across a wide range of regional climates, and during dry, normal and wet growing seasons.

2.7 References

1. Morrison, J.; Morikawa, M.; Murphy, M.; Schulte, P. *Water Scarcity and Climate Change: Growing Risks for Businesses and Investors*; A Ceres Report; Pacific Institute: Oakland, CA, USA, 2009.
2. Ibrahim, A.M. The Nile Basin Cooperative Framework Agreement: The Beginning of the End of Egyptian Hydro-Political Hegemony. *Mo. Environ. Law Policy Rev.* **2011**, *18(2)*. Available online: http://scholarship.law.missouri.edu/cgi/viewcontent.cgi?article=1395&context=jesl (accessed on Nov 28, 2017)
3. Nebraska Department of Natural Resources (NDNR). Annual Report and Plan of Work for the Nebraska State Water Planning and Review Process. Nebraska Department of Natural Resources, 15 September 2007. Available online: http://govdocs.nebraska.gov/epubs/N1500/A004-2007.pdf (accessed on Nov 28, 2017).
4. Aiken, J.D. The Republican River: Negotiation, arbitration, and a federal water master. *Cornhusker Econ.* **2008,** 382. Available online: http://digitalcommons.unl.edu/agecon_cornhusker/382/
5. Ozdogan, M.; Yang, Y.; Allez, G.; Cervantes, C. Remote sensing of irrigated agriculture: Opportunities and challenges. *Remote Sens*. **2010**, 2, 2274–2304.
6. Alexandris, T.K.; Zalidis, G.C.; Silleos, N.G. Mapping irrigated area in Mediterranean basins using low cost satellite Earth Observation. *Comput. Electr. Agric.* **2008**, *64*, 93–103.
7. Wardlow, B.D.; Egbert, S.L. Large-area crop mapping using time-series MODIS 250 m NDVI data: An assessment for the U.S. Central Great Plains. *Remote Sens. Environ.* **2008**, *112*, 1096–1116.
8. Jin, N.; Ren, W.; Feng, M.; Sun, R.; He, L.; Zhuang, W.; Yu, Qiang. Mapping Irrigated and Rainfed Wheat Areas Using Multi-Temporal Satellite Data. *Remote Sens*. 2016, 8, 207, doi:10.3390/rs8030207.

9. Ambika, A.K.; Wardlow, B.; Mishra, V. Remotely sensed high resolution irrigated area mapping in India for 2000 to 2015. *Sci. Data* **2016**, *3*, 160118, doi:10.1038/sdata.2016.118.
10. Pervez, M.S.; Brown, J.F. Mapping irrigated lands at 250-m scale by merging MODIS data and national agricultural statistics. *Remote Sens.* **2010**, *2*, 2388–2412.
11. Pervez, S.M.; Budde, M.; Rowland, J. Mapping irrigated areas in Afghanistan over the past decade using MODIS NDVI. *Remote Sens. Environ.* **2014**, *149*, 155–165.
12. Brown, J.F.; Pervez, M.S. Merging remote sensing data and national agricultural statistics to model change in irrigated agriculture. *Agric. Syst.* **2014**, *127*, doi:10.1016/j.agsy.2014.01.004.
13. Gitelson, A.A.; Gritz, U.; Merzlyak, M.N. Relationships between leaf chlorophyll content and spectral reflectance and algorithms for non-destructive chlorophyll assessment in higher plant leaves. *J. Plant Physiol.* **2003**, *160*, 271–282.
14. Gitelson, A.A.; Vina, A.; Ciganda, V.; Rundquist, D.C.; Arkebauer, T.J. Remote estimation of canopy chlorophyll content in crops. *Geophys. Res. Lett.* **2005**, *32*, L08403, doi:10.1029/2005GL022688.
15. Su, Z. The surface energy balance system (SEBS) for estimation of turbulent heat fluxes. *Hydrol. Earth Syst. Sci.* **2002**, *6*, 85–99.
16. Dappen, P.; Merchant, J.; Ratcliffe, I.; Robbins, C. Delineation of 2005 Land Use Patterns for the State of Nebraska Department of Natural Resources; Final Report; *Center for Advanced Land Management Information Technologies (CALMIT)*: Lincoln, NE, USA, 2007.
17. Szilagyi, J.; Jozsa, J. MODIS-Aided Statewide Net Groundwater-Recharge Estimation in Nebraska. *Ground Water* **2013**, *51*, 735–744.
18. Han, W.; Yang, Z.; Di, L.; Mueller, R. CropScape: A Web service based application for exploring and disseminating US conterminous geospatial cropland data products for decision support. *Computers and Electronics in Agriculture*. **2012**, 84, 111–123.
19. Riverside Technology, Inc. 2014 COHYST Ground Truth Data Collection for Use in Landcover Classification Task 1: Image Processing and Ground Truth Data Collection; Report; *Cooperative Hydrology Study (COHYST):* Lincoln, NE, USA, 2015.
20. Goward, S.N.; Markham, B.; Dye, D.; Dulaney, W.; Yang, J. Normalized difference vegetation index measurements from the Advanced Very High Resolution Radiometer. *Remote Sens. Environ.* **1991**, *35*, 257–277.
21. DeFries, R.S.; Hansen, M.; Townshend, J.R.G.; Sohlberg, R. Global land cover classifications at 8 km spatial resolution: The use of training data derived from Landsat imagery in decision tree classifiers. *Int. J. Remote Sens.* **1998**, *19*, 3141–3168.
22. Mutiibwa, D.; Irmak, S. Estimation of crop coefficients from AVHRR-based NDVI for analyzing long-term trends in evapotranspiration in relation to changing climate in the USA High Plains. *Water Resour. Res.* **2012**, *49*, 231–244.
23. Ozdogan, M.; Gutman, G. A new methodology to map irrigated areas using multi-temporal MODIS and ancillary data: An application example in the continental US. *Remote Sens. Environ.* **2008**, *112*, 3520–3537.

24. Gitelson, A.A.; Viña, A.; Masek, J.G.; Verma, S.B.; Suyker, A.E. Synoptic monitoring of gross primary productivity of maize using Landsat data. *IEEE Geosci. Remote Sens. Lett.* **2008**, *5*, 2, doi:10.1109/LGRS.2008.915598.
25. Huete, A.R.; Justice, C.O.; van Leeuwen, W.J.D. MODIS Vegetation Index, Algorithm Theoretical Basis Document, 30 April 1999, NASA Goddard Space Flight Centre: Greenbelt, MD, USA. Available online: http://gis-lab.info/docs/atbd_mod13.pdf (accessed on Nov 28, 2017)
26. Gitelson, A.A. Wide dynamic range vegetation index for remote quantification of biophysical characteristics of vegetation. *J. Plant Physiol.* **2004**, *161*, 165–173.
27. Thomas, J.R.; Gaussman, H.W. Leaf reflectance vs. leaf chlorophyll and carotenoid concentration for eight crops. *Agron. J.* **1977**, *69*, 799–802.
28. Buschmann, C.; Nagel, E. In vivo spectroscopy and internal optics of leaves as basis for remote sensing of vegetation. *Int. J. Remote Sens*. **1993**, *14*, 711–722.
29. Gitelson, A.A.; Merzlyak, M.N. Quantitative estimation of chlorophyll a using reflectance spectra: Experiments with autumn chestnut and maple leaves. *J. Photochem. Photobiol. B* **1994**, *22*, 247–252.
30. Merzlyak, M.N.; Gitelson, A.A. Why and what for the leaves are yellow in autumn? On the interpretation of optical spectra of senescing leaves (*Acer platanoides* L.). *J. Plant Physiol.* **1995**, *145*, 315–320.
31. Su, Z.; Pelgrum, H.; Menenti, M. Aggregation effects of surface heterogeneity in land surface processes. *Hydrol. Earth Syst. Sci.* **1999**, *3*, 549–563.
32. Su, Z. A Surface Energy Balance System (SEBS) for estimation of turbulent heat fluxes from point to continental scale. In *Advanced Earth Observation—Land Surface Climate*; Su, Z., Jacobs, C., Eds.; Publications of the National Remote Sensing Board (BCRS): 2001; USP-2, 01–02, p. 184.
33. Samani, Z.; Bawazir, A.S.; Bleiweiss, M.; Skaggs, R.; Tran, V.D. Estimating daily net radiation over vegetation canopy through remote sensing and climatic data. *J. Irrig. Drain. Eng.* **2007**, *133*, 291–297.
34. Choudhury, B.J.; Idso, S.B.; Reginato, R.J. Analysis of an empirical model for soil heat flux under a growing wheat crop for estimating evaporation by an infrared-temperature based energy balance equation. *Agric. For. Meteorol.* **1987**, *39*, 283–297.
35. Monteith, J.L. *Principles of Environmental Physics*; Edward Arnold Press: London, UK, 1973; p. 241.
36. Kustas, W.P.; Daughtry, C.S.T. Estimation of the soil heat flux/net radiation ratio from spectral data. *Agric. For. Meteorol.* **1989**, *49*, 205–223.
37. Press, W.H.; Teukolsky, S.A.; Vetterling, W.T.; Flannery, B.P. *Numerical Recipes in C: The Art of Scientific Computing*; Cambridge University Press: Cambridge, UK, 1997; 994p.
38. Anderson, M.C.; Zolin, C.; Sentelhas, P.C.; Hain, C.R.; Semmens, K.; Tugrul Yilmaz, M.; Gao, F.; Otkin, J.A.; Tetrault, R. The Evaporative Stress Index as an indicator of agricultural drought in Brazil: an assessment based on crop yield impacts. *Remote Sens. Environ.* **2016**, *174*, 82–99.
39. Humboldt State University. Introduction to Remote Sensing. Available online: http://gsp.humboldt.edu/olm_2015/Courses/GSP_216_Online/lesson6-2/metrics.html (accessed on Oct. 14, 2018).

40. Suyker, A.; Verma, B.S. Evapotranspiration of irrigated and rainfed maize–soybean cropping systems. *Agric. For. Meteorol.* **2009**, *149*, 443–452, doi:10.1016/j.agrformet.2008.09.010.
41. Daly, C.; Halbleib, M.; Smith, J.I.; Gibson, W.P.; Doggett, M.K.; Taylor, G.H.; Curtis, J.; Pasteris, P.A. Physiographically-sensitive mapping of temperature and precipitation across the conterminous United States. *Int. J. Climatol.* **2008**, *28*, 2031–2064.
42. Zhu, X.; Zhu, W.; Zhang, J.; Pan, Y. Mapping irrigated areas in China from remote sensing and statistical data. *IEEE J. Sel. Top. Appl. Earth Obs. Remote Sens.* **2014**, *7*, 4490–4504, doi:10.1109/JSTARS.2013.2296899.
43. Ozdogan, M.; Salvucci, G.D.; Anderson, B.C. Examination of the Bouchet-Morton complementary relationship using a mesoscale climate model and observations under a progressive irrigation scenario. *J. Hydrometeorol.* **2006**, *7*, 235–251.
44. Kamthonkiat, D.; Honda, K.; Turral, H.; Tripathi, N.K.; Wuwongse, V. Discrimination of irrigated and rainfed rice in a tropical agricultural system using spot vegetation NDVI and rainfall data. *Int. J. Remote Sens.* **2005**, *26*, 2527–2547.
45. Peterson, D.; Whistler, J.; Egbert, S.; Brown, C.J. Mapping irrigated lands by crop type in Kansas. *Pecora 18 Proc.* **2011**.
46. Huete, A.R.; Didan, K.; Rodriguez, E.P.; Gao, X.; Ferreira, L.G. Overview of the radiometric and biophysical performance of the MODIS vegetation indices. *Remote Sens. Environ.* **2002**, *83*, 195–2*13*.
47. Allen, R.G.; Irmak, A.; Trezza, R.; Hendrickx, J. M. H.; Bastiaanssen, W.; Kjaersgaard, J. Satellite-based ET estimation in agriculture using SEBAL and METRIC. *Hydrological Processes*. **2011**, 25, 4011-4027.
48. Anderson, M. C.; Allen, R. G.; Morse, A.; Kustas, W. P. Use of Landsat thermal imagery in monitoring evapotranspiration and managing water resources. *Remote Sensing of Environment*. **2012**, doi: 10.1016/j.rse.2011.08.025
49. Allen, R.G.; Pereira, L.S.; Raes, D.; Smith, M. *Crop Evapotranspiration—Guidelines for Computing Crop Water Requirements—FAO Irrigation and Drainage Paper 56*; Food and Agriculture Organization of the United Nations (FAO): Rome, Italy, 1998.
50. Hergert, G.W.; Margheim, J.F.; Pavlistaa, A.D; Martin, D.L.; Supallab, R.J.; Isbellc, T.A. Yield, irrigation response, and water productivity of deficit to fully irrigated spring canola. *Agric. Water Manag.* **2016**, *168*, 96–103.
51. Gowda, P.H.; Chavez, J.L.; Colaizzi, P.D.; Evett, S.R.; Howell, T.A.; Tolk, J.A. ET Mapping for Agricultural Water Management: Present Status and Challenges. *Irrigation Science*. **2008**, 26, 223-237.
52. Lillesand, T.M.; Kiefer, R.W. *Remote Sensing and Image Interpretation*; John Wiley & Sons, New York, USA., 2000; p. 736.
53. Mutiibwa, D.; Vavrus, S.J.; McAfee, S.A.; Albright, T.P. Recent spatiotemporal patterns in temperature extremes across conterminous United States. *J. Geophys. Res. Atmos.* **2015**, *120*, doi:10.1002/2015JD023598.

CHAPTER 3: APPLICATION OF MODIS DATA FOR FIELD SCALE ANALYSIS

3.1 Abstract

Coarse spatial resolution of Moderate Resolution Imaging Spectroradiometer (MODIS) images and the existing gridded methodology of re-projecting MODIS images makes it difficult to conduct a field scale analysis of agricultural crops. A new method of re-projecting MODIS satellite images that preserves the geometric orientation of satellite sensor pixel "footprint method" was developed in this study. There are two advantages of this method over the existing gridded method of re-projecting MODIS images. First is the elimination of artifacts introduced by gridding, which evolve from a mismatch between the sensor pixel and the pre-defined grid cell geometric orientation. Second is the ability to locate satellite sensor pixel orientation in agricultural fields for more accurate field scale analysis. Field scale accuracy of the footprint method and existing gridded method was assessed with Green Leaf Area Index (LAI) data of AmeriFlux two center pivot maize fields from Mead, Nebraska (US-Ne1 and US-Ne2). The statistical analysis of MODIS LAI estimates based on LAI equation of Myneni et al. and Green LAI field measurements indicates that the footprint methodology of handling MODIS datasets when applied for field scale analysis provides better results. In field US-Ne1, using the footprint method to estimate LAI reduces the RMSE by 10.1%, the ubRMSE by 16.5% and the nRMSE by 10.2%. Similarly, in field US-Ne2 using the footprint method reduces the RMSE by 22%, the ubRMSE by 36%, and nRMSE by 22%. On the contrary, the results of statistical analysis of MODIS Green LAI estimates based on Green LAI equation of Viña et al. does

not support this conclusion. The results of t-test analysis show that the improvement of MODIS LAI and Green LAI estimates from footprint method when compared to that of gridded method is relatively small.

3.2 Introduction

Remotely sensed satellite images are increasingly used in water resources planning and management. Landsat images with spatial resolution of 30m by 30m grid size have been frequently used to study land cover characteristics, but a dis-advantage of Landsat satellite imagery is its temporal resolution, with time intervals of around two weeks for repeated area coverage. In any given month only two images can be retrieved for a particular location. If weather conditions are not ideal during the satellite overpass (E.g. cloudy conditions), images are not as useful for analysis.

The Moderate Resolution Spectroradiometers (MODIS) on-board NASA's Earth Observing System (EOS) Terra and Aqua satellites provide data on global land, atmosphere, and ocean dynamics [1]. MODIS satellite images are useful when high temporal resolution is preferred over high spatial resolution. With spatial resolutions of 250m, 500m, and 1000m for different bands, MODIS data are useful for studying land cover characteristics at lower spatial resolution than Landsat. MODIS data products are available in two formats; granule and gridded data. A granule corresponds to a five-minute interval of un-gridded MODIS swath data where users have the option of overlaying grids anywhere spatially and projecting MODIS data into the grids. Gridded MODIS data are

data that are georeferenced with fixed, grids and stored as fixed non-overlapping, earth-located tiles in a Sinusoidal projection [2].

The geometric orientation of MODIS satellite sensor pixels is not represented by either Granule or gridded data formats. This is of less concern when analysis of land cover is needed at the regional scale, but might raise some concern when the MODIS data are applied for field scale analysis. The disadvantage of coarse spatial resolution compared to Landsat data accompanied by projection related issues limits the use of MODIS data at field scales, especially for fields with irregular shapes and sizes and adjacent irrigated and non-irrigated fields. A detailed description of MODIS satellite sensors, its geometric orientation, and different types of MODIS data products available is included in Appendix B of this dissertation.

The demand for satellite images with higher spatial resolution in the scientific community needs to be reassessed. There are different sizes of agricultural fields in different parts of the world. Figure 3.1 illustrates the spatial distribution of irrigated and non-irrigated maize fields in a part of Seward county in Nebraska. A 250m MODIS grid is overlaid on the figure. Green areas are irrigated fields and orange areas are non-irrigated fields.

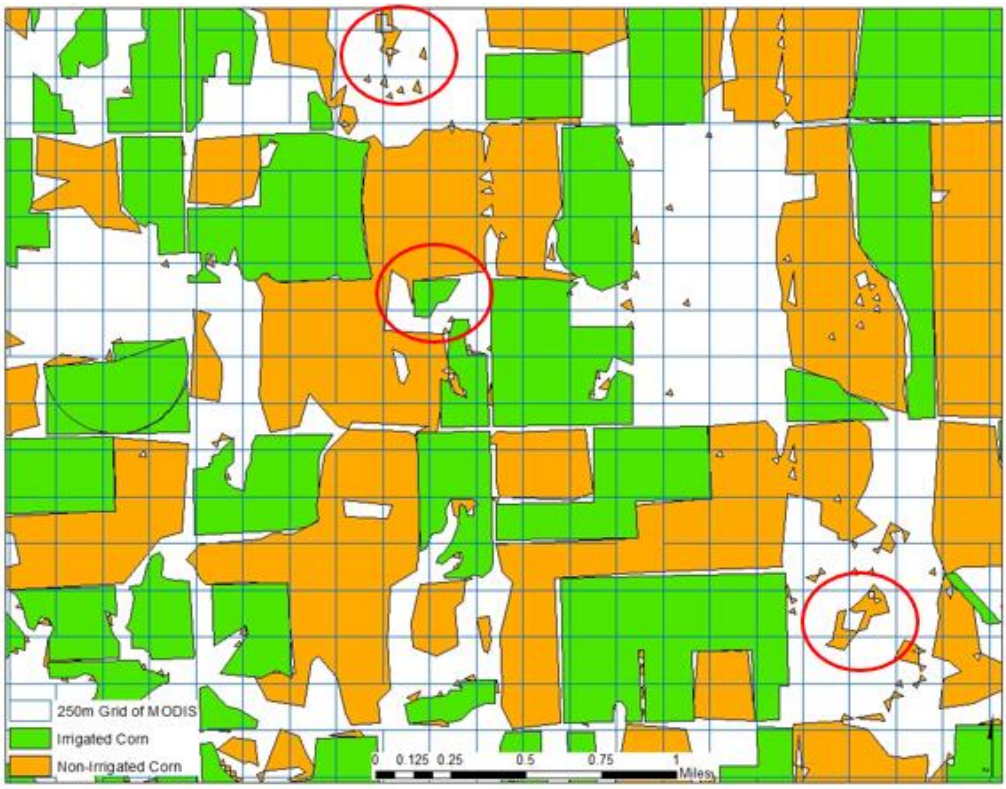

***Figure 3.1**: Spatial distribution of irrigated and non-irrigated maize fields*

Figure 3.1 shows that within a single thermal pixel there exists areas of multiple fields. It is only possible to perform field scale analysis if there exist homogeneous fields which are equal to or greater than the area of 250m pixel resolution. Fields of this size are rare. Figure 3.1 shows that in some small sized fields it is impossible to perform field scale analysis with existing resolutions. Around the world, agricultural practices have developed as a function of topography, soil type, crop type, annual rainfall, and tradition [41]. The images of fields in Figure 3.2 [3] shows differences in field geometry and size in different parts of the world.

The demand for satellite images with increased spatial resolution will never come to an end given the different shapes and sizes of agricultural fields that exists in different parts of the world.

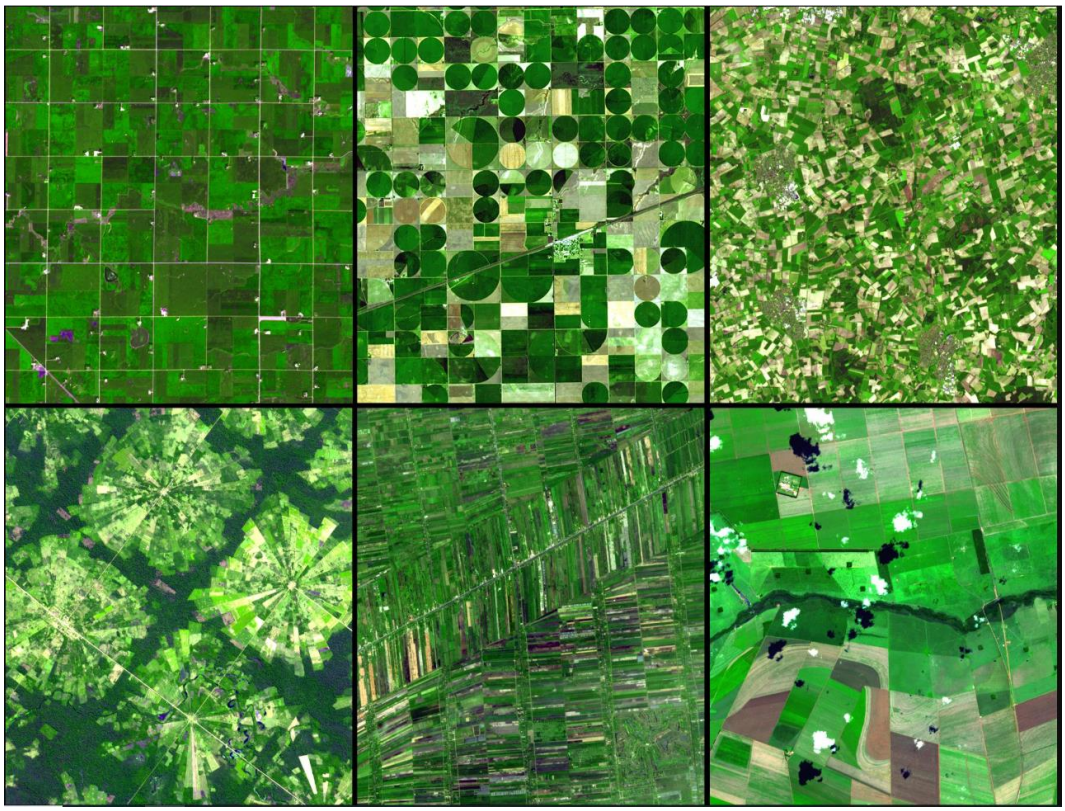

Figure 3.2*: Different shape and sizes of fields (Earth Observatory, 2006)*

The research of this chapter explores optimization of available MODIS data for field scale study. A new methodology of handling MODIS data – the "footprint method", is developed, which projects MODIS swath data while preserving the geometric orientation of satellite pixels. This method further aids in preventing pixel value contamination during data projection which is discussed in detail in later sections. MODIS Swath granule data projected using the footprint method and gridded method are compared to ground truth field data to analyze the advantages of the footprint methodology over the existing gridded methodology. The second part of the research study explores the usefulness of MODIS data in monitoring crop fields for agricultural water management. The advantage of high temporal resolution of MODIS data (over Landsat data) is explored to determine potential

benefits for irrigation management of crop fields (irrigation scheduling in fields) with more frequent monitoring of irrigated crop fields.

The objectives of this research chapter include:

1. Development of a methodology (footprint method) that can project MODIS data while preserving the geometric orientation of satellite pixel data.
2. Assessment of field scale accuracy of projected MODIS data from the gridded methodology and from the footprint method by comparing them to ground truth field data:

a. Measured Green Leaf Area Index (LAI) of irrigated field maize is compared with LAI and Green LAI derived from re-projected MODIS swath data using the gridded and footprint methods.

b. Evaluate the performance of LAI and Green LAI determined by footprint method for field scale analysis compared to that of conventional gridded method of MODIS data re-projection.

3. Explore the opportunity of taking advantage of increased frequency data collection of MODIS satellite images over Landsat satellite images (twice per month for repeated area coverage) for agricultural water management at field scales:

a. The Soil Adjusted Vegetation Index (SAVI) of irrigated maize for a single growing season will be calculated to generate a crop characteristic curve and the features of curve will be compared to that of characteristic curve generated from Landsat images over multiple years (11 years). It will be evaluated if the crop characteristic cure developed from Landsat satellite data using over 11 years can be developed using only one year of MODIS satellite data.

3.3 Implications of Existing MODIS Data Handling Method for Field Scale Analysis

For regional scale analysis the existing method of re-projecting MODIS data into gridded format are suitable, but for field scale analysis of agricultural fields the existing method is not suitable due to the problem of signal contamination of a grid pixel from its surrounding neighbor pixels during re-projection. This results in a measurement that has a spatial extent that is greater than what is useful for field scale analysis.

3.3.1 Sensor Pixels and Fixed Grids in Agricultural Fields

Figure 3.3 illustrates the orientation of fixed 250m by 250m defined grid cells for gridded data and the actual orientation of MODIS satellite sensor pixels over a center pivot field. The orientation of defined grid cells and the actual pixel orientation of satellite sensor are never the same, adding complexity to assigning sensor pixel values to fixed grid cells. Figure 3.4 shows the overlap of fixed grid cells and un-projected satellite sensor pixels over the same field. It is clear in the figure that no single grid cell covers only one sensor pixel, which makes it difficult to assess which sensor pixel should be assigned to a fixed grid cell that covers multiple sensor pixels.

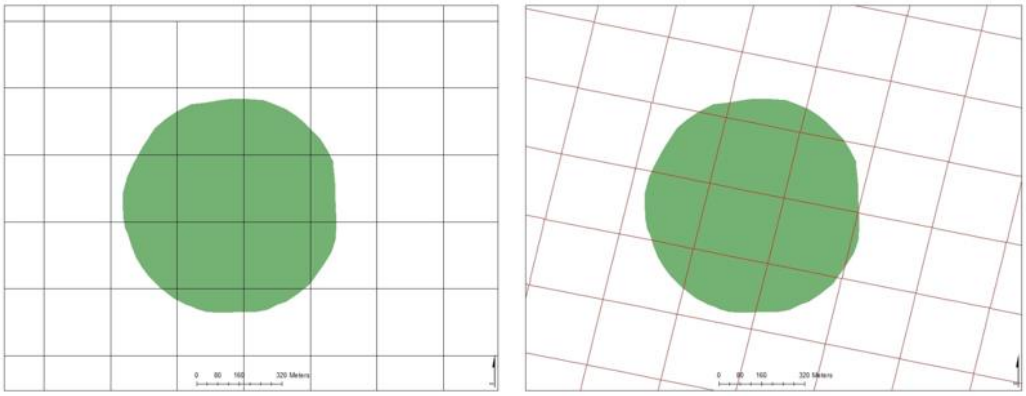

Figure 3.3*: Spatial orientation of fixed grid cells (left) and satellite sensor pixels (right) overlaid on a center pivot field (green)*

The existing methodology for re-projecting MODIS swath data and higher-level MODIS gridded data allows resampling of sensor pixels cells and assignment of a value to a corresponding fixed grid cell. Three types of resampling techniques; nearest neighbor, bilinear, and cubic convolution are available. In the nearest neighbor resampling method, a grid cell is assigned the value of the nearest sensor pixel. The original value of the sensor pixel is not manipulated by the process. Figure 3.5 illustrates the process of assigning a sensor pixel value to a grid cell using the nearest neighbor resampling technique. In the figure, the grid cell identified by the solid black outline is assigned the value of the MODIS pixel identified by solid red outline, because this is the sensor pixel closest to the center of the grid cell.

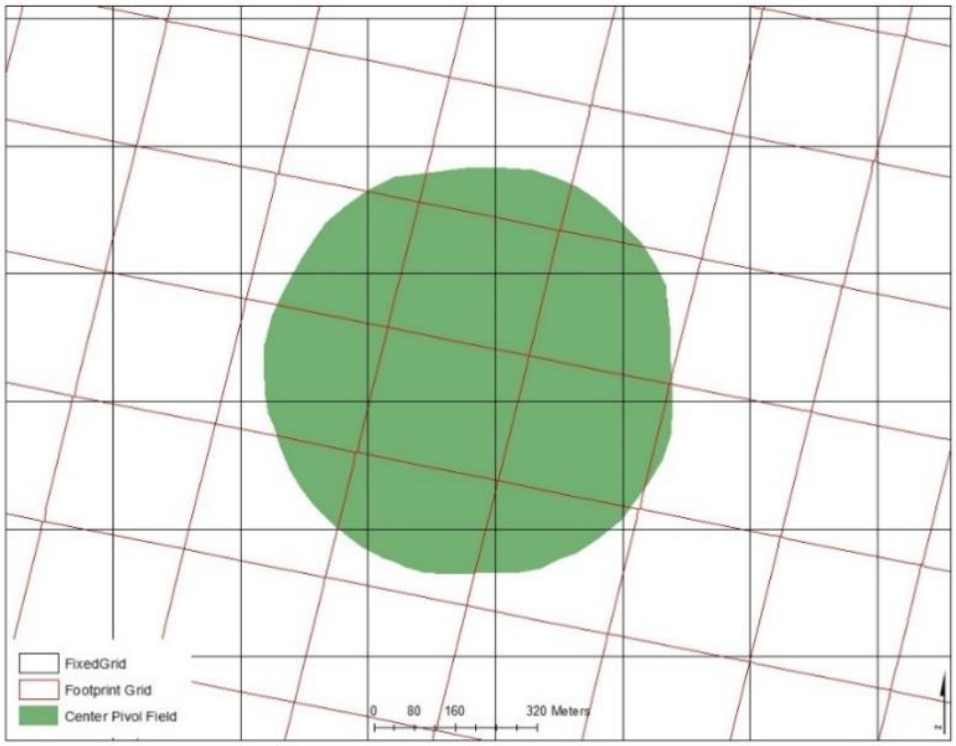

***Figure 3.4**: Overlapping of fixed grid cells and satellite sensor pixels overlaid on a center pivot field (green)*

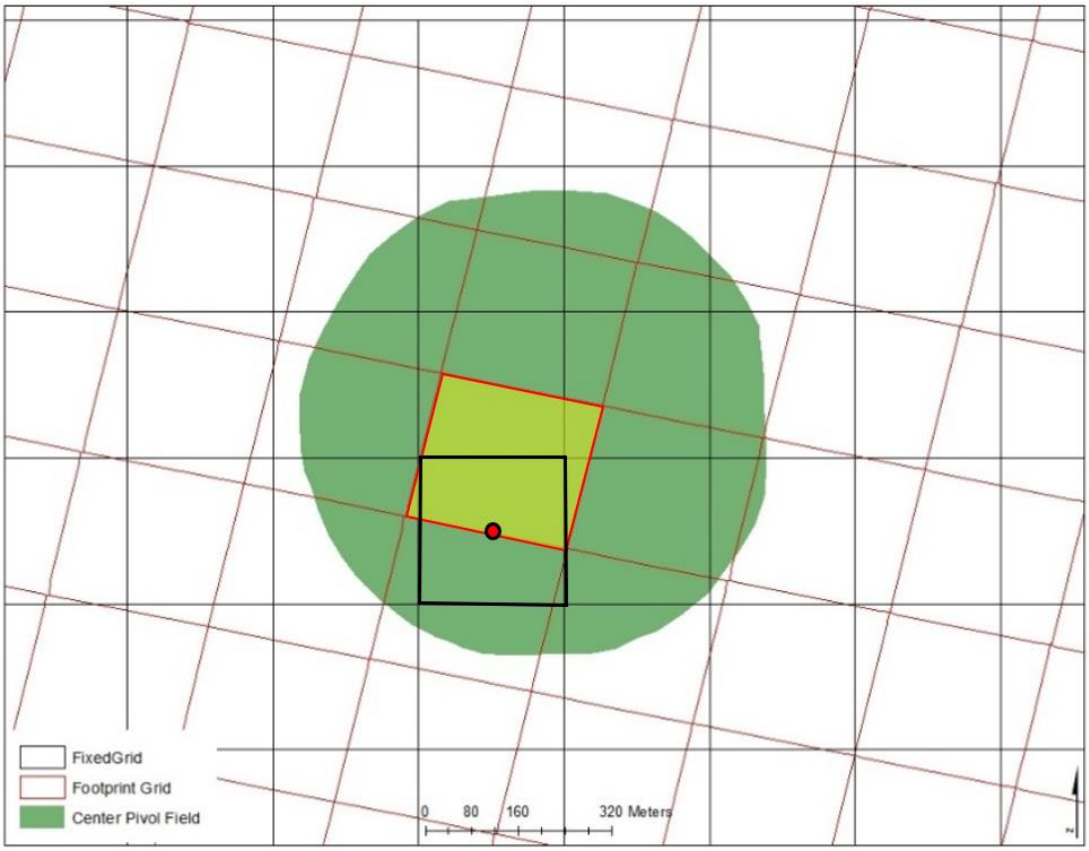

Figure 3.5*: Value assignment to grid cells using Nearest Neighbor resampling technique*

In the case of bilinear and cubic convolution resampling methods, the values of neighboring sensor pixels are averaged and assigned to a fixed grid cell. In these cases, the original values of the sensor pixels are not preserved, rather the value of the grid cell is a weighted average of surrounding sensor values. Figure 3.6 illustrates an example of how selected sensor pixels contribute to the value of a fixed grid cell during the process of MODIS data reprojection, reducing the true spatial resolution of the data.

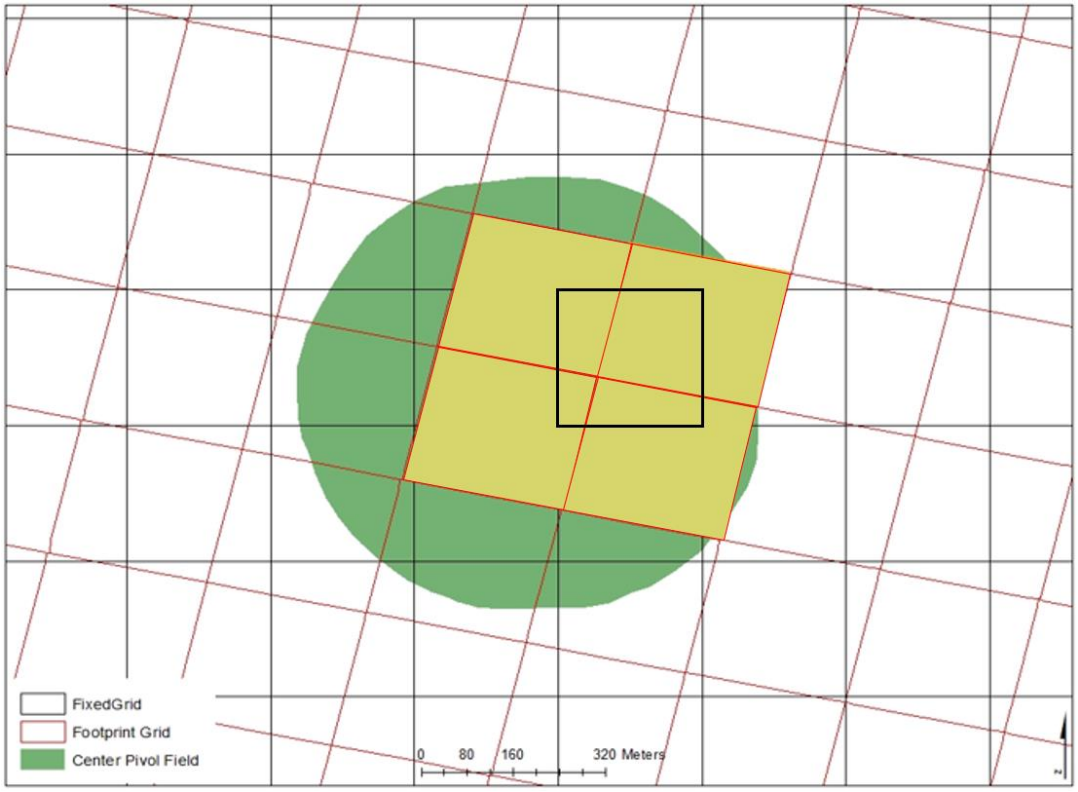

***Figure 3.6**: Value assignment to grid cells using Bilinear and Cubic Convolution resampling techniques*

3.3.2 Problems with the Existing Methodology of MODIS Data Reprojection in Field Scale Analysis

MODIS data are provided in HDF format to users, and tools like the MODIS Swath tool and the MODIS Reprojection Tool (MRT) are used to handle and re-project HDF format data into gridded raster images. Users can only view the orientation of output grid cells after re-projection of the data. There is no option available in these tools to view the orientation of satellite sensor pixels before re-projection of the data. This adds to confusion about how satellite sensor pixels are assigned to grid cells. Users must generally accept this and use the gridded re-projected raster data, which is reasonable for analysis at the regional scale but is not optimal at the field scale.

Several authors have reported on errors caused by contamination of the signal from neighboring pixels and suggested improvements to per-pixel estimates of land cover by incorporating known sensor characteristics [4,5]. In the process of re-sampling data, a grid cell that falls well within a field can have a value assigned from sensor pixels that are partly or mostly outside the field area, receiving partial signals from land adjacent to the field. In the cases of bilinear and cubic convolution resampling methods, in addition to weighting of original sensor pixel values while assigning a value to a grid cell, some contributing sensor pixels may be outside of the target field and capture signals from vegetation which are not representative of the field, assigning those signals to a grid cell that is well within the field. This creates problems in field scale analysis of agricultural fields where irrigated and non-irrigated fields are present next to each other. Figure 3.7 illustrates two examples of pixel contamination from sensor pixels that contribute to the value of a grid cell that is well within a field when using the bilinear or cubic convolution resampling methods.

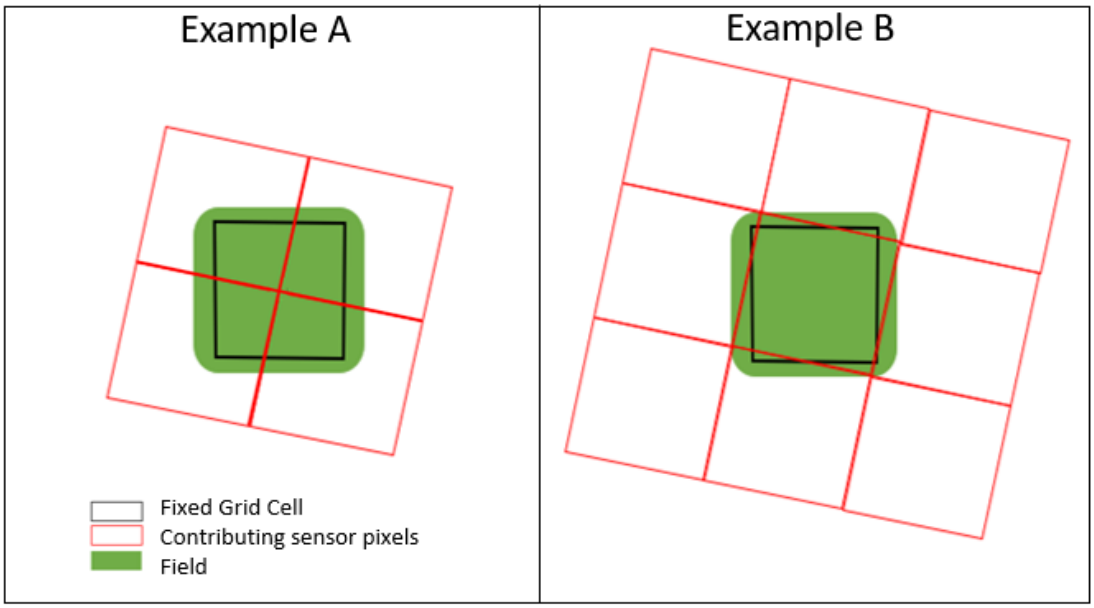

***Figure 3.7**: Problem of pixel value contamination in a grid cell well within a field*

In the case of Example A, during the resampling process (bilinear or cubic convolution) the fixed grid cell which is within the field will have a value dependent on all of the contributing sensor pixels. If nearest neighbor resampling method is used, the value of the sensor pixel that is closest to the center of fixed grid cell will be assigned. Since all contributing sensor cells are partly outside the field, the value assigned to the fixed grid cell will be contaminated, and will not represent the true value of the field. In the case of Example B, if bilinear or cubic convolution resampling method are used, the fixed grid cell value will be contaminated; but if the nearest neighbor resampling method is used the value of the fixed grid cell will take on the value of the only sensor cell that is within the field.

Even if the nearest neighbor technique is used to ensure that the original value of a sensor pixel is assigned to a grid cell during data re-projection, the sensor pixel that is assigned may not be representative of a particular field. Figure 3.8 illustrates examples of pixel contamination when using the nearest neighbor resampling method from sensor pixels that lie outside of a field, even though the grid cell is well within the field. The red dots in the figures represent the centers of the fixed grid cells.

Reduction of the geometric variability can be achieved through smoothing of data by aggregation of pixels to increasingly coarse resolutions. Pixel resolutions of at least 1000m, four times the nominal 250m detector size, are required to mitigate the geometric influence from most land cover types tested. However, complete removal of the noise from variable geometries is not achieved, even at 2000m or 8x nominal resolution [6]. Furthermore, upscaling the MODIS grid cell data to coarse resolution has a disadvantage in terms of its applicability to field scale analysis of agricultural fields with irregular boundaries and small size.

Gridding artifacts between observations and predefined grid cells strongly influence the local spatial properties of MODIS images. The mismatch between observations and grid cells increases as view zenith angle (θ_v) increases because the size of the observations increases while the size of the grid cells remains unchanged [2]. The gridding artifacts together with the effects of viewing geometry weaken the relationship between the location of grid cells and corresponding observations has implications for the use of reference data for the validation of MODIS products [7].

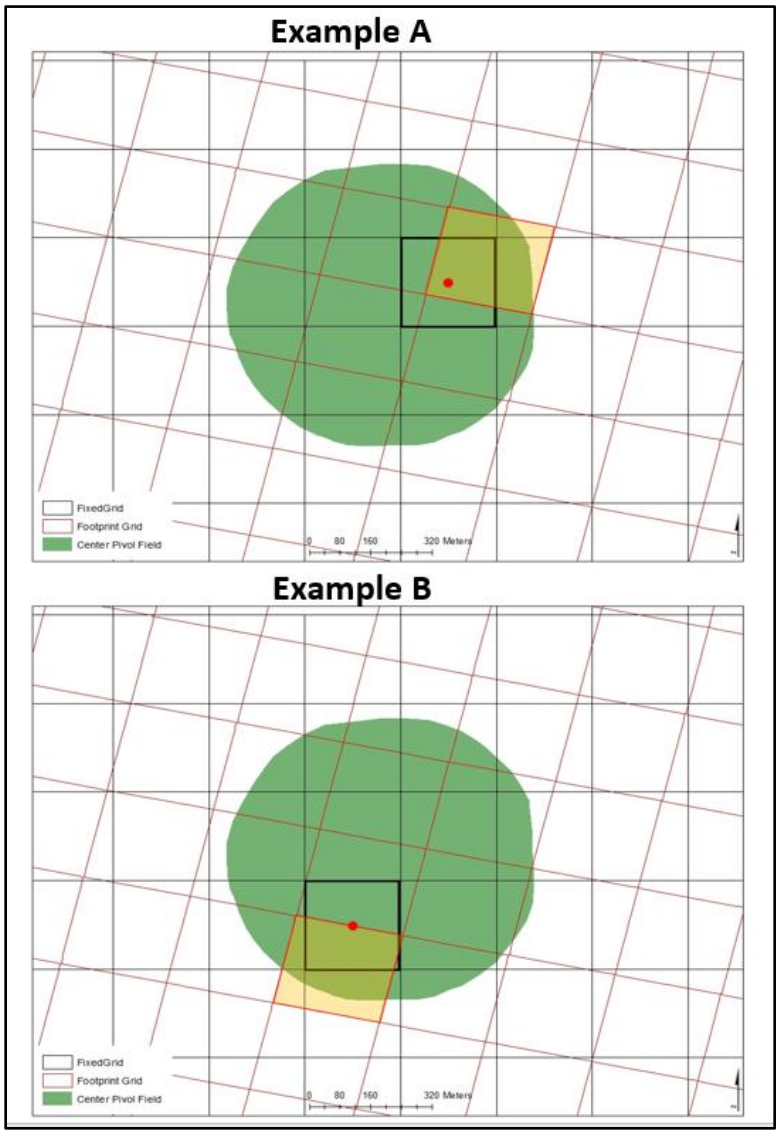

***Figure 3.8**: Pixel contamination problem in Nearest Neighbor resampling technique*

3.4 Footprint Methodology: Re-projecting MODIS Data in Native Sensor Pixel Orientation

A method of re-projecting MODIS images with the intention of preserving geometric orientation of satellite sensor pixels called the “footprint method” was developed. The method eliminates artifacts caused by the gridding process and increases the applicability of MODIS data for field scale analysis. Field scale analysis is more reliable if it is known whether or not the pixels representing a particular field are contaminated by signals from outside the field boundaries. The goal of this method is to eliminate the fixed grid cell structure and to utilize the native pixel orientation of the MODIS data. Since the footprint method only use measurements from sensor pixels that only fall within the field, it represents vegetation characteristic of that particular field more realistically compared to the conventional gridded method. In contrast, due to the projection process, the gridded method sometimes includes radiation from areas outside of the study area, despite the fact that the grid cells themselves are within the field.

In order to re-project the MODIS swath image while preserving the geometry of satellite sensor pixels, the nearest neighbor resampling technique with an output pixel resolution finer than that of the native image was selected during the process of re-projecting each image. As the output pixel resolution was increased, the footprint of the original 250m sensor pixels was revealed. The initial idea of re-projecting MODIS image with finer output pixel size for viewing the footprint of sensor pixel geometric orientation originated during a research discussion [8]. The MODIS Swath Tool provided by NASA is unable to re-project images with pixel resolutions finer than those of native MODIS images. Initially this Tool was used to test the new method, but distortion in the footprints

of sensor pixels appeared in parts of the image when the resolution of the output image was high. Figure 3.9 illustrates a MODIS image re-projected with the MODIS Swath Tool and examples of problem areas.

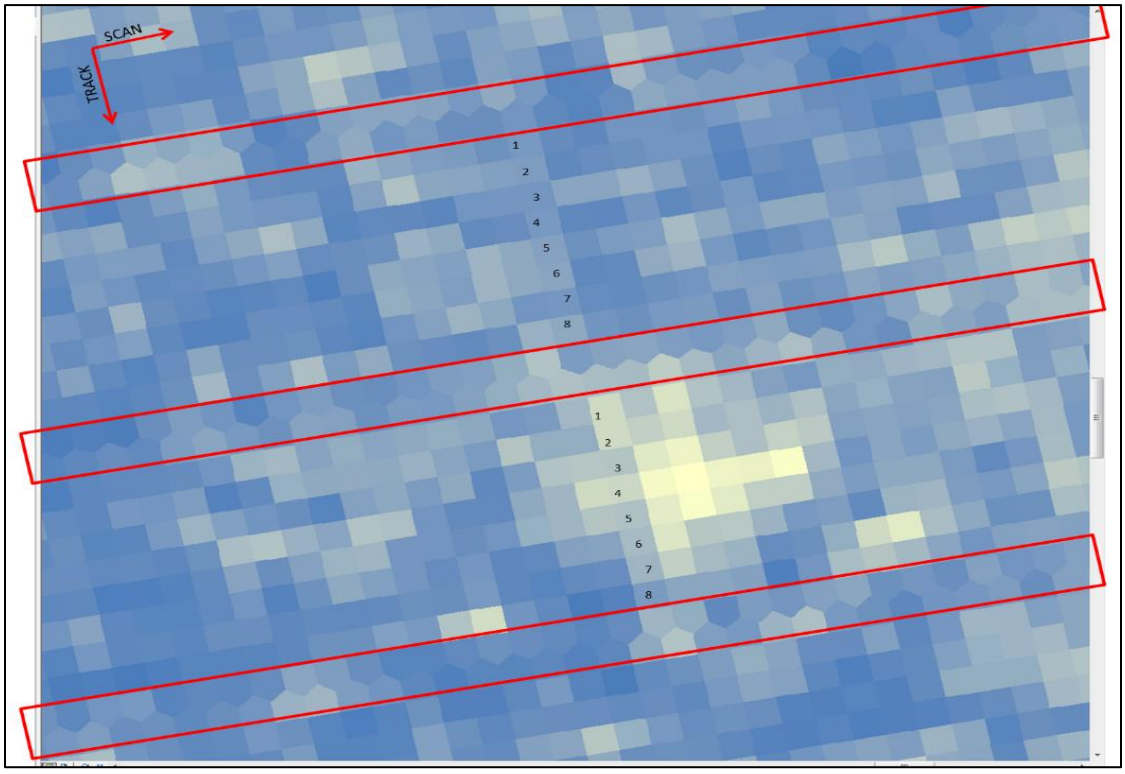

***Figure 3.9**: Problem of re-projecting MODIS data in finer resolution using MODIS swath tool*

Due to the unavailability of tools which could re-project images with resolutions that were finer than the native resolution of the MODIS images, programming scripts were written to do the task. Open source Python version 2.7 with supported packages for geo-spatial analysis was used while writing the scripts (Appendix E). The output of the footprint methodology script is a MODIS image with grid cells of 10m resolution and a visible footprint of the native sensor pixel orientation (250m, 500m, and 1000m resolution). There are two purposes of refining grid cells: 1) reducing the boundary size with respect to the

conventional grid cell (re-establishing grid cell resolution that is equal to the sensor pixel resolution), and 2) reproducing the native satellite sensor pixel orientation of the MODIS images.

The main advantages of using the footprint method for re-projecting MODIS images instead of using traditional gridding methods for field scale analysis are that the output of this method 1) shows exactly where the sensed area overlays the field, and 2) eliminates the problem of artifacts introduced by the gridding process during re-projection. Users are able to see the outline of each sensed area within the field, which assists them in carrying out more accurate field scale analysis. The problems of pixel weighting and repositioning introduced by gridding artifacts are eliminated by the footprint method during MODIS data re-projection. Since the pre-defined fixed grid cells are eliminated during the grid cell refinement process, the problem of a mismatch between the sensor pixel and the grid cells is eliminated. Figure 3.10 shows the re-projected MODIS image with step by step refined output pixel size, from a grid cell sampling resolution of 250 m to one of 10m. As the sampling resolution is increased, the original sensor pixel images are revealed. It shows how the orientation of fixed grid starts to disarrange and the native orientation of sensor pixels starts to appear with increasing sampling resolution during MODIS image re-projection. While the re-projection of the image is done in 10m resolution, the analysis of data should be performed in the native resolution of sensor cells (250m, 500m, and 1000m), and considering the revealed footprint of geometric orientation of sensor cells.

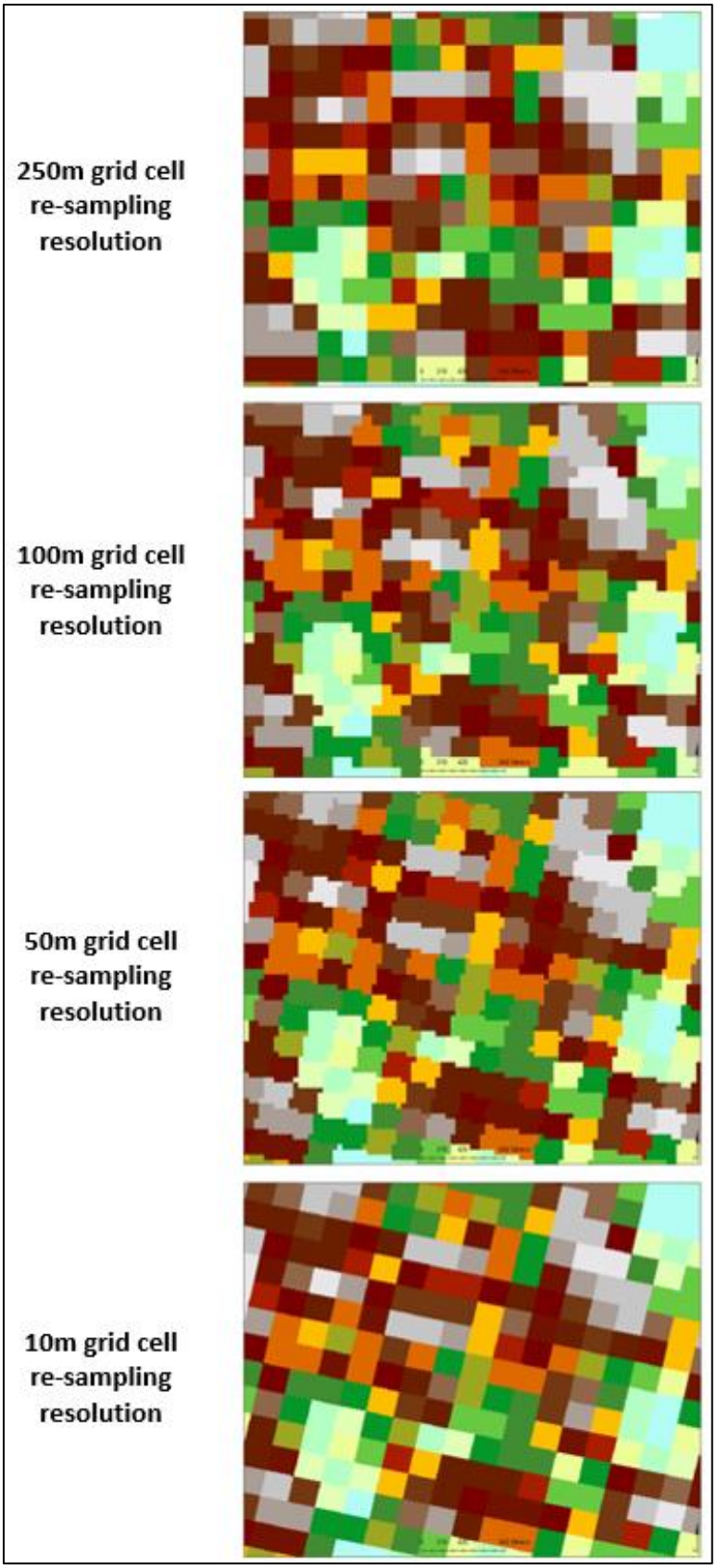

***Figure 3.10**: Step by step refinement of grid cell resampling resolution*

In the output MODIS image, each footprint sensor pixel contains hundreds of grid cells of 10m resolution with identical values that represent that particular sensor pixel. Fig 3.11 illustrates an example of fine resolution grid cells within a footprint sensor pixel. The field scale analysis is then performed in the native resolution of sensor cells (250m, 500m, and 1000m) as determined from the 10m grid cells (finer grid cell resolution assigned for re-projecting MODIS image). The re-projection of image in finer resolution (10m) assist in navigating the geometric orientation of sensor cells and avoids the problem of pixel contamination. Pixel footprints that only fall partly within a study area are easily identified and can be discarded since they do not fully represent emission and reflection from the field.

During the development of the footprint method, the first two bands of MODIS images were used, both having a sensor pixel resolution of 250m. Sensor pixel resolutions of other MODIS bands are 500m and 1000m. When the spatial resolution of a pixel increases, the area of mismatch in geometric orientation between pre-defined grid cells and sensor pixels increases. An example is illustrated in Figure 3.12. The red box is sensor pixel location and the black box is a pre-defined grid cell location.

This could lead to increases in differences between sensor pixel and grid cell values as the resolution increases. There is a possibility of pixel contamination from more neighboring area during grid value assignment in grid cells when the grid size increases. Similarly, the surface energy balance model uses the MODIS thermal band of 1000m pixel resolution and generates ET maps in 1000m spatial resolution grid cells. If the footprint method is applied and ET maps are produced and compared to maps generated with 1000m

grid cells, there is the possibility of large differences in estimated ET rates at the same location due to the aforementioned reason.

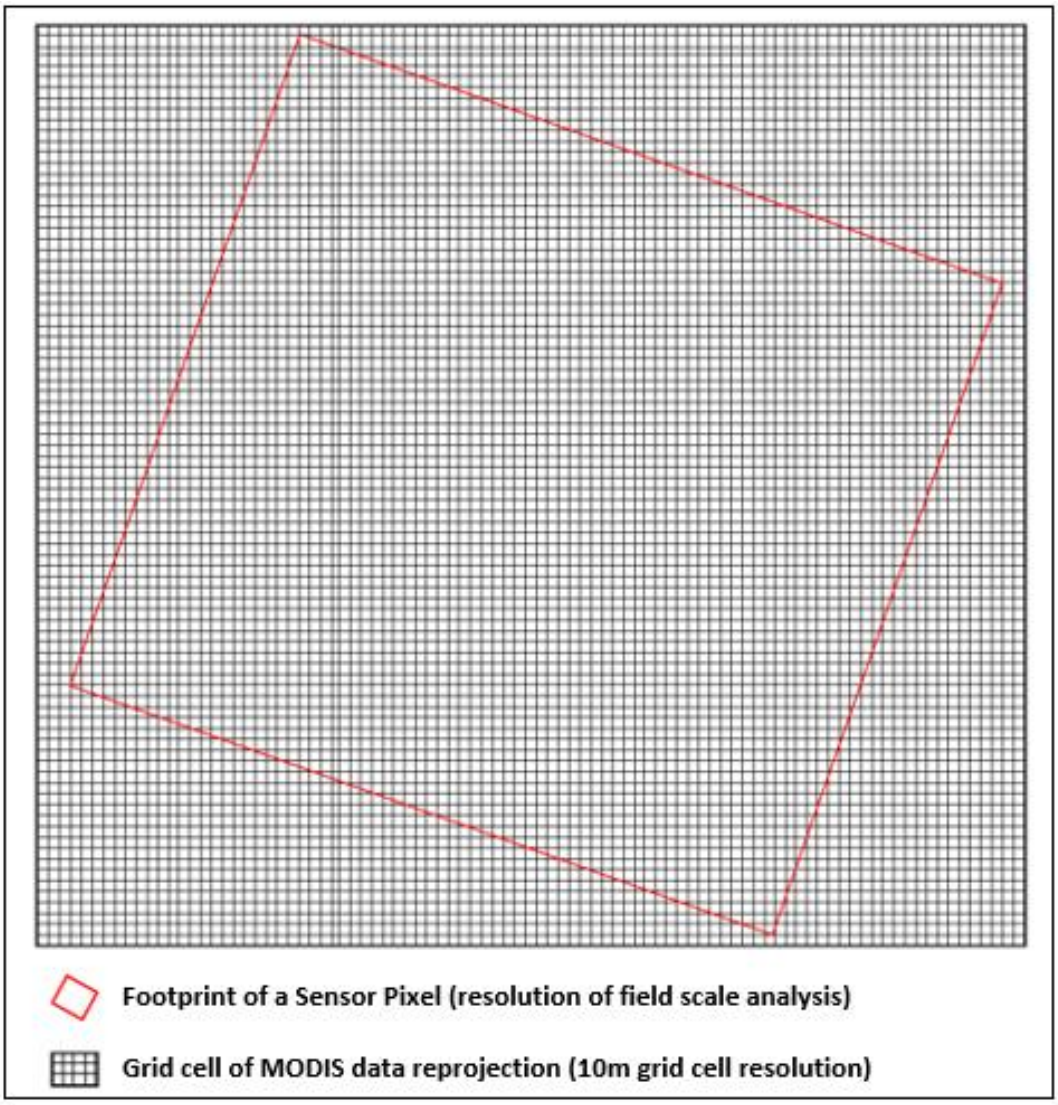

Figure 3.11*: 10 m grid cells within a sensor footprint pixel*

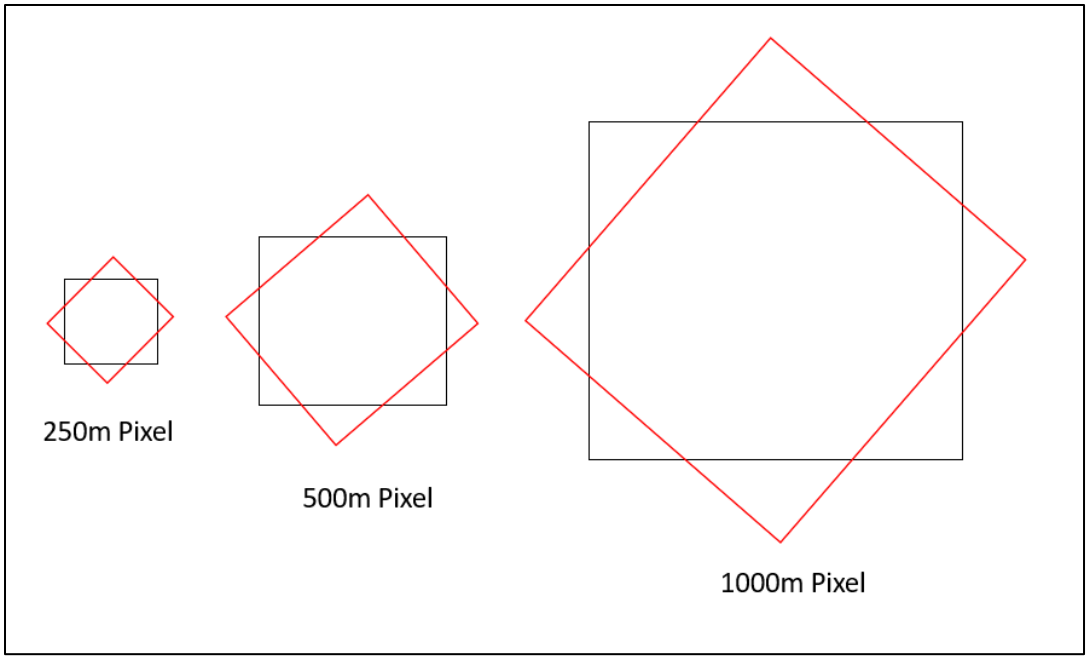

***Figure 3.12**: Increase in mismatch area with increase in pixel spatial resolution*

3.5 Field Scale Accuracy Assessment of Footprint Methodology and Gridded Methodology

An assessment of the improvement in the quality of the vegetation signal of the MODIS data for field scale analysis would be beneficial. For this purpose, vegetation parameters estimated using both the conventional gridded method and the footprint method were compared to field measured ground truth data.

3.5.1 Study Area

Green Leaf Area Index (LAI) data collected during the 2012 growing season at AmeriFlux field sites (US-Ne1 and US-Ne2) at Mead, Nebraska (Figure 3.13 and 3.14) were compared with LAI estimated with both the conventional gridded method and the footprint method. Field data of maize Green LAI were provided by Dr. Andrew E. Suyker

and Dr. Timothy J. Arkebauer from University of Nebraska-Lincoln, School of Natural Resources, and Department of Agronomy and Horticulture respectively as part of the Carbon Sequestration Program and AmeriFlux Network of Eddy Covariance towers [9]. Figure 3.15 shows the locations of sampling sites within two center pivot maize fields: US-Ne1 and US-Ne2. The measured Green LAI parameter values from all six sampling sites within each field were averaged to represent the Green LAI value of the field.

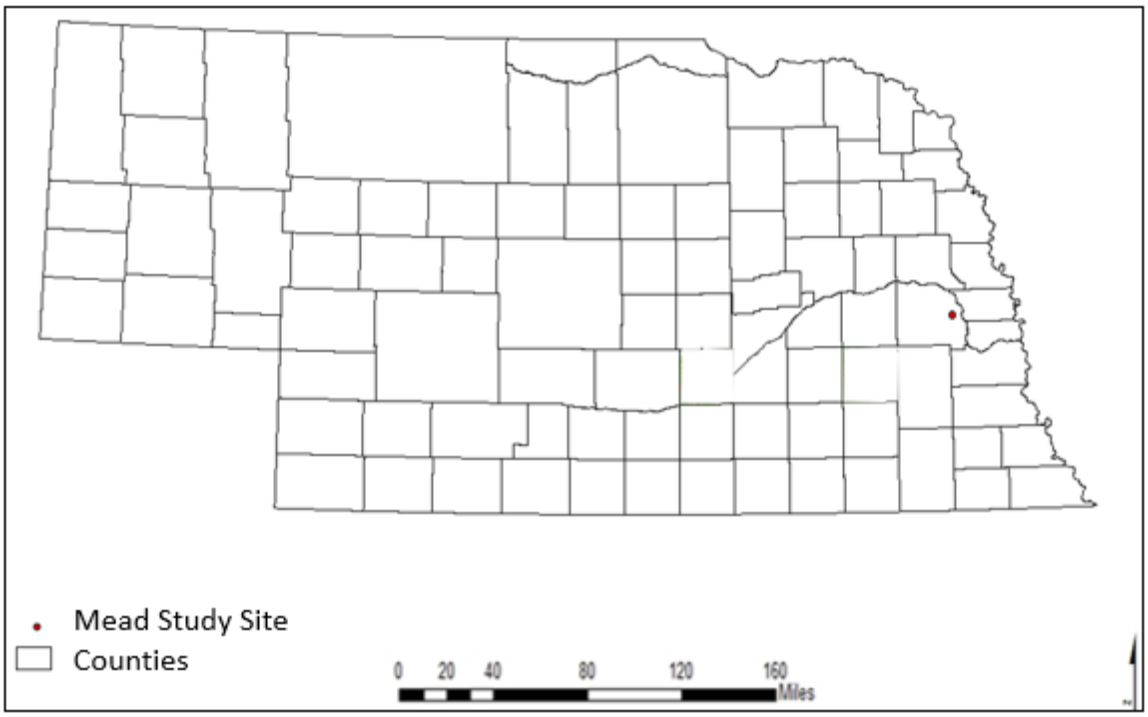

***Figure 3.13**: Location of the study site in Nebraska*

***Figure 3.14**: Field analysis study area location*

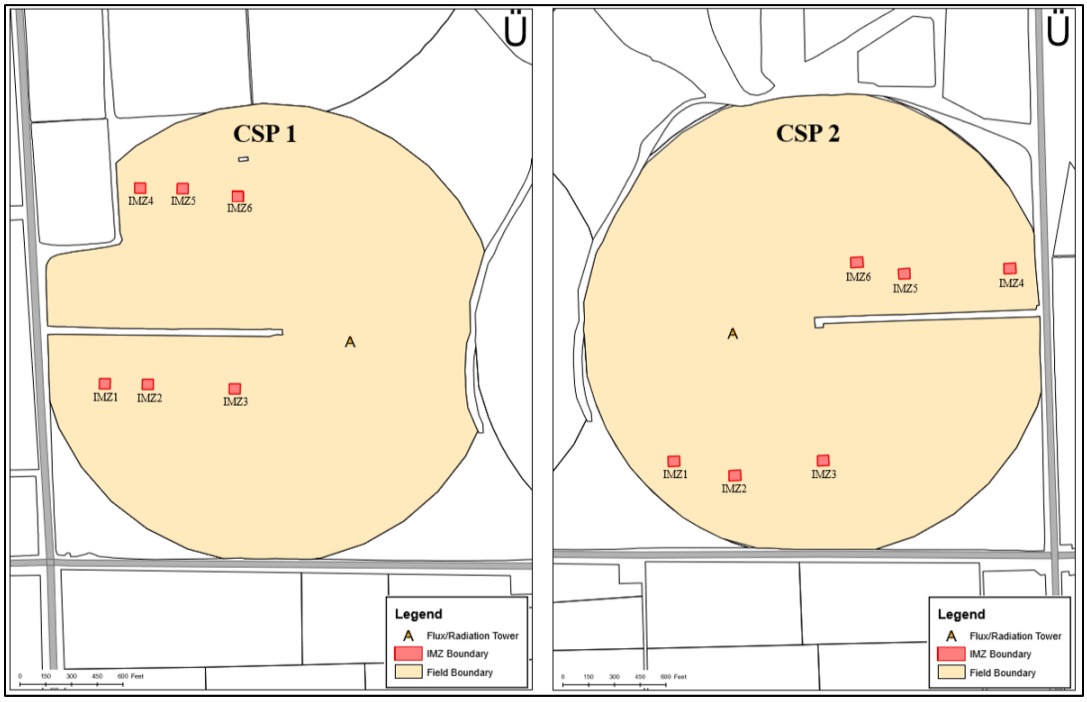

***Figure 3.15**: Ground truth locations within center pivot fields*

LAI is calculated based on the Normalized Difference Vegetation Index (NDVI) which is a ratio of m^2 leaf area to m^2 ground area. The first two bands of MODIS data with spatial resolution of 250m were used to estimate NDVI. The range of the wavelength of the first band (b1) in the visible red region is 620 – 670 nm, and that of the second band (b2) near infrared region is 841 – 876 nm. Equations (2) and (3) show how NDVI and LAI are estimated with two MODIS bands based on work by Huete et al.[10-13] and Myneni et al. [14] respectively.

$$NDVI = \frac{(\rho_{NIR} - \rho_{Red})}{(\rho_{NIR} + \rho_{Red})} = \frac{(b2 - b1)}{(b2 + b1)} \quad (2)$$

$$LAI = 9.519NDVI^3 + 0.104NDVI^2 + 1.236NDVI - 0.257 \quad (3)$$

Only grid cells and footprint pixels that fell completely within a field were selected, and their LAI values were averaged to represent the LAI value of the field. Figure 3.16 illustrates an example of selected grid cells and footprint cells in center pivot maize fields US-Ne1 and US-Ne2.

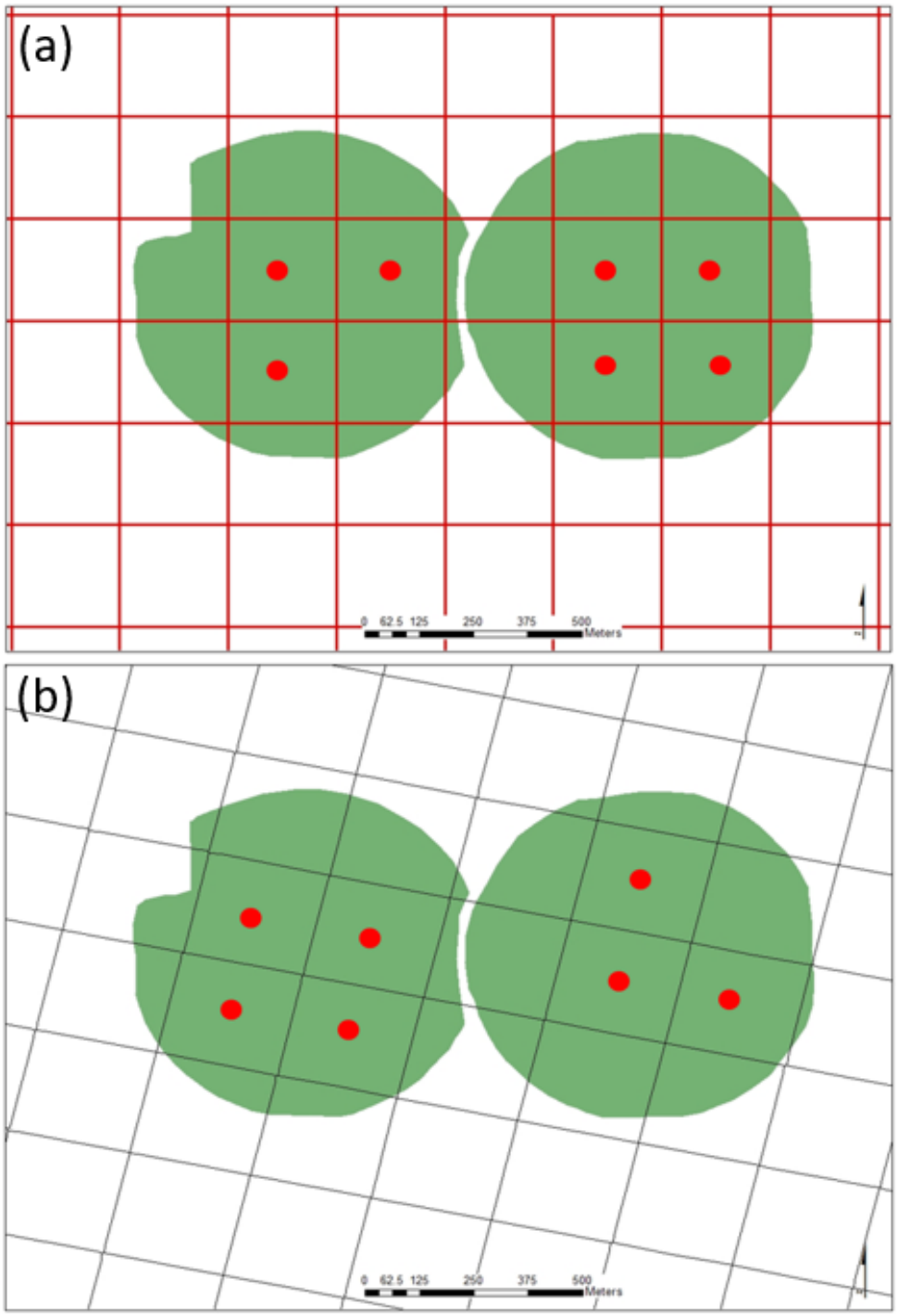

***Figure 3.16**: Grid cells and sensor pixels representing center pivot maize fields. (a) gridded data, and (b) footprint data*

The combination of MODIS - TERRA and AQUA satellites can provide image of an area on a daily basis, but the θ_v associated with an area will be variable from day to day.

Images coming from MODIS can have θ_v up to 56 degrees, far enough from Nadir to produce substantial pixel deformation. MODIS images with maximum θ_v less than 15 to 20 degrees is preferred to avoid pixel deformation [15]. Images of a particular area with θ_v within 20 degrees can be retrieved in 3 to 4 day intervals, and therefore all the images with θ_v within 20 degrees of mead irrigated maize fields were retrieved and analyzed for the 2012 growing season.

3.5.2 Accuracy Assessment of Results

In Appendix C Table C.1 and Table C.2 lists the values of LAI (equation of Myneni et al.) estimated from MODIS data using the footprint and gridded methods and the corresponding Green LAI values measured at the sampling sites during the 2012 growing season in field US-Ne1.

LAI values (equation of Myneni et al.) estimated using the footprint and gridded methods, and Green LAI values sampled in the fields are plotted against cumulative Growing Degree Days (GDD) for field US-Ne1 and US-Ne2 in Figure 3.17 and Figure 3.18 respectively.

LAI data measured at the sampling sites and estimated from the MODIS data using the footprint and gridded data for days in which all three data were collected were used for statistical comparison. Table 3.1 and Table 3.2 lists the observed Green LAI data and LAI estimated (equation of Myneni et al.) data using footprint and gridded methods for maize fields US-Ne1 and US-Ne2 respectively. Only five sampling points (days) were available in which all three data were available that could be used for statistical analysis

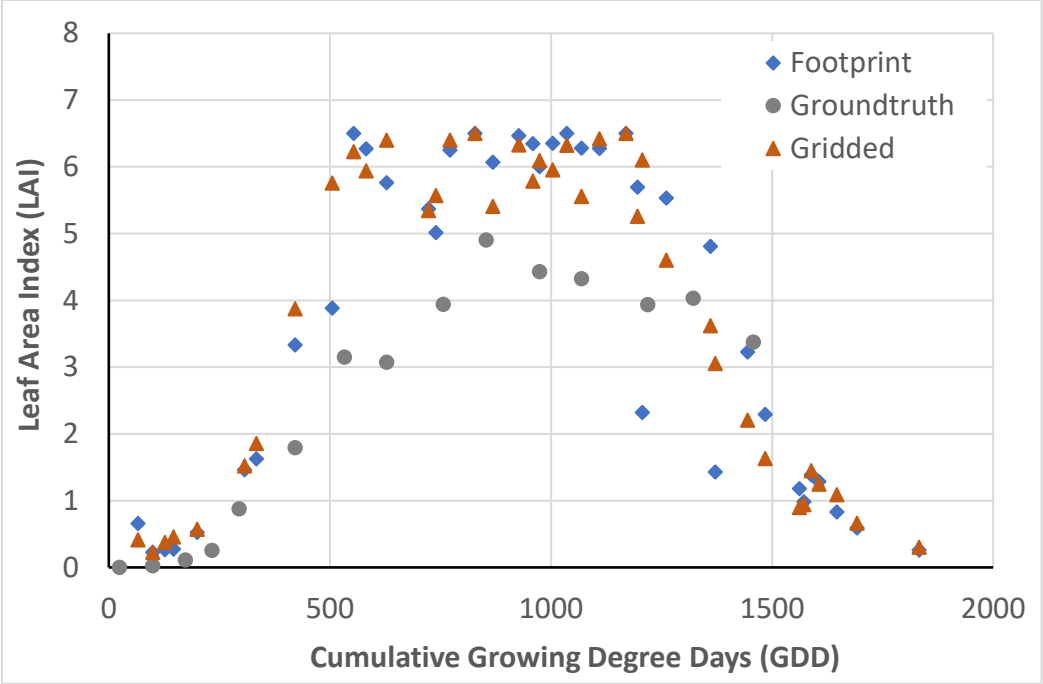

***Figure3.17**: LAI values estimated using the footprint and gridded methods, and ground truth measurements for field US-Ne1, using LAI equation of Myneni et al.*

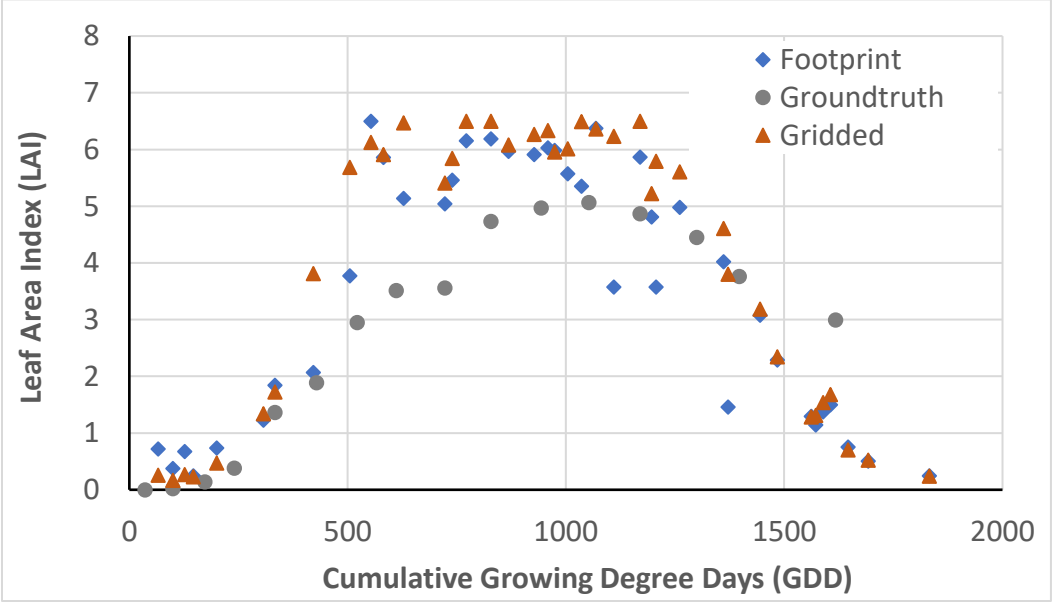

***Figure 3.18**: LAI values estimated using the footprint and gridded method, and ground truth measurements for field US-Ne2, using LAI equation of Myneni et al.*

Table 3.1: *MODIS estimated and field ground truth LAI values for field US-Ne1*

Date	Footprint LAI	Gridded LAI	Ground truth Green LAI
5/10/2012	0.226	0.227	0.023
6/11/2012	3.332	3.874	1.792
6/27/2012	5.762	6.401	3.072
7/20/2012	6.001	6.094	4.430
7/26/2012	6.282	5.557	4.324

Table 3.2: *MODIS estimated and field ground truth LAI values for field US-Ne2*

Date	Footprint LAI	Gridded LAI	Ground truth Green LAI
5/10/2012	0.376	0.167	0.022
6/4/2012	1.844	1.725	1.365
7/3/2012	5.041	5.409	3.559
7/10/2012	6.190	6.500	4.733
8/2/2012	5.867	6.497	4.872

Three statistical parameters were compared using the MODIS – estimated LAI and measured ground truth Green LAI data for both fields [16]; Root Mean Square Error (RMSE), unbiased Root Mean Square Error (unRMSE), and Normalized Root Mean Square Error (nRMSE). Equations (4), (5) and (6) show how these statistical parameters were calculated.

$$RMSE = \sqrt{\sum \frac{(LAI_{est} - LAI_{ref})^2}{n}} \tag{4}$$

$$ubRMSE = \sqrt{\sum \frac{\left[(LAI_{est} - \frac{1}{n}\sum LAI_{est}) - (LAI_{ref} - \frac{1}{n}\sum LAI_{ref})\right]^2}{n}} \tag{5}$$

$$nRMSE = \frac{RMSE}{LAI_{ref}^{MAX} - LAI_{ref}^{MIN}} \tag{6}$$

where LAI_{est} is the MODIS estimated LAI value, LAI_{ref} is the ground truth measured LAI value, LAI_{ref}^{MAX} is the maximum LAI value of measured ground truth, and LAI_{ref}^{MIN} is the minimum LAI value of measured ground truth.

Table 3.3 show a side by side comparison of statistical results for fields US-Ne1 and US-Ne2 based on five sampling points.

Table 3.3: *Statistical comparison of LAI estimates from footprint and gridded data for field US-Ne1 and US-Ne2 (LAI equation of Myneni et al.)*

	Field US-Ne1		**Field US-Ne2**	
	Footprint	**Gridded**	**Footprint**	**Gridded**
RMSE (m^2/m^2)	1.786	1.987	1.065	1.366
ubRMSE (m^2/m^2)	0.856	1.025	0.473	0.739
NRMSE (m^2/m^2)	0.405	0.451	0.220	0.282

The statistical analysis based on the LAI values of five sampling points estimated by using equation of Myneni et al., shows that LAI values of the MODIS footprint method are closer to measured ground truth data than those of the MODIS gridded method in both center pivot maize fields. This suggests that the footprint method is more accurate than the conventional gridded method for field scale analysis. Statistical results of both fields show that there is an improvement in LAI estimation when the footprint method is applied. In field US-Ne1, using the footprint method to estimate LAI reduces the RMSE by 10.1%, the ubRMSE by 16.5% and the nRMSE by 10.2%. Similarly, in field US-Ne2 using the footprint method reduces the RMSE by 22%, the ubRMSE by 36%, and nRMSE by 22%.

Separate plots of LAI versus Cumulative GDD were created by fitting fourth order polynomial equations to estimated and measured LAI from Table C.1 and C.2 (Appendix C). Figure 3.19 and Figure 3.20 show curve fits of LAI data against cumulative GDD.

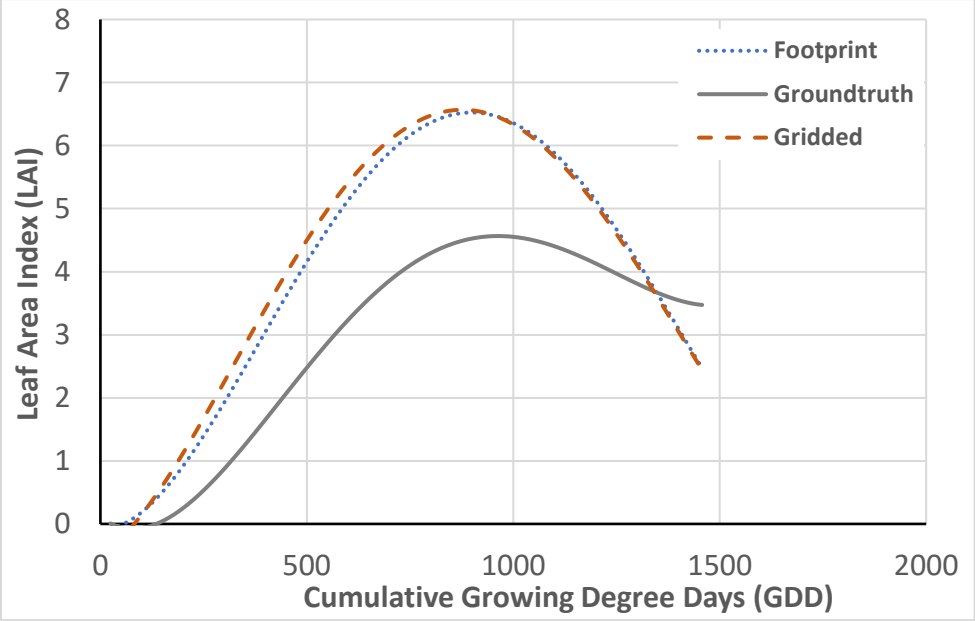

***Figure 3.19**: LAI (equation of Myneni et al.) as a function of growing degree days using the MODIS footprint and gridded methods and ground truth measurements (Field US-Ne1)*

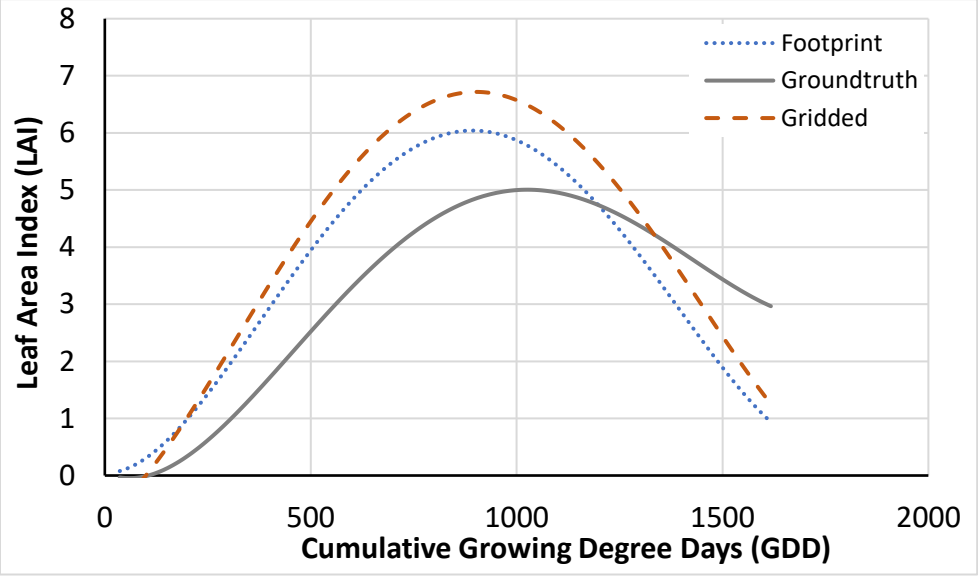

***Figure 3.20**: LAI (equation of Myneni et al.) as a function of growing degree days using the MODIS footprint and gridded methods and ground truth measurements (Field US-Ne2)*

After data gaps were filled by applying fourth order polynomial equations, statistical parameters of both fields were again calculated. Table 3.6 shows a side by side comparison of statistical results for fields US-Ne1 and US-Ne2.

Table 3.4: *Statistical comparison of fields with gap filled LAI data*

	Field US-Ne1		**Field US-Ne2**	
	Footprint	**Gridded**	**Footprint**	**Gridded**
RMSE (m^2/m^2)	1.331	1.468	1.110	1.351
ubRMSE (m^2/m^2)	0.800	0.896	1.049	1.091
NRMSE (m^2/m^2)	0.287	0.316	0.220	0.268

The statistical results of both fields show smaller LAI error for the footprint method than for the gridded method. In field US-Ne1, error in LAI estimates decreased by 9.3% in RMSE, 10.7% in ubRMSE, and 9.2% in nRMSE when the footprint method was used. Similarly, in field US-Ne2, error in LAI estimates decreased by 17.8% in RMSE, 3.8% in ubRMSE, and 17.9% in nRMSE.

Viña et al. [17] developed an equation to estimate Green LAI based on the site specific measurement of Green LAI data and remotely sensed NDVI data from the Mead AmeriFlux fields. Measured Green LAI data of four growing seasons (year 2001 to year 2004) were used in the study. Equation (7) show how Green LAI is calculated from NDVI data.

$$Green\ LAI = \frac{\ln\left[\left(1-\frac{NDVI-0.2064}{0.7298}\right)^{-1}\right]}{0.6159} \quad (7)$$

Based on this field specific Green LAI equation of Viña et al., Green LAI were estimated from MODIS data using footprint and gridded methods. Statistical analysis based

on Green LAI estimates was performed. Table C.3 and Table C.4 in Appendix C lists the values of Green LAI (equation of Viña et al.) estimated from MODIS data using the footprint and gridded methods and the corresponding Green LAI values measured at the sampling sites during the 2012 growing season in fields US-Ne1 and US-Ne2, respectively. Green LAI values (equation of Viña et al.) estimated using the footprint and gridded methods, and Green LAI values sampled in the fields are plotted against cumulative Growing Degree Days (GDD) for field US-Ne1 and US-Ne2 in Figure 3.21 and Figure 3.22 respectively.

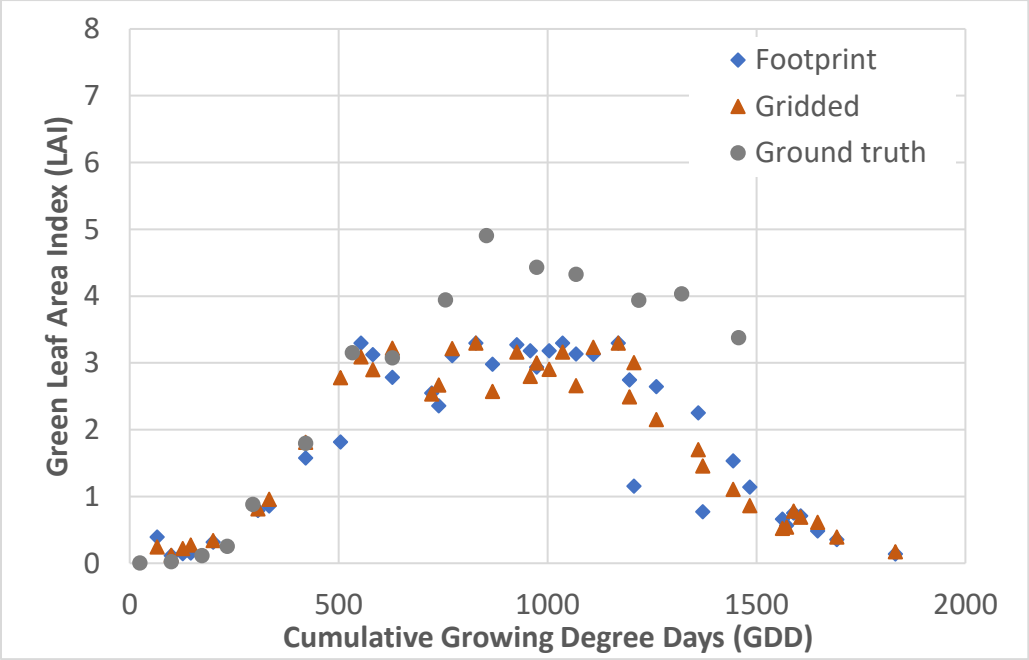

***Figure 3.21**: Green LAI values estimated (equation of Viña et al.) using the footprint and gridded methods, and ground truth measurements for field US-Ne1*

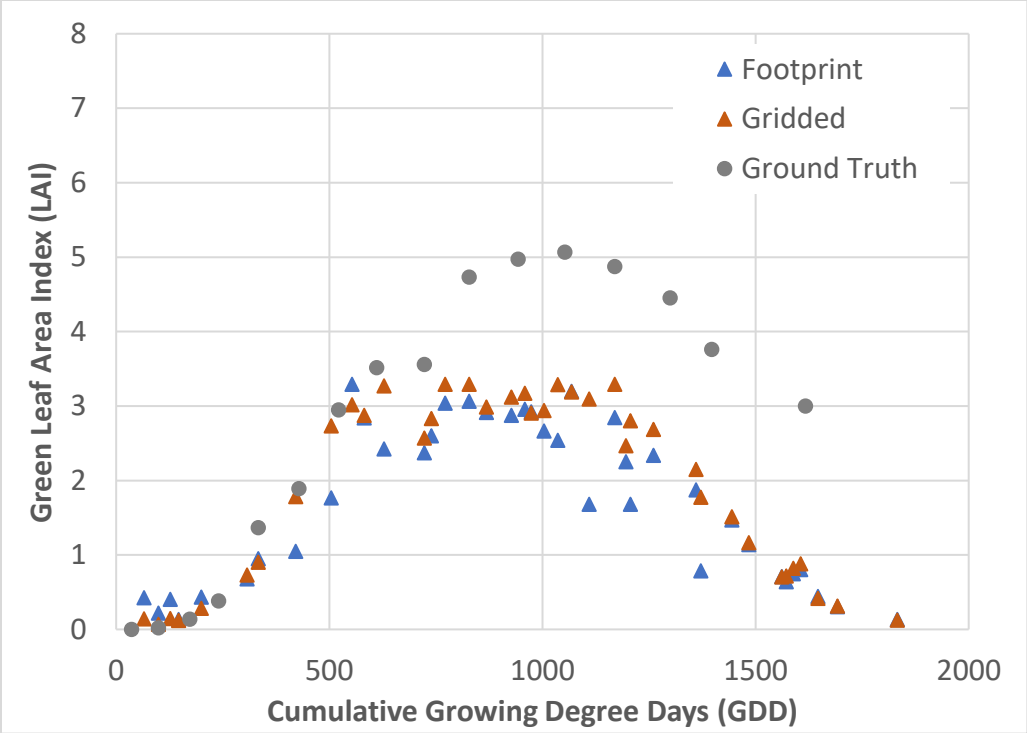

***Figure 3.22**: Green LAI values estimated (equation of Viña et al.) using the footprint and gridded method, and ground truth measurements for field US-Ne2*

Table 3.5 and Table 3.6 list the observed Green LAI data and Green LAI estimated (equation of Viña et al.) using footprint and gridded methods for maize fields US-Ne1 and US-Ne2 respectively. Only five sampling points (days) were available in which all three data were available that could be used for statistical analysis.

***Table 3.5:** MODIS estimated (equation of Viña et al.) and field ground truth Green LAI values for field US-Ne1*

Date	Footprint LAI	Gridded LAI	Ground truth Green LAI
5/10/2012	0.114	0.115	0.023
6/11/2012	0.574	1.809	1.792
6/27/2012	2.780	3.216	3.072
7/20/2012	2.933	2.996	4.430
7/26/2012	3.129	2.657	4.324

Table 3.6: *MODIS estimated (equation of Viña et al.) and field ground truth Green LAI values for field US-Ne2*

Date	Footprint LAI	Gridded LAI	Ground truth Green LAI
5/10/2012	0.220	0.068	0.022
6/4/2012	0.951	0.900	1.365
7/3/2012	2.370	2.571	3.559
7/10/2012	3.063	3.293	4.733
8/2/2012	2.847	3.290	4.872

Table 3.7 shows a side by side comparison of statistical results for fields US-Ne1 and US-Ne2 based on five sampling points.

Table 3.7: *Statistical comparison of Green LAI estimates from footprint and gridded data for field US-Ne1 and US-Ne2*

	Field US-Ne1		Field US-Ne2	
	Footprint	**Gridded**	**Footprint**	**Gridded**
RMSE (m^2/m^2)	0.873	0.986	1.305	1.074
ubRMSE (m^2/m^2)	1.723	0.805	0.814	0.608
NRMSE (m^2/m^2)	0.198	0.224	0.269	0.222

The results of statistical analysis of five sampling points based on the Green LAI values estimated by using equation of Viña et al. are different from that of previous analysis which is based on the LAI values estimated by using Myneni et al. In field US-Ne1, although the RMSE and NRMSE declined by 11.4% and 11.6% respectively; ubRMSE actually increased by 114% while comparing footprint method with gridded method. In the case of field US-Ne2, all statistical parameters increased when the footprint method was compared with the gridded method. The RMSE, ubRMSE, and NRMSE of footprint method increased by 21.5%, 33.9%, and 21.1% respectively.

As previously, separate plots of Green LAI versus Cumulative GDD were created by fitting fourth order polynomial equations to estimated and measured LAI from Table C.3 and C.4 (Appendix C). Figure 3.23 and Figure 3.24 show curve fits of LAI data against cumulative GDD. Separate plots of LAI versus Cumulative GDD were created by fitting fourth order polynomial equations to estimated and measured LAI from Table C.1 and C.2 (Appendix C). Figure 3.23 and Figure 3.24 show curve fits of LAI data against cumulative GDD.

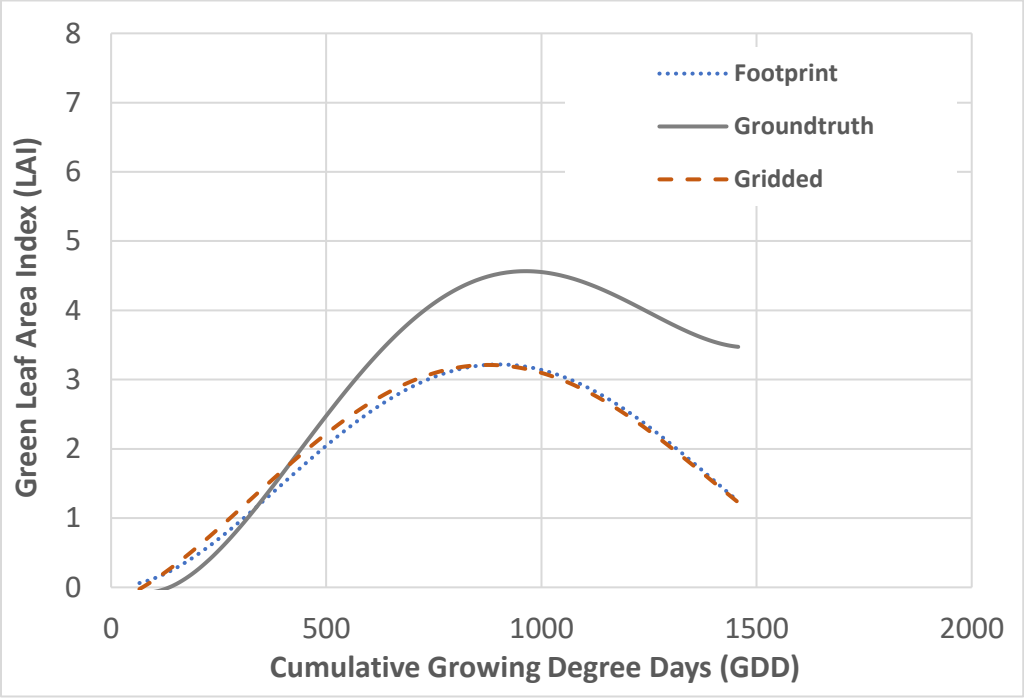

***Figure 3.23**: Green LAI (equation of Viña et al.) as a function of growing degree days using the MODIS footprint and gridded methods and ground truth measurements (Field US-Ne1)*

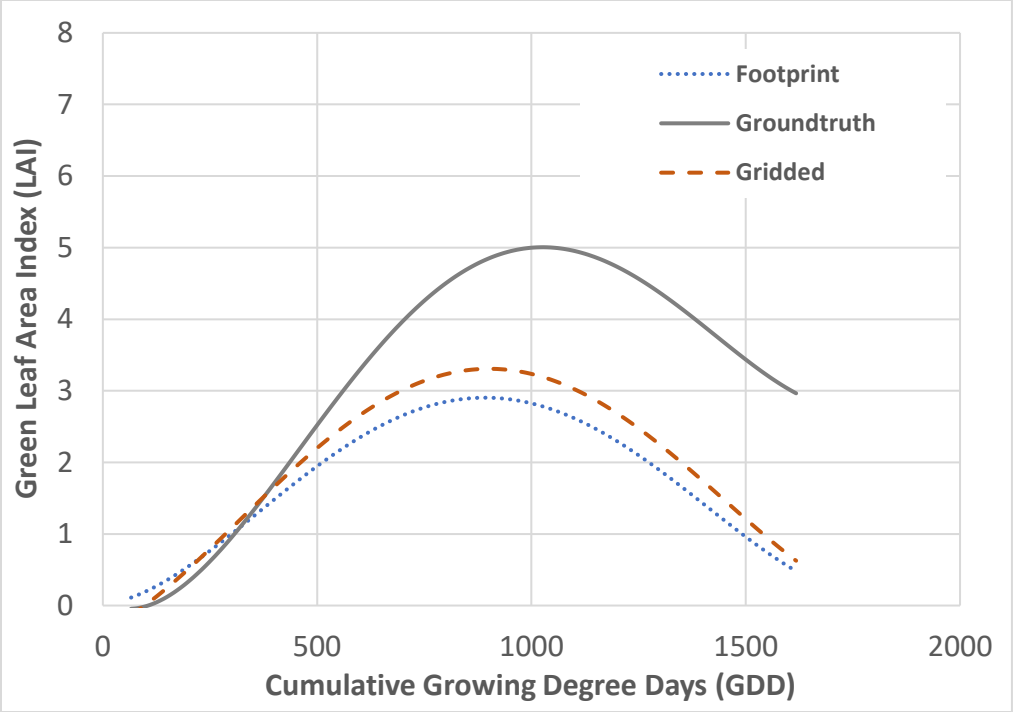

***Figure 3.24**: Green LAI (equation of Viña et al.) as a function of growing degree days using the MODIS footprint and gridded methods and ground truth measurements (Field US-Ne2)*

After gaps were filled by applying fourth order polynomial equations, statistical parameters of both fields were again calculated. Table 3.8 shows a side by side comparison of statistical results for fields US-Ne1 and US-Ne2.

***Table 3.8:** Statistical comparison of fields with gap filled Green LAI data*

	Field US-Ne1		**Field US-Ne2**	
	Footprint	**Gridded**	**Footprint**	**Gridded**
RMSE (m^2/m^2)	1.146	1.161	1.730	1.468
ubRMSE (m^2/m^2)	0.786	0.852	1.093	0.957
NRMSE (m^2/m^2)	0.247	0.25	0.343	0.291

This analysis should be done with data from multiple years for a more concrete conclusion of decreased error in LAI estimates with footprint methodology compared to that of gridded method.

The statistical analysis of MODIS LAI estimates based on LAI equation of Myneni et al. and Green LAI field measurements indicates that the footprint methodology of handling MODIS datasets when applied for field scale analysis provides better results. On the contrary, the results of statistical analysis of MODIS Green LAI estimates based on Green LAI equation of Viña et al. does not support this conclusion. The equation of Viña et al. was developed as a Mead site specific equation using five years of field data, whereas the equation of Myneni et al. is a general LAI equation developed for world wide application. This could be the reason for different results of statistical analysis when the LAI equation of Myneni et al. and the Green LAI equation of Viña et al. are applied in MODIS data.

3.5.3 Paired T-Test Analysis

A paired t-test was performed to analyze if there is a significant improvement when the footprint method is used to estimate MODIS LAI values. The daily values of footprint and gridded MODIS LAI data estimated from fourth order polynomial curves and ground truth Green LAI estimated by applying fourth order polynomials were used for this test with a null hypothesis that the difference between gridded and ground truth data is the same as the difference between footprint and ground truth data. Statistical parameters needed to conduct the paired t-test were calculated which are described in steps below:

1. The absolute difference between footprint LAI and ground truth Green LAI values; and between gridded LAI and ground truth Green LAI value were calculated at each sampling point as;
    a. The absolute value of [footprint LAI – ground truth Green LAI]
    b. The absolute value of [gridded LAI – ground truth Green LAI]
2. The difference of the products from ***a*** and ***b*** of step 1 were calculated at each sampling point as ***"b – a"***. This was done so that a positive value in the mean difference would show that the difference between gridded method data and ground truth data is greater than the difference between footprint method data and ground truth data.
3. The mean difference *(d)* and standard deviation *(S_d)* of all the values computed at step 2 were calculated.
4. Standard error of the mean difference *(SE(d))* [18] was calculated as;

    $$SE(d) = \frac{S_d}{\sqrt{n}} \qquad (8)$$

    where *n* is the number of sampling points
5. The t-statistic value [19] was calculated as;

    $$T = \frac{d}{SE(d)} \qquad (9)$$

6. The probability value *(p-value)* for the t-test was estimated by looking at the t-distribution.

First, the paired t-test was done for the MODIS LAI values calculated by using the LAI equation of Myneni et al. Table 3.9 lists the value of computed statistical parameters and the final calculated probability value of paired t-test for fields US-Ne1 and US-Ne2.

Table 3.9*: Statistical parameters and final p-value computed for MODIS LAI estimated using Myneni et al. LAI equation*

	Field US-Ne1	**Field US-Ne2**
D	0.117	0.173
Sd	0.162	0.485
SE(d)	0.015	0.043
T	7.796	4.066
Degrees of Freedom	115	129
p-value	< 0.00001	0.000083

It is seen from Table 3.9 that for both fields T values are very high, and p-values are very small. This implies that the level of significance is very high and shows evidence of improvement of the footprint method over gridded method; however, the improvement of LAI estimates is only 0.117 m^2/m^2 and 0.173 m^2/m^2 in fields US-NE1 and US-Ne2, respectively. The confidence interval for the mean difference was calculated to see within what limits of LAI data, the estimates the improvement of footprint method took place. A 95% confidence interval for mean difference was calculated [20] as;

95% confidence interval for true $\boldsymbol{d = d \pm [T^* \times SE(d)]}$ *(10)*

where ***T**** is the 2.5% point of the t-distribution on ***n-1*** degrees of freedom. A value of 1.96 was chosen from a t-distribution table, since the degrees of freedom are very high for LAI data. Based on equation (10), *w*ith 95% certainty, the improvement of LAI estimates by the footprint method lies between LAI estimates of 0.088 $m^2/m^2$and 0.147 m^2/m^2. Similarly, for field US-Ne2, the improvement of LAI estimates by the footprint method lies between 0.090 m^2/m^2 and 0.256 m^2/m^2 with 95% certainty.

The statistical parameters and final p-value of paired t-test for fields US-Ne1 and US-Ne2 were again calculated for MODIS Green LAI calculated by using Viña et al. Table

3.10 lists the value of computed statistical parameters and final calculated probability value of paired t-test for fields US-Ne1 and US-Ne2.

Table 3.10*: Statistical parameters and final p-value computed for MODIS LAI estimated using Viña et al. LAI equation*

	Field US-Ne1	**Field US-Ne2**
D	0.008	-0.250
Sd	0.099	0.147
SE(d)	0.009	0.013
T	0.854	-19.405
Degrees of Freedom	115	129
p-value	0.39488	< 0.00001

It is seen from Table 3.10 that in the case of Field US-Ne2, the mean difference *(d)* and T value are negative, which means that the footprint method did not improve Green LAI estimates compared to the gridded method. In the case of Field US-Ne1, the value of *T* is low and *p-value* is high which implies that the level of significance is low. The improvement of LAI estimates is only 0.008 m^2/m^2. By applying equation (10), the interval calculated for field US-Ne1 was (0.026, -0.01). With 95% certainty, the improvement of LAI estimates by the footprint method does not exceed 0.026 m^2/m^2.

3.6 Potential Use of MODIS Data in Irrigation Water Management

The precise estimation of water requirements for irrigated crops over large areas is still a paramount concern in agriculture, and methodologies based on remote sensing can assist in estimation of actual water requirements [21]. The scheduling of water irrigation based on the response of different indices to different growth stages of crops can potentially lead

to efficient use of irrigation water and higher crop yield. Landsat images are available once every two weeks, and data from multiple years are needed to generate crop characteristic curves. The advantage of the higher temporal resolution of MODIS satellite images is that it has a potential to generate crop characteristic curve with only data from one year.

Huete et al. [22] developed the Soil Adjusted Vegetation Index (SAVI), an index similar to NDVI but with added computation to minimize soil brightness influences. Equation (7) shows how SAVI is estimated using the first two bands of MODIS.

$$SAVI = \frac{(1+\mathrm{L})(\rho_{NIR}-\rho_{Red})}{(\rho_{NIR}+\rho_{Red}+L)} = \frac{(1+L)(b2-b1)}{(b2+b1+L)} \quad (7)$$

In equation (7) L is a canopy background adjustment factor, a value of 0.5 is used to minimize soil brightness variations and eliminate the need for additional calibration for different soils.

Campos et al. [21] utilized 11 years of Landsat data and generated SAVI curve of different crops. Figure 3.25 shows SAVI plot of irrigated maize from 11 years, and Figure 3.26 shows the development of SAVI curve combining 11 years of Landsat data.

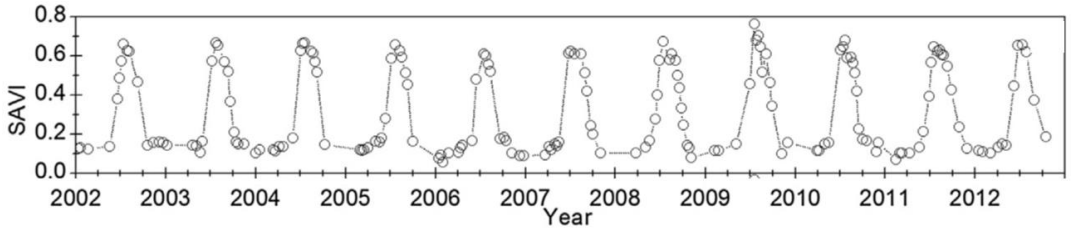

Figure 3.25: *SAVI curve of irrigated maize for different growing seasons derived from Landsat images (2002 – 2012). (modified figure from Campos et. al., 2017, figure 1)*

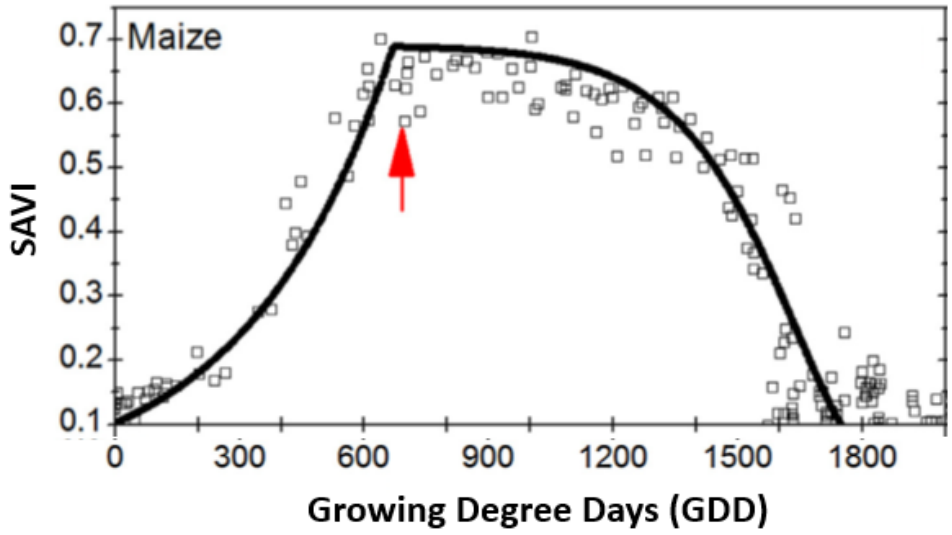

Figure 3.26: *Refined crop characteristic curve of irrigated maize after combining multiple years of Landsat images. (modified figure from Campos et. al., 2017, figure 2)*

The SAVI index responds differently during different growth phases of maize crops. The initial phase is characterized by fast development of the SAVI values from bare soil conditions to the peak values of SAVI. The second phase is a plateau period characterized by relative stability with a slightly decreasing trend in SAVI values. In the third phase, SAVI values describe the crop senescence, reaching minimum values corresponding to bare soil conditions [21]. This plot is useful for identifying times in the growing season when different growth phases begin, allowing irrigation to be efficiently scheduled.

The SAVI values were calculated for a growing season of year 2012 using MODIS data with footprint methods of reprojection for irrigated maize. Figure 3.27 shows a plot of SAVI response during different phases of the growing season of field US-Ne2.

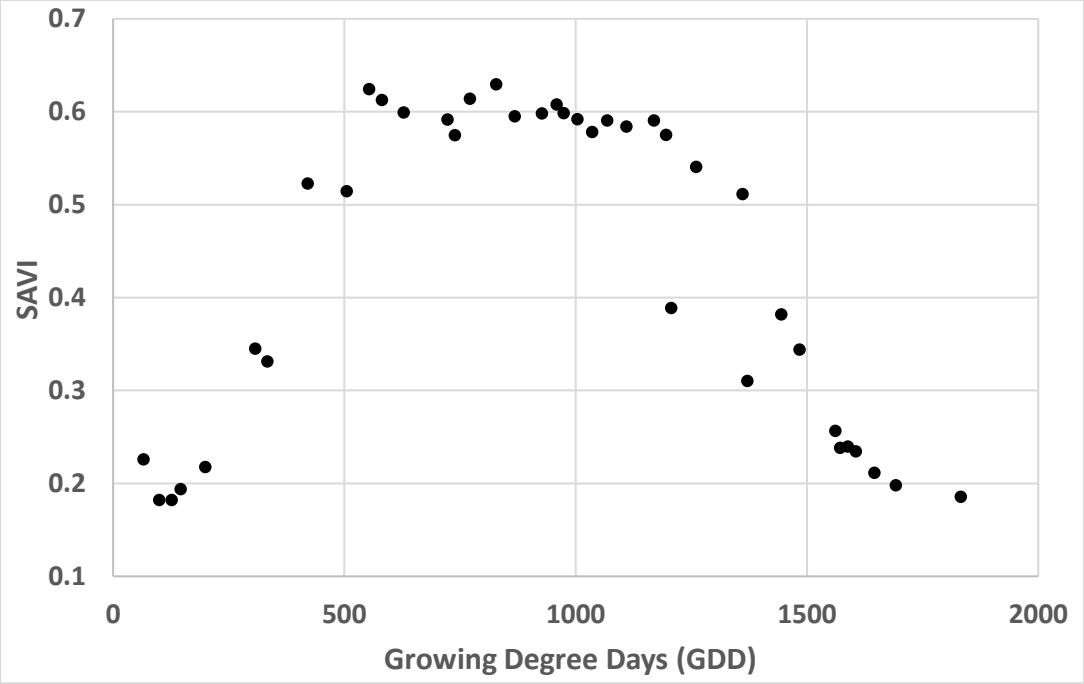

Figure 3.27: *SAVI curve of irrigated maize field US-Ne2 for a single growing season of year 2012 derived from MODIS images using footprint method*

The SAVI plot of Figure 3.27 using only one year of MODIS data is comparable to SAVI plot of Figure 3.26 where 11 years of Landsat data were used to generate SAVI curve. The nature of SAVI index response of irrigated maize in initial, second, and third phase of growth described by Campos et al. [21] is captured in the SAVI plot using MODIS data of only one growing season.

3.7 Conclusions

This study explored the use of MODIS satellite images with good temporal resolution to compensate for the problem of coarse temporal resolution of Landsat satellite images in field scale analysis of agricultural crops. The existing method of re-projecting MODIS images in a grid cell format did not preserve the geometric orientation of sensor

pixels, posing a risk of pixel value contamination. To avoid this problem and enable the use of MODIS images for field scale analysis, a new method of re-projecting MODIS satellite images called the “footprint method” was developed. The new method preserves the geometric orientation of satellite sensor pixels.

To evaluate the advantages of the footprint method over the gridded method of data re-projection, field scale accuracy assessment was performed with LAI data from maize from fields in Mead, Nebraska from the year 2012. The measured Green LAI data from were closer to LAI estimate from MODIS data with the footprint method than to estimates from the gridded method. The Root Mean Square (RMSE), unbiased RMSE (ubRMSE), and normalized RMSE (NRMSE) from the footprint method of field US-Ne1 decreased by 0.201 m^2/m^2, 0.169m^2/m^2, and 0.046 m^2/m^2 , respectively when compared to the gridded method. Similarly, for field US-Ne2, RMSE, ubRMSE, and NRMSE decreased by 0.301 m^2/m^2, 0.266m^2/m^2, and 0.062 m^2/m^2 respectively. On the contrary, the results of statistical analysis of MODIS Green LAI estimates based on Green LAI equation of Viña et al. does not support this conclusion. The results of t-test analysis show that the improvement of MODIS LAI and Green LAI estimates from footprint method when compared to that of gridded method is relatively very small.

After developing the footprint method and enabling MODIS data to be more accurate for field scale analysis of crops, the temporal resolution of MODIS satellite images was explored. Frequent MODIS satellite images within a growing season re-projected with the footprint method were tested to analyze the characteristics of crops at different growth stages. The SAVI index estimated from MODIS images were able to show detailed curve characteristics of SAVI at different phases of the growing season for maize.

This analysis improves the capability of MODIS images to be used for monitoring crops on a more frequent basis. Scheduling of water irrigation based on different growth stages of crops will then be possible, leading to efficient use of irrigation water and higher crop yield. Furthermore, the impacts of droughts on crops can be closely analyzed at field and regional scales due to higher temporal resolution of MODIS images.

3.8 References

1. Salomonson, V.V.; Barnes, W.L; Maymon, Montgomery, H.E.; Ostrow, H. MODIS: Advanced facility instrument for studies of the Earth as a system. *IEEE Transactions on Geoscience and Remote Sensing*. **1989**, 27, 145-153.
2. Wolfe, R.E.; Roy, D.P.; Vermote, E. MODIS Land data storage, gridding and compositing methodology: Level 2 Grid. *IEEE Transactions on Geoscience and Remote Sensing*. **1998**, 36, 1324-1338.
3. NASA Earth Observatory. Agricultural Patterns, 30 May 2006. Available online: https://earthdata.nasa. (accessed on Oct. 14, 2018).
4. Huang, C.; Townshend, R.J.; Liang, S.; Kalluri, S.N.V.; DeFries, R.S. Impact of sensor's point spread function on land cover characterization: Assessment and deconvolution. *Remote Sensing of Environment*. **2002**, 80, 203-212.
5. Townshend, J.R.G.; Huang, C.; Kalluri, S.N.V.; Defries, R.S.; Liang, S.; Yang, K. Beware of per-pixel characterization of land cover. *Int. J. Remote Sens*. **2000**, 21, 839-843.
6. Montano, E.L. *Impact of Satellite Geometric Distortions on Landscape Analysis: Effects on Albedo*. Diss. University of Maryland, 2015. Web. 6 May 2016.
7. Tan, B.; Woodcock, C.E.; Hu, J.; Zhang, P.; Ozdogan, M.; Huang, D.; Yang, W.; Knyazikhin, Y.; Myneni, R.B. The impact of gridding artifacts on the local spatial properties of MODIS data: Implications for validation, compositing, and band-to-band registration across resolutions. *Remote Sensing of Environment*. **2006**, 105, 98-114.
8. Allen, R.G.; Kilic, A. Personal communication, 15 Sept. 2015.
9. Suyker, A. E.; Verma, S. B.; Burba, G. G.; Arkebauer, T. J.; Walters, D. T.; Hubbard, K. G. Growing season carbon dioxide exchange in irrigated and rainfed maize, *Agric. For. Meteorol.* **2004**,*124*(1-2), 1-13. doi:10.1016/j.agrformet.2004.01.011.
10. Huete, A. R.; Didan, K.; Miura, T.; Rodriguez, E. P.; Gao, X.; Ferreira, G. Overview of the Radiometric and Biophysical Performance of the MODIS Vegetation Indices. *Remote Sensing of Environment*. **2002a**, 83, 195-213.

11. Deering, D. W.; Rouse, J. W.; Haas, R. H.; Schell, J.A. Measuring Forage Production of Grazing Units from Landsat MSS Data. *Proceedings, 10th Intl. Symposium on Remote Sensing of Environment.* Ann Arbor: ERIM. **1975**, 2, 1169-1178.
12. Rouse, J. W.; Haas, R. H.; Schell, J. A.; Deering, D. W. Monitoring Vegetation Systems in the Great Plains with ERTS. *Proceedings, Third Earth Resources Technology Satellite-1 Symposium*. Greenbelt: NASA. **1974**, SP-351, 3010-3017.
13. Schlerf, M.; Atzberger, C.; Hill, J. Remote Sensing of Forest Biophysical Variables Using HyMap Imaging Spectrometer Data. *Remote Sensing of Environment*. **2005**, 95, 177-194.
14. Myneni, R.B.; Knyazikhin, Y.; Glassy, J.; Privette, J.L.; Tian, Y.; A. Lotsch, Zhang, Y.; Wang, Y.; Morisette, J.T.; Votava, P.; Nemani, R.R.; Running, S.W. MODIS Leaf Area Index (LAI) and Fraction of Photosynthetically Active Radiation Absorbed by Vegetation (FPAR) Product (MOD15) Algorithm Theoretical Basis Document. https://modis.gsfc.nasa.gov/data/atbd/atbd_mod15.pdf.. **1999**.
15. Trezza, R.; Allen, R. G.; Tasumi, M. Estimation of Evapotranspiration from MODIS using METRIC along the Middle Rio Grande of New Mexico. *Remote Sens.* **2013**, 5, 5397-5423. doi:10.3390/rs5105397
16. Entekhabi, D.; Reichle, R. H.; Koster, R. D.; Crow, W. T. Performance Metrics for Soil Moisture Retrievals and Application Requirements. *Journal of Hydrometerology*. **2010**, 11, 832-840.
17. Viña, Andrés; Gitelson, A.A.; Nguy-Robertson, A.L.; Peng, Y. Comparison of different vegetation indices for the remote assessment of green leaf area index of crops. *Remote Sensing of Environment*. **2011**, doi:10.1016/j.rse.2011.08.010
18. Lee HB, Comrey AL. Elementary statistics: A Problem Solving Approach. 4th ed. UK: William Brown; 2007.
19. Goulden, C. H. *Methods of Statistical Analysis, 2nd ed.* New York: Wiley, pp. 50-55, 1956.
20. Shier, R. Paired t-tests. Mathematics Learning Support Center. 2004.
21. Campos, I.; Neale, C.M.U.; Suyker, A.E.; Arkebauer, T.J. Reflectance-based crop coefficients REDUX: For operational evapotranspiration estimates in the age of high producing hybrid varieties. *Agricultural Water Management*. **2017**, 187, 140-153.
22. Huete, A.R. A soil-adjusted vegetation index (SAVI). *Remote Sensing of Environment*. **1988**, 25, 259-309.

CHAPTER 4: POTENTIAL APPLICATION OF REMOTELY SENSED GRIDDED PRECIPITATION DATA IN WATER RESOURCES MANAGEMENT

4.1 Abstract

In this study the potential opportunities of applying remotely sensed gridded precipitation data in water resources modeling are explored. The differences in spatial patterns and volumes between precipitation maps generated by interpolating data from weather stations and precipitation maps generated by combination of radar technology and weather station were analyzed. The percent difference in annual average precipitation volume over 16 million acres of Republican Model area (area of RRCA model) was around 14%, and the percent difference in annual average recharge volume was around 30% between two the sources of precipitation maps. The differences in patterns of precipitation and recharge maps generated were found to be substantial as well. The level influence of precipitation rate in a soil water balance model and a groundwater model were analyzed in a sensitivity analysis. The deep percolation and runoff components of the field soil water balance are substantially affected for different types of crops and soils by different rates of precipitation. Similarly, evapotranspiration and deep percolation components are substantially affected in the case of irrigated and non-irrigated crop fields. The groundwater model simulated baseflow at different gage stations are also sensitive to different rates of precipitation. Artifacts such as bull's eye effect and the influence of local storm events from a weather station during the interpolation process are some of the disadvantages of generating precipitation maps using the interpolation method. The remotely sensed gridded

method on the other hand is capable of capturing more spatial variability in detailed form at a regional scale.

4.2 Introduction

The traditional method of generating precipitation maps is to interpolate weather station precipitation data to create continuous data. The maps are then applied as input data to water resources models. Precipitation maps generated with remote sensing methods such as Doppler Radar technology are now widely available. There is an opportunity to use these remotely sensed gridded precipitation data in the field of water resources modeling. The research of this chapter explores the potential opportunities of using remotely sensed gridded precipitation data in water resources models. The importance of precipitation in water resources model output is analyzed by sensitivity analysis. Disadvantages of using an interpolation method for generating precipitation maps are identified and discussed, and the advantages of using combination of weather station and remotely sensed precipitation data instead of weather station interpolated data in water resources modeling are identified and discussed in different sections of this chapter.

A disadvantage of generating precipitation maps by interpolating data between sparsely located weather stations is that the effects of localized storm events are difficult to represent. An example case of this problem is the complication introduced in the calibration of Co-operative Hydrology Study 2010 (COHYST2010) hydrologic model. During the model development, precipitation data from weather stations were interpolated to generate precipitation data for model grid cells. In the year 2002 there was a local storm event with

a large precipitation rate near the Ogallala weather station location. During the process of interpolating precipitation data, the higher precipitation rates were transferred to the surrounding area at a regional scale. To analyze this, the hourly precipitation data at different weather stations located in the COHYST2010 model region were summed up to annual precipitation volume for year 2002. The annual volumes of precipitation at different weather stations were then interpolated using Inverse Distance Weighted (IDW) interpolation technique to make annual precipitation maps of year 2002. Two types of annual precipitation maps were generated; one excluding the data of Ogallala weather station, and another including the data of Ogallala weather station. The annual precipitation map generated by excluding Ogallala station data was then subtracted from the map generated by including the Ogallala station Figure 4.1 shows the influence of the local storm event of 2002 near the Ogallala weather station after the process of interpolation.

The artifacts introduced during the process of data interpolation can have impacts on water resources model results. Figure 4.2 shows the percent difference map of Net Irrigation Requirement (NIR) for year 2002 when the watershed model was simulated with and without including the Ogallala weather station data.

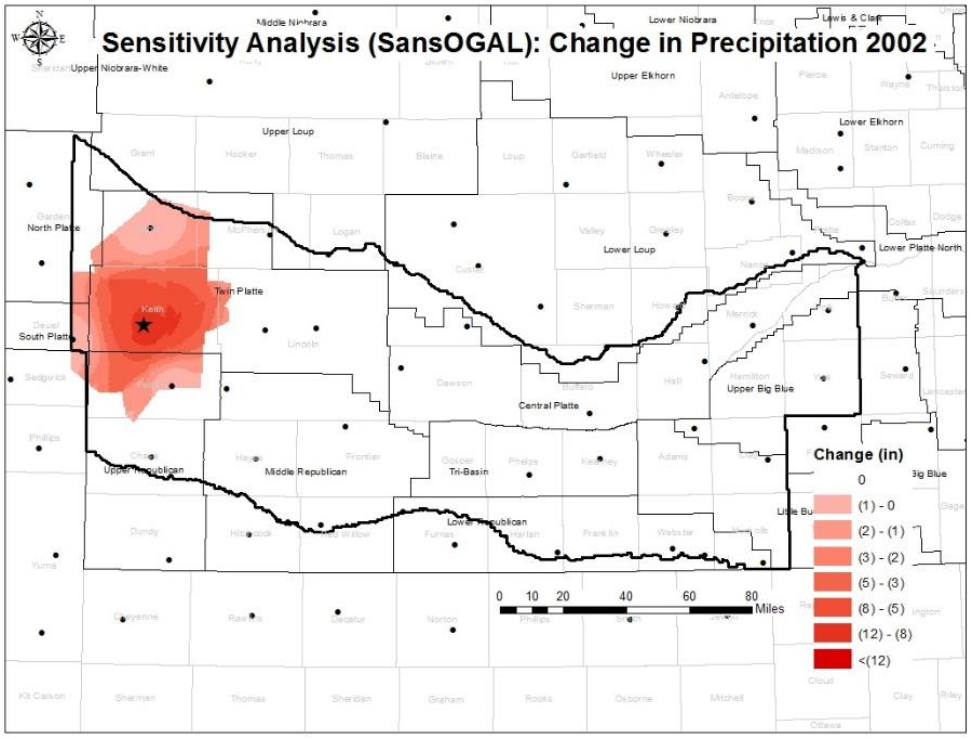

Figure 4.1: *Effect of a local storm event near the Ogallala weather station caused by the interpolation process*

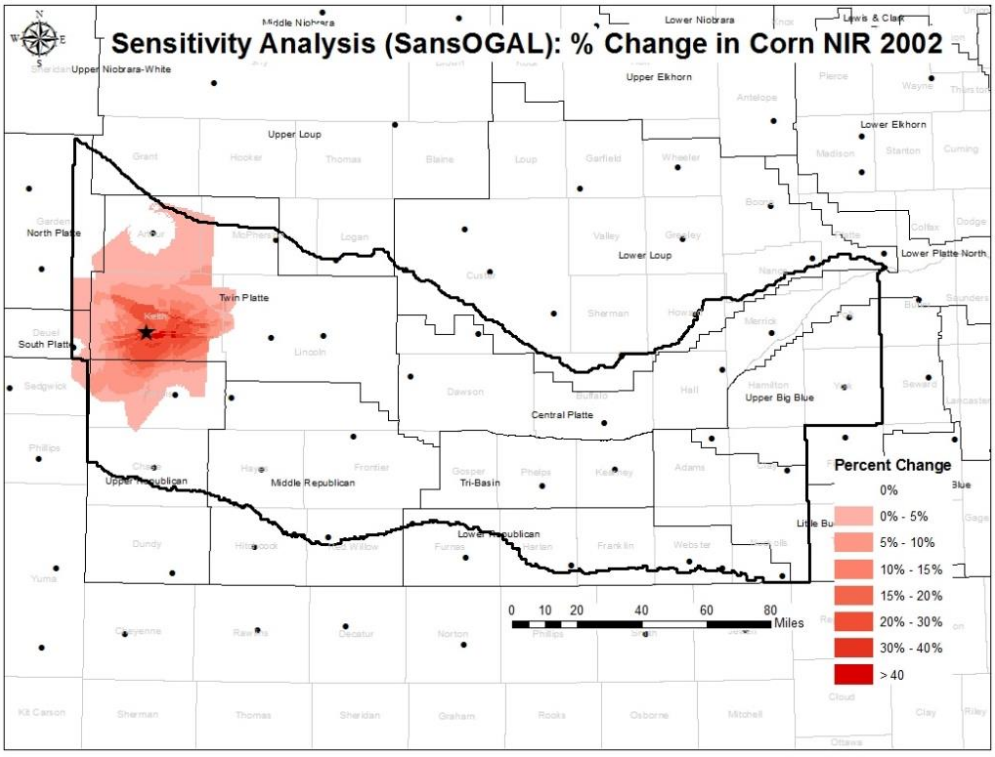

Figure 4.2: *Percent difference in NIR in COHYST2010 model area of year 2002*

These artifacts introduced during the process of interpolation influence the results of watershed and groundwater models. When the results of models are compared to the field data such as groundwater elevation and baseflows, there can be substantial differences between simulated results and field data, further complicating the process of calibration. When point based soil water balance model are upscaled to regional soil water balance model and hydrologic fluxes are estimated, a small error (less accurate) in the precipitation rate of point-based measurements can propagate to large errors in volumes of hydrologic components in regional scale. Since the results of a point-based soil water balance model are used to create the gridded regional watershed model, where different combinations of soils, crops, and irrigation settings exist in grid cells of the model area; it is essential to have precipitation data in model grid cells that closely represent real conditions.

Radar sends send radio waves into the atmosphere in pulses and radio waves are sent back when the wave makes contact with a raindrop. The system calculates the distance and direction of the rain and uses the Doppler Effect to provide precipitation characteristics like reflectivity and droplet size [1]. The Precipitation Processing Subsystem (PPS), by using reflectivity-to-rainfall equation estimates the amount of rainfall [2].

Although it is not perfect, this dataset is one of the best sources of timely, high resolution precipitation information available. It is hard to quantify the accuracy of gridded data since it depends on the topography of the region (the accuracy of precipitation gets lower with increase in elevation) [3]. Besides topography, there are uncertainty and errors associated with radar and rain gauge data. Some examples of errors in radar data includes accuracy of the reflectivity - rainfall relationship in use, calibration of the radar, radar location and elevation, and radar's effective coverage (e.g., physical obstructions such as

mountains) [3]. Similarly, uncertainties in field rain gauge data such as gauge wetting, evaporative losses, precipitation under-catch, and freezing precipitation are present [4].

Seo et al. compared eleven months (May 2008 to August 2009) of high-density hourly rain gauge network data of Iowa City with radar based gridded precipitation data (NEXRAD Stage III product) provided by the National Oceanic and Atmospheric Administration (NOAA)'s National Climatic Data Center (NCDC) commonly used by hydrologic users. A correlation of 0.87 and root mean square error (RMSE) of 0.64 was found between radar based precipitation data and 14 rain gauges data [5]. Comparison of radar based gridded precipitation data (NEXRAD Stage III product) with ten meteorological stations in central New Mexico was done by Xie et al. with hourly data from 1995 to 2001. The comparison indicated that radar based precipitation data overestimates the seasonal precipitation accumulation by 11 to 88 percent in monsoon season and underestimates by 18 to 89 percent in the non-monsoon season [6]. Klazura et al. compared gauges data from 43 storms rain events across the country with NEXRAD radar data. In the case of 25 storm rain events with high-reflectivity gradient, the correlation between radar data and gauge data was 0.88, and in the case of 18 storm events with low-reflectivity gradient, the correlation was 0.44 [7].

Studies have shown that algorithms which combine sensor inputs -- radar, gauge, satellite yield more accurate precipitation estimates than those which rely on a single sensor (i.e. radar-only, gauge-only, satellite-only [3]. PRISM precipitation gridded data is generated by combining ground gauge stations from multiple sources and radar products [8]. Comparison was done between PRISM precipitation data and 69 field stations located in western North Carolina. for years from 1951 to 1958. The average monthly mean

absolute error (MAE) was found to be 3.31% [4]. Velasco-Forero et al. used the technique based on kriging with external drift to compute rainfall maps by blending radar and rain gauges which improved the correlation of radar with rain gauge data from 0.76 to 0.89 [9].

Kalin et al. modeled the hydrology in the Pocono Creek watershed located in Monroe County, PA; by applying NEXRAD gridded precipitation data in Soil Water Assessment Tool (SWAT) model. Of particular interest in in their research was to explore potential use of NEXRAD precipitation data as an alternative source of precipitation data to the conventional surface rain gauges [10]. NEXRAD estimated areal average precipitations are shown to compare well with the gauge measured ones at two climate stations in the study area. Hydrographs generated from both gauge and NEXRAD driven model simulations compared well with observed flow hydrographs. In the validation period, NEXRAD simulations generated higher model efficiencies at the monthly scale. On the other hand, simulations with gauge precipitations resulted in slightly better model efficiencies at the daily time scale.

Similarly, Sexton et al. examined the implications of using surface rain gauge and NEXRAD precipitation data sets on the performance of the SWAT model by modeling the hydrology of German Branch watershed located in the Coastal Plain of Maryland on the eastern shore of Chesapeake Bay [11]. In the absence of a spatially representative network of rain gauges within the watershed, NEXRAD data produced good estimates of stream flow at the outlet of the watershed. Three NEXRAD datasets; non-corrected, bias-corrected, and inverse distance weighted corrected NEXRAD data, produced were used in the model. Nash-Sutcliffe efficiency coefficients for daily stream flow simulation using these three NEXRAD data ranged from 0.46 to 0.58 during calibration and from 0.68 to

0.76 during validation. Overall, correcting NEXRAD with rain gauge data is promising to produce better hydrologic modeling results. Furthermore, The PRISM gridded precipitation was applied in the Central Valley Hydrologic model developed by US Geological Survey. The monthly PRISM precipitation data of 11 years from 1962 to 2003 was applied in the model to access the groundwater availability of Central Valley, CA. [12].

4.3 Comparison of Gridded and Weather Station Interpolated Precipitation Data

It is important to make comparison both quantitatively and qualitatively the difference between the precipitation maps generated from Weather Station Interpolation method (WSI), and radar and weather station data blended method (gridded). It is important to understand this difference before applying the precipitation maps generated from gridded method in water resources models. The following sub-sections describe the methods and results of comparing the precipitation maps generated from WSI and gridded method.

4.3.1 Methods

The Republican River Compact Administration groundwater model (RRCA model) was used to compare the use of gridded and WSI products in a water resources model. The Republican River groundwater model area covers parts of three states; Colorado, Nebraska, and Kansas, as shown in Figure 4.3.

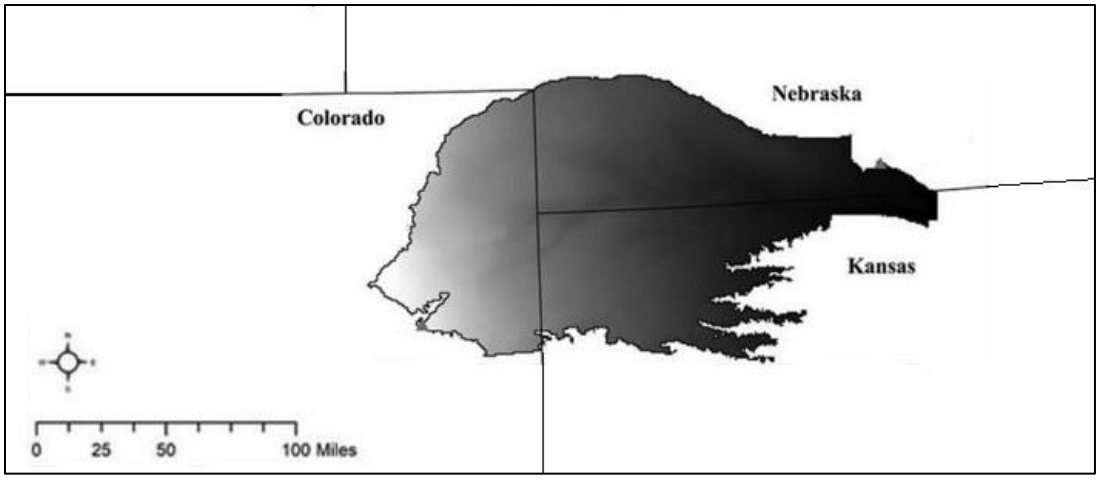

***Figure 4.3**: Spatial coverage of Republican River groundwater model in Colorado, Nebraska, and Kansas*

The National Weather Service through the Advanced Hydrologic Prediction Service provides Stage IV 1 km spatial resolution gridded precipitation data in daily, monthly, and yearly time intervals. The gridded precipitation maps are generated by utilizing the combination of remotely sensed precipitation data from radar technology and point weather station data [13]. The comparison of precipitation maps between gridded and WSI method was done on yearly basis for three years from 2005 to 2007. The monthly gridded precipitation maps in raster format were added to generate yearly precipitation maps for RRCA model area.

In the case of the WSI method, only point weather stations are used for generating precipitation maps. The precipitation data are interpolated between point measurements from weather stations using inverse distance weighted interpolation techniques. Precipitation data in hourly interval were summed up to yearly values for weather stations in and around RRCA model area. Inverse distance weighted interpolation technique was then applied to generate yearly precipitation maps for year 2005 to 2007.

The gridded and WSI precipitation data for three years from 2005 to 2007 were compiled to analyze the differences in spatial patterns and volumes of rainfall in the groundwater model area on a yearly basis. Precipitation maps generated were compared in a spatial sense to see where in the RRCA model area is substantial difference in precipitation. The yearly volume in the entire RRCA model area between precipitation maps generated by WSI and gridded method for three years were calculated, including the volume difference in precipitation for years 2005, 2006, and 2007 respectively.

In the Republican groundwater model, aquifer recharge is estimated using the relation between soil type and precipitation rate. Figure 4.4 illustrates the spatial distribution of soil types within the model area [14], and Figure 4.5 shows the precipitation and recharge relationship curves for different types of soils [15].

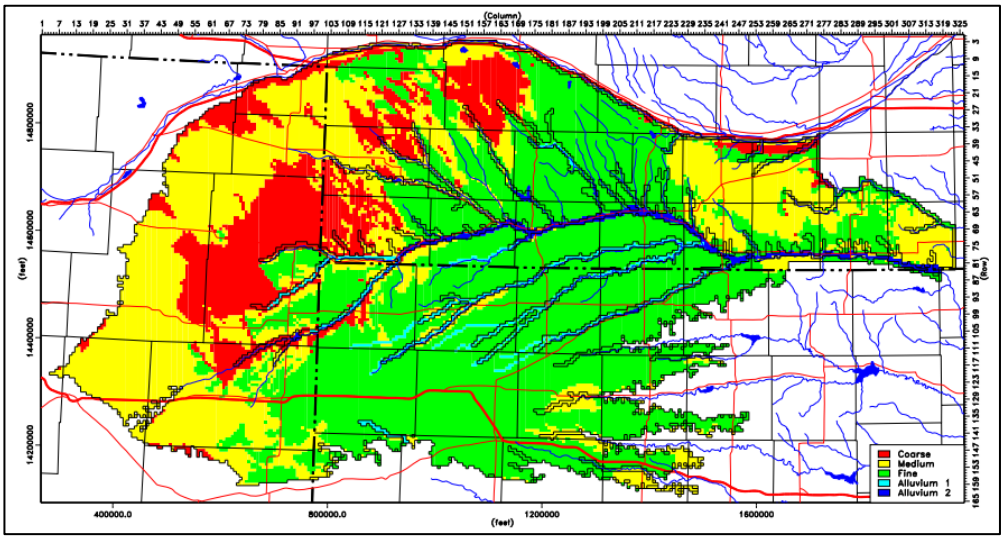

***Figure 4.4**: Spatial distribution of soil types in the Republican River model area (RRCA Ground Water Model, 2003, Appendix E)*

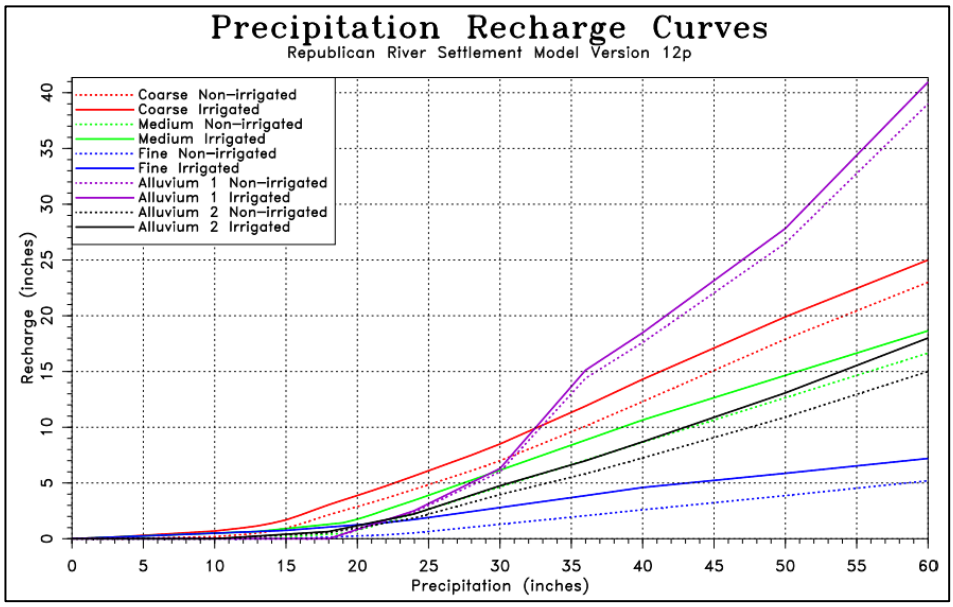

***Figure 4.5**: Precipitation-Recharge curves for different soil types used in Republican River model (RRCA Ground Water Model, 2003, Appendix F)*

For gridded method, available monthly precipitation maps were retrieved. For WSI method, precipitation data in hourly interval were summed up to monthly values for weather stations in and around RRCA model area. Inverse distance weighted interpolation technique was then applied to generate monthly precipitation maps for year 2005 to 2007. The monthly precipitation values from gridded and WSI method were then assigned to the RRCA model grid cells and model was simulated for three years from 2005 to 2007 in monthly stress periods. The RRCA model incorporates soil coverage data and applies the precipitation and recharge relationship curve, and then accounts the groundwater pumping data and produce monthly recharge maps. The model output of monthly recharge maps was then aggregated to generate yearly recharge maps of 2005 to 2007.

4.3.2 Results

4.3.2.1 Precipitation Analysis

The spatial distribution of yearly precipitation in RRCA model area generated from WSI and gridded methods for year 2005, 2006, and 2007 are shown in Figure 4.6, Figure 4.7, and Figure 4.8 respectively. The patterns of spatial distribution of annual precipitation are markedly different. For example, in Figure 4.6 and Figure 4.8 the bull's eye effect of interpolation from point locations is clearly visible, especially in years 2005 and 2007 for the WSI method. The spatial pattern of precipitation appears to be overly simplified due to the lack of sufficient weather stations in some regions. The spatial distribution pattern of precipitation given by the gridded method, on the other hand, shows variability of precipitation in the model area with much more detailed information and assumed to be a better representation of reality. The differences in spatial patterns of precipitation between gridded and WSI methods from year 2005 to 2007 are illustrated in Figures 4.9 to 4.11.

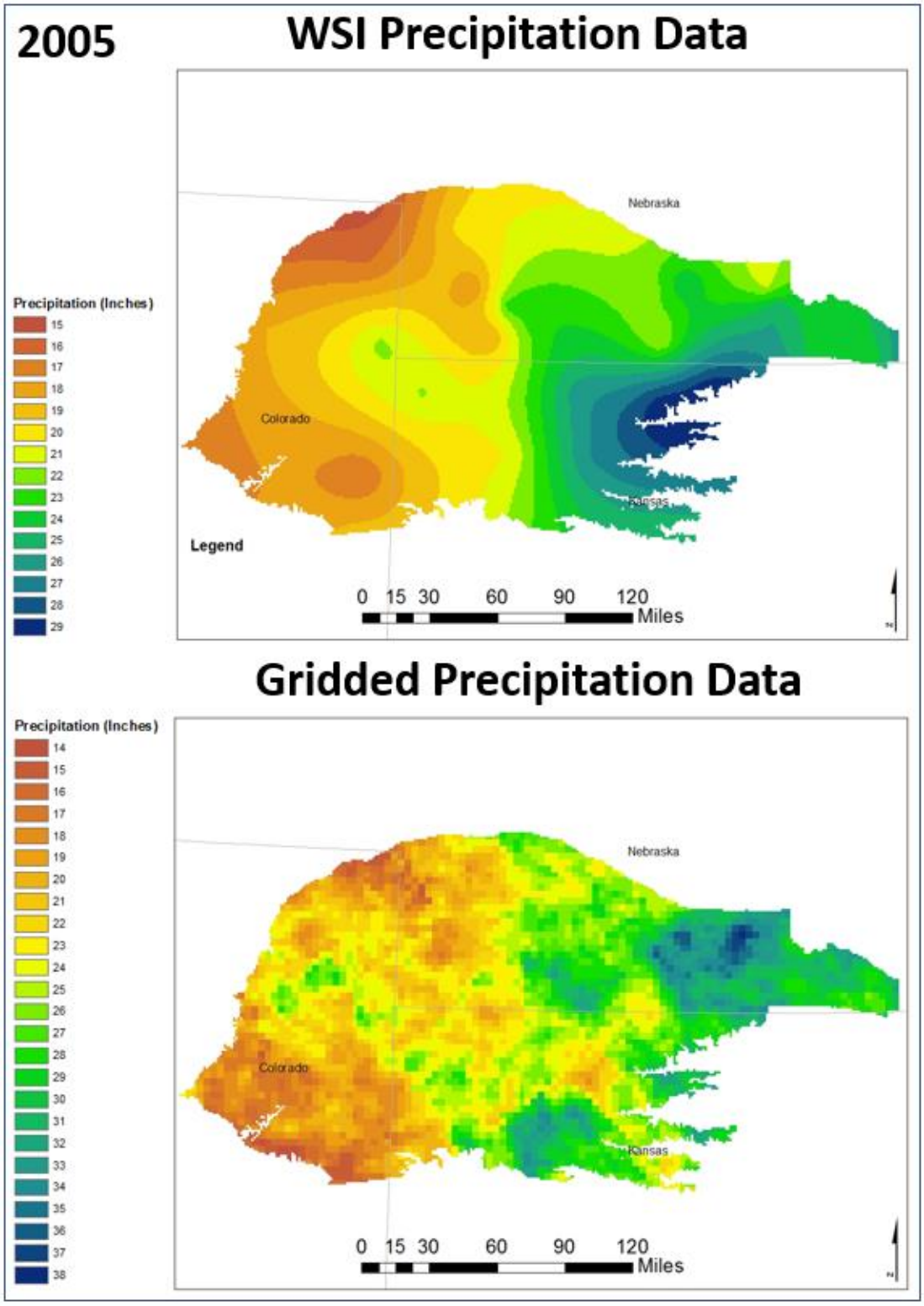

Figure 4.6*: Spatial distribution of yearly precipitation rate from WSI and gridded Data of year 2005*

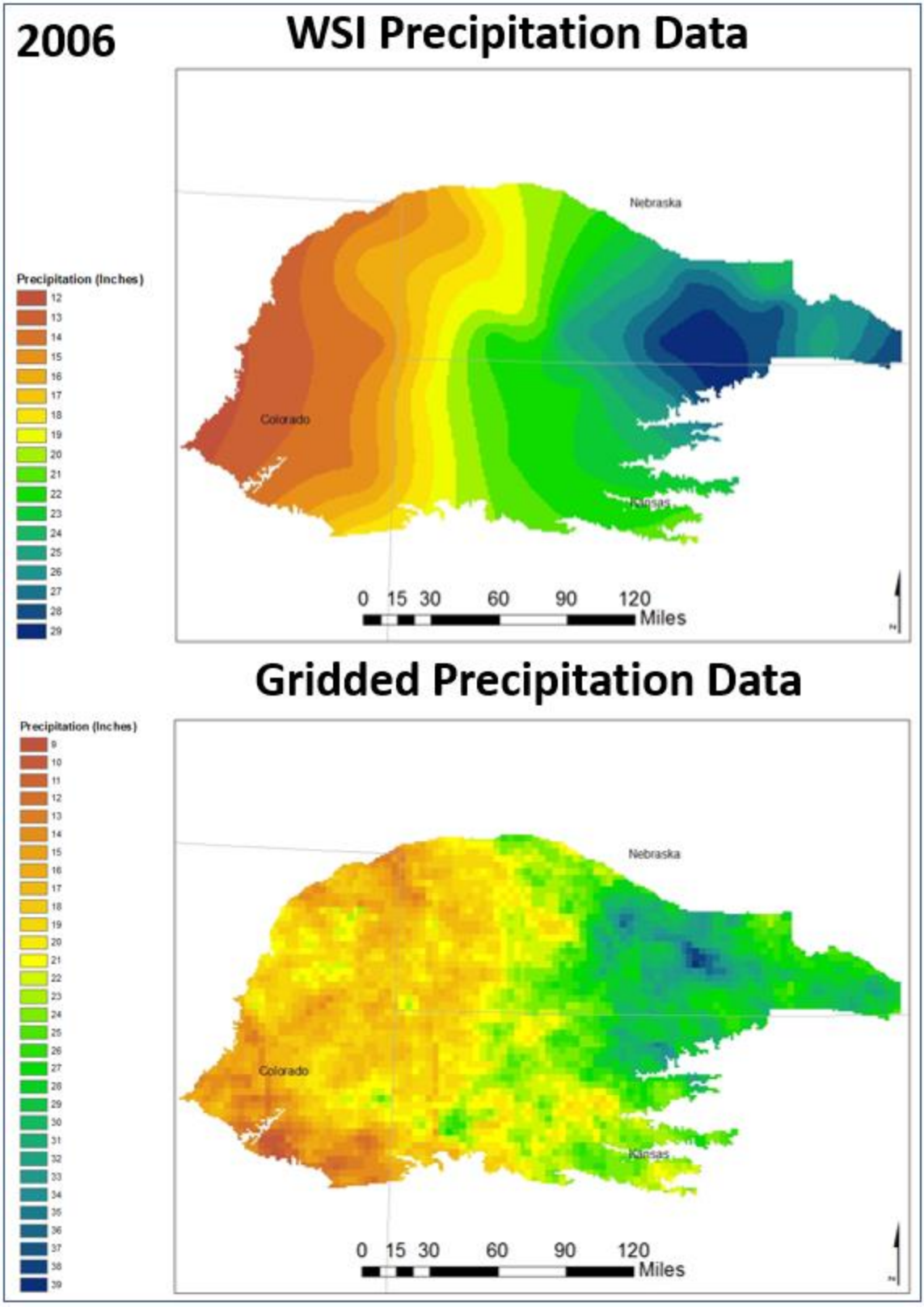

***Figure 4.7**: Spatial distribution of yearly precipitation rate from WSI and gridded Data of year 2006*

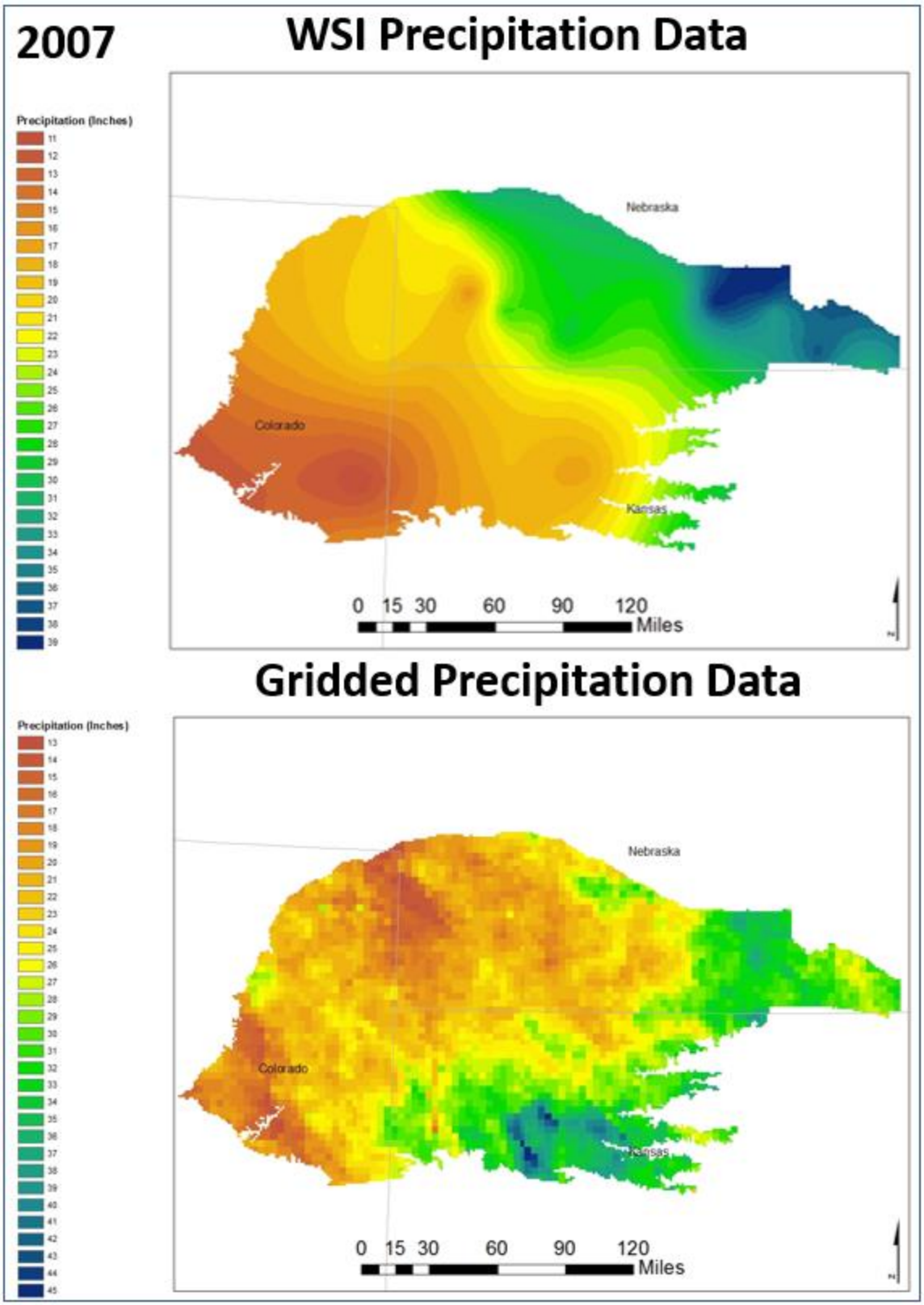

***Figure 4.8**: Spatial distribution of yearly precipitation rate from WSI and gridded Data of year 2007*

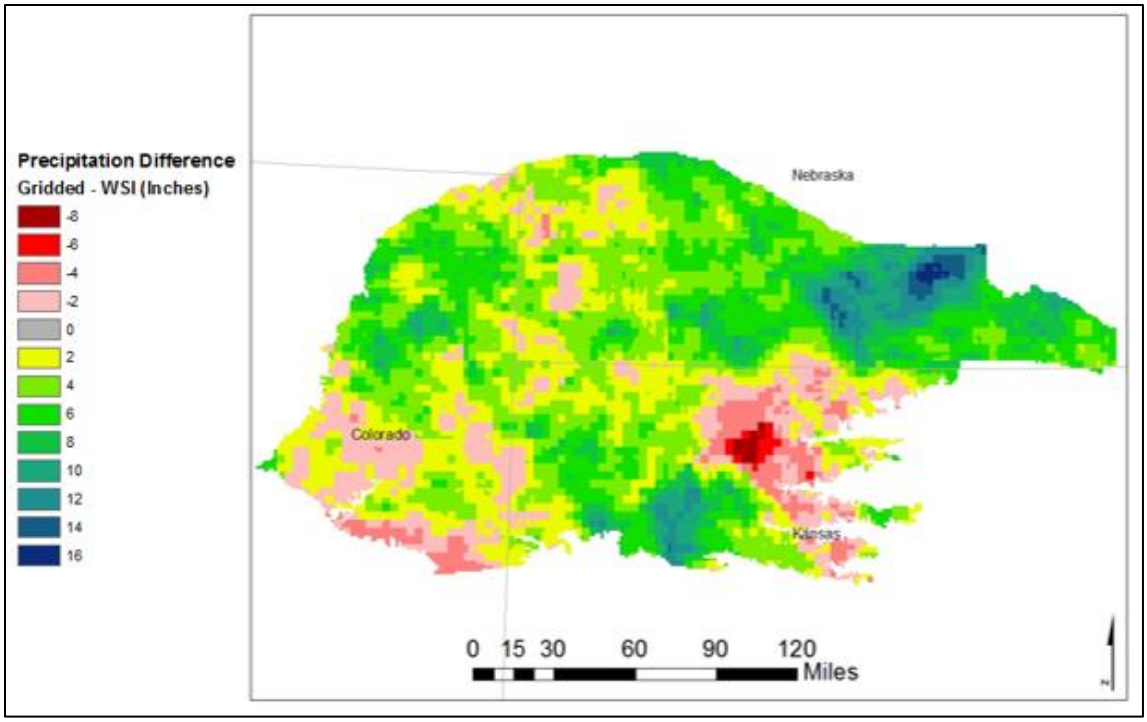

***Figure 4.9**: Spatial distribution of difference in precipitation between WSI and gridded method for year 2005*

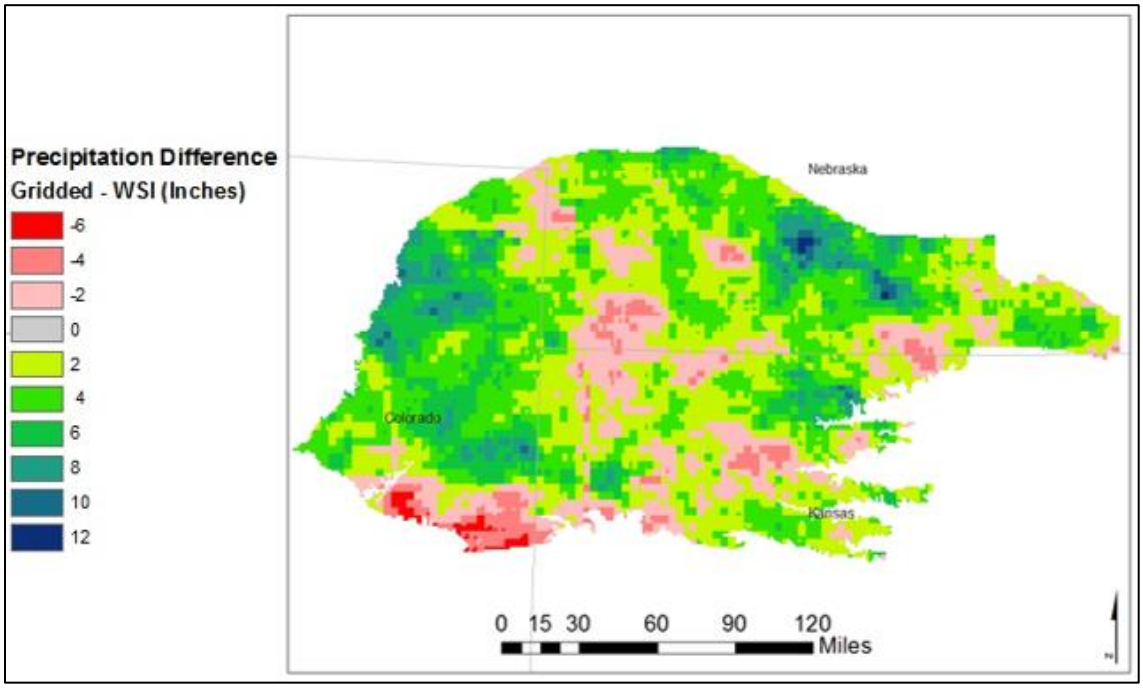

***Figure 4.10**: Spatial distribution of difference in precipitation between WSI and gridded method for year 2006*

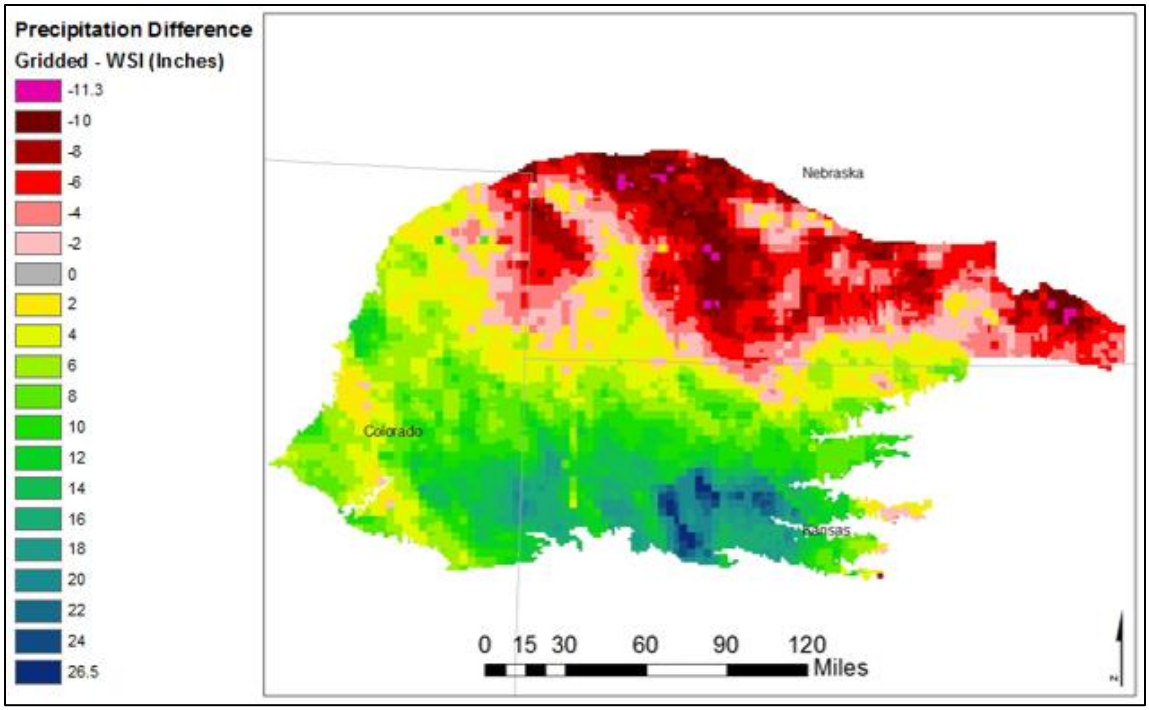

***Figure 4.11**: Spatial distribution of difference in precipitation between WSI and gridded method for year 2007*

Table 4.1 shows the total annual volume of precipitation over the groundwater model area determined from WSI and gridded data as well as the differences in volume measured by the two methods and percent difference in precipitation volumes.

***Table 4.1:** Yearly precipitation volume of WSI and gridded Data in groundwater model area*

	Precipitation (ac-ft)		
	2005	**2006**	**2007**
WSI Method	33,586,506	31,374,186	34,477,333
Gridded Method	38,937,755	35,021,639	39,561,740
Difference	**5,351,249**	**3,647,453**	**5,084,407**
Percent Difference	**15.93%**	**11.63%**	**14.57%**

The differences in annual volume of precipitation in the model area measured by the gridded and WSI method are relatively large. In every year that was analyzed, precipitation volume measured with the gridded method was higher than that from the WSI method. In watershed modeling and water balance studies, these two sources of precipitation data may result in substantially different rate and volume estimates of water budget components. Considering the precipitation analysis of data from three years from Table 4.1, it is seen that the range of increase in precipitation volume percentage of gridded method compared to WSI method is 10% to 20%. To keep the analysis relevant to this range, the sensitivity analysis of soil water balance model and groundwater model baseflow to precipitation data was done in this range of 10% and 20% increase in precipitation, which are discussed in sections 4.4 and 4.5.

When these two sources of precipitation data are used for watershed model construction and calibration, estimates of model parameters can be strongly affected during the model calibration process. Because of the more detailed information included in the spatial pattern of precipitation from gridded data, the watershed model benefits more during model calibration when it is calibrated to stream gage flows at different locations.

4.3.2.2 Recharge Analysis

Figure 4.12 to Figure 4.14 illustrate spatial differences in recharge within the model coverage area as determined from gridded and WSI precipitation data for the years 2005 to 2007.

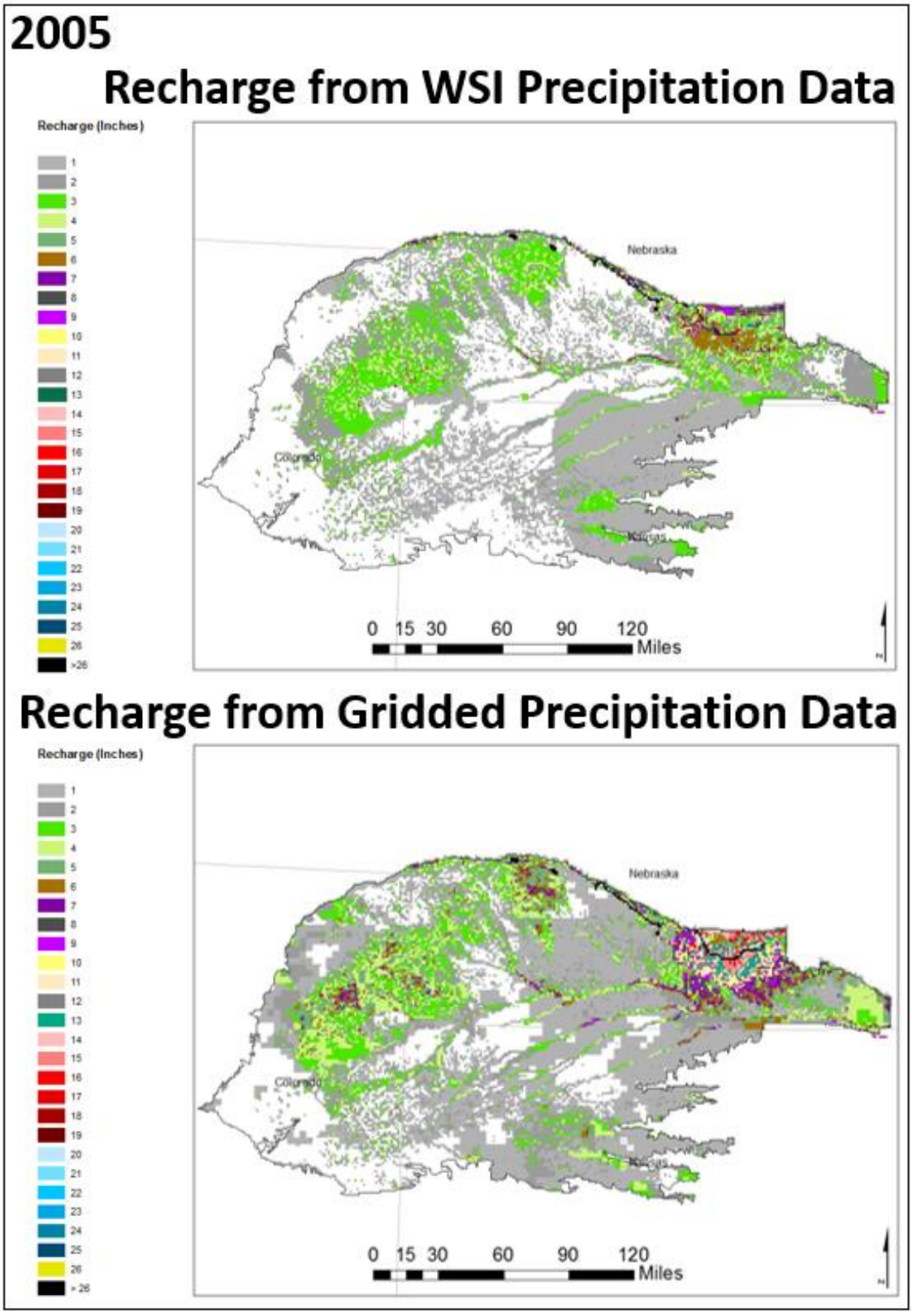

***Figure 4.12**: Spatial distribution of yearly recharge rate as determined from WSI and gridded precipitation of year 2005*

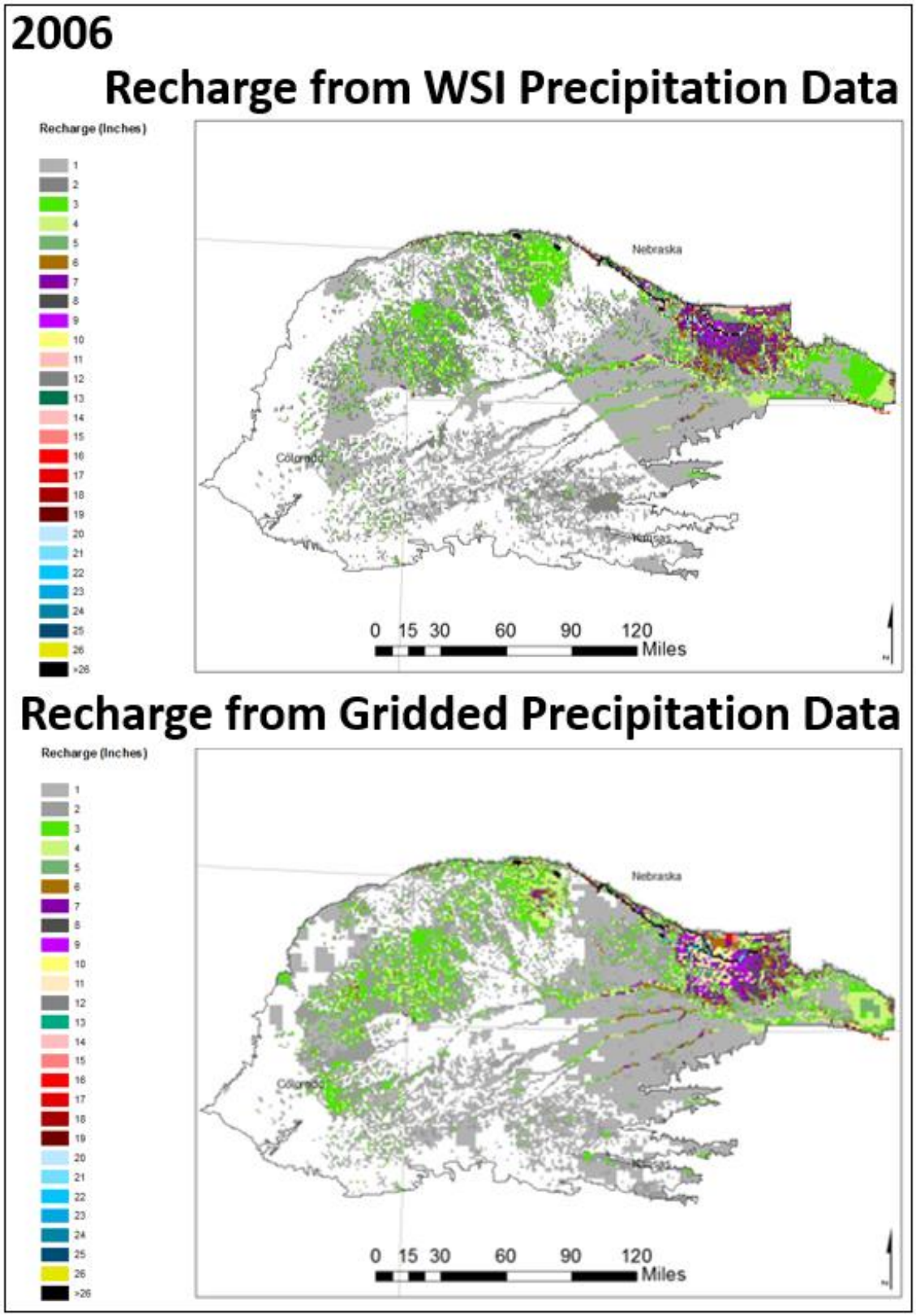

***Figure 4.13**: Spatial distribution of yearly recharge rate as determined from WSI and gridded precipitation of year 2006*

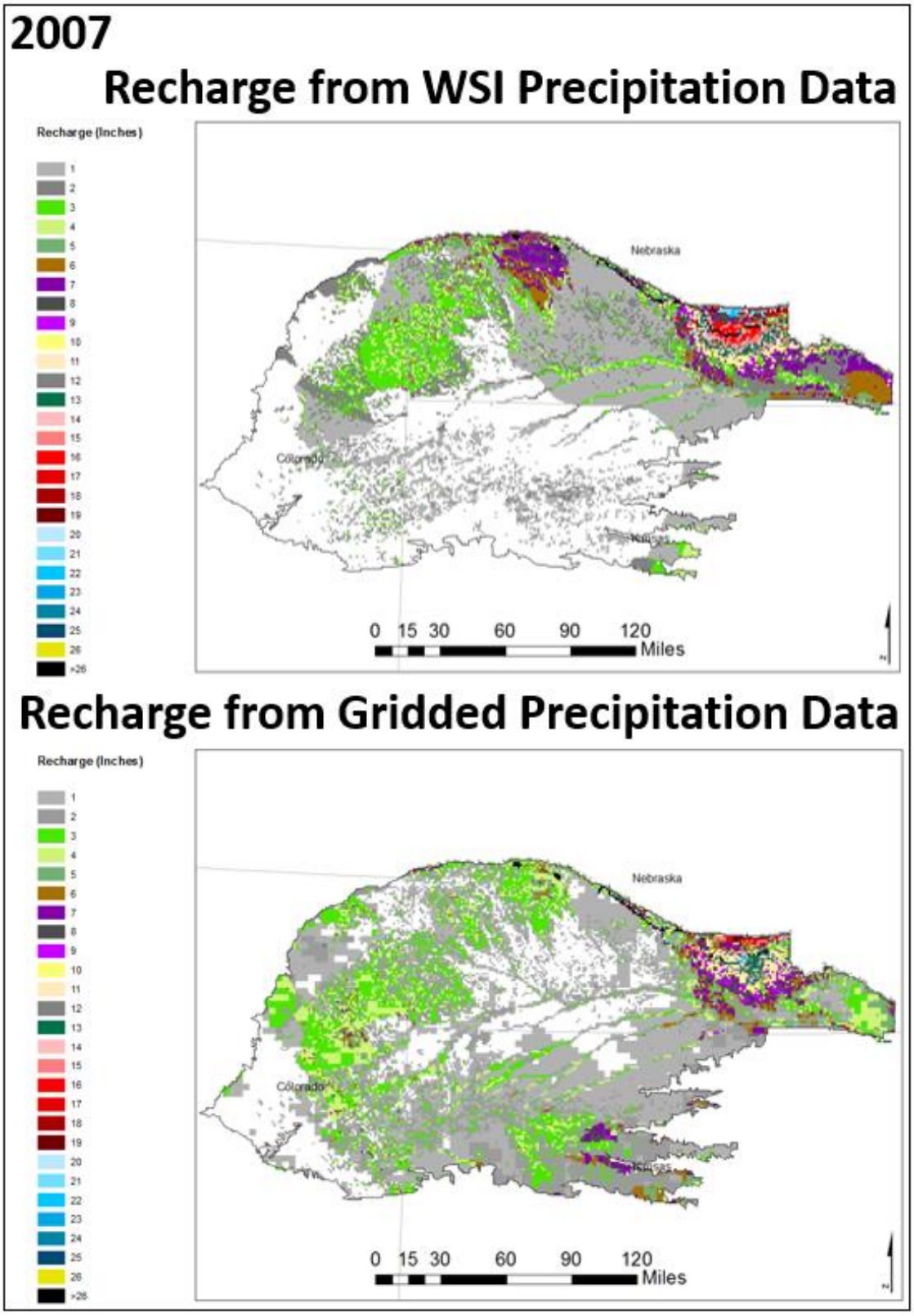

Figure 4.14*: Spatial distribution of difference in recharge between WSI and gridded method for year 2005*

The patterns of spatial distribution of annual recharge are different between WSI and gridded method. Notably the bull's eye effect of interpolation from point locations is not seen in the recharge maps. The soil and groundwater pumping data which are in grid cell format of RRCA model have reduced the interpolation artifacts spatially during watershed model simulation while generating recharge maps, although quantitively the effect of precipitation values introduced by bull's eye effect is still transferred in water budget of hydrological components.

The differences in spatial patterns of precipitation between gridded and WSI methods from year 2005 to 2007 are illustrated in Figures 4.15 to 4.17.

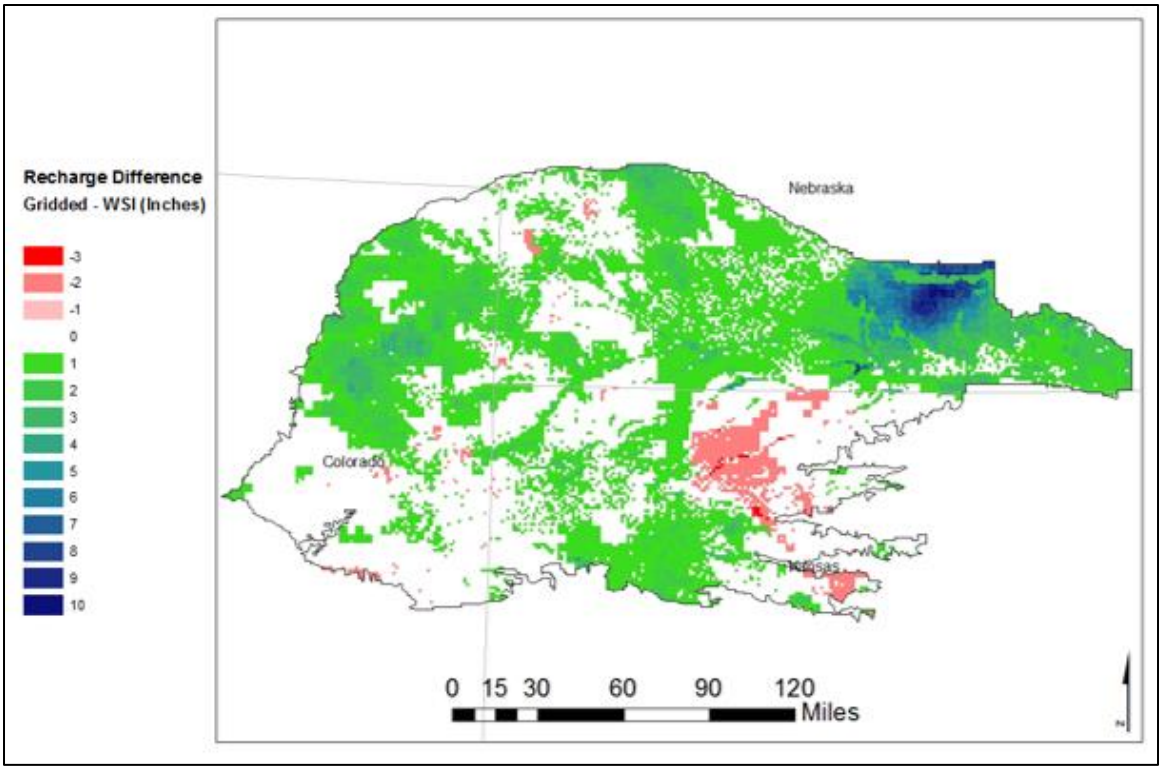

***Figure 4.15**: Spatial distribution of difference in recharge between WSI and gridded method for year 2005*

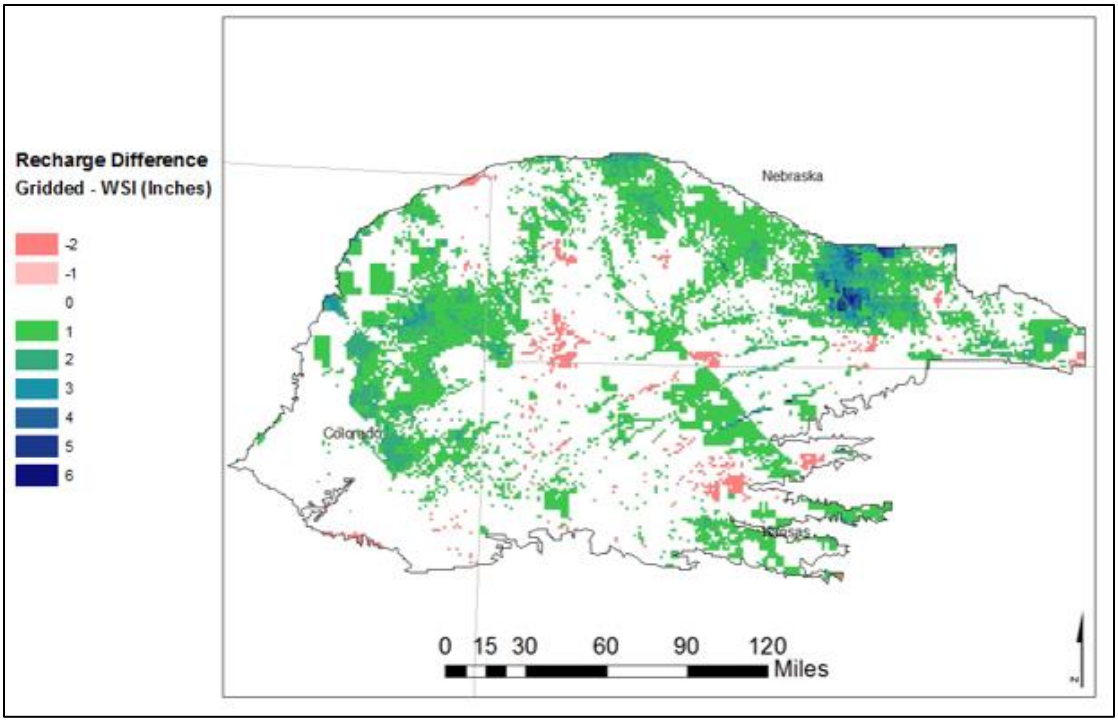

***Figure 4.16**: Spatial distribution of difference in recharge between WSI and gridded method for year 2006*

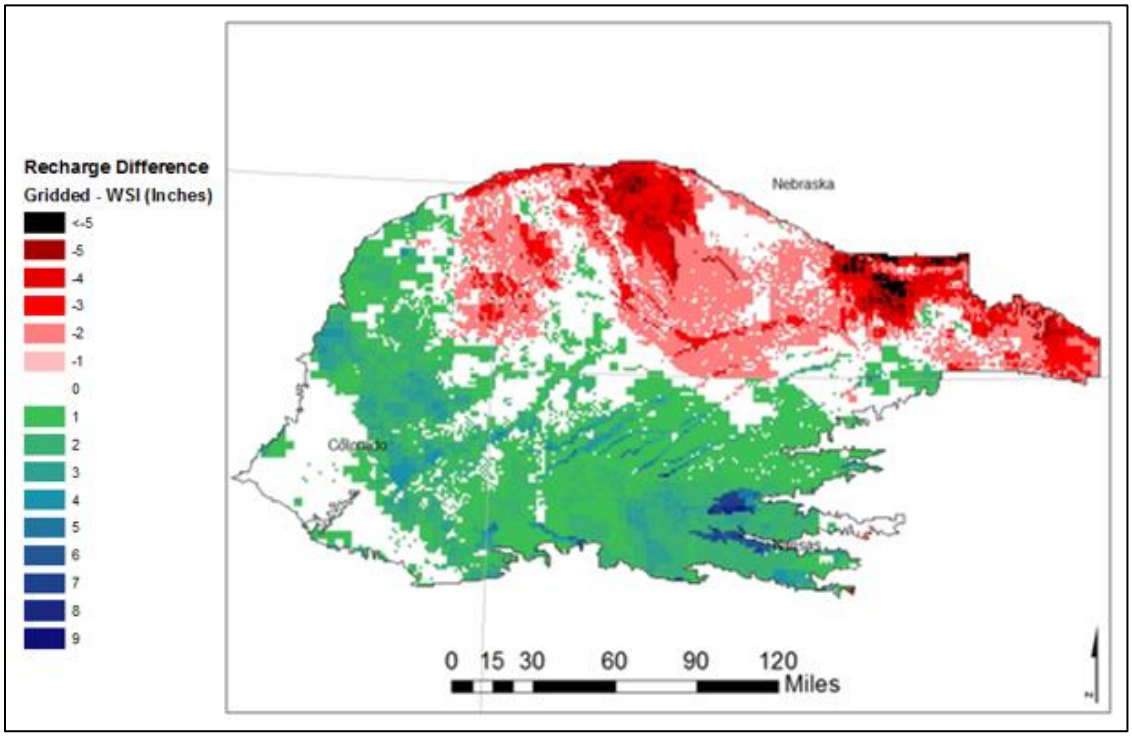

***Figure 4.17**: Spatial distribution of difference in recharge between WSI and gridded method for year 2007*

In general, the pattern of spatial difference in recharge maps between WSI and gridded methods for three years follows similar to that of precipitation difference maps. The difference in spatial distribution of recharge between gridded and WSI have carried over (transferred) from the difference in spatial pattern of precipitation between gridded and WSI.

Table 4.2 shows the total annual volume of recharge for the groundwater model area as determined from WSI and gridded precipitation data as well as the differences in recharge volume measured by the two methods and percent difference in recharge volume.

Table 4.2: *Annual groundwater recharge volume determined from WSI and gridded precipitation data for the model coverage area*

	Recharge (ac-ft)		
	2005	**2006**	**2007**
WSI Method	2,563,094	2,418,881	3,527,680
Gridded Method	3,914,614	3,036,267	3,948,214
Difference	**1,351,520**	**617,386**	**420,534**
Percent Difference	**52.73%**	**25.52%**	**11.92%**

Similar to the comparison of different sources of precipitation data, the differences in yearly volume of recharge in the model area between the gridded and WSI methods are substantial. The spatial distribution of recharge is also different between recharge maps produced by applying the gridded and WSI precipitation data. When these two different sources of precipitation data are applied for development and calibration of the groundwater flow model, the groundwater budget estimates of different hydrological components can be significantly different. Because of the more detailed information included in spatial patterns of precipitation from the gridded data, recharge maps generated

from using it could also provide more detailed spatial information, which could be more helpful during the calibration phase of the groundwater model, where the model is calibrated to the groundwater elevation and baseflows at different locations within the model area.

4.4 Sensitivity Analysis of the Soil Water Balance Model to Precipitation Data

4.4.1 Methods

The Crop Simulation (CROPSIM) model version 7.0 (Martin et. al, 1984) [16], was used to perform sensitivity analysis of precipitation and to analyze its effects on different hydrologic components such as Deep Percolation (DP), Evapotranspiration (ET), and Runoff (RO) for different combinations of irrigation, crop type (maize, soybean, alfalfa, and pasture), and soil type. CROPSIM is a point-based soil water balance model developed by Dr. Derrel Martin at the University of Nebraska-Lincoln. This is a customized model which is calibrated to the settings of Nebraska, and most of the regionalized soil water balance model of Nebraska is based on the output results of this model.

Within the CROPSIM program, soils are classified by three characteristics:

1. Available Water Holding Capacity; number of $\frac{1}{4}$ inch increments per foot of soil
2. Hydrologic Soil Group (1-a, 2-b, 3-c, 4-d), and
3. Distance to Groundwater (1= less than 6 inches, 2= more than 6 inches)

Examples of types of soils with different soil codes include:

621 soil: 1.5’; Valentine, Thurman, Nora, Boelus-loamy fine sand, Silt loam; < 6’

622 soil: 1.5’; Santana, Rosebud, Kuma-loam, Silt loam, Clay loam; > 6’

642 soil: 1.5’; Sansara, Labu, Boyd-silty clay, Clay; > 6’

722 soil: 1.75’; Valentine, Holdrege, Hersh-fine loamy sand, Silt loam; > 6’

422 soil: 1.0’; Valentine-fine sand, > 6’

The CROPSIM model was simulated in daily time steps with weather data for 1950 to 2013 from the Gothenburg, Nebraska weather station. Multipliers for precipitation rate from 1.1 and 1.2 i.e. increase in precipitation by 10% and 20% respectively were applied and the CROPSIM model was run. Increasing precipitation by 10% and 20% during sensitivity analysis was to keep the analysis relevant to the analysis results of difference in yearly precipitation volume where the percentage range of increase in precipitation volume of gridded method compared to WSI method was found to be 10% to 20%.

The results of the model simulation were compiled as annual results. The graph in Figure 4.18 shows how precipitation changes annually from 1950 to 2013 with baseline precipitation data and multipliers applied to it. Figure 4.19 shows the annual average precipitation rate of the baseline run and for runs with different multipliers applied to the precipitation. The data labels on the tops of the bar plots show change in precipitation as a percentage compared to baseline precipitation value. A constant soil type of loam (soil code 622) was applied for irrigated and non-irrigated maize model simulations, and change in crop type model simulations. Similarly, irrigated status of crops was applied for all crops during change in crops model simulations, and irrigated maize was applied during change in soil type model simulations. This was done during sensitivity analysis to isolate and only analyze the effect of CROPSIM model parameter being changed. All of the results of the

sensitivity analysis of precipitation which are described in the sub-sections below are illustrated in this graph format.

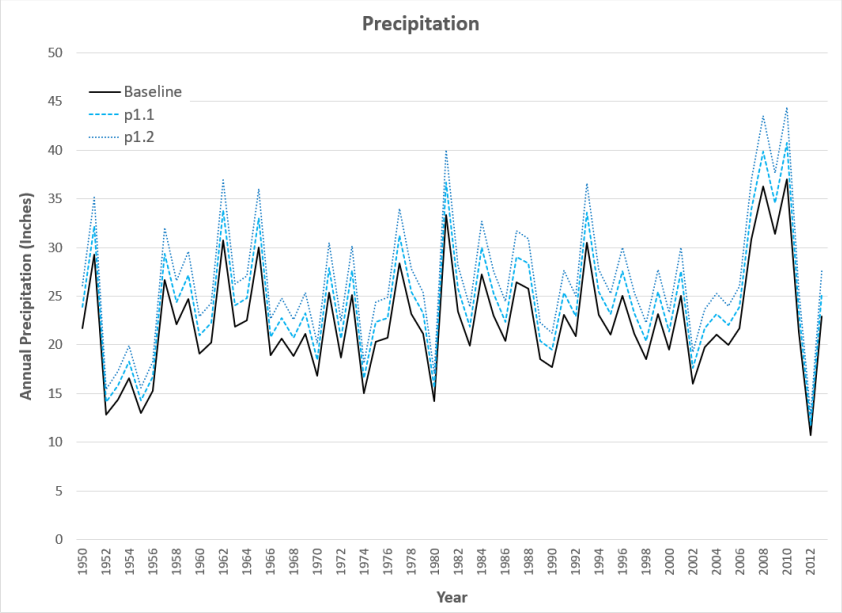

***Figure 4.18**: Annual baseline precipitation rate and multiplier rates from 1950 to 2013 for the Gothenburg weather station data*

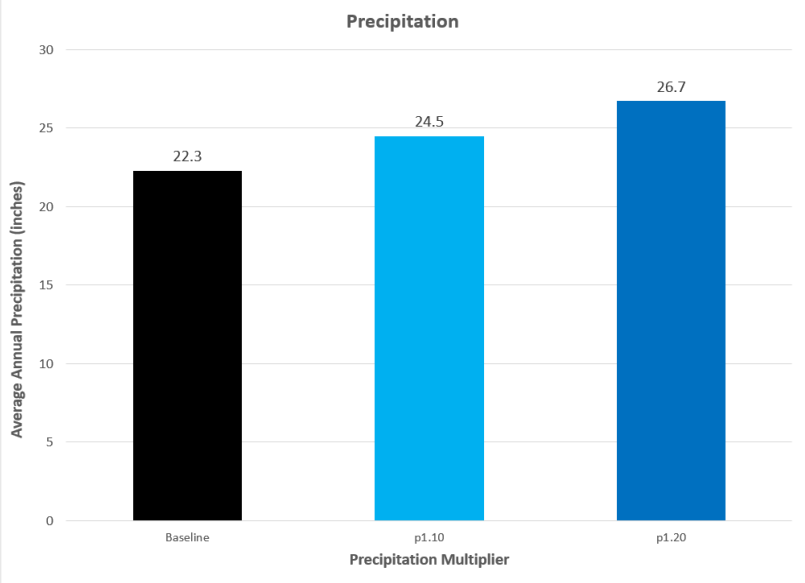

***Figure 4.19**: Average annual precipitation of baseline run and runs with multipliers applied*

4.4.2 Results

4.4.2.1 Effects of Precipitation Rates in an Irrigation Setting

As the state of Nebraska continues to grow and develop, understanding and management of available water resources is necessary to maintain and sustain an effective supply for its water users. In the state of Nebraska, the majority of the land area can be classified as agriculture. The land area can be generally classified as irrigated cropland, non-irrigated cropland, and non-irrigated pasture. The climate of Nebraska yields varying suitability to non-irrigated agricultural production. Fortunately, Nebraska is located over several aquifers which are used to supplement insufficient precipitation with irrigation water. Nebraska is among the national leaders in irrigated acres; rendering the analysis of the use of irrigation water of significant importance to water management in the state. Crop water demand not met by precipitation is supplemented by irrigation water in irrigated crop fields, whereas it is left as it is in non-irrigated crop fields. Therefore, it is important to estimate and understand how sensitive the hydrologic components are to different rates of precipitation for different irrigation setting.

Sensitivity analysis of precipitation rates in different irrigation settings (irrigated and non-irrigated) shows that DP and ET components have substantially different response to different rates (multipliers) of precipitation when the irrigation settings are different. Figure 4.20 shows the annual average DP rate of irrigated and non-irrigated maize in a field with different multipliers applied to the precipitation. The data labels on the tops of the bar plots show a change in DP as a percentage compared to the baseline DP value.

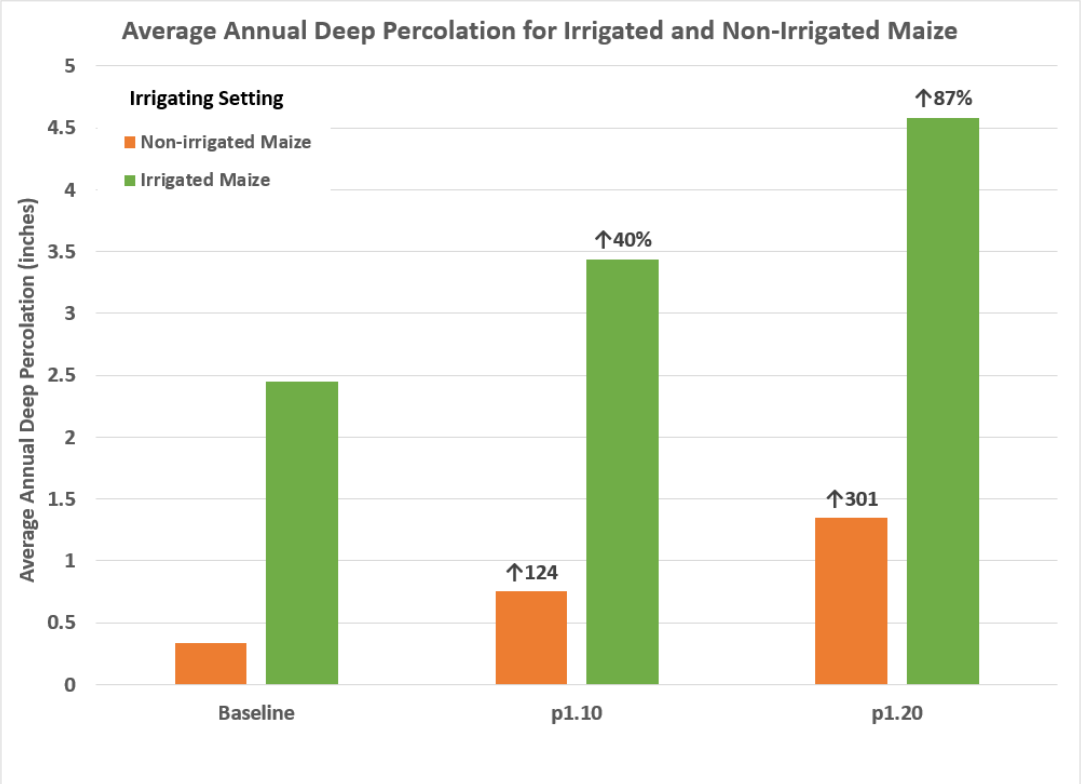

***Figure 4.20**: Response of DP to a range of precipitation multipliers for irrigated and non-irrigated maize*

Figure 4.20 shows that with different precipitation multipliers, the percent change of DP is not similar between irrigated and non-irrigated maize. The percent increase of DP for non-irrigated maize is significantly higher than for irrigated maize. With increasing precipitation rates the percent increase in DP between irrigated and non-irrigated maize are substantially different. For example, when the precipitation rate is increased by 20%, there is a 301% increase in DP for non-irrigated maize, whereas there is a 87% increase in DP for irrigated maize, as shown in Figure 4.20.

Similarly, precipitation rates affect ET components differently for irrigated and non-irrigated fields. Figure 4.21 shows the average annual ET rates of irrigated and non-irrigated maize in fields with different precipitation.

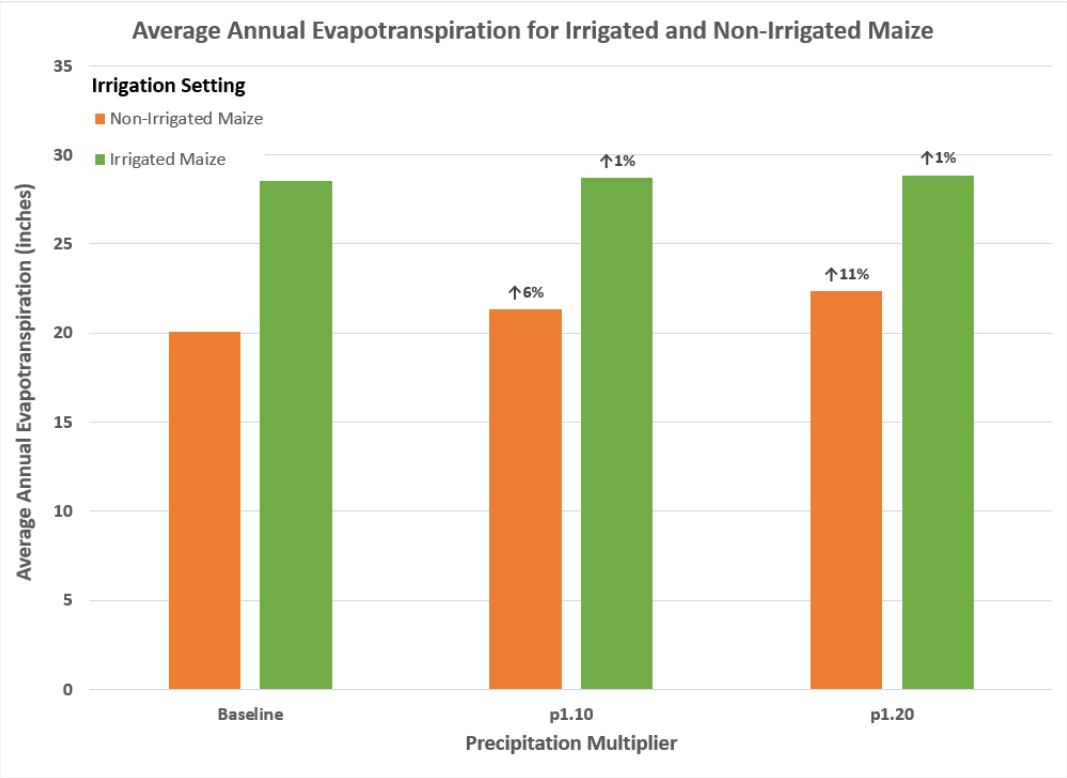

***Figure 4.21**: Response of ET to precipitation multipliers for irrigated and non-irrigated maize*

In the case of an irrigated maize field, precipitation multipliers have less effect on the percent change in the ET component, since the field is being irrigated with more water for full crop growth when the precipitation starts to decline. On the other hand, since non-irrigated maize fields are only dependent on precipitation for water consumption, the percent changes in ET compared to baseline values are sizable when compared to those of irrigated maize fields. It shows in Figure 4.21 that when precipitation increase by 20%, ET of irrigated maize is not much effected, but for non-irrigated maize ET increased by 11%. For the irrigated scenarios precipitation ET remains constant (Full ET) and the portion of ET met by precipitation is changing. If a larger portion is met by precipitation, then the

portion met by irrigation would decrease. Improving the accuracy of the precipitation data will improve the accuracy of estimating irrigation needs.

4.4.2.2 Effects of Precipitation Rates on Different Crop Types

DP and RO components have different responses to different rates (multipliers) of precipitation for different crops. Figure 4.22 shows the annual average DP rates for alfalfa, maize, and soybeans with different multipliers applied to the precipitation. It shows that with different precipitation multipliers, the percent change of DP for alfalfa is much higher than that for maize and soybeans, when the precipitation starts increasing above the baseline. For example, when the precipitation rate is increased by 20%, the percent increase in DP is by 250% for alfalfa, whereas percent increase in DP is by 87% and 47% for maize and soybeans respectively.

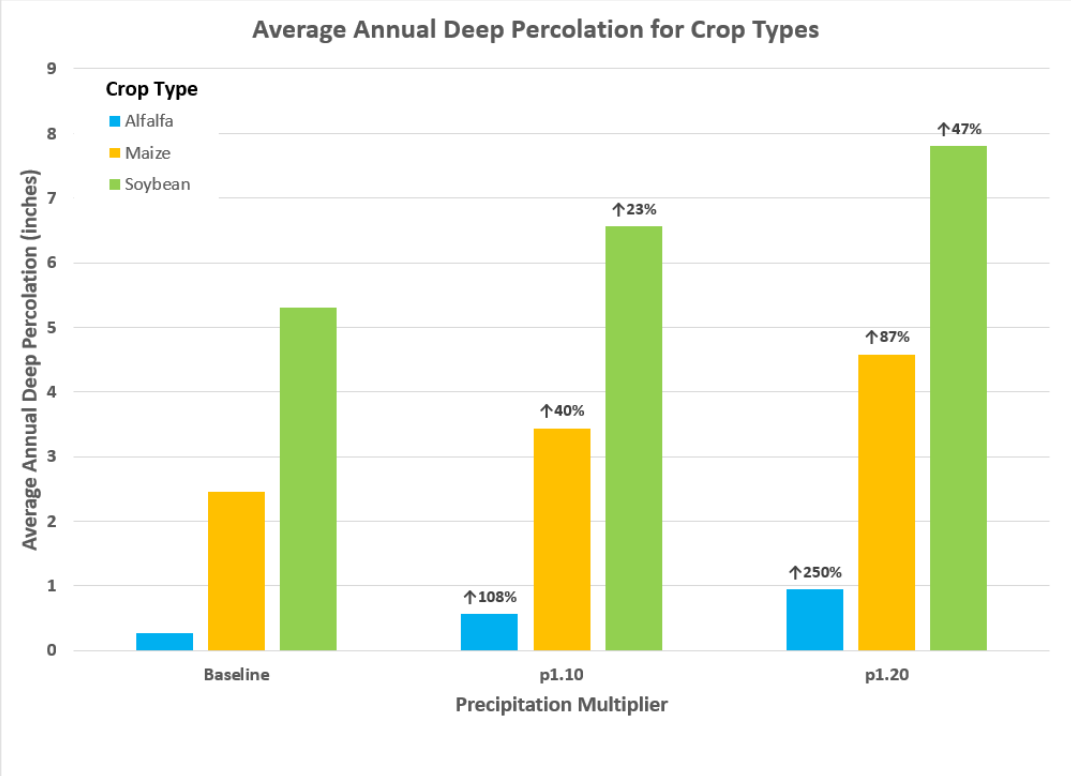

***Figure 4.22**: Response of DP to precipitation multipliers for different crop types*

Similarly, different rates of precipitation cause different percent changes in annual average RO for the pasture, maize, and soybean (Figure 4.23). The percent increase of RO is significantly higher than for all crops for the same precipitation multiplier. When the precipitation rate is increased by 20%, the RO increases by 67%, 58% and 54% for pasture, maize, and soybeans respectively.

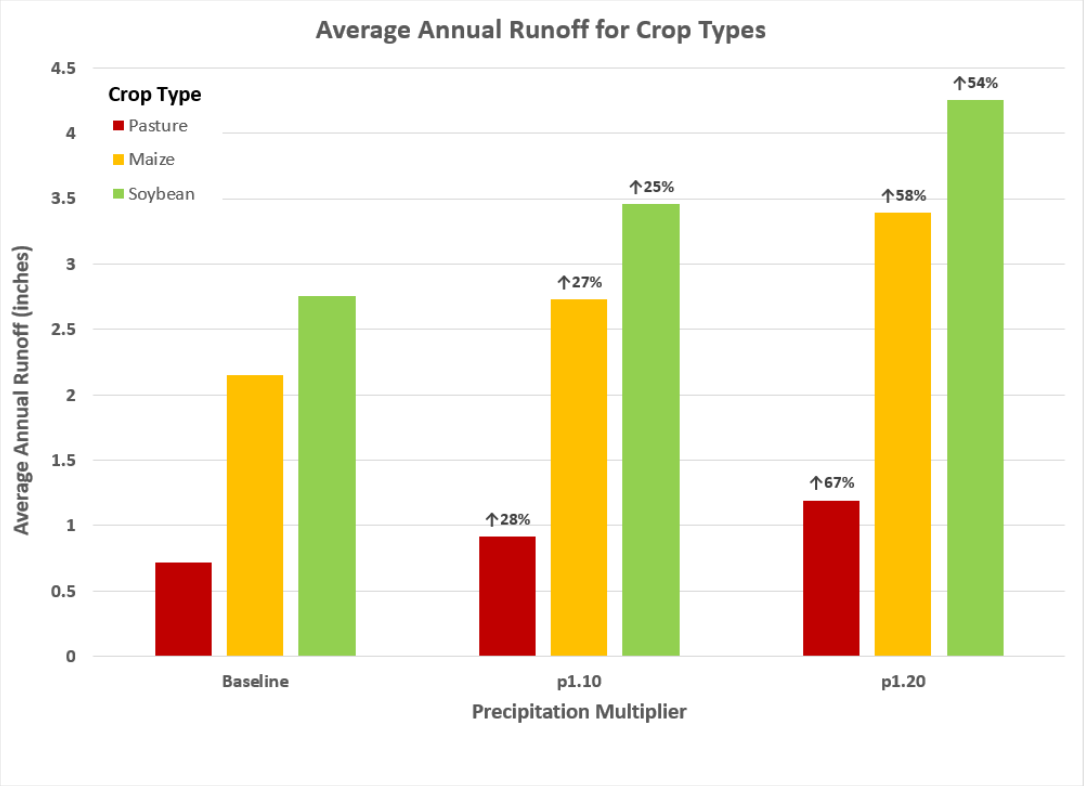

***Figure 4.23**: Responses of RO to precipitation multipliers for different crop types*

Net Irrigation Requirement (NIR) is not a hydrologic component but a term used in agriculture which represents the net amount of water that needs to be provided to supplement the soil moisture for full growth of crops. Figure 4.24 shows the response of percent change in NIR from baseline values for alfalfa, maize and soybean with different rates of precipitation. The percent increase in NIR for maize is significantly higher than for alfalfa and soybeans with increasing precipitation.

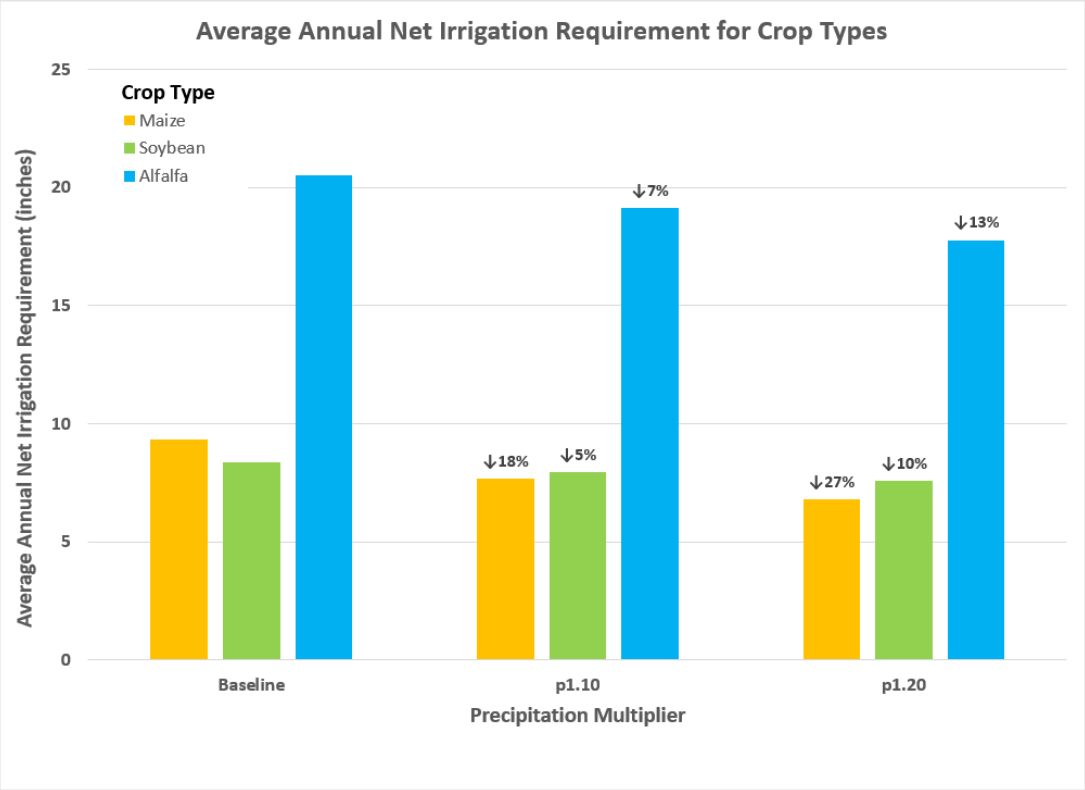

***Figure 4.24**: Response of NIR to precipitation multipliers for different crop types*

4.4.2.3 Effects of Precipitation Rates in Different Soil Types

DP and RO components have different responses to different multipliers of precipitation for different types of soils (Figure 4.25). Soil codes 612, 622, and 642 in the figure represent hydrologic soil groups sandy, silt loam, and clay soils respectively.

The percent change of DP for clay (code 642) soil is much higher than for sandy (code 621) soil with different precipitation multipliers, when the precipitation increases above the baseline value. The percent increase trend of DP for silt loam (code 622) soil is between those of sand and clay soil. For example, when the precipitation is increased by 20%, the percent increase in DP is by 111% for clay, whereas percent increase in DP is by 59% and

87% for sandy (code 621) and silt loam (code 622) soils, respectively, as shown in the Figure 4.25.

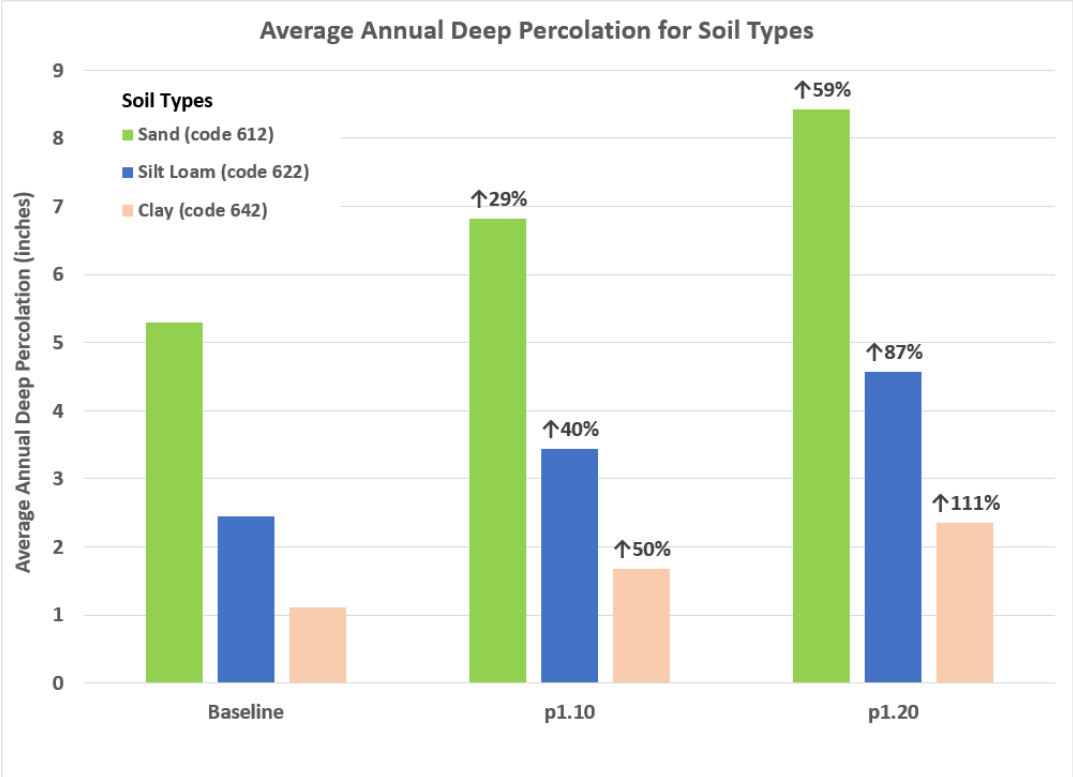

***Figure 4.25**: Response of DP to changes in precipitation multipliers for soil types*

Similarly, different multipliers of precipitation substantially impact percent changes in the RO component for the different soils (Figure 4.26). The percent changes in RO for sandy (code 612) soil are much higher than for clay (code 642) soil with increasing precipitation multipliers when the precipitation is above baseline values. The percent increase trend of DP for silt loam (code 622) soil is between that of sand and clay soils, as shown in the graph. The soil curve numbers are directly related to the type of soil. Sandy soils which falls in hydrologic group "a" are more prone to infiltrate (low curve number). These soils tend to be well developed soils with good pore space. On the other hand, clay soils which falls in hydrologic group "d" tends to restrict infiltration yielding higher runoff.

The percent change is higher in the sandy (code 612) soil because the baseline has a relatively small amount of runoff compared to the clay (code 642) soil. Therefore, the proportional change is greater on the sandy soil; but the absolute depth change is greater on the clay soil.

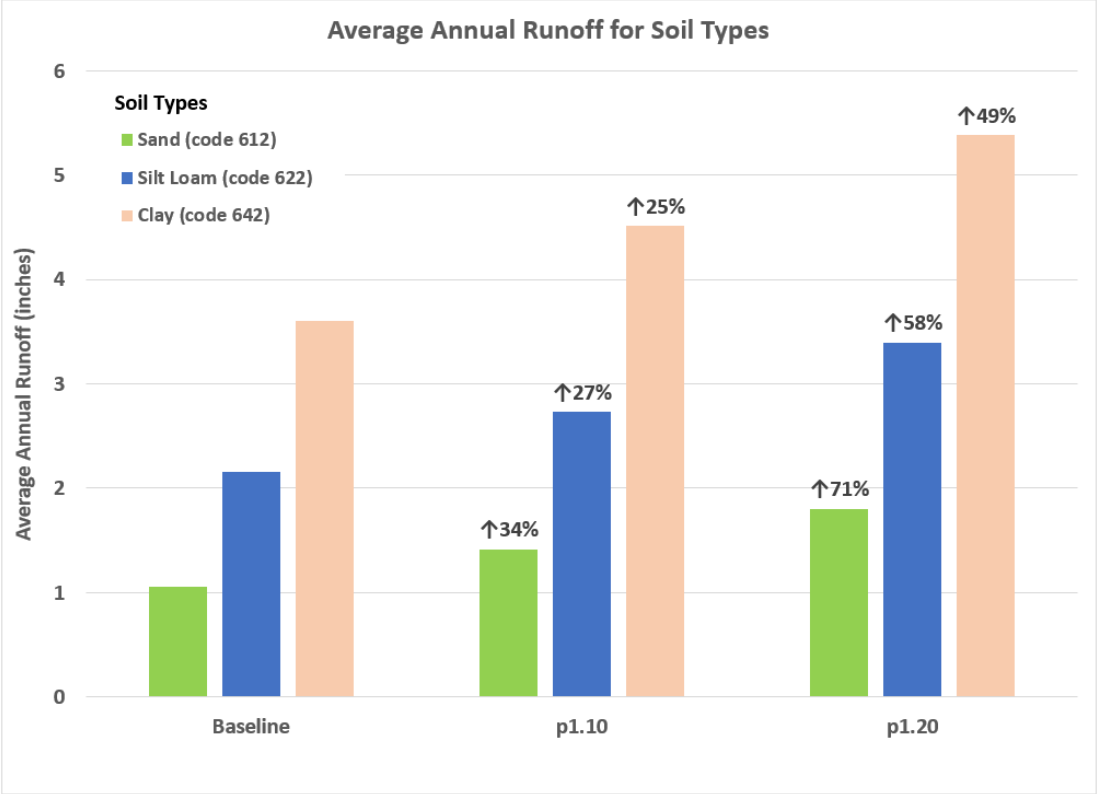

***Figure 4.26**: Responses of RO to variations in the Precipitation multipliers for different soil types*

DP hydrologic components also have different responses to different multipliers of precipitation for soils with different water holding capacity (WHC) (Figure 4.27). The percent change of DP for silt loam soil with 1.75 inches of WHC is much higher than for same soil with 1.0 inch of WHC at different precipitation multipliers. The percent increase trend of DP for silt loam soil with 1.5 inches of WHC is between DP of same soil with WHC of 1.75 inches and 1.0 inch.

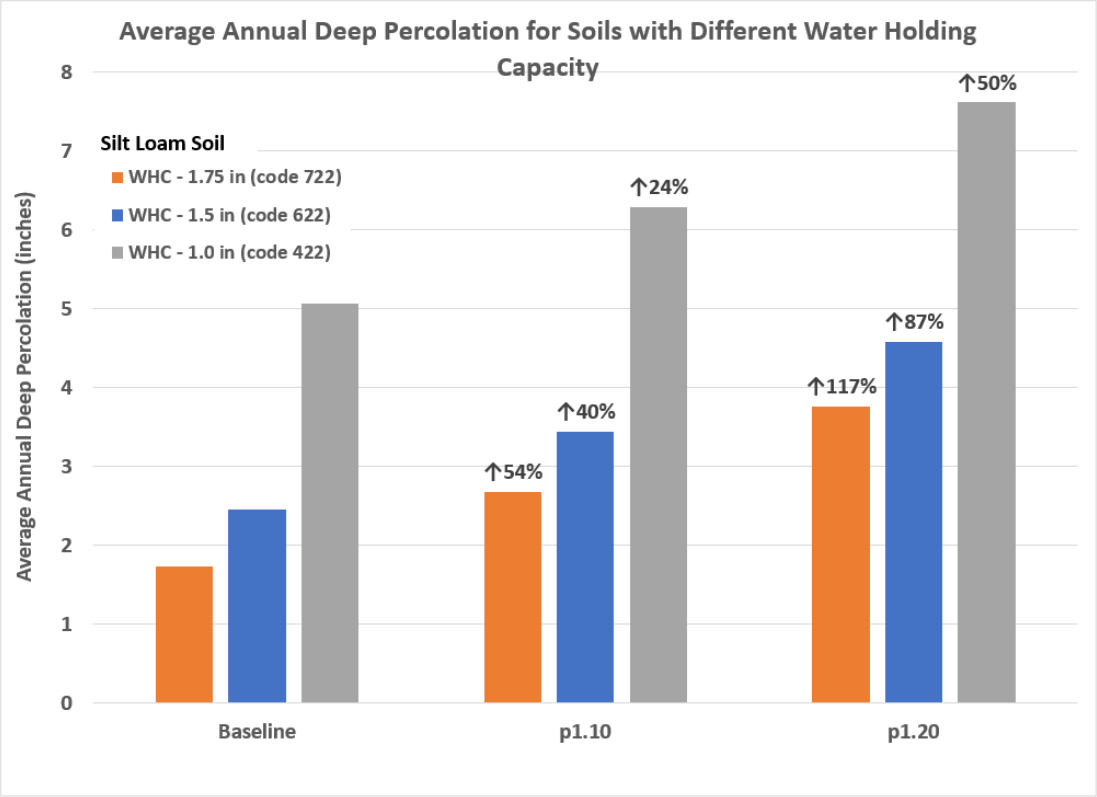

***Figure 4.27**: Response of DP to varying multipliers of precipitation for soils with different Water Holding Capacity*

The sensitivity analysis of different hydrologic components to variations in the precipitation rate using a soil water balance model shows that the responses of hydrologic components like ET, RO, and DP for different combinations of irrigation, crop, and soil types can be sizeable.

4.4.3 Summary of Sensitivity Analysis of the Soil Water Balance Model to Precipitation

The average annual flux rate (in/yr) of hydrologic components (ET, DP, RO, and NIR) from the CROPSIM model simulation with variable precipitation multipliers and different parameters are listed in Table 4.3. The tested model parameters were ranked based on the

level of response (change in magnitude of flux rate from baseline) as indicated by the sensitivity analysis; their ranks are as given in last column in Table 4.3.

***Table 4.3**: Response of hydrologic components in flux rates to variable precipitation multipliers*

Sensitivity Analysis Parameter	Hydrologic Component	Baseline (in/yr)	p1.10 (in/yr)	p1.20 (in/yr)	Rank
Irrigation Setting					
Non-Irrigated Maize	ET	20.07	**21.32**	**22.34**	16
Irrigated Maize	ET	28.52	**28.69**	**28.85**	18
Non-Irrigated Maize	DP	0.34	**0.75**	**1.34**	1
Irrigated Maize	DP	2.45	**3.44**	**4.58**	5
Crop Types					
Maize	DP	2.45	**3.44**	**4.58**	5
Soybeans	DP	5.31	**6.56**	**7.80**	13
Alfalfa	DP	0.27	**0.56**	**0.94**	2
Maize	RO	2.15	**2.73**	**3.39**	9
Soybean	RO	2.76	**3.46**	**4.26**	10
Pasture	RO	0.72	**0.92**	**1.19**	7
Maize	NIR	9.35	**7.65**	**6.80**	14
Soybean	NIR	8.37	**7.93**	**7.57**	17
Alfalfa	NIR	20.53	**19.11**	**17.77**	15
Soil Types					
Soil code 612	DP	5.29	**6.82**	**8.42**	8
Soil code 622	DP	2.45	**3.44**	**4.58**	5
Soil code 642	DP	1.12	**1.68**	**2.36**	4
Soil code 612	RO	1.05	**1.41**	**1.80**	6
Soil code 622	RO	2.15	**2.73**	**3.39**	9
Soil code 642	RO	3.61	**4.51**	**5.38**	12
Soil Water Holding Capitity					
Soil code 422	DP	5.06	**6.29**	**7.61**	11
Soil code 622	DP	2.45	**3.44**	**4.58**	5
Soil code 722	DP	1.73	**2.67**	**3.76**	3

Similarly, Table 4.4 summarizes the same results of sensitivity analysis but the flux rate expressed as a percent change from the baseline condition.

***Table 4.4**: Response of hydrologic components in percent change of flux rates to variable precipitation multipliers*

Sensitivity Analysis Parameter	Hydrologic Component	Baseline (%)	p1.10 (%)	p1.20 (%)	Rank
Irrigation Setting					
Non-Irrigated Maize	ET	-	6	11	16
Irrigated Maize	ET	-	1	1	18
Non-Irrigated Maize	DP	-	124	301	1
Irrigated Maize	DP	-	40	87	5
Crop Types					
Maize	DP	-	40	87	5
Soybeans	DP	-	23	47	13
Alfalfa	DP	-	108	250	2
Maize	RO	-	27	58	9
Soybean	RO	-	25	54	10
Pasture	RO	-	28	67	7
Maize	NIR	-	-18	-27	14
Soybean	NIR	-	-5	-10	17
Alfalfa	NIR	-	-7	-13	15
Soil Types					
Soil code 612	DP	-	29	59	8
Soil code 622	DP	-	40	87	5
Soil code 642	DP	-	50	111	4
Soil code 612	RO	-	34	71	6
Soil code 622	RO	-	27	58	9
Soil code 642	RO	-	25	49	12
Soil Water Holding Capitity					
Soil code 422	DP	-	24	50	11
Soil code 622	DP	-	40	87	5
Soil code 722	DP	-	54	117	3

Tables 4.3 and 4.4 show that areas with maize crop under non-irrigated management on soils with high WHC (1.75 inches) are highly impacted by the precipitation rates with

increase in flux rate up to 301% when precipitation is increased by 20%. Of all the hydrologic components, DP was found to be highly impacted by the change in precipitation rates. This is an important issue in the field of water resources modeling. It can make the process of model calibration difficult. For example, the increase in groundwater recharge volume (DP) in Republican River model were around 53%, 26%, and 12% for year 2005, 2006, and 2007 respectively (Table 4.2) when precipitation data source was switched from WSI to gridded method. This can increase the level of groundwater of model aquifer and increase the baseflow of the river system in groundwater model, and make the process of groundwater model calibration difficult.

Beside performing sensitivity analysis by applying multipliers of 1.1 and 1.2, a full range of precipitation multipliers were applied from 0.5 (half the precipitation) to 1.5 (increase precipitation by half) and analysis results were compiled. The results are included in Appendix F.

4.5 Sensitivity Analysis of Precipitation to Baseflow of a River System

4.5.1 Methods

The effects of different precipitation multipliers on baseflow of a river system were analyzed using a water resources model. The Cooperative Hydrology Study 2010 (COHYST2010) model was developed for water resources management of the Platte River in the state of Nebraska. One of the objectives of this model was to estimate the effects of agricultural pumping on the baseflow of the Platte River. Figure 4.28 shows the spatial coverage of the COHYST2010 model in Nebraska.

To study the effects of precipitation on baseflow, the precipitation rates provided by weather stations used in the COHYST2010 groundwater model were multiplied by factors of 1.1 and 1.2. The point-based soil water balance CROPSIM model was then used to generate recharge and pumping rates for the watershed model. The output of the simulation model from years 1984 to 2005 was processed, and baseflows at different gage locations; North Platte, Brady, Cozad, Overton, Odessa, Grand Island, and Duncan as shown in Figure 4.28 were analyzed.

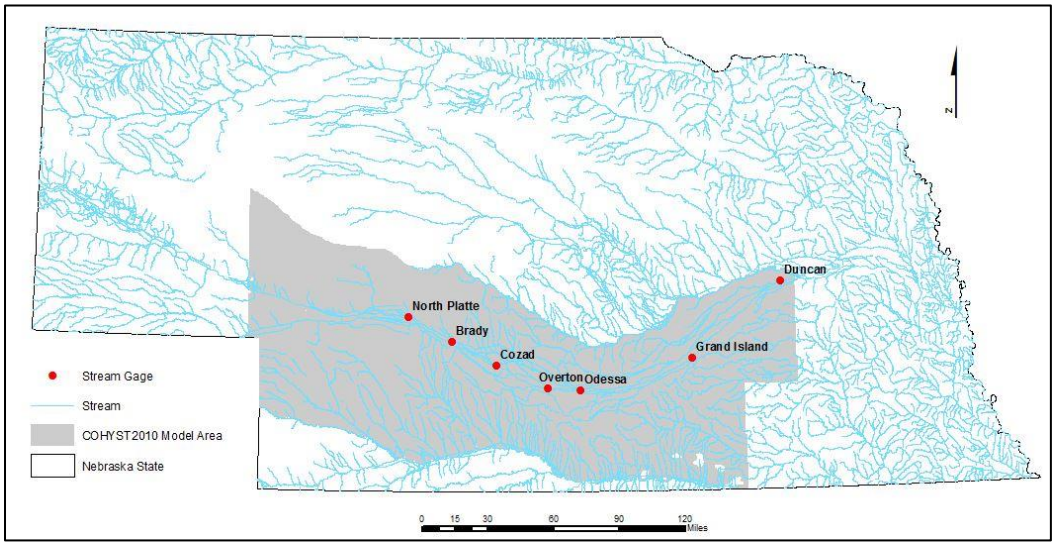

***Figure 4.28**: Spatial coverage of COHYST2010 model in Nebraska state*

4.5.2 Results

Figure 4.29 shows a general representation of simulated (a) monthly baseflows and (b) cumulative annual baseflows at different gage locations using the baseline precipitation, the 1.1 and 1.2 multipliers for the seven gage locations on the Platte River. In each figure, the upper graph is the simulated monthly baseflow, and the lower graph is the cumulative annual baseflow.

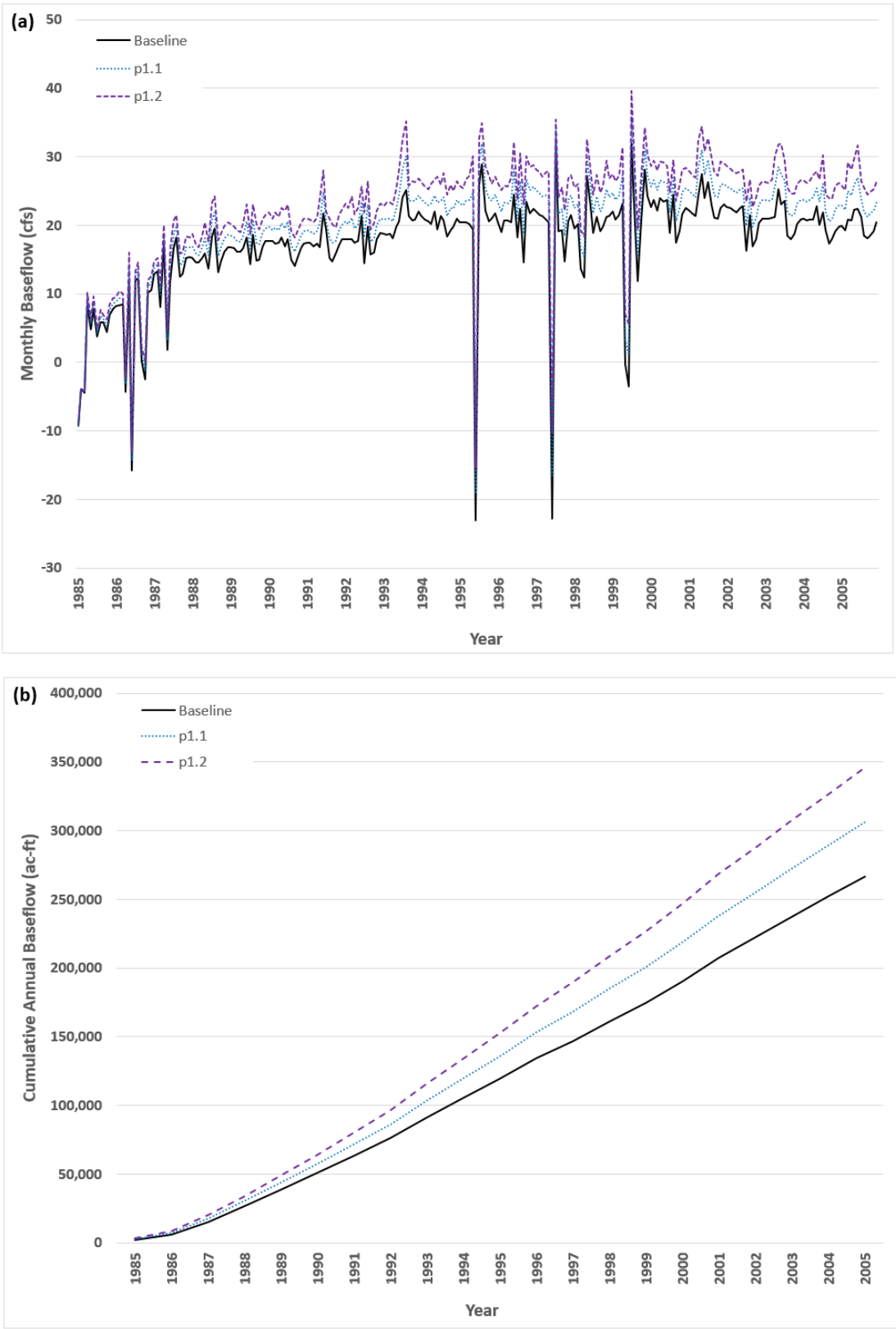

***Figure 4.29**: Baseflow comparison at the Cozad gaging station. (a) monthly baseflow and (b) cumulative annual baseflow*

In general, increase in stream baseflow is observed at different gage locations when precipitation was increased by 10% and 20%. The average annual baseflow volume from COHYST2010 groundwater model at different gage locations with variable precipitation multipliers are listed in Table 4.5.

***Table 4.5**: Response of model baseflow in annual average volume to variable precipitation multipliers at different gage locations*

Gage Station	Baseline (ac-ft/yr)	p1.1 (ac-ft/yr)	p1.2 (ac-ft/yr)
North Platte	1,497	1,650	1,803
Brady	6,498	7,211	7,924
Cozad	12,695	14,581	16,468
Overton	1,731	2,439	3,148
Odessa	10,054	10,731	11,409
Grand Island	-6,022	-3,281	-541
Duncan	1,823	2,541	3,258

Similarly, Table 4.6 summarizes the same results of sensitivity analysis but the annual baseflow volume expressed as a percent change from the baseline condition.

***Table 4.6**: Response of model baseflow in percent change to variable precipitation multipliers at different gage locations*

Gage Station	Baseline (%)	p1.1 (%)	p1.2 (%)
North Platte	-	10	20
Brady	-	11	22
Cozad	-	15	30
Overton	-	41	82
Odessa	-	7	13
Grand Island	-	46	91
Duncan	-	39	79

At the North Platte gage location, there was increase in annual average baseflow from 1,497 ac-ft to 1,650 ac-ft (10%) and 1,803 ac-ft (20%) when precipitation was increased by 10% and 20% respectively in COHYST2010 model. The Brady gage location had similar percentage increase in baseflow. In the case of Overton and Duncan gage locations, the increase in stream baseflow was around 40% and 80% when the precipitation was increased by 10% and 20% respectively. The Platte river in Grand Island area is a losing reach where water enters aquifer from the stream. Increases in precipitation of 10% and 20% led to decreases in loss of water to the aquifer by 46% and 91% respectively.

The analysis of different multipliers in precipitation and model simulations shows that the precipitation strongly influences the rate of baseflow discharge to the river system at different gage locations. It is essential that the precipitation data that are input to the water resources model represent close to real conditions. Since the baseflow of the model simulation is sensitive to precipitation rates, refined high quality precipitation data would be helpful in development of a well-calibrated groundwater model that better represents the real conditions.

Besides performing sensitivity analysis by applying multipliers of 1.1 and 1.2, a full range of precipitation multipliers were applied from 0.5 (half the precipitation) to 1.5 (increase precipitation by half) and analysis results were compiled. The results are included in Appendix G.

4.6 Summary and Conclusions

The precipitation maps generated using the WSI method appear to be very simplified due to the lack of a dense distribution of weather stations in some regional areas. The gridded method which is the combination of remotely sensed and weather stations data, on the other hand, is capable of capturing more variability in detail at a regional scale. Furthermore, artifacts such as the bull's eye effect and the influence of localized storm events near weather stations on the results of the interpolation process are some of the disadvantages of generating precipitation maps using the WSI method.

While analyzing and comparing the precipitation maps generated with WSI method and gridded method, patterns of spatial distributions of precipitation were found to be substantially different. The volumes of precipitation attributed to different areas were also substantially different. The percent difference in average annual precipitation volume over 16 million acres of Republican Model area (area of RRCA model) was around 14%, and the percent difference in average annual recharge volume was around 30% between two sources of precipitation maps. The differences in patterns of precipitation and generated recharge maps were also found to be substantial.

The results of point-based soil water balance models are used as input data for regional water resources models where different combinations of soils, crops, and irrigation settings exist in grid cells of the model. Different multipliers of precipitation have strong impacts on the responses of hydrological components. Different crops, soils, and irrigation settings respond differently to increasing or decreasing the precipitation rate. The sensitivity analysis performed using a soil water balance model showed that deep percolation and runoff components are strongly affected for different types of crops and soils by different

rates of precipitation. Similarly, evapotranspiration and deep percolation components are strongly affected in the case of irrigated and non-irrigated crop fields. The baseflows simulated by the model at different gaging stations are also sensitive to different multipliers of precipitation. It is essential to have precipitation data that closely represent real conditions for accurate results during water resources model development.

When these two different sources of precipitation data are applied to water resources models, the results of the model simulations were markedly different. The volume and rates estimates of water budgets from the model were different, contributing to uncertainty in the results provided by the model. Similarly, during the process of model development it is essential to have input data that provide more detailed information regarding spatial precipitation patterns. Water resources models are calibrated to field observation data at different locations within the model area, therefore precipitation data with more detailed spatial information are helpful to develop a well calibrated model.

During model development at a regional scale, precipitation maps generated with the WSI method from a dense network of weather stations are helpful since they can capture more spatial information about the precipitation. If there are a limited number of weather stations in the model area, remotely sensed gridded precipitation data are valuable. Since the gridded precipitation data preserve spatial rainfall patterns at both local and regional scales, they can aid in development of water resources models with more accurate water budget estimates of hydrological components and better calibration statistics.

4.7 References

1. NOAA. (2017). National Oceanic and Atmospheric Administration. National Centers for Environmental Information. *Data Access.* Retrieved 04/20, 2017, from https://www.ncdc.noaa.gov/data-access
2. Nelson, B. R.; Seo, D. J.; Kim, D. (2010). Multisensor Precipitation Reanalysis. *Journal of Hydrometeorology, 11*(3), 666-682. doi: 10.1175/2010JHM1210.1
3. NOAA. About the precipitation analysis pages. Available online: https://water.weather.gov/precip/about.php (accessed on Nov 23, 2018).
4. Daly, C.; Slater, M. E.; Roberti, J. A.; Laseter, S. H.; Swift Jr., L. W. High-resolution precipitation mapping in a mountainous watershed: ground truth for evaluating uncertainty in a national precipitation dataset. *Int. J. Climatol*. **2017**. doi: 10.1002/joc.4986
5. Seo, B; Krajewski, W. F. Scale dependence of radar rainfall uncertainty: initial evaluation of NEXRAD's new super-resolution data for hydrologic applications. *American Meteorological Society*. **2010**. doi: 10.1175/2010JHM1265.1
6. Vie, H.; Zhou, X.; Hendrickx, J. M. H.; Vivoni, E. Evaluation of NEXRAD Stage III precipitation data over a semiarid region. *J. American Water Resources Assoc.* **2006**. doi: 10.1111/j.1752-1688.2006.tb03837.x
7. Klazura, G. E.; Thomale, J. M.; Kelly, D. S.; Jendrowski, P. A comparison of NEXRAD WSR-88D radar estimates of rain accumulation with gauge measurements for high- and low-reflectivity horizontal gradient precipitation events. *J. Atmospheric and Oceanic Technology.* **1999**, 16, 1842-1850.
8. Sitterson, J.; Knightes, C.; Parmar, R.; Wolfe, K.; Avant, B.; Ignatius, A., Smith, D. A survey of precipitation data for environmental modeling. *U.S. Environmental Protection Agency Report.* **2017**.
9. Velasco-Forero, C.; Sempere-Torres, D.; Sanchez-Diezma, R.; Cassiraga, E.; Gomez-Harnandez, J. Automatic estimation of rainfall fields for hydrological applications: blending radar and rain gauge data in real time. *The 32nd Conference on Radar Meteorology, Albuquerque, NM. 2005.*
10. Kalin, L.; Hantush, M.M. Hydrologic modeling of an eastern Pennsylvania watershed with NEXRAD and rain gauge data. *Journal of Hydrologic Engineering*. **2006**, 11 (6). doi: 10.1061/(ASCE)1084-0699(2006)11:6(555)
11. Sexton, A.M.; Sadeghi, A.M.; Zhang, X.; Srinivasan, R.; Shirmohammadi, A. Using NEXRAD and rain gauge precipitation data for hydrologic calibration of SWAT in a northeastern watershed. *American Society of Agricultural and Biological Engineers*. **2010**, 53 (5), 1501-1510.
12. Faunt, C.C.; Hanson, R.T.; Belitz, K.; Schmid, W.; Predmore, S.P.; Rewis, D.L.; McPherson, K. Groundwater availability of the central valley aquifer, California. *U.S. Geological Survey*. **2009**.
13. National Weather Service. Advanced Hydrologic Prediction Service, 23 May 2017. Available online: https://water.weather.gov/precip/ (accessed on Jun. 15, 2017).
14. Republican River Compact Administration. Republican River Compact Administration Ground Water Model – Appendix E, 30 June 2003. Available

online:
http://www.republicanrivercompact.org/v12p/RRCAModelDocumentation.pdf
(accessed on Jun. 21, 2017).

15. Republican River Compact Administration. Republican River Compact Administration Ground Water Model – Appendix F, 30 June 2003. Available online:
http://www.republicanrivercompact.org/v12p/RRCAModelDocumentation.pdf
(accessed on Jun. 21, 2017).
16. Martin, D.L.; Watts D.G.; Gilley, J.R. Model and Production Function for Irrigation Management. *Journal of Irrigation and Drainage Engineering*. **1984**,100(2): 149-164.

CHAPTER 5: SUMMARY AND CONCLUSIONS

5.1 Overall Conclusion

People responsible for managing the earth's natural resources and planning future development recognize the importance of accurate spatial information [1]. The effective management of natural resources at local, regional, and global scales highly depends on the accuracy of data that are in spatial and temporal domain, upon which assessments are done to develop effective plans and policies. With the current advancement in image processing and hardware computational ability, remote sensing technology could be used to generate highly accurate environmental data with more refinement in spatial and temporal domain. Two major important data; climate and land use, when produced with improved spatial accuracy and frequency, could be useful to perform assessments related to water resources management with more accurate results. Some examples are: accurately identifying acres related to different irrigated and non-irrigated crops from field to regional scales, development of water resources models that represent the real environment with more accuracy, etc.

In this study, the potential of remote sensing technology for generating more accurate data that could be used for agricultural water resources management was investigated. A remote sensing classification method was developed that integrates surface energy balance (SEB) partitioning and vegetation indices to classify irrigated and non-irrigated croplands at high spatial resolution (Chapter 2). In the method, the Normalized Difference Vegetation Index (NDVI) and Green Index (GI), indices sensitive to phenological development of

crops, were combined with SEB fluxes, which account for soil moisture stress, and energy and mass exchange between the vegetation surface and the atmosphere over irrigated and non-irrigated surfaces. The phenological contrasts and variation in SEB fluxes over non-irrigated and irrigated surfaces are combined and evaluated in this study to classify irrigated and non-irrigated crops. The method was applied to a region with wide climate variation and to multiple growing seasons. The results revealed that across multiple growing seasons, the classification method was 92.1% accurate and explained 97% variation in National Agricultural Statistics Service (NASS) county irrigation statistics.

A new method of re-projecting Moderate Resolution Imaging Spectroradiometer (MODIS) satellite images that preserves the geometric orientation of the satellite sensor pixel (referred to as the "footprint method") was developed (Chapter 3). There are two advantages of this method over the existing gridded method of re-projecting MODIS images. First is the elimination of artifacts introduced by gridding, artifacts which evolve from a mismatch between the sensor pixel and the orientation of pre-defined grid cells. The second advantage is the ability to identify satellite sensor pixel orientation in agricultural fields for more accurate field scale analysis. Field scale accuracy assessment of the footprint method and the existing gridded method was done with Green Leaf Area Index (LAI) data of two center pivot maize fields US-Ne1 and US-Ne2 from Mead, Nebraska. Green LAI data from the fields were closer to LAI estimates determined from MODIS data using the footprint method than estimates based on the gridded method. The Root Mean Square Error (RMSE), unbiased RMSE (ubRMSE), and normalized RMSE (NRMSE) of LAI estimates based on the footprint method for field US-Ne1 and decreased by 0.201 m^2/m^2, 0.169m^2/m^2, and 0.046 m^2/m^2 respectively when compared LAI estimates based on

the gridded method. Similarly, in field US-Ne2, RMSE, ubRMSE, and NRMSE decreased by 0.301 m^2/m^2, 0.266m^2/m^2, and 0.062 m^2/m^2 respectively when the footprint method was applied. On the contrary, the results of statistical analysis of MODIS Green LAI estimates based on Green LAI equation of Viña et al. does not support this conclusion. Furthermore, the results of t-test analysis show that the improvement of MODIS LAI and Green LAI estimates from footprint method when compared to that of gridded method is relatively very small.

Potential opportunities and benefits of utilizing remotely sensed precipitation data in water resources models were explored (Chapter 4). The differences in spatial patterns and rainfall volumes predicted using precipitation maps generated by interpolating data from weather stations and by using precipitation maps generated by combining radar technology with weather station data were analyzed. The percent difference in annual average precipitation volume for 16 million acres of Republican River model area was around 14%, and the percent difference in annual average recharge volume was around 30%. The difference in patterns of precipitation and recharge maps generated were found to have a substantial influence. The level of influence of precipitation rate in a soil water balance model and groundwater model were analyzed by sensitivity analysis. The effects of different rates of precipitation were influenced by different soils, crops, and irrigation settings. The sensitivity analysis of precipitation using a soil water balance model showed that deep percolation and runoff components of the field soil water balance are significantly affected for different types of crops and soils by different rates of precipitation. Similarly, evapotranspiration and deep percolation components are significantly affected in the case of irrigated and non-irrigated crop fields. Artifacts such as the bull's eye effect and the

influence of local storm events on weather station data used for interpolation are some of the problems associated with generating precipitation maps using the interpolation method. The remotely sensed gridded method on the other hand is able to capture more spatial variability at a regional scale.

5.2 Recommendations for Future Research

The following recommendations for future research are suggested based on the experience gained from out this research:

- In chapter 2, the method for classifying irrigated and non-irrigated fields was applied only in the COHYST model area. Since the methodology was developed to be applied in different climate regions and for different levels of water stress, this method should be tested in additional climate regions to evaluate its performance.
- In chapter 3, estimated LAI values from the footprint and gridded method of re-projecting MODIS images in 250m pixel resolution were compared with ground truth data. LAI values were derived from the NDVI index in MODIS images. NASA also provides LAI products in 1000m pixel resolution. LAI values from the footprint and gridded method of MODIS images in 1000m pixel resolution can be compared with the same ground truth data. This could help in evaluating the impact of spatial resolution on data quality. Furthermore, the surface energy balance model can be used to compare the footprint and gridded method at 1000m pixel resolution (thermal band) for predictions crop evapotranspiration rate and comparing with ground truth data.

- Regarding the remotely sensed precipitation data study in chapter 4, precipitation rate of remotely sensed data should be compared with weather station data at station locations using the station data as ground truth, and evaluating the differences at the station locations. This could lead to an opportunity of developing a method to correct or adjust the remotely sensed precipitation maps before applying them for water balance studies.

5.3 References

1. Jensen, J.R. Remote Sensing of the Environment: An Earth Resource Perspective. **2000**. Prentice Hall, Upper Saddle River, New Jersey.

APPENDIX A: LIST OF SATELLITE IMAGES USED IN ANALYSIS

***Table A.1**: Landsat scene identification (ID), acquisition spacecraft and date, and path and row of images used for the project*

SCENE ID	SPACECRAFT ID	DATE	PATH	ROW
LE70310312010207EDC00	Landsat 7	26 July 10	31	31
LE70310312010239EDC00	Landsat 7	27 July 10	31	31
LE70310322010207EDC00	Landsat 7	26 July 10	31	32
LE70310322010239EDC00	Landsat 7	27 July 10	31	32
LT50310322010247EDC00	Landsat 5	04 Sept 10	31	32
LE70320312010230EDC00	Landsat 7	18 Aug 10	32	31
LT50320312010222PAC01	Landsat 5	10 Aug 10	32	31
LE70320312010246EDC00	Landsat 7	03 Sept 10	32	31
LE70320322010198EDC00	Landsat 7	17 July 10	32	32
LT50320322010222PAC01	Landsat 5	10 Aug 10	32	32
LE70320322010246EDC00	Landsat 7	03 Sept 10	32	32
LT50290312010217EDC00	Landsat 7	05 Aug 10	29	31
LT50290312010233EDC00	Landsat 5	21 Aug 10	29	31
LE70290322010177EDC00	Landsat 7	26 June 10	29	32
LT50290322010233EDC00	Landsat 5	21 Aug 10	29	32
LT50300312010208PAC01	Landsat 5	27 July 10	30	31
LT50300312010176EDC00	Landsat 5	25 June 10	30	31
LT50300322010208PAC01	Landsat 5	27 July 10	30	32
LT50300322010192EDC00	Landsat 5	11 July 10	30	32
LC80290312015199LGN00	Landsat 8	18 July 15	29	31
LE70290312015223EDC00	Landsat 7	11 Aug 15	29	31
LE70290312015255EDC00	Landsat 7	12 Sept 15	29	31
LC80290322015199LGN00	Landsat 8	18 July 15	29	32
LC80290322015215LGN00	Landsat 8	03 Aug 15	29	32
LE70300312015198EDC00	Landsat 7	17 July 15	30	31
LE70300312015214EDC00	Landsat 7	02 Aug 15	30	31
LC80300312015238LGN00	Landsat 8	26 Aug 15	30	31

LE70300322015198EDC00	Landsat 7	17 July 15	30	32
LE70300322015214EDC00	Landsat 7	02 Aug 15	30	32
LC80300322015238LGN00	Landsat 8	26 Aug 15	30	32
LC80310312015197LGN00	Landsat 8	16 July 15	31	31
LC80310312015245LGN00	Landsat 8	02 Sept 15	31	31
LC80310322015197LGN00	Landsat 8	16 July 15	31	32
LC80310322015213LGN00	Landsat 8	01 Aug 15	31	32
LC80310322015245LGN00	Landsat 8	02 Sept 15	31	32
LC80320312015204LGN00	Landsat 8	23 July 15	32	31
LC80320312015236LGN00	Landsat 8	24 Aug 15	32	31
LC80320322015204LGN00	Landsat 8	23 July 15	32	32
LC80320322015236LGN00	Landsat 8	24 Aug 15	32	32

APPENDIX B: MODIS BACKGROUND INFORMATION

MODIS refers to a type of sensor installed on the two NASA satellite platforms “TERRA” and “AQUA”. These satellites are designed to provide measurements of large-scale global dynamics, including changes in Earth's cloud cover, radiation budget, and processes occurring in the oceans, on land, and in the lower atmosphere [1]. The TERRA satellite orbits over the equator in the morning, and the AQUA satellite moves in the opposite direction, passing over the equator in the afternoon. Together, the Terra MODIS and Aqua MODIS provide a complete view of the Earth every one to two days [2]. The MODIS satellites acquire data in 36 spectral bands. Among these spectral bands the spatial resolution of the first two bands is 250m followed by a spatial resolution of 500m for the next five bands (band 3 to band 7). The rest of the 29 bands (band 8 to band 36) have a spatial resolution of 1000m. The wavelength at which MODIS bands sense and acquire earth related data ranges from 0.4 micrometers to 14.4 micrometers [3].

B.1 MODIS Satellite and Sensor Description

The MODIS satellites utilize a whiskbroom system where sensors collect electromagnetic energy reflected or radiated from the coverage area of the earth surface. The path which the MODIS satellite takes while revolving around the earth is known as a “track”, and the direction which the sensors of the satellite scan and collect electromagnetic energy from the earth’s surface is known as a “scan”. The track and scan directions are perpendicular to each other as illustrated by Wolfe et al., 2002 [4] in Figure B.1. In a single

rotation of its scan mirror, MODIS captures an area on Earth about 2300 kilometers wide by 10 kilometers long (imagine a long, thin rectangle). An image is put together by stitching adjacent scans to each other [5].

A key to properly representing features on the ground is understanding how those features are measured in space and how that space is a function of the spatial resolution of the imaging system [6]. Spatial resolution in remote sensing is often considered only as the characteristic pixel resolution reported for the sensing system used, but it is in fact, far more complex [7].

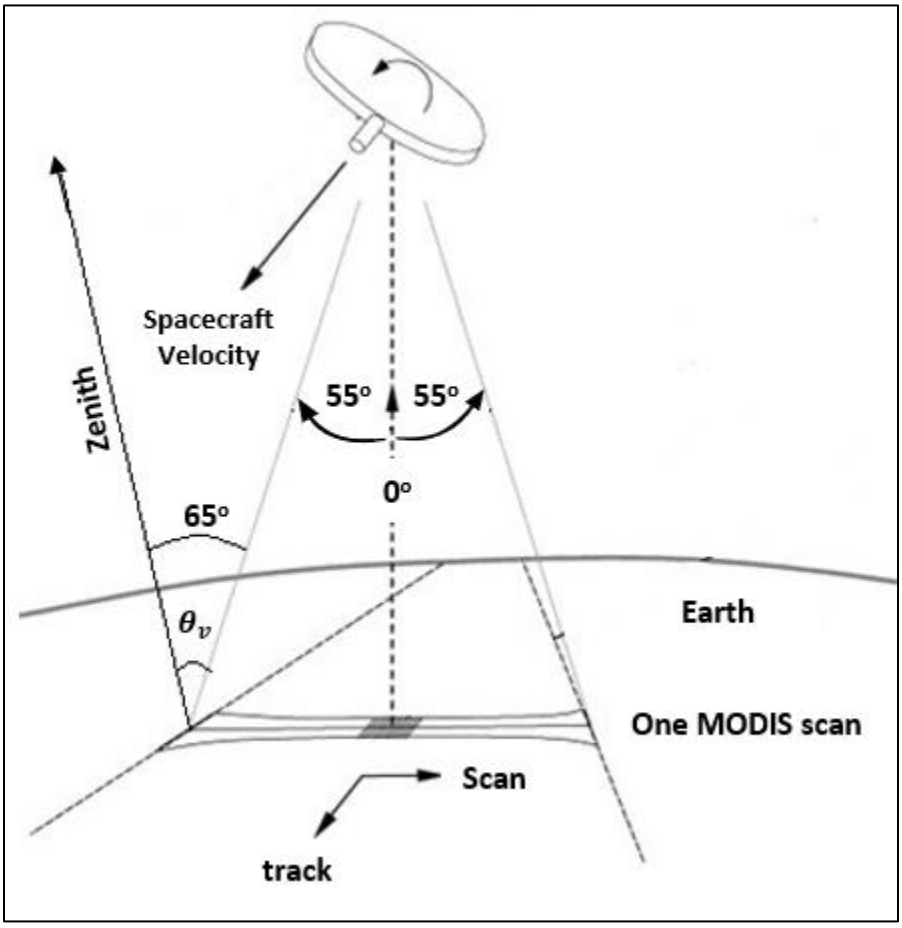

***Figure B.1**: Path of satellite and sensor scanning orientation of MODIS (modified from Wolfe et al., 2002, fig.1)*

B.2 Sensor Pixel Orientation

Along the track direction of the MODIS sensor, the pixels of the different spatial resolutions for the spectral bands overlap, i.e. two 250 m band pixels are nested within one 500 m and, and four 250 m band pixels are nested within one 1 km band pixel. Likewise, two 500 m band pixels are nested within a 1 km band pixel. Along the scan direction, 500 m band pixels are offset by 250 m at nadir (the point directly below the satellite) relative to the 1 km band pixels and the 250 m band pixels are offset by 125 m and 375 m relative to the 500-m and 1 km band pixels, respectively [8]. Figure B.2, Figure B.3 and Figure B.4 illustrates the orientation of the 500m band pixels relative to the 1 km band pixels, and the 250 m band pixels relative to the 1 km band pixels along the scan direction, respectively.

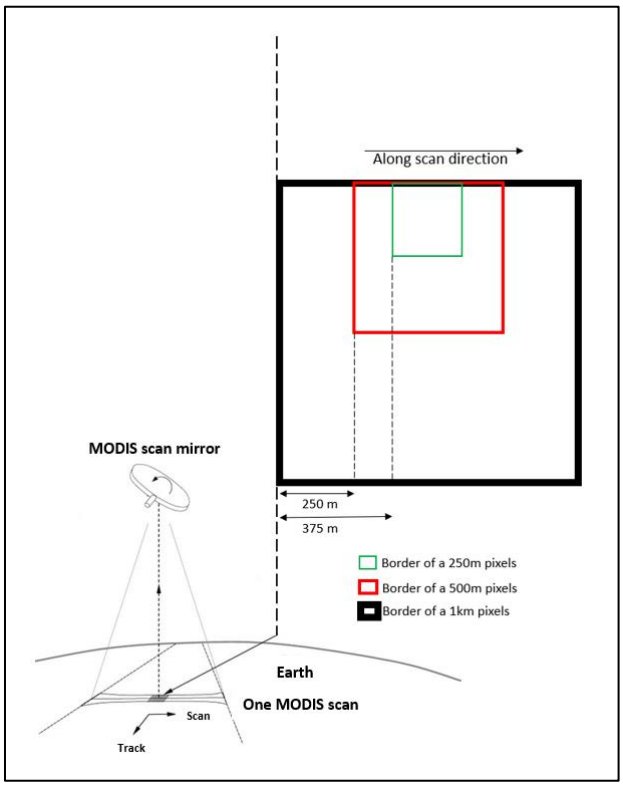

***Figure B.2**: Orientation of 500 m band pixels and 1 km band pixels in MODIS sensor along the scan direction*

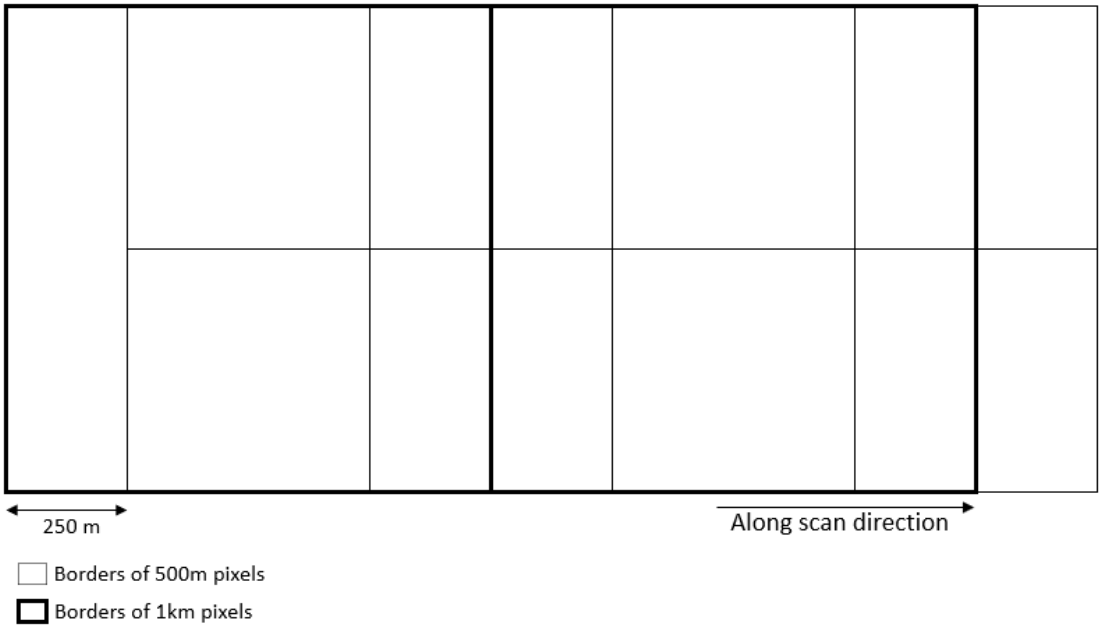

***Figure B.3**: Orientation of 500 m band pixels and 1 km band pixels in MODIS sensor along the scan direction*

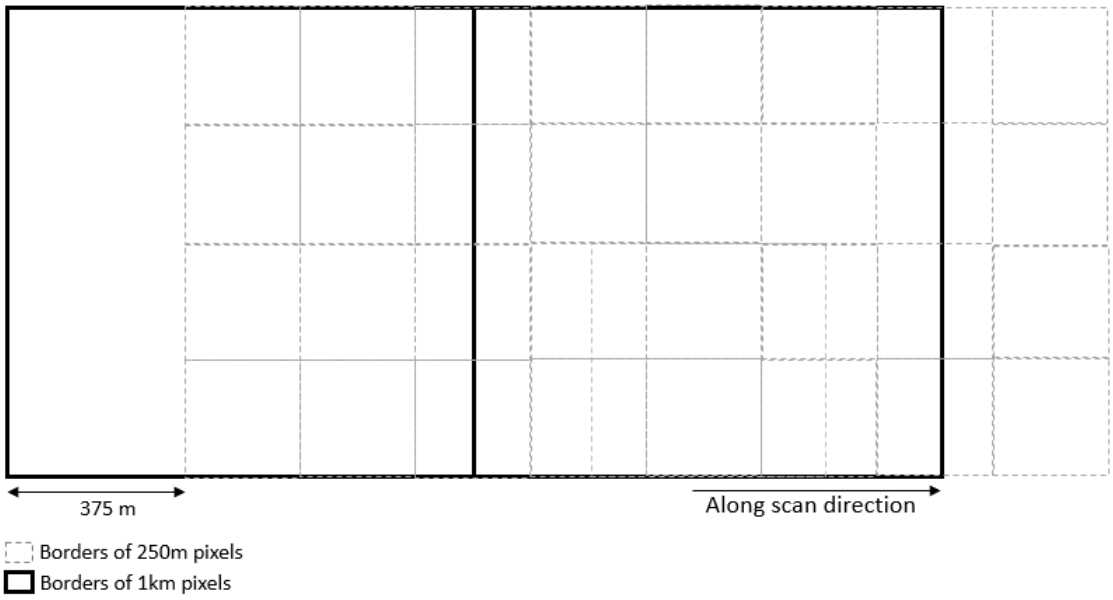

***Figure B.4**: Orientation of 250m band pixels and 1 km band pixels in MODIS sensor along the scan direction*

The geo-location information of MODIS images is stored in a 1000m pixel resolution image. To use this band information and to geo-locate pixels of 250m, 500m, and 1000m resolution, a “Point-Spread Function” is used to orient pixels of three different spatial resolutions relative to each other. The MODIS point-spread function is triangular in the scan direction. The centers of the integration areas of the first observation in each scan are aligned in a “peak-to-peak” alignment as illustrated in Figure B.5 [4].

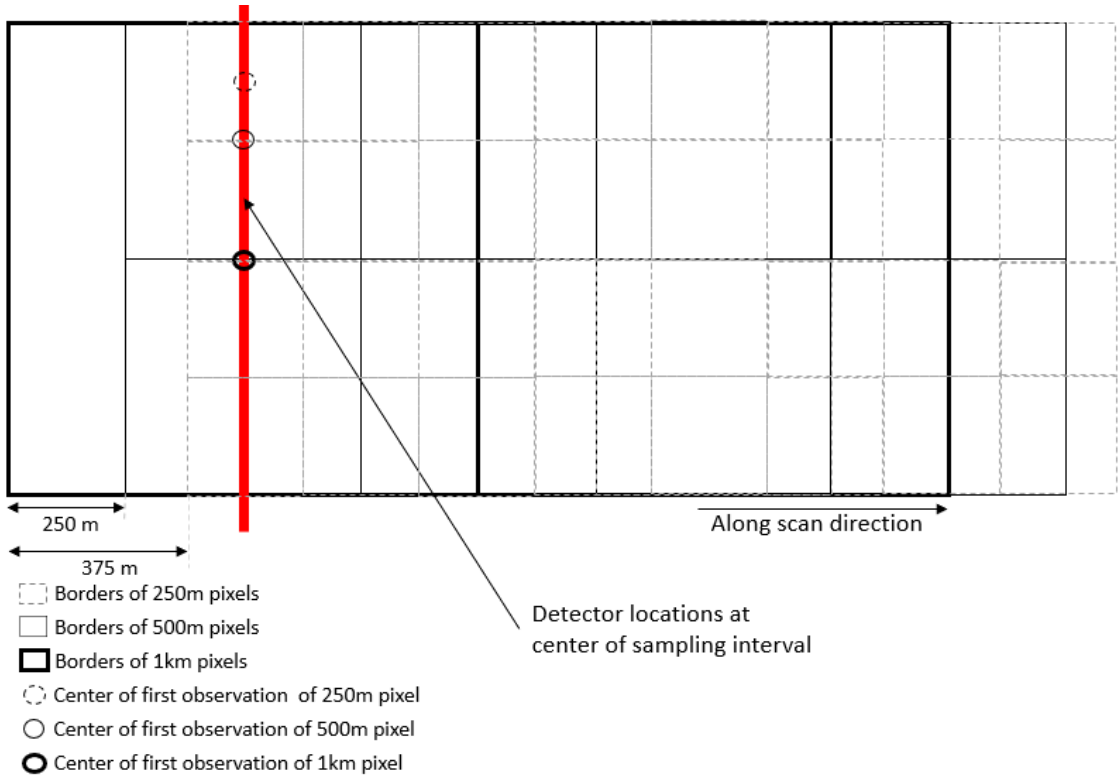

***Figure B.5**: Detector along-scan triangular point spread function and the peak-to-peak alignment of the three MODIS spatial resolutions*

B.3 Triangular Point Spread Function

During the MODIS satellite sensor operation, the constant scan speed of the mirror along the scan direction causes integration of the signal from the adjacent preceding and following neighbor pixels, with the signal being collected from the center pixel (75%) and

from each of its neighbors (12.5%), leading to the triangular Point Spread Function (PSF) [9]. The surface area contributing to a MODIS observation is always larger than the pixel size, even at nadir, due to the triangular PSF in the along scan direction. In the best possible situation, or when the grid cell coincides exactly with its nominal observation, the area covered by a grid cell contributes 75% of the signal to the observation assigned to it, as illustrated by Nishihama et al., 1997 [10] in Figure B.6. [10].

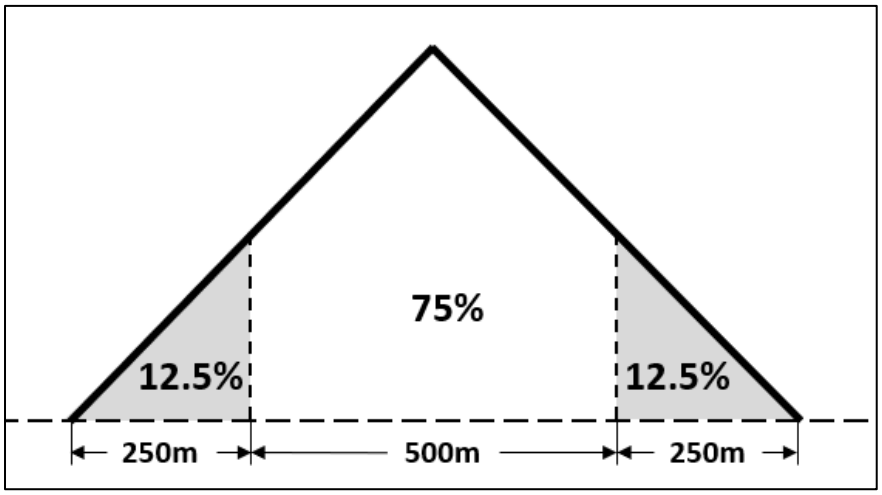

Figure B.6*: Sensor triangular PSF (example at 500 m resolution) which better models that of MODIS, in which nominal observation area contributes 75% of the actual observation (Nishihama et al., 1997, Figure 2-6)*

The registration of 250 m, 500 m, and 1 km MODIS observations in the along-scan direction illustrated by Nishihama et al., 1997 [10] is shown in Figure B.7. A single 1 km observation covers the same area as three 500 m observations and seven 250 m observations. When aggregating 500 m resolution data to 1 km, two 500 m observations in the along-scan direction are not enough because they cover a smaller area than a 1 km observation [10].

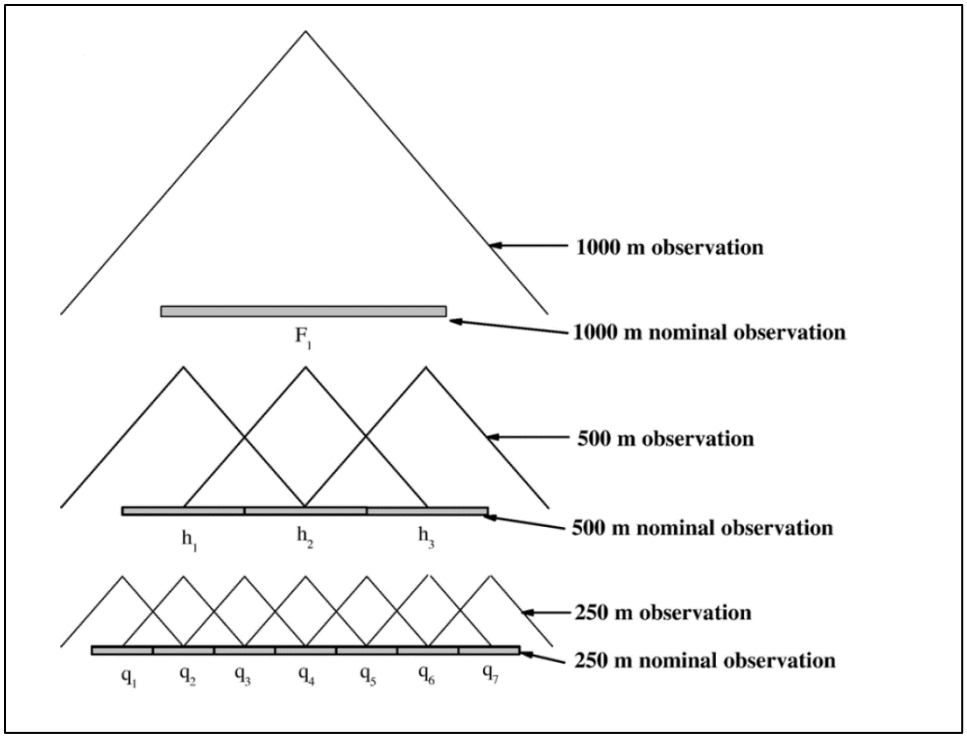

Figure B.7*: Registration of 250 m, 500 m, and 1 km MODIS observations showing the PSFs of various resolutions of MODIS data observation (B. Tan et al., 2006 fig.4a)*

In the track direction, the point spread function is rectangular and the observations at the different resolutions are nested, allowing four rows of 250m observations and two rows of 500m observations to cover the same areas as one row of 1km observations [4]. Due to the nature of the triangular point spread function in the along scan direction an error in spatial accuracy is introduced in the sensor pixel observation value while scanning the earth's surface. Further complicating the matter due to the triangular PSF is the effect of pixel growth at increasing view zenith angles (θ_v).

B.4 View Zenith Angle

MODIS is a paddle broom (sometimes called a whiskbroom) electro-optical instrument that uses the forward motion of the satellite to provide the along-track direction of scan [4].

The across-track scan angle of MODIS ranges from 0 to 55 degrees. One MODIS scan line is composed of 1354 observations at 1 km, 2708 at 500 m, and 5416 at 250 m [4]. The curvature of the earth elongates the scan line to approximately 2340 km and makes the θ_v larger than the scan angle. The θ_v is the angle at the ground position between a ray pointing toward the sensor and one pointing toward the zenith [9]. At the end of a scan line, θ_v can be as large as 65 degrees [4]. The scan angle is related to the larger θ_v by the expression

$$\theta_v = \arcsin\left(\left(\frac{\mathrm{R+H}}{\mathrm{R}}\right)\sin(scan\ angle)\right) \quad (1)$$

where R is the Earth's radius and H is the satellite's altitude, for a spherical Earth model [11].

In an image from a MODIS satellite, not all image pixels cover the same area of the earth's surface. Since the satellite sensor scans the earth's surface at different angles, the pixels around the center of the image with less θ_v cover approximately the same area of the earth's surface as that of a pixel. As the θ_v of the satellite sensor increases as it scans farther from the center of the image, sensor pixels start to represent more earth surface area than the area of a pixel at nadir, as illustrated by Peng et al., 2015 [12] in Figure B.8. The observation footprint grows in size with the scan angle.

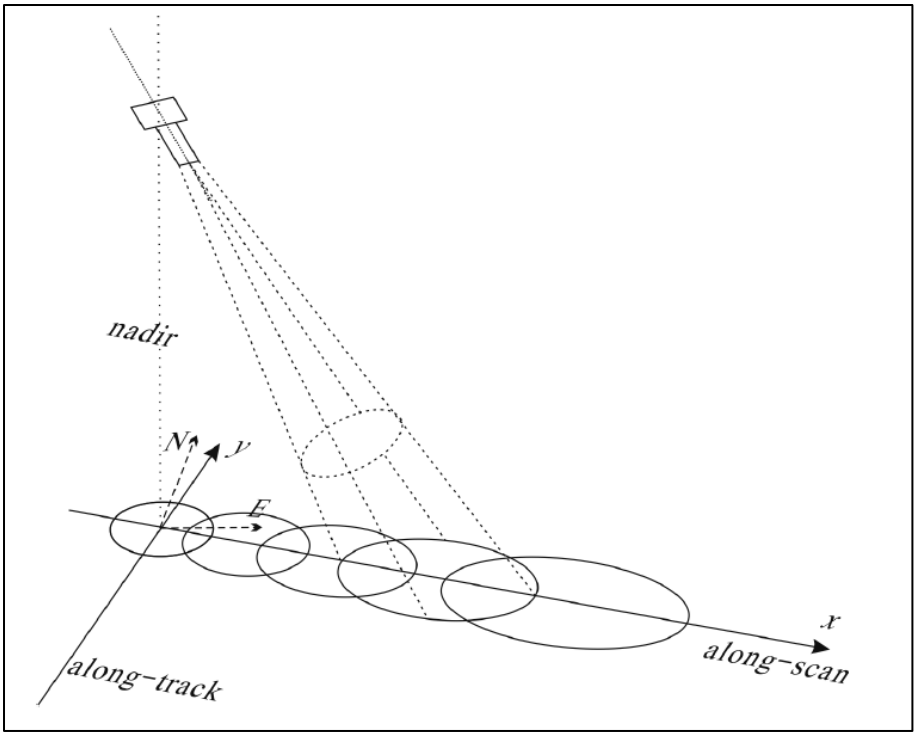

***Figure B.8**: Satellite sensor pixels covering more earth surface area with increasing view zenith angle (θ_v) (Peng et al, 2015, Figure 4)*

Along-track and along-scan dimension of MODIS 1 km observation footprint (earth surface coverage) as a function of θ_v (as illustrated by Wolfe et al., 1998 [4]) is shown in Figure B.9.

B.5 Bowtie Effect

The increase in observation dimension with increasing θ_v leads to overlapping observations toward the edge of the scan, a behavior referred to as the bow-tie effect [11]. The typical coverage of three consecutive scans on the earth's surface as illustrated by Wolfe et al., 1998 [4] is shown in Figure B.10. The whiskbroom configuration and the forward velocity of the satellite are configured such that the leading edge of one scan will

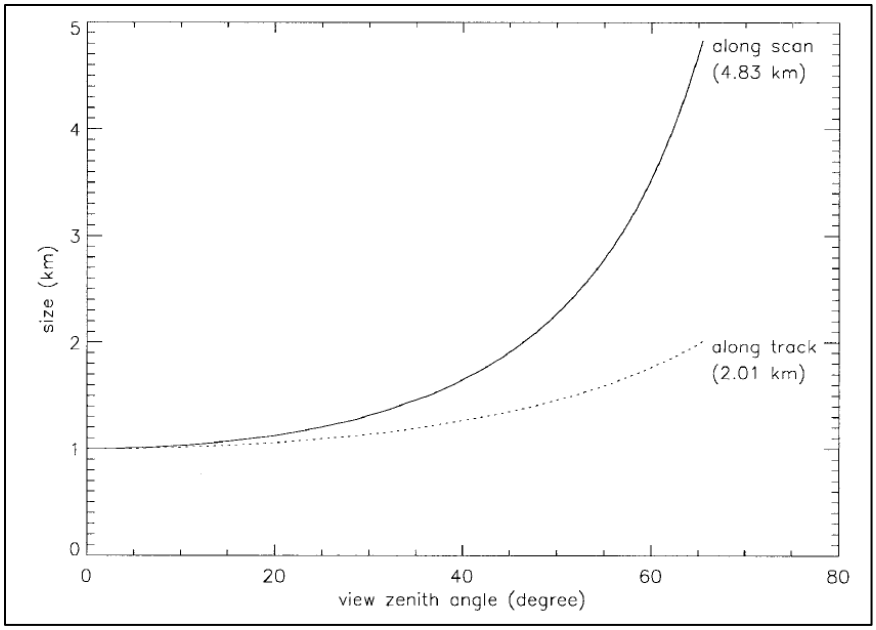

***Figure B.9**: Pixel observation dimension as a function of view zenith angle (θ_v) (Wolfe et al., 1998, Figure 2a)*

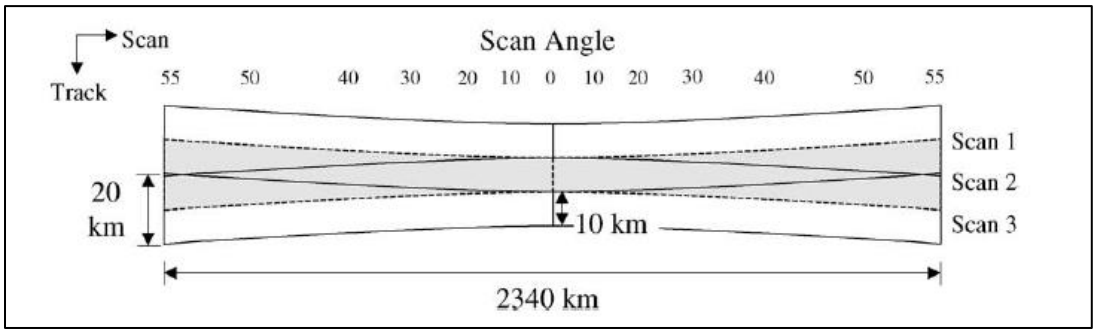

***Figure B.10**: Three consecutive MODIS scans showing the "bowtie" effect (scan 2 is shaded) (Wolfe, 1998, Figure 2b)*

start to overlap the trailing edge of the next scan (10% overlap) at scan angles greater than 24º from nadir. This overlap increases until at the scan edge there is almost 50% overlap [13].

The wide field of view and high temporal frequency of MODIS provide nearly daily global coverage. However, this coverage comes at the cost of spatial resolution due to

known effects of pixel growth at increasing θ_v. Further complicating the matter of variable viewing geometry is the application of a fixed grid for the geolocation of MODIS observations [11]. The increasing observation dimensions lead to two effects in MODIS data; the bowtie effect and the effect of an individual sensor observation grid covering several adjacent grid cells at high θ_v, degrading the quality of MODIS data at high θ_v [4,10,14].

B.6 MODIS Data Products

As θ_v of a satellite sensor increases, sensor pixels represent more of the earth's surface area. An observation at any given time and location is the integration of signal from the ground sample footprint based on the viewing geometry, which is assigned to a grid with a fixed pixel size [15]. A relationship between this irregular observation space (dotted line) and the fixed-pixel projected grid space (solid line) illustrated by Montano, 2015 [15] is shown in Figure B.11.

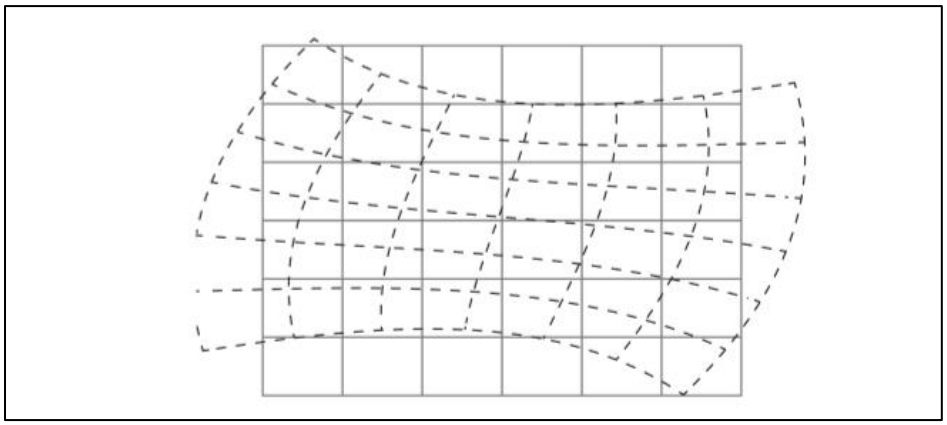

Figure B.11*: Relationship between irregular observation space and fixed-pixel projected grid space (Montano, 2015, Figure 1.1)*

All MODIS data products are written in HDF-EOS, a superset of NCSA's Hierarchical Data Format, which was developed to support the storage and display of data in an instrument swath or in global grids [16]. Earth location and related spatial information are generated as part of the initial processing for each granule of data. This information is needed to understand the location and viewing geometry for the individual elements of every Level 1 and 2 products [16]. The procedure for handling MODIS satellite images includes downloading MODIS products from the NASA FTP site in HDF format, and projecting image bands using tools provided by NASA. The MODIS team provides data to users in two formats; MODIS Swath data (Level 1 and Level 2 products) and MODIS gridded data (Level 2 gridded and Level 3 products).

B.6.1 MODIS Swath Data

MODIS Swath data are the satellite image snapshots in different locations at 5 minute intervals, as the TERRA and AQUA satellites revolve around the earth's surface. Satellite data must be geometrically corrected to remove geometric distortions caused by the instrument viewing geometry, the curvature of the earth, surface relief, and perturbations in the motion of the instrument relative to the surface. The geometric correction process reconstructs remotely sensed data into a new image grid with known earth-based coordinates that may be navigated like a map. Geometric correction can be considered a two-stage process. First, the sensed image observations are geolocated, and then secondly, the geolocated observations are gridded into an output grid [4].

It is very important to understand the process of how the ModisSwath Tool handles MODIS images and re-projects them for the purpose of geo-location accuracy. The pixel

orientation of a re-projected image is never the same as the pixel orientation of a satellite image, and the pixel value of a re-projected image could be different depending on the resampling technique (Nearest Neighbor, Cubic Convolution, Bi-Linear, etc.) assigned by the user.

Swath image granule products (Swath image data) offered by NASA can be processed with the ModisSwath Tool developed by NASA where it transforms Level 1 and Level 2 products from a swath format to a uniformly gridded image that is geographically referenced according to the user's preference. The ModisSwath Tool accepts MODIS products with different band data and geo-location files (in 1000m spatial resolution) as inputs, conforms to the user's setting of image re-projection, image resampling technique, and bounding co-ordinates for the subset of the entire image; and provides re-projected MODIS images for application. Figure B.12 shows a screenshot of the ModisSwath Tool Graphic User Interface (GUI) [17].

Some of the important features and options of the ModisSwath Tool that users should consider while re-projecting a MODIS image are:

Spectral Subsetting: After the MODIS data are uploaded into the ModisSwath Tool GUI, it provides the option to either re-project only selected bands or all of the available bands. To exclude certain bands from processing, bands may be manually deselected. In the example shown in Figure B.13, 2 (LST and QC) of the 7 available bands will be processed.

Spatial Subsetting: Unless otherwise specified, ModisSwath will project the entire input file. Users have the option to override this default and extract spatial subsets from any input swath. Spatial information is entered in the bottom third of the source panel. Users can

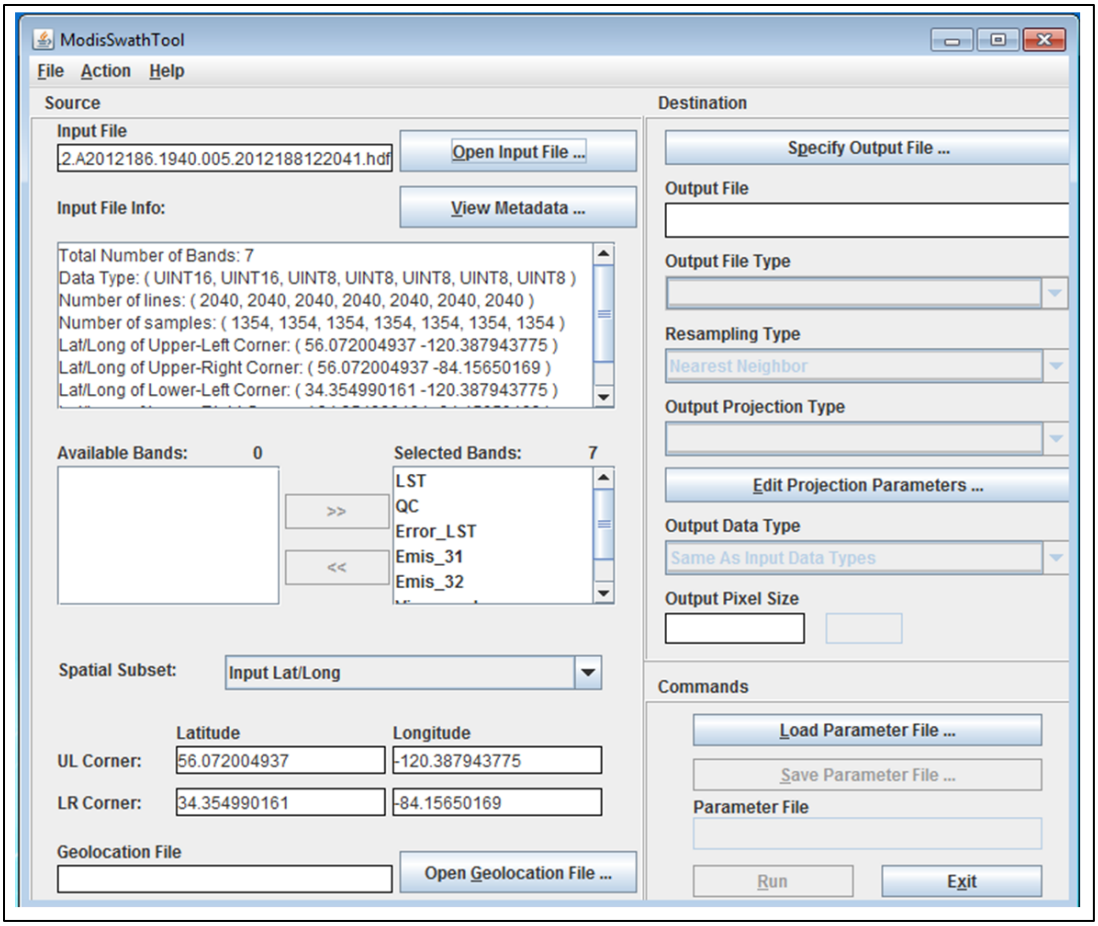

***Figure B.12**: ModisSwath Tool Graphic User Interface*

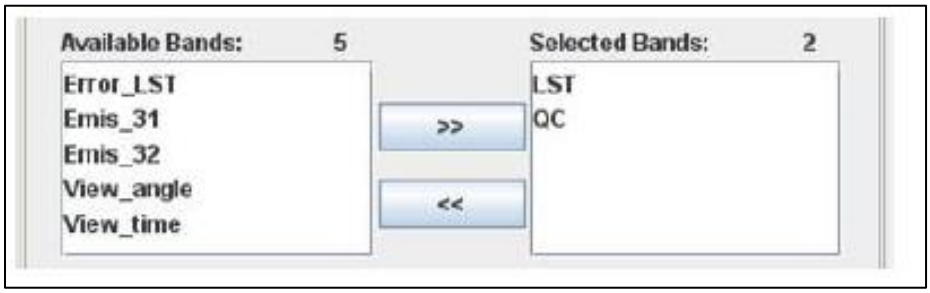

***Figure B.13**: Step of selecting bands for re-projection*

define subset corner points either in input or output space by selecting Input Lat/Long, Input Line/sample, or Output Projection X/Y from the Spatial Subset drop-down as shown in Figure B.14.

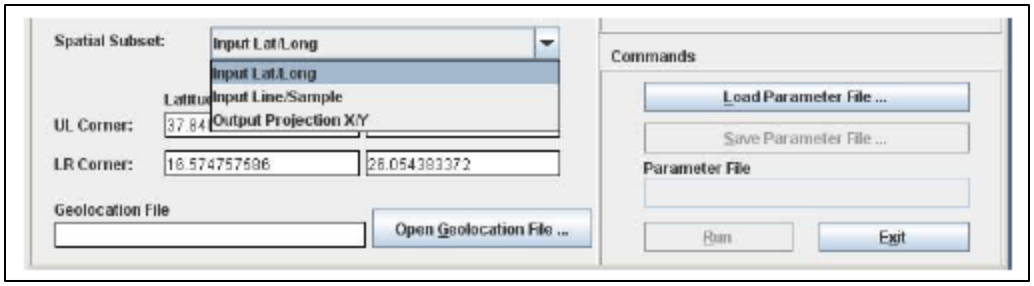

***Figure B.14**: Steps for spatial subsetting*

UL Corner and LR Corner co-ordinate fields can be edited to specify an area (spatial subset). If the Spatial Subset type is set to Input Lat/Long, corner points must be entered in decimal degrees. When creating a subset based on Output Projection X/Y, these coordinates must be specified in the same units used for the projection (i.e., decimal degrees for Geographic and meters for all other projections).

Resampling Option: The MRTSwath Tool offers three resampling methods; nearest neighbor, bilinear, and cubic convolution as shown in Figure B.15.

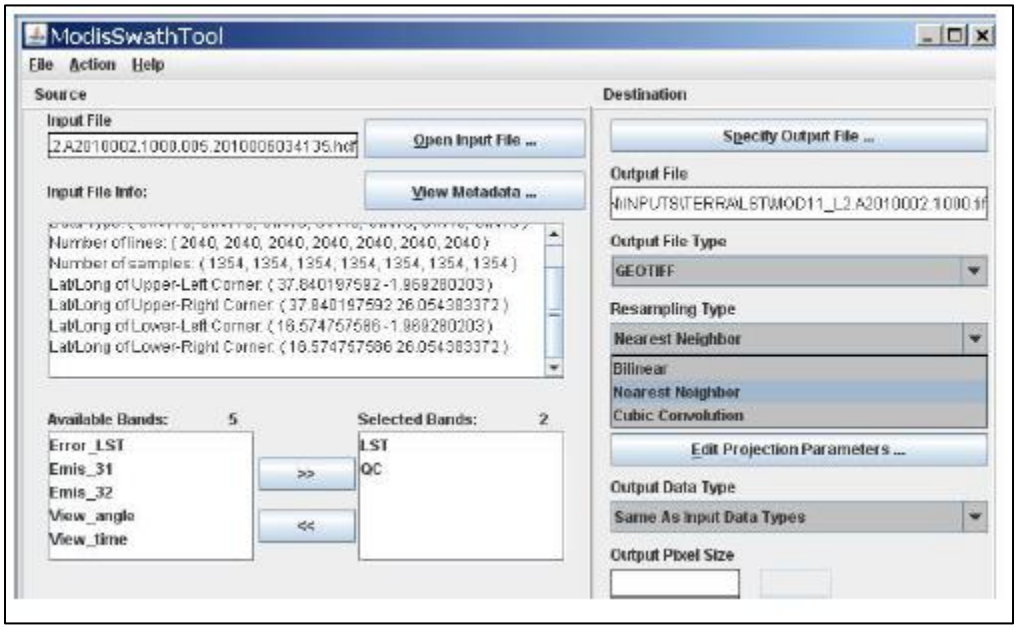

***Figure B.15**: Step for selecting resampling option*

Nearest-Neighbor (NN) resampling is the simplest resampling method and works by allocating the value of the nearest observation to the grid cell. NN resampling is computationally simple and does not alter the values of the original sensed data. It may, however, introduce subpixel geometric discontinuities (up to a maximum of $\frac{\sqrt{2}}{2}$ of an observation dimension) and ignore some observations completely if the resolution of sampling points is lower than the resolution of the original data [18-20]. Other resampling methods alter the radiometric values of the original sensed data.

Output Pixel Size : The Output Pixel Size of a re-projected image can be specified to either down-scale or up-scale from the pixel size of the original MODIS image. If the pixel size is not specified, the output pixel size of the re-projected image remains the same as the corresponding input pixel size of the MODIS image. The input pixel size of any given swath is not likely to be exactly as advertised. For example, 250 m products actually contain 231.7 m pixels; 500 m products have 463.3 m pixels; and 1,000 m products have 926.6 m pixels. Figure B.16 illustrates the geometric orientation of a MODIS satellite sensor pixel grid and the grid orientation of the output image re-projected using the ModisSwath tool.

B.6.2 MODIS Gridded Data

The MODIS sensor simultaneously senses 10 rows of 1000 m detector pixels, 20 rows of 500 m detector pixels, and 40 rows of 250 m detector pixels as the scan mirror sweeps across the track. Sensor output consist of progressively overlapping observations farther from nadir as the θ_v of satellite sensor increases [4]. The allocation of geolocated image

observations to an output image grid are termed gridding and the pixels defined by the output image grid are referred to as grid cells [4]. Coordinates of the grid cells are predefined by specifying the cell dimensions and the origin and orientation of the grid cells, globally. In contrast to Level 1 and 2 MODIS swath data that are stored as granules, gridded MODIS products are stored as tiles which are gridded and stored as fixed, non-overlapping, earth-located tiles [4]. Gridded MODIS products are projected onto the Sinusoidal 10-degree grid, where the globe is divided for production and distribution purposes into 36 tiles along the east-west axis, and 18 tiles along the north-south axis, each approximately 1200 by 1200 km [10]. Figure B.17 shows the earth divided into different fixed tiles where higher levels of MODIS products are stored.

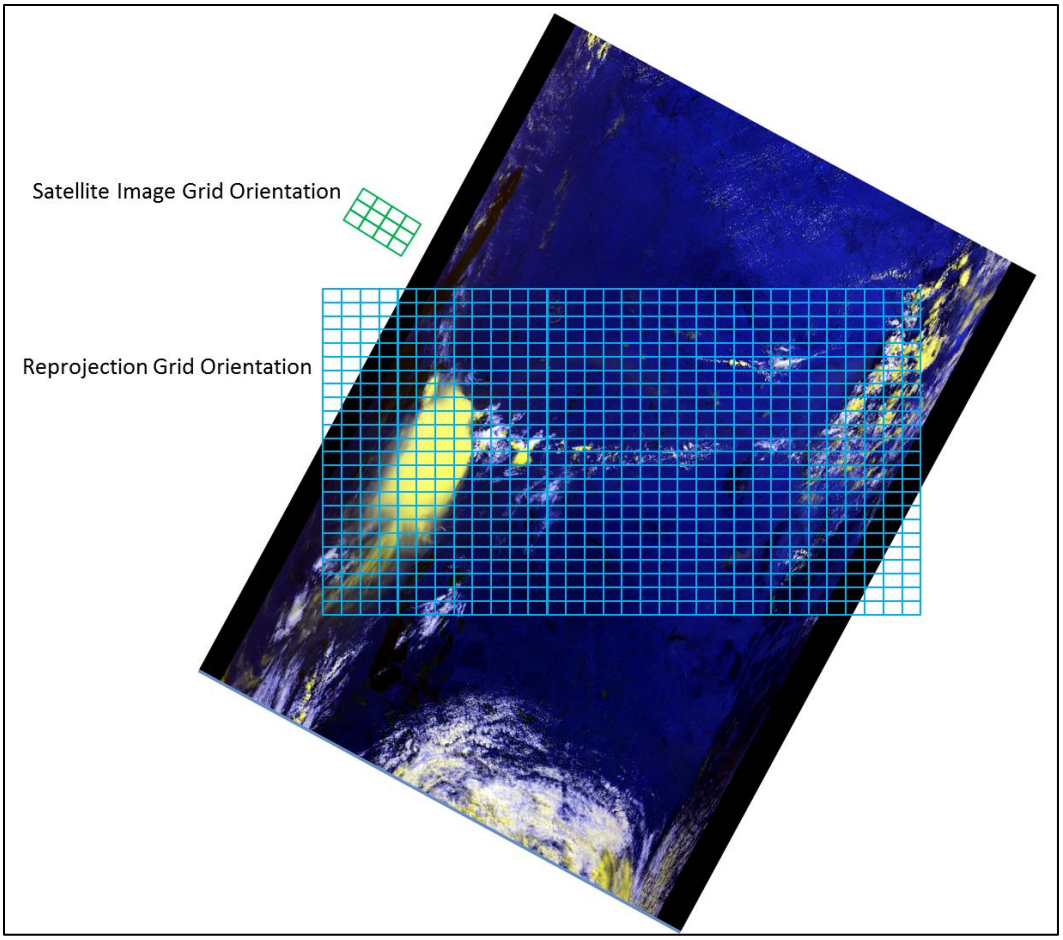

***Figure B.16**: Geometric orientation of satellite sensor grid and re-projected output image grid*

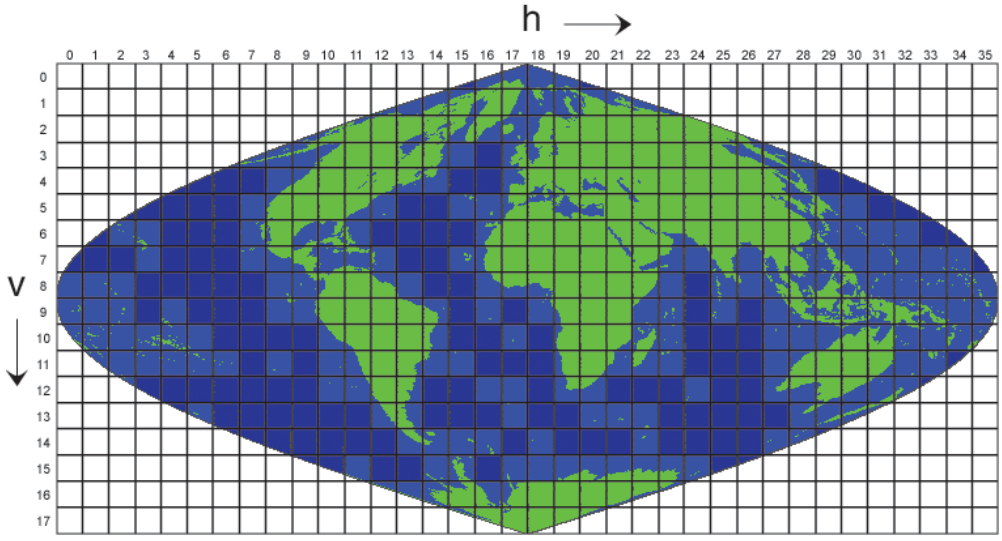

***Figure B.17**: MODIS gridded tiles covering the earth's surface*

There are two methods of storing remotely sensed data in gridded format; the simple and complex method. Grid cells are assigned a remotely sensed data value based on the percentage area of the observation that falls within the grid cell. In the simple method all of the observations that fall in a fixed grid cell are ranked based on the percentage of the area of observation that falls within the grid and are stored in the grid cell using the Nearest Neighbor sampling method [4]. The overlapping of an observation in a fixed grid cell as illustrated by Wolfe et al., 1998 [4] is shown in Figure B.18.

In the complex method a final observation value for a grid cell is calculated by weighting all observations that overlap with the grid cell. Observations are weighted according to the percentage of area of the observation that falls within the grid cell [10].

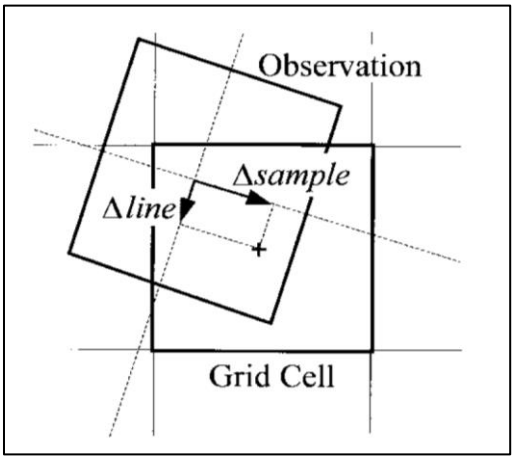

Figure B.18*: Overlapping of an observation in a fixed grid cell (Wolfe et al., 1998, Figure 5)*

The availability of MODIS data is reduced by the presence of clouds and atmospheric contamination, and a common approach to remove or reduce such problems is to composite image data from multiple days into a single dataset [21,22]. The compositing procedures are applied to a time series of image data to produce a single representative data set.

MODIS gridded products are composited to create 8-day, 16-day, and 32-day products. They either select the “best” observation of a grid cell based on some criteria or combine multiple observations of the same grid cell. Compositing criteria have included the maximum NDVI, maximum brightness temperature, maximum surface temperature, minimum difference in red and near-infrared reflectance, minimum scan angle, maximum. thermal radiance, and combinations of these [21,23-26]. The criteria are designed to ideally select from the time series only near-nadir observations that have reduced cloud and atmospheric contamination [4].

During the process of compositing MODIS data, spectral criteria besides minimum θ_v criteria are used such as Maximum Normalized Difference Vegetation Index (NDVI) and Minimum Blue for its ability to avoid clouds and bad observations [10]. The Minimum θ_v compositing is the best and keeps most of the ground information but other spectral criteria produce artifacts. For example, with Minimum Blue and Maximum NDVI compositing criteria, size of vegetated area increases and small towns in MODIS image disappear or shrink. Similarly, water area shrinks if the water is surrounded by dense vegetation with Maximum NDVI compositing criteria [10]. These artifacts of changing feature boundaries and eliminating small features present in MODIS composite data makes the data unsuitable for fine field scale analysis.

B.7 References

1. Wikipedia. Moderate Resolution Imaging Spectroradiometer, 15 Apr.2015. Available online: https://en.wikipedia.org/wiki/Moderate_Resolution_Imaging_Spectroradiometer. (accessed on Jun. 2, 2015).

2. National Aeronautics and Space Administration. MODIS: Moderate Resolution Imaging Spectroradiometer. Available online: https://modis.gsfc.nasa.gov/about/. (accessed on Jun. 21, 2015).
3. NASA Atmospheric Archive and Distribution System (LAADS). MODIS Level 1B Calibrated Radiances 1km: MOD021KM, 12 Jan. 2012. Available online: https://ladsweb.modaps.eosdis.nasa.gov/missions-and-measurements/products/modis-L0L1/MOD021KM/ . (Accessed on Apr. 12, 2016).
4. Wolfe, R.E.; Nishihama, M.; Fleig, A.J.; Kuyper, J.A.; Roy, D.P.; Storey, J.C.; Patt. F.S. Achieving sub-pixel geolocation accuracy in support of MODIS land science. *Remote Sensing of Environment*. **2002**, 83, 31-49.
5. National Aeronautics and Space Administration. Frequently Asked Questions, 21 Jan. 2012. Available online: https://earthdata.nasa.gov/faq (accessed on Jun. 17, 2015).
6. Joseph, G. How well do we understand Earth observation electro-optical sensor parameters? *ISPRS J. Photogramm. Remote Sens.* **2000**, 55, 9-12.
7. Forshaw, M.R.B.; Haskell, A.; Miller, P.F.; Stanley, D.J.; Townshend, J.R.G. Spatial resolution of remotely sensed imagery a review paper. *Int. J. Remote Sens.* **1983**, 4, 497-520.
8. Wolfe, R.E.; Storey, J.C.; Masuoka, E.; Fleig, A.J. MODIS level 1A earth location algorithm theoretical basis document. *NASA Tech. Memo. Number 104594*. Greenbelt, MD: Goddard Space Flight Center. **1995**, 5.
9. Nishihama, M.; Wolfe, R.E.; Solomon, D.; Patt, F.S; Blanchette, J.; Fleig, A.J; Masuoka, E. MODIS L1A Earth Location Algorithm Theoretical Basis Document. NASA, Greenbelt, MD, USA, Tech. Rep. **1997**.
10. Tan, B.; Woodcock, C.E.; Hu, J.; Zhang, P.; Ozdogan, M.; Huang, D.; Yang, W.; Knyazikhin, Y.; Myneni, R.B. The impact of gridding artifacts on the local spatial properties of MODIS data: Implications for validation, compositing, and band-to-band registration across resolutions. *Remote Sensing of Environment*. **2006**, 105, 98-114.
11. Campagnolo, M.L.; Montano, E.L Estimation of Effective Resolution for Daily MODIS Gridded Surface Reflectance Products. *IEEE Transactions on Geoscience and Remote Sensing*. **2014**, 52, 5622-5632.
12. Peng, J.; Liu, Q.; Wang, L.; Liu, Q.; Fan, W.; Lu, M. Characterizing the Pixel Footprint of satellite Albedo Products Derived from MODIS Reflectance in the Heihe River Basin, China. *Remote Sensing.* **2015**, 7, 6886-6907.
13. R. A. Schowengerdt, *Remote Sensing Models and Methods for Image Processing*. San Diego, CA: Academic, 1997.
14. Justice, C.O.; Townshend, J.R.G.; Vermote, E.F.; Wolfe, R.E.; Saleous, N. An overview of MODIS land data processing and product status. *Remote Sensing of Environment*. **2002**, 83, 3-15.
15. Montano, E.L. *Impact of Satellite Geometric Distortions on Landscape Analysis: Effects on Albedo*. Diss. University of Maryland, 2015. Web. 6 May 2016.
16. Masuoka, E.; Fleig, A.; Wolfe, R.E.; Patt, F. Key Characteristics of MODIS Data Products. *IEEE Transactions on Geoscience and Remote Sensing*. **1998**, 36, 1313-1323.

17. Land Processes Distributed Active Archive Center. MODIS Reprojection Tool Swath User Manual, December 2010. Available online: https://lpdaac.usgs.gov/sites/default/files/public/MRTSwath_Users_Manual_2.2_Dec2010.pdf (accessed on Aug. 4, 2011).
18. Keys, R.G. Cubic convolution interpolation for digital image processing. *IEEE Trans. Acoust., Speech, Signal Processing*. **1981**, 29, 1153-1160.
19. Park, S.K.; Schowengerdt, R.A. Image reconstruction by parametric cubic convolution. *Comput. Vision, Graph. Image Processing*. **1983**, 23, 258-272.
20. Khan, B.; Hayes, L.W.B.; Cracknell, A.P. The effects of higher order resampling on AVHRR data. *Int. J. Remote Sensing*. **1995**, 16, 147-163.
21. Holben, B.N. Characteristics of maximum-value composite images for temporal AVHRR data. *International Journal of Remote Sensing*. **1986**, 7, 1435-1445.
22. Los, S.O.; Justice, C.O.; Tucker, C.J. A global 1o by 1o NDVI data set for climate studies derived from GIMMS continental NDVI data. *International Journal of Remote Sensing*. **1994**, 15, 3493-3518.
23. Choudhury, B.J.; Digirolamo, N.E.; Dorman, T.J. A comparison of reflectances and vegetation indices from three methods of compositing the AVHRR-GAC data over Northern Africa. *Remote Sens. Rev.* **1994**, 10, 245-263.
24. Cihlar, J.; Manak, D.; D'Iorio, M. Evaluation of compositing algorithms for AVHRR data over land. *IEEE Trans. Geosci. Remote Sensing*. **1994**, 32, 4427-4437.
25. Roy, D.P. Investigation of the maximum normalized difference vegetation index (NDVI) and the maximum surface temperature (Ts) AVHRR compositing procedures for the extraction of NDVI and Ts over forest. *Int. J. Remote Sensing*. **1997**, 18, 2383-2401.
26. Stoms, D.M.; Bueno, M.J.; David, F.W. Viewing geometry of AVHRR image composites derived using multiple criteria. *Photogramm. Eng. Remote Sensing*, **1997**, 63, 681-689.

APPENDIX C: MODIS ESTIMATED AND GROUND TRUTH DATA

Table C.1: *LAI values for center pivot maize field US-Ne1 determined from MODIS data and field samples.*

Date	Cum. Growing Degree Days	Footprint	Gridded	Ground truth
2-May-12	24			0.000
5-May-12	66	0.659	0.412	
10-May-12	100	0.226	0.227	0.023
14-May-12	127	0.264	0.375	
16-May-12	147	0.272	0.455	
18-May-12	173			0.111
21-May-12	200	0.522	0.569	
24-May-12	233			0.253
31-May-12	294			0.879
2-Jun-12	307	1.465	1.520	
4-Jun-12	334	1.625	1.854	
11-Jun-12	421	3.332	3.874	1.792
18-Jun-12	505	3.882	5.757	
20-Jun-12	533			3.151
22-Jun-12	554	6.500	6.226	
24-Jun-12	582	6.269	5.941	
27-Jun-12	629	5.762	6.401	3.072
3-Jul-12	723	5.367	5.343	
4-Jul-12	739	5.014	5.570	
5-Jul-12	756			3.940
6-Jul-12	772	6.249	6.397	
10-Jul-12	828	6.500	6.500	
12-Jul-12	854			4.904
13-Jul-12	869	6.070	5.408	
17-Jul-12	927	6.469	6.326	
19-Jul-12	959	6.349	5.787	
20-Jul-12	974	6.001	6.094	4.430
22-Jul-12	1004	6.350	5.953	
24-Jul-12	1036	6.500	6.323	
26-Jul-12	1069	6.282	5.557	4.324
29-Jul-12	1110	6.277	6.419	
2-Aug-12	1170	6.500	6.500	
4-Aug-12	1196	5.697	5.258	
5-Aug-12	1207	2.323	6.101	
6-Aug-12	1219			3.938
9-Aug-12	1261	5.533	4.605	
15-Aug-12	1321			4.032
20-Aug-12	1361	4.807	3.622	
21-Aug-12	1372	1.430	3.052	
27-Aug-12	1445	3.225	2.207	
28-Aug-12	1457			3.377
30-Aug-12	1484	2.290	1.632	
5-Sep-12	1562	1.181	0.897	
6-Sep-12	1572	0.982	0.940	
8-Sep-12	1589	1.385	1.449	
10-Sep-12	1606	1.288	1.249	
15-Sep-12	1646	0.831	1.088	
22-Sep-12	1692	0.588	0.661	
21-Oct-12	1833	0.257	0.300	

Table C.2: *LAI values for center pivot maize field US-Ne2 determined from MODIS data and field samples.*

Date	Cum. Growing Degree Days	Footprint	Gridded	Ground truth
5-May-12	66	0.724	0.260	
10-May-12	100	0.376	0.167	0.022
14-May-12	127	0.679	0.271	
16-May-12	147	0.248	0.232	
18-May-12	173			0.138
21-May-12	200	0.737	0.474	
25-May-12	240			0.383
2-Jun-12	307	1.228	1.341	
4-Jun-12	334	1.844	1.725	1.365
11-Jun-12	421	2.069	3.815	
12-Jun-12	429			1.890
18-Jun-12	505	3.775	5.687	
19-Jun-12	522			2.950
22-Jun-12	554	6.500	6.124	
24-Jun-12	582	5.860	5.910	
26-Jun-12	611			3.517
27-Jun-12	629	5.139	6.470	
3-Jul-12	723	5.041	5.409	3.559
4-Jul-12	739	5.460	5.844	
6-Jul-12	772	6.155	6.500	
10-Jul-12	828	6.190	6.500	4.733
13-Jul-12	869	5.968	6.080	
17-Jul-12	927	5.912	6.269	
18-Jul-12	943			4.972
19-Jul-12	959	6.032	6.338	
20-Jul-12	974	5.987	5.960	
22-Jul-12	1004	5.572	6.012	
24-Jul-12	1036	5.354	6.493	
25-Jul-12	1053			5.067
26-Jul-12	1069	6.377	6.366	
29-Jul-12	1110	3.577	6.234	
2-Aug-12	1170	5.867	6.497	4.872
4-Aug-12	1196	4.814	5.223	
5-Aug-12	1207	3.577	5.793	
9-Aug-12	1261	4.982	5.608	
13-Aug-12	1300			4.454
20-Aug-12	1361	4.020	4.607	
21-Aug-12	1372	1.462	3.800	
23-Aug-12	1397			3.762
27-Aug-12	1445	3.080	3.189	
30-Aug-12	1484	2.292	2.349	
5-Sep-12	1562	1.294	1.288	
6-Sep-12	1572	1.145	1.313	
8-Sep-12	1589	1.376	1.542	
10-Sep-12	1606	1.501	1.680	
11-Sep-12	1618			2.998
15-Sep-12	1646	0.754	0.704	
22-Sep-12	1692	0.507	0.526	
21-Oct-12	1833	0.249	0.242	

***Table C.3**: LAI values for center pivot maize field US-Ne1 determined from MODIS data and field samples*

Date	Cum. Growing Degree Days	Footprint	Gridded	Ground truth
2-May-12	24			0.000
5-May-12	66	0.391	0.243	
10-May-12	100	0.114	0.115	0.023
14-May-12	127	0.143	0.220	
16-May-12	147	0.149	0.271	
18-May-12	173			0.111
21-May-12	200	0.312	0.340	
24-May-12	233			0.253
31-May-12	294			0.879
2-Jun-12	307	0.786	0.811	
4-Jun-12	334	0.857	0.955	
11-Jun-12	421	1.574	1.809	1.792
18-Jun-12	505	1.813	2.777	
20-Jun-12	533			3.151
22-Jun-12	554	3.293	3.088	
24-Jun-12	582	3.119	2.894	
27-Jun-12	629	2.780	3.216	3.072
3-Jul-12	723	2.547	2.534	
4-Jul-12	739	2.356	2.664	
5-Jul-12	756			3.940
6-Jul-12	772	3.105	3.214	
10-Jul-12	828	3.293	3.293	
12-Jul-12	854			4.904
13-Jul-12	869	2.980	2.571	
17-Jul-12	927	3.269	3.160	
19-Jul-12	959	3.177	2.796	
20-Jul-12	974	2.933	2.996	4.430
22-Jul-12	1004	3.178	2.902	
24-Jul-12	1036	3.293	3.159	
26-Jul-12	1069	3.129	2.657	4.324
29-Jul-12	1110	3.125	3.230	
2-Aug-12	1170	3.293	3.293	
4-Aug-12	1196	2.740	2.487	
5-Aug-12	1207	1.152	3.001	
6-Aug-12	1219			3.938
9-Aug-12	1261	2.643	2.149	
15-Aug-12	1321			4.032
20-Aug-12	1361	2.250	1.698	
21-Aug-12	1372	0.771	1.456	
27-Aug-12	1445	1.529	1.104	
28-Aug-12	1457			3.377
30-Aug-12	1484	1.139	0.860	
5-Sep-12	1562	0.656	0.518	
6-Sep-12	1572	0.560	0.539	
8-Sep-12	1589	0.750	0.779	
10-Sep-12	1606	0.706	0.688	
15-Sep-12	1646	0.484	0.612	
22-Sep-12	1692	0.351	0.393	
21-Oct-12	1833	0.138	0.169	

***Table C.4**: LAI values for center pivot maize field US-Ne2 determined from MODIS data and field samples*

Date	Cum. Growing Degree Days	Footprint	Gridded	Ground truth
5-May-12	66	0.427	0.139	
10-May-12	100	0.220	0.068	0.022
14-May-12	127	0.402	0.148	
16-May-12	147	0.131	0.119	
18-May-12	173			0.138
21-May-12	200	0.434	0.283	
25-May-12	240			0.383
2-Jun-12	307	0.678	0.730	
4-Jun-12	334	0.951	0.900	1.365
11-Jun-12	421	1.046	1.783	
12-Jun-12	429			1.890
18-Jun-12	505	1.766	2.735	
19-Jun-12	522			2.950
22-Jun-12	554	3.293	3.017	
24-Jun-12	582	2.842	2.874	
26-Jun-12	611			3.517
27-Jun-12	629	2.422	3.270	
3-Jul-12	723	2.370	2.571	3.559
4-Jul-12	739	2.600	2.832	
6-Jul-12	772	3.039	3.293	
10-Jul-12	828	3.063	3.293	4.733
13-Jul-12	869	2.912	2.987	
17-Jul-12	927	2.875	3.119	
18-Jul-12	943			4.972
19-Jul-12	959	2.955	3.170	
20-Jul-12	974	2.924	2.907	
22-Jul-12	1004	2.666	2.941	
24-Jul-12	1036	2.540	3.287	
25-Jul-12	1053			5.067
26-Jul-12	1069	3.198	3.191	
29-Jul-12	1110	1.679	3.094	
2-Aug-12	1170	2.847	3.290	4.872
4-Aug-12	1196	2.253	2.468	
5-Aug-12	1207	1.679	2.800	
9-Aug-12	1261	2.339	2.687	
13-Aug-12	1300			4.454
20-Aug-12	1361	1.875	2.150	
21-Aug-12	1372	0.785	1.776	
23-Aug-12	1397			3.762
27-Aug-12	1445	1.467	1.513	
30-Aug-12	1484	1.139	1.163	
5-Sep-12	1562	0.709	0.706	
6-Sep-12	1572	0.639	0.718	
8-Sep-12	1589	0.746	0.820	
10-Sep-12	1606	0.802	0.881	
11-Sep-12	1618			2.998
15-Sep-12	1646	0.443	0.416	
22-Sep-12	1692	0.303	0.314	
21-Oct-12	1833	0.131	0.126	

APPENDIX D: FIXED GRID CELLS WITH PIXEL CONTAMINATION IN MODIS IMAGES DURING FIELD SCALE ANALYSIS

The figures below show the MODIS fixed grid cells which are well within center pivot fields, but contaminated with pixels that lie mostly or partly outside the center pivot fields. Red lines represent boundaries of fixed grid cells, and black lines represent those of footprint pixels. Red dots show the fixed grid cells that lie well within the fields, and red dots with yellow circles identify the fixed grid cells that are contaminated.

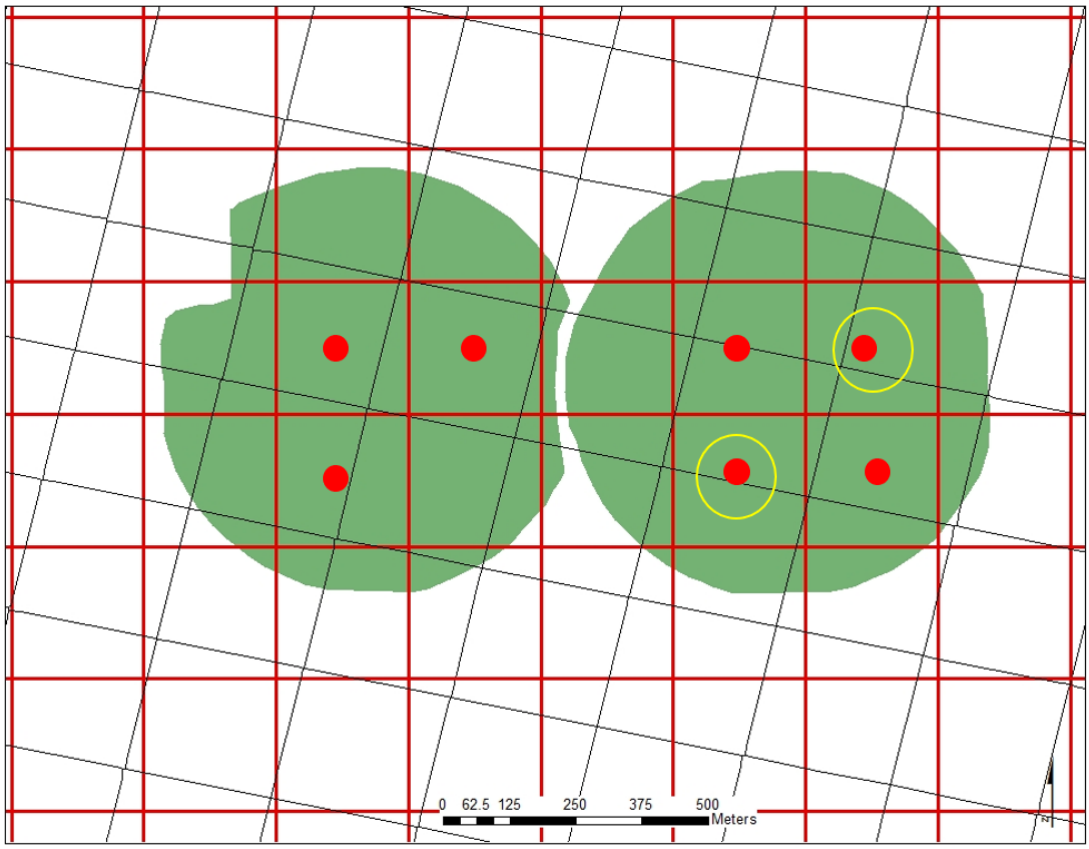

Figure D.1*: Grid cells with contaminated pixels for MODIS image (fields US-Ne1 in left and US-Ne2 in right) from 05/05/12*

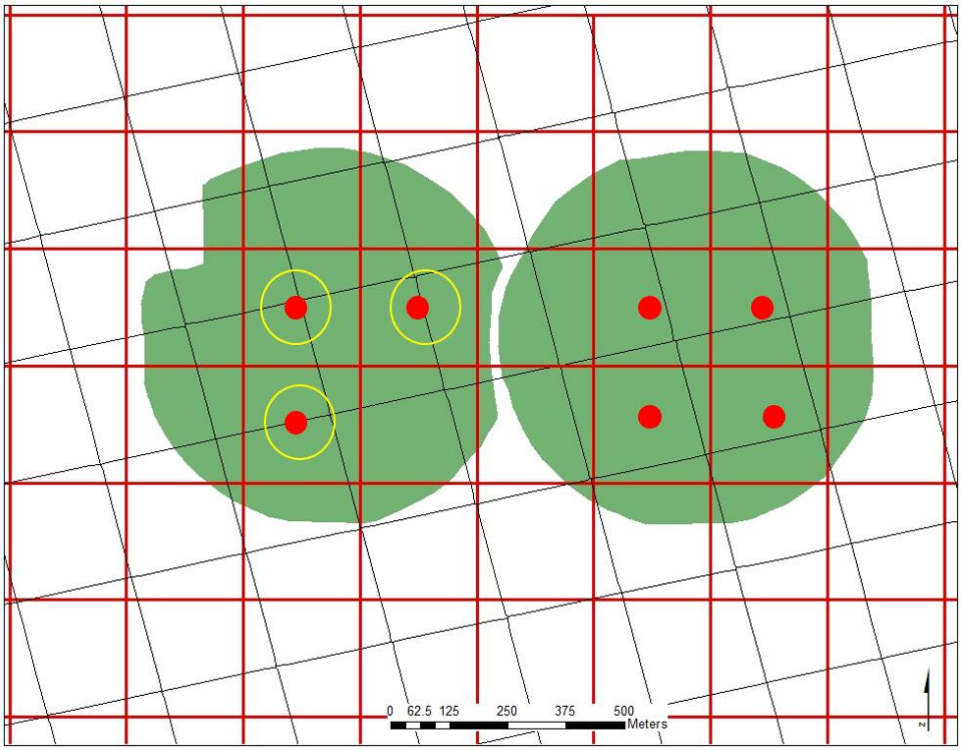

***Figure D.2**: Grid cells with contaminated pixels for MODIS image (fields US-Ne1 in left and US-Ne2 in right) from 05/10/12*

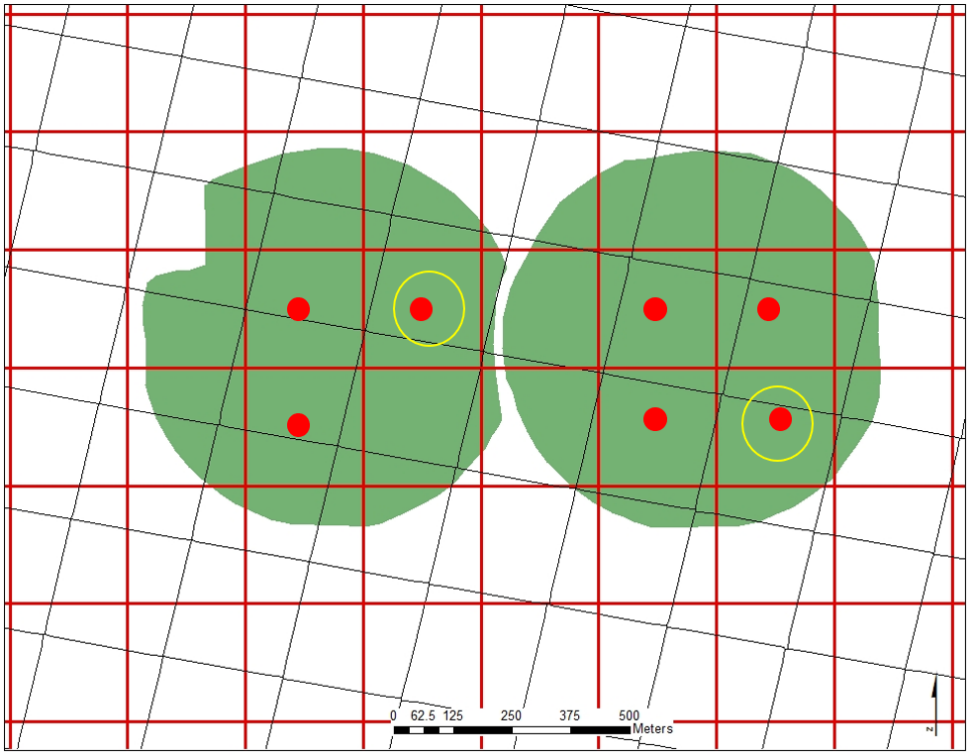

***Figure D.3**: Grid cells with contaminated pixels for MODIS image (fields US-Ne1 in left and US-Ne2 in right) from 05/14/12*

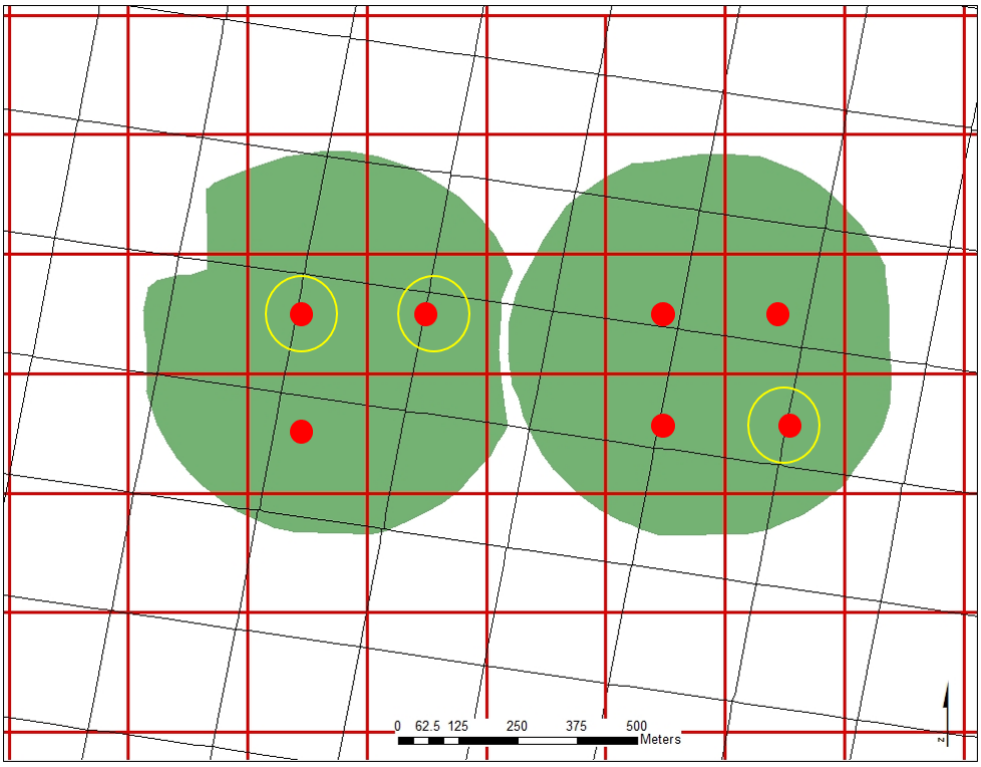

***Figure D.4**: Grid cells with contaminated pixels for MODIS image (fields US-Ne1 in left and US-Ne2 in right) from 05/16/12*

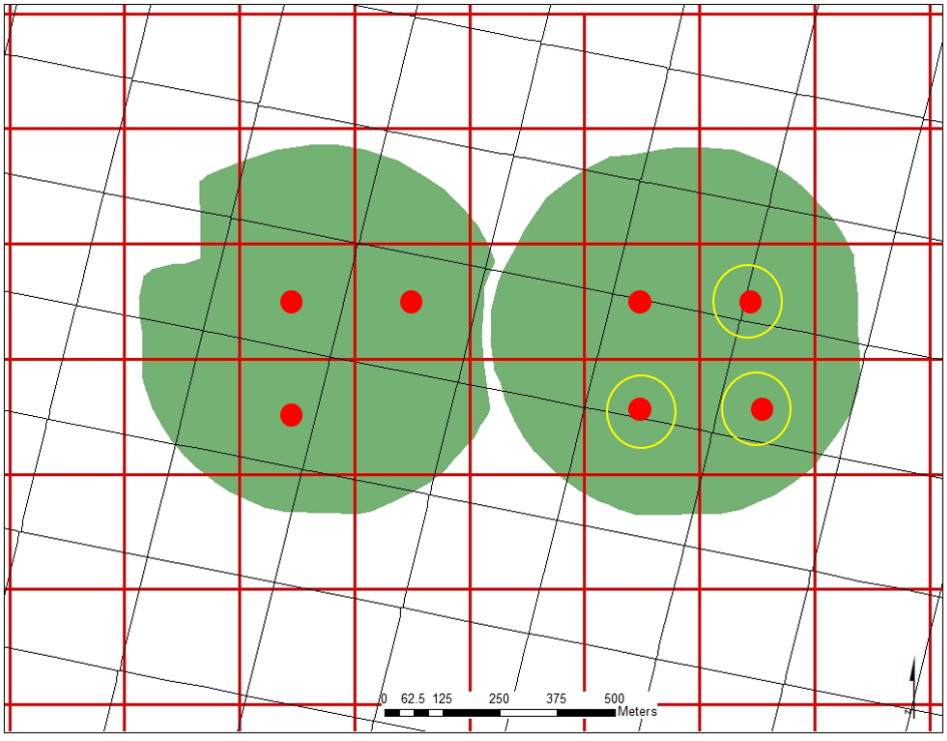

***Figure D.5**: Grid cells with contaminated pixels for MODIS image (fields US-Ne1 in left and US-Ne2 in right) from 05/21/12*

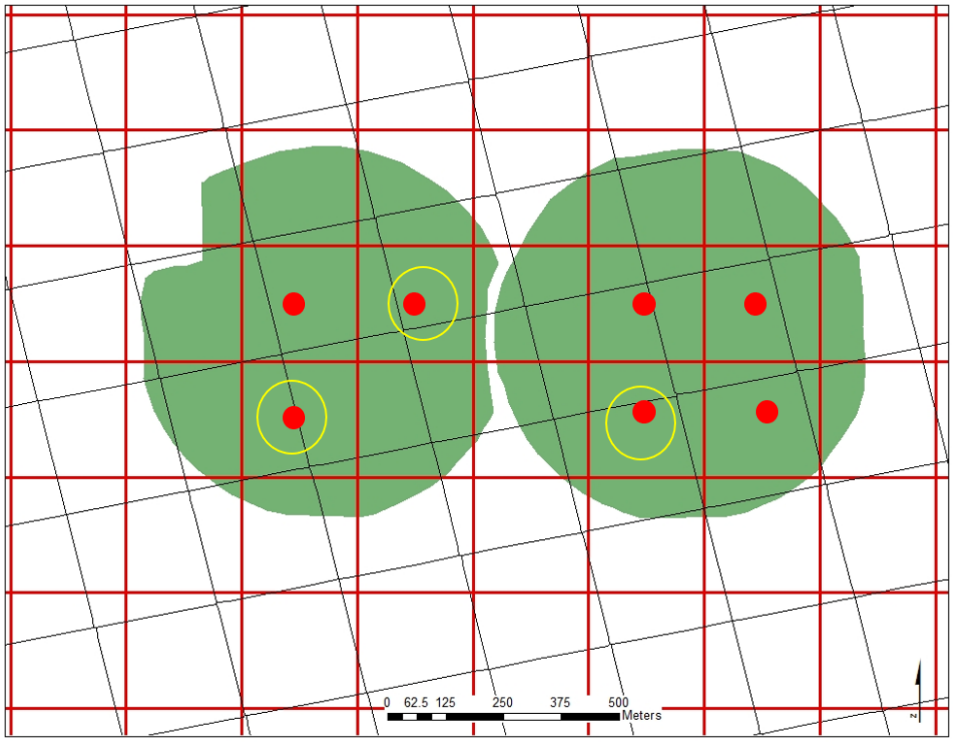

***Figure D.6**: Grid cells with contaminated pixels for MODIS image (fields US-Ne1 in left and US-Ne2 in right) from 06/02/12*

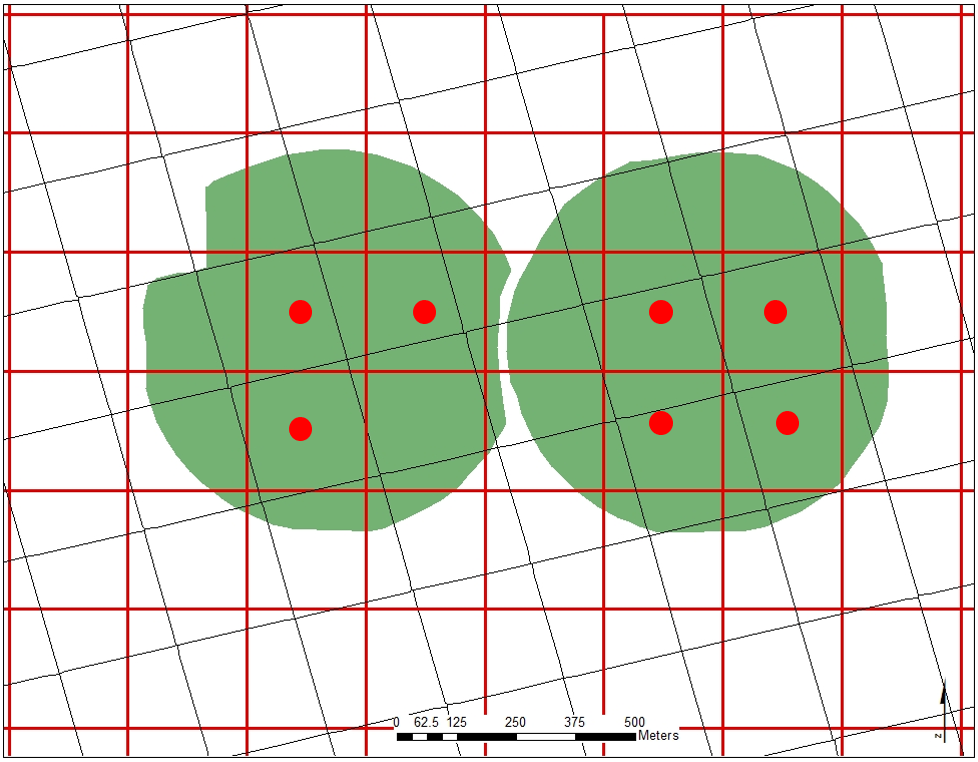

***Figure D.7**: Grid cells with contaminated pixels for MODIS image (fields US-Ne1 in left and US-Ne2 in right) from 06/04/12*

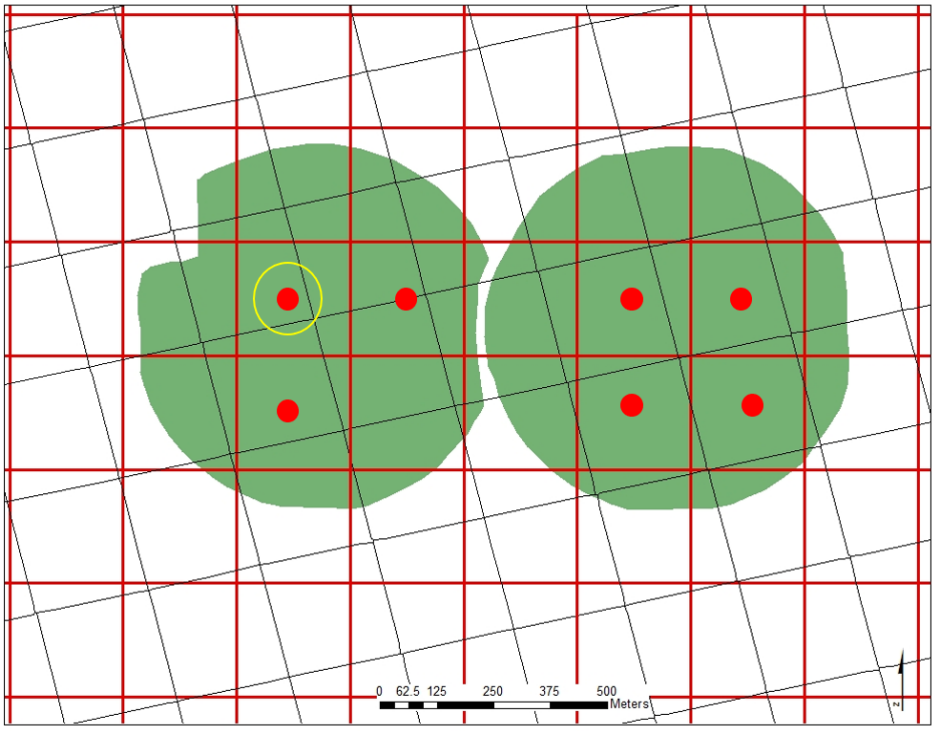

***Figure D.8**: Grid cells with contaminated pixels for MODIS image (fields US-Ne1 in left and US-Ne2 in right) from 06/11/12*

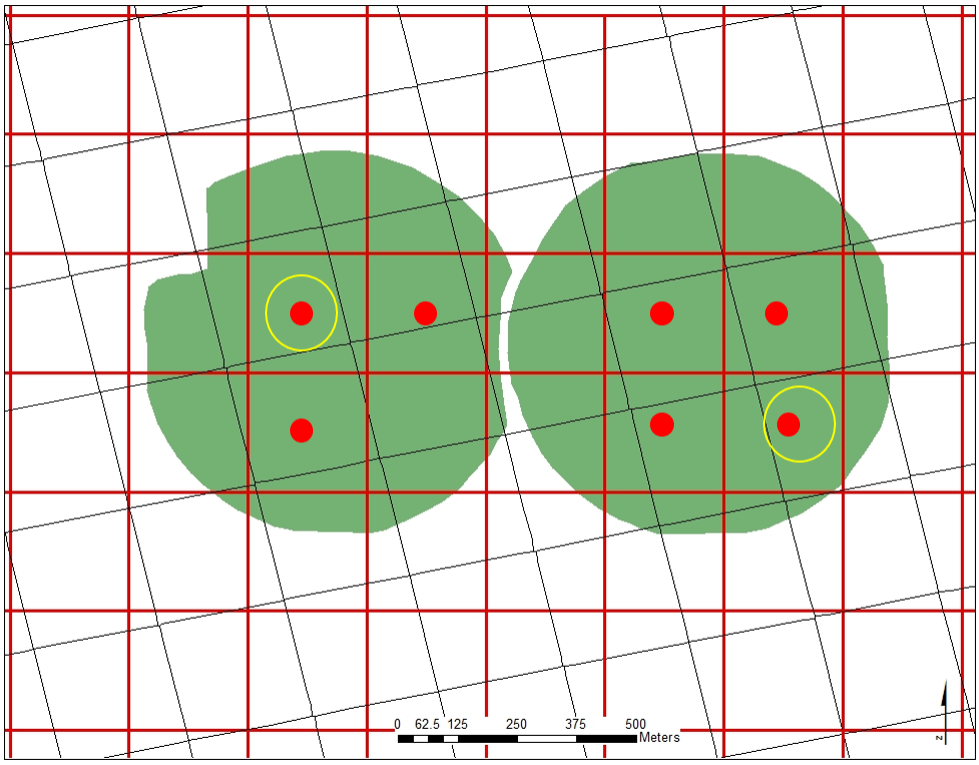

***Figure D.9**: Grid cells with contaminated pixels for MODIS image (fields US-Ne1 in left and US-Ne2 in right) from 06/18/12*

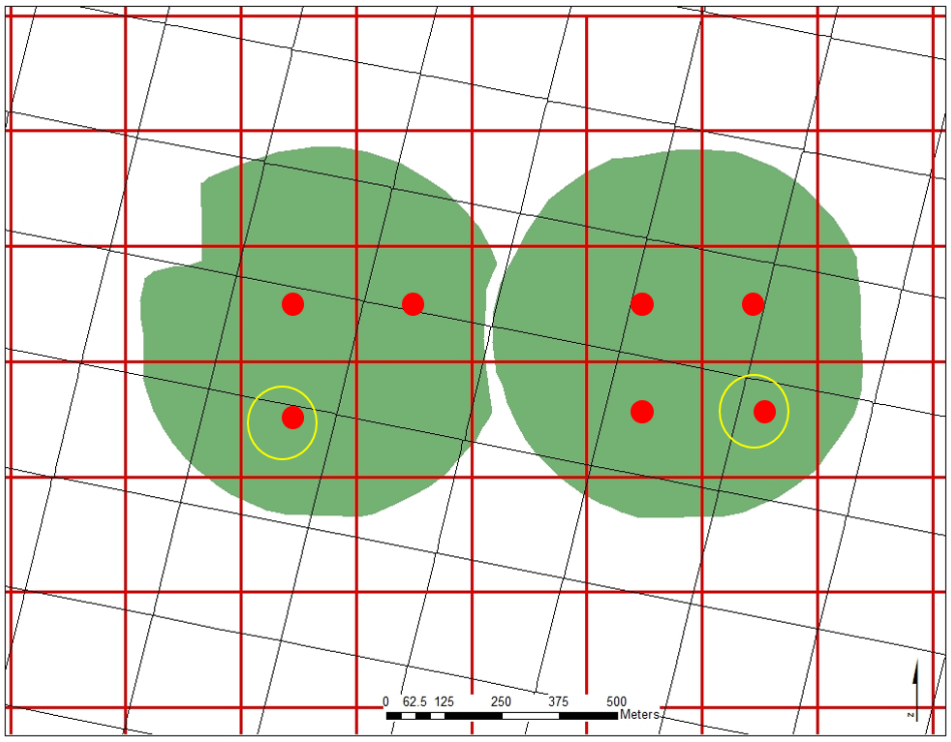

***Figure D.10**: Grid cells with contaminated pixels for MODIS image (fields US-Ne1 in left and US-Ne2 in right) from 06/22/12*

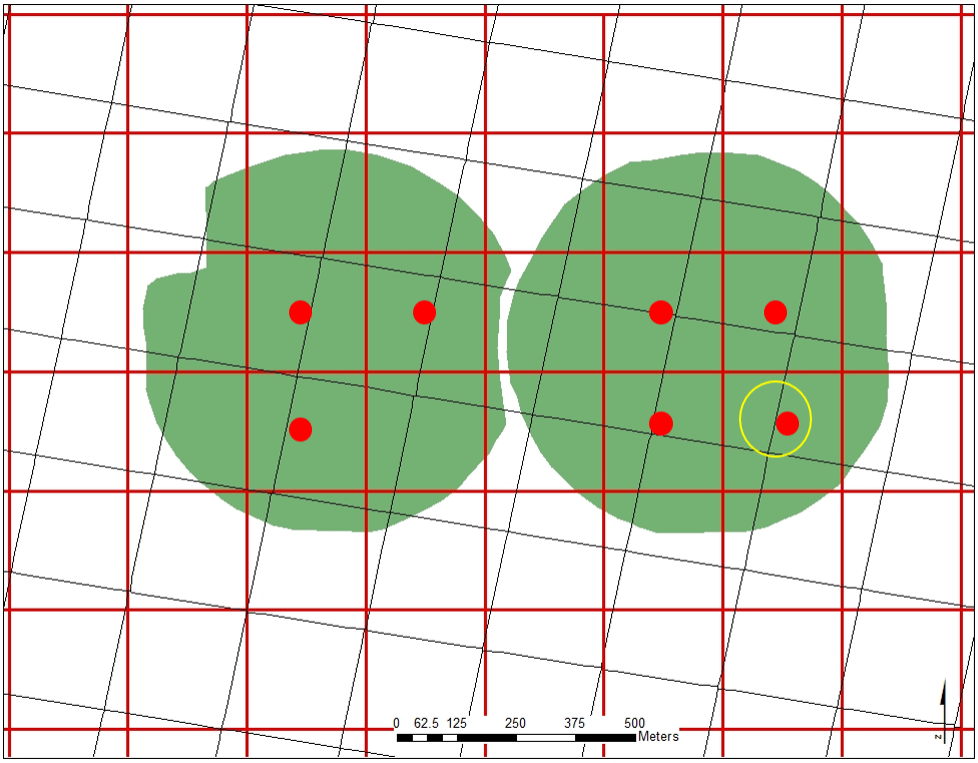

***Figure D.11**: Grid cells with contaminated pixels for MODIS image (fields US-Ne1 in left and US-Ne2 in right) from 06/24/12*

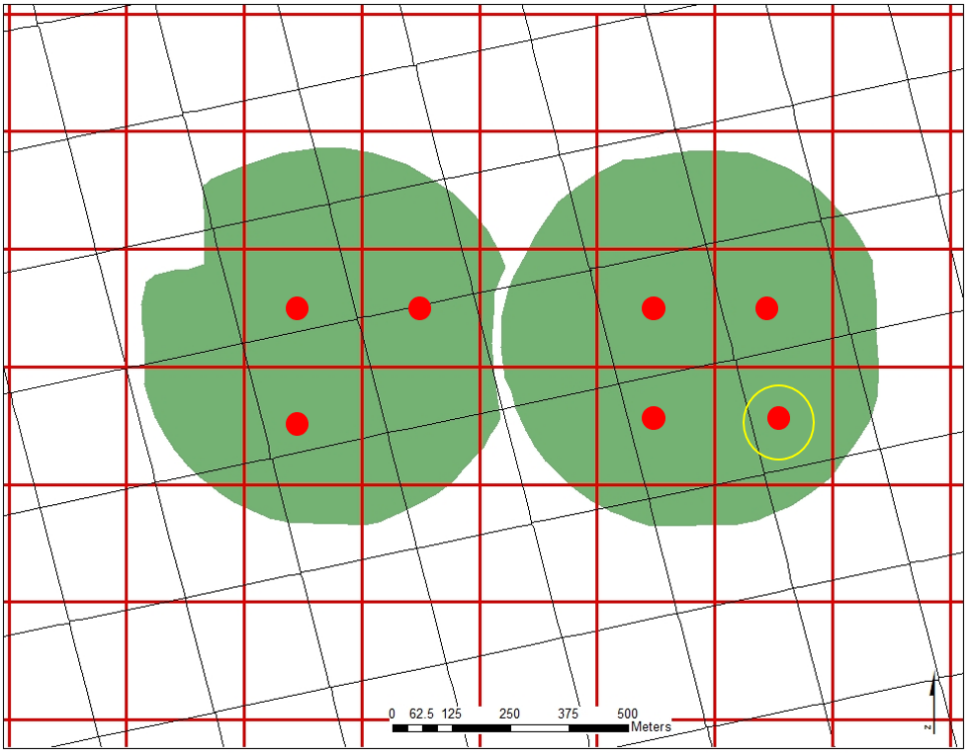

***Figure D.12**: Grid cells with contaminated pixels for MODIS image (fields US-Ne1 in left and US-Ne2 in right) from 06/27/12*

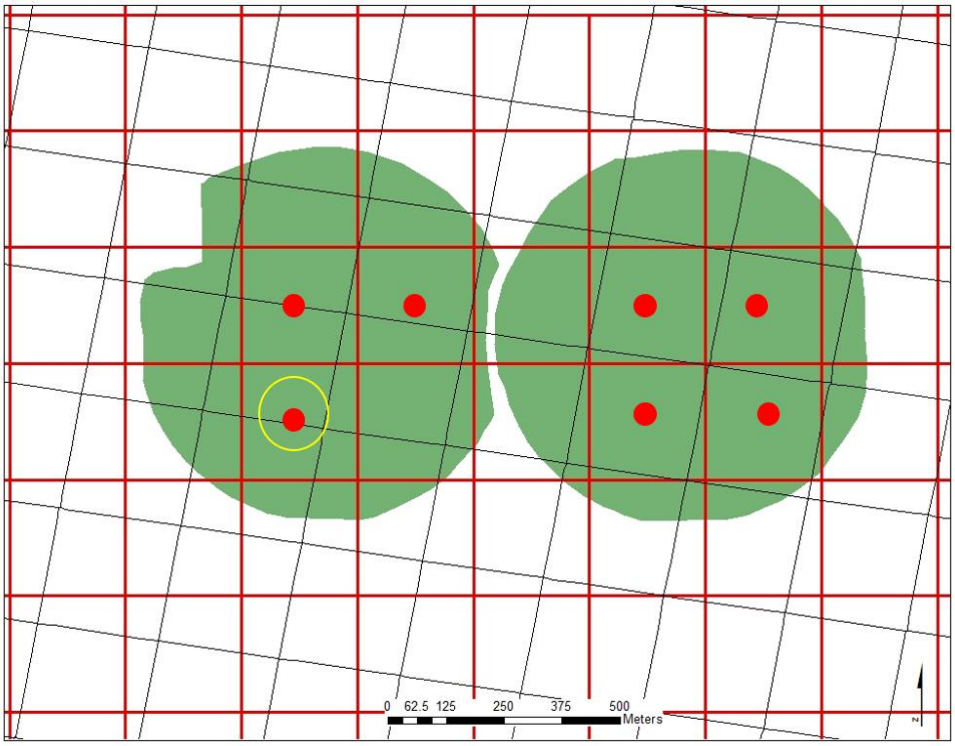

***Figure D.13**: Grid cells with contaminated pixels for MODIS image (fields US-Ne1 in left and US-Ne2 in right) from 07/03/12*

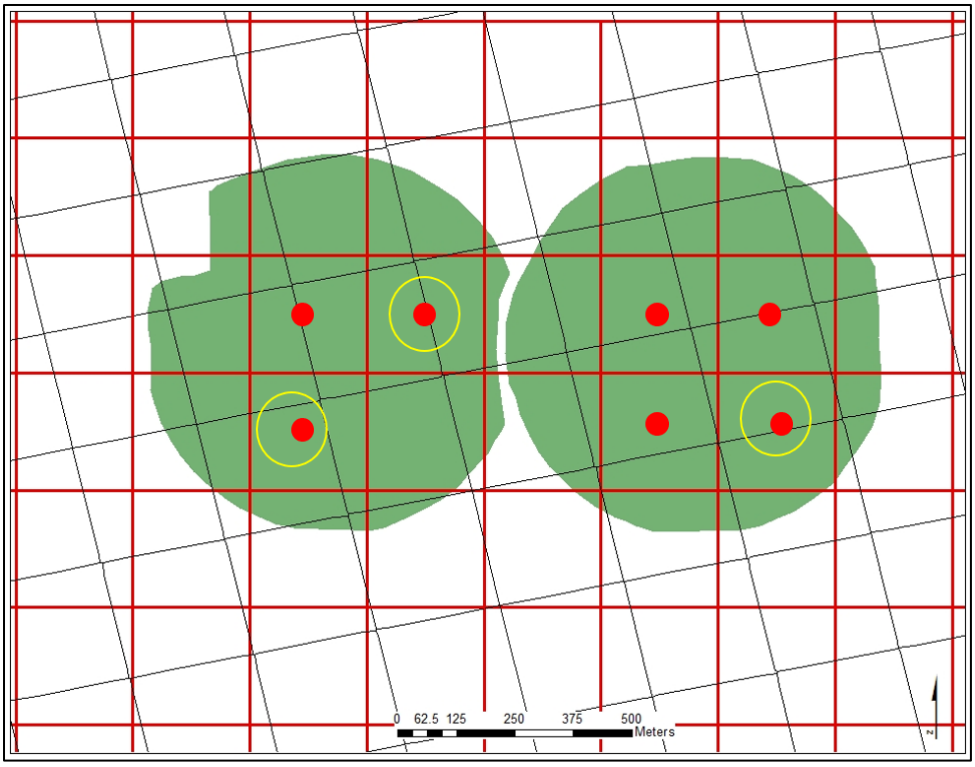

***Figure D.14**: Grid cells with contaminated pixels for MODIS image (fields US-Ne1 in left and US-Ne2 in right) from 07/04/12*

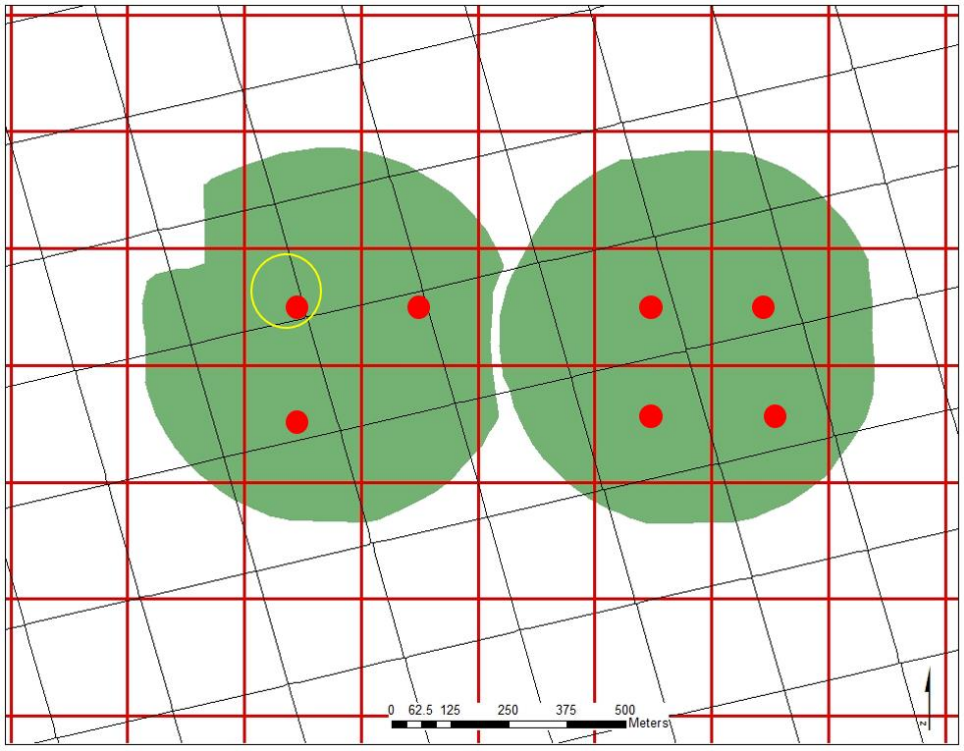

***Figure D.15**: Grid cells with contaminated pixels for MODIS image (fields US-Ne1 in left and US-Ne2 in right) from 07/06/12*

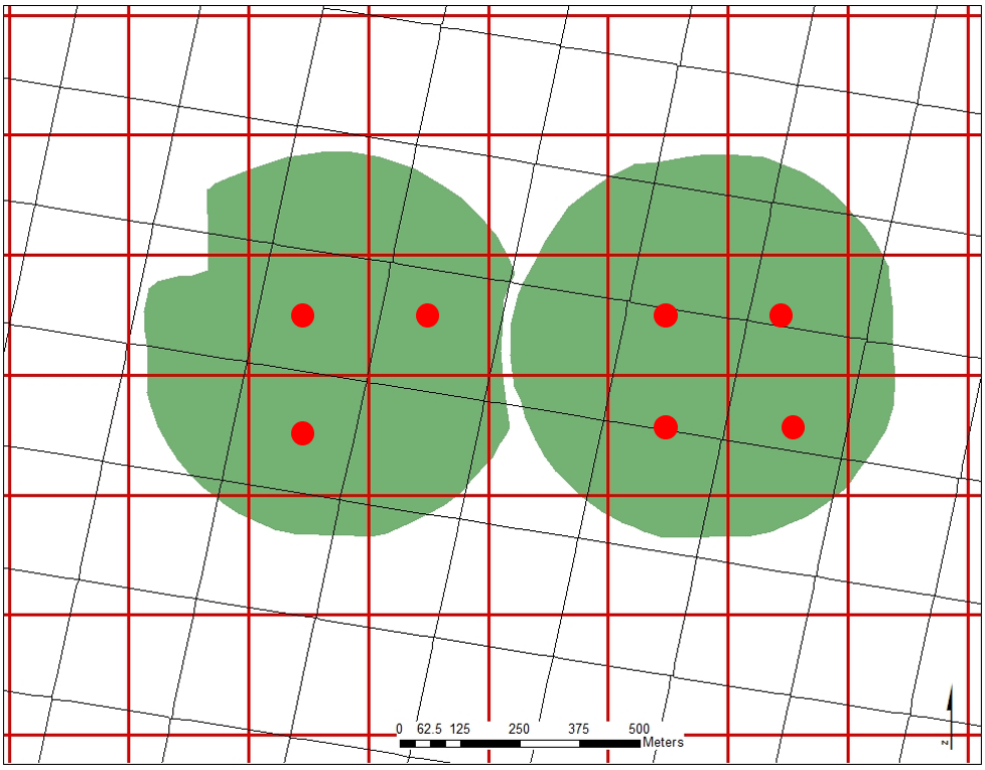

***Figure D.16**: Grid cells with contaminated pixels for MODIS image (fields US-Ne1 in left and US-Ne2 in right) from 07/10/12*

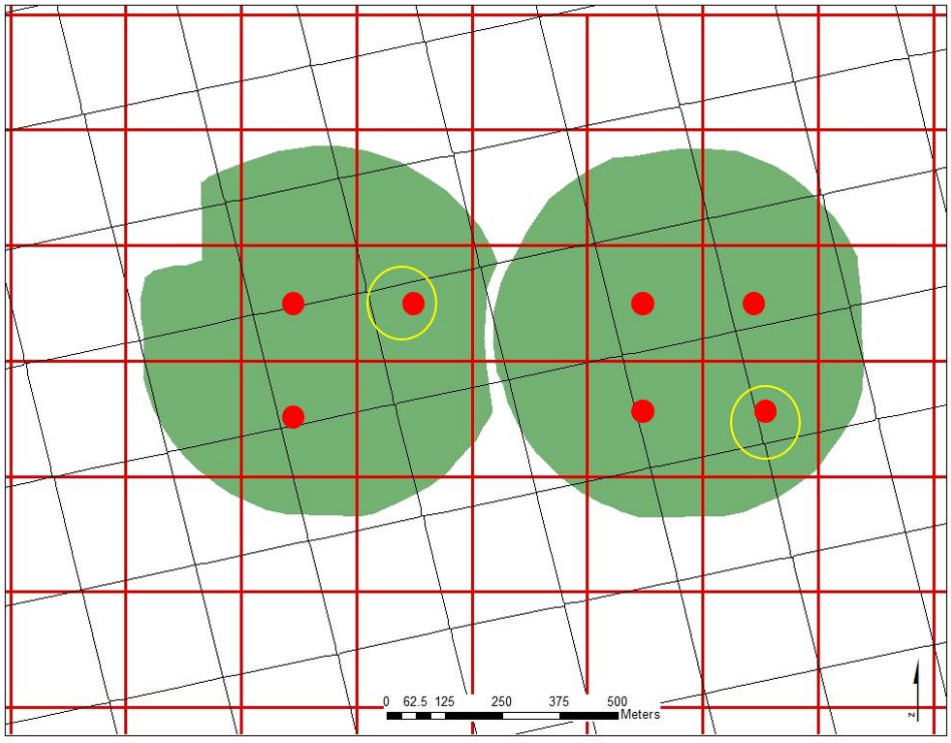

***Figure D.17**: Grid cells with contaminated pixels for MODIS image (fields US-Ne1 in left and US-Ne2 in right) from 07/13/12*

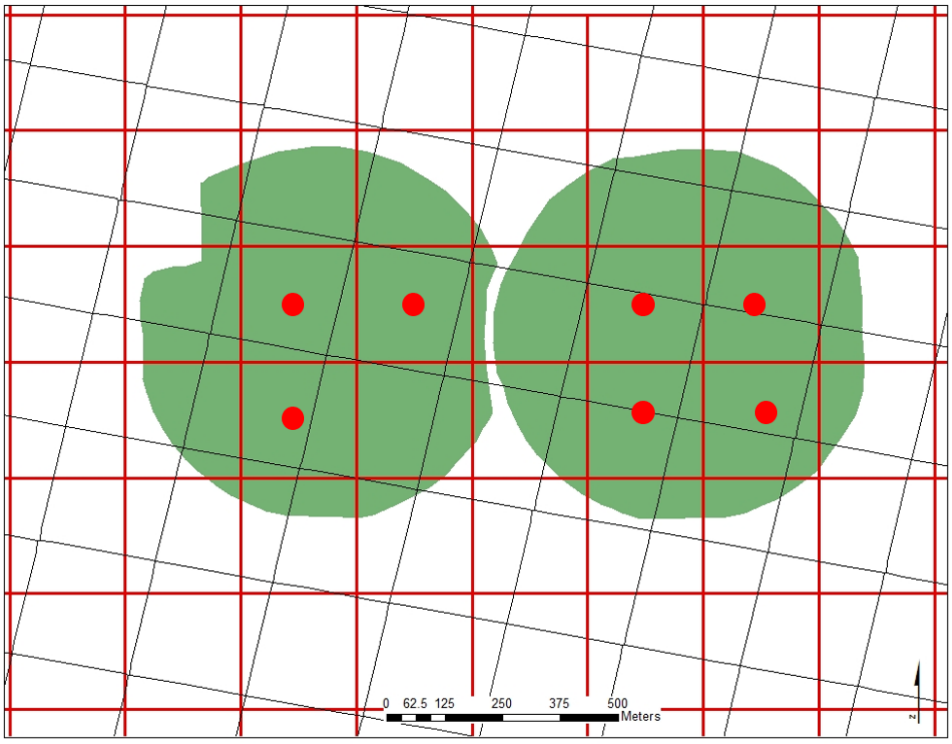

***Figure D.18**: Grid cells with contaminated pixels for MODIS image (fields US-Ne1 in left and US-Ne2 in right) from 07/17/12*

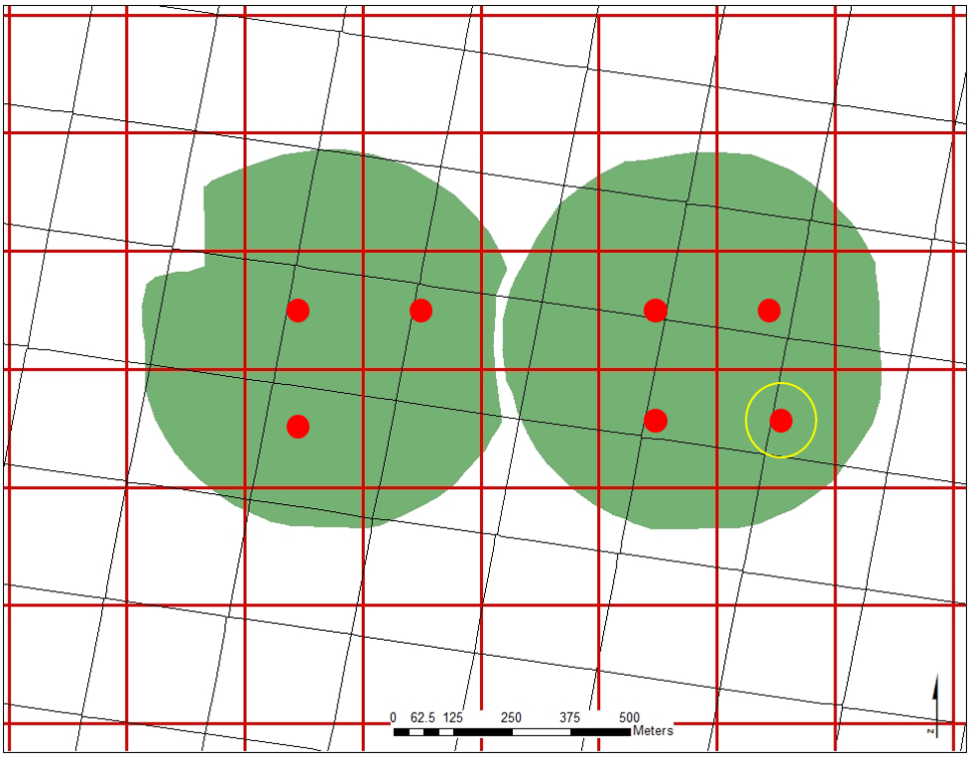

***Figure D.19**: Grid cells with contaminated pixels for MODIS image (fields US-Ne1 in left and US-Ne2 in right) from 07/19/12*

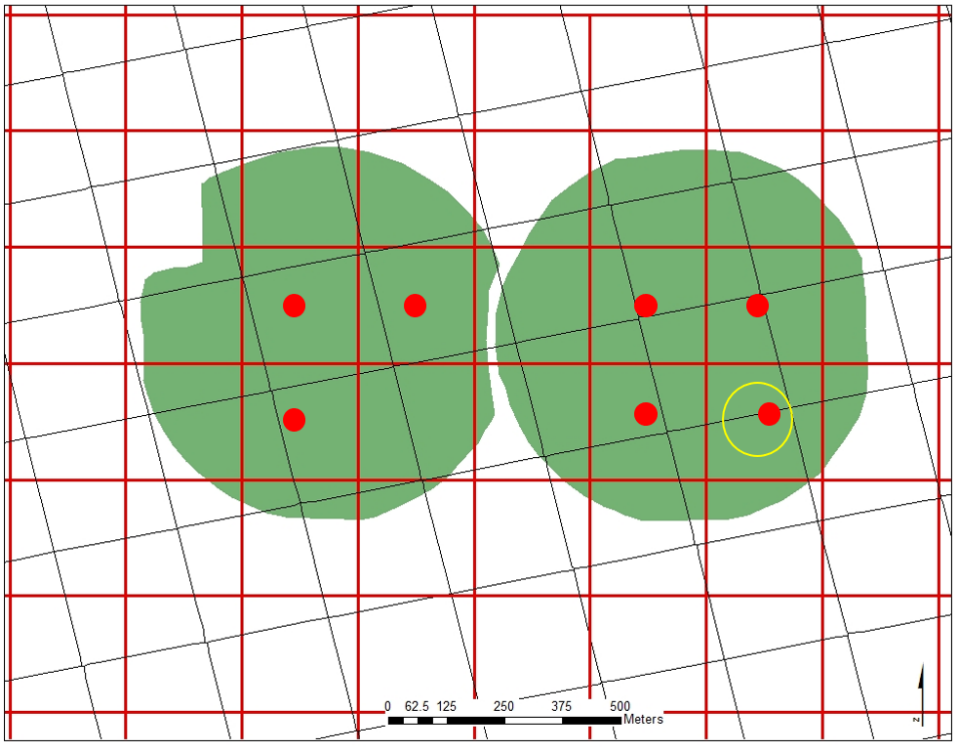

***Figure D.20**: Grid cells with contaminated pixels for MODIS image (fields US-Ne1 in left and US-Ne2 in right) from 07/20/12*

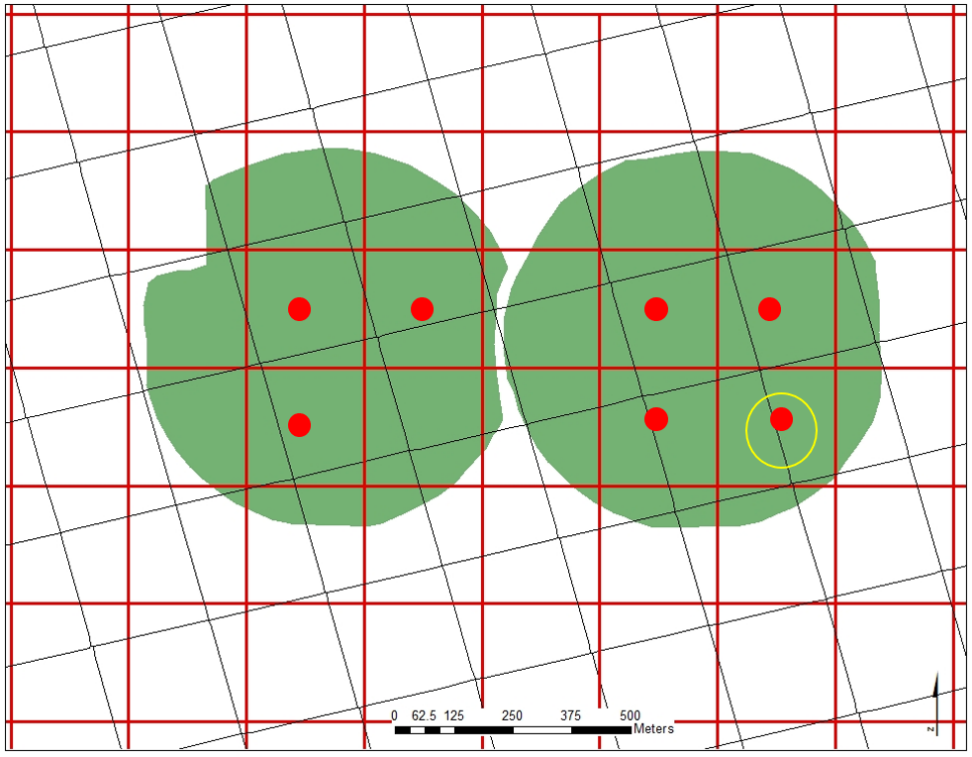

***Figure D.21**: Grid cells with contaminated pixels for MODIS image (fields US-Ne1 in left and US-Ne2 in right) from 07/22/12*

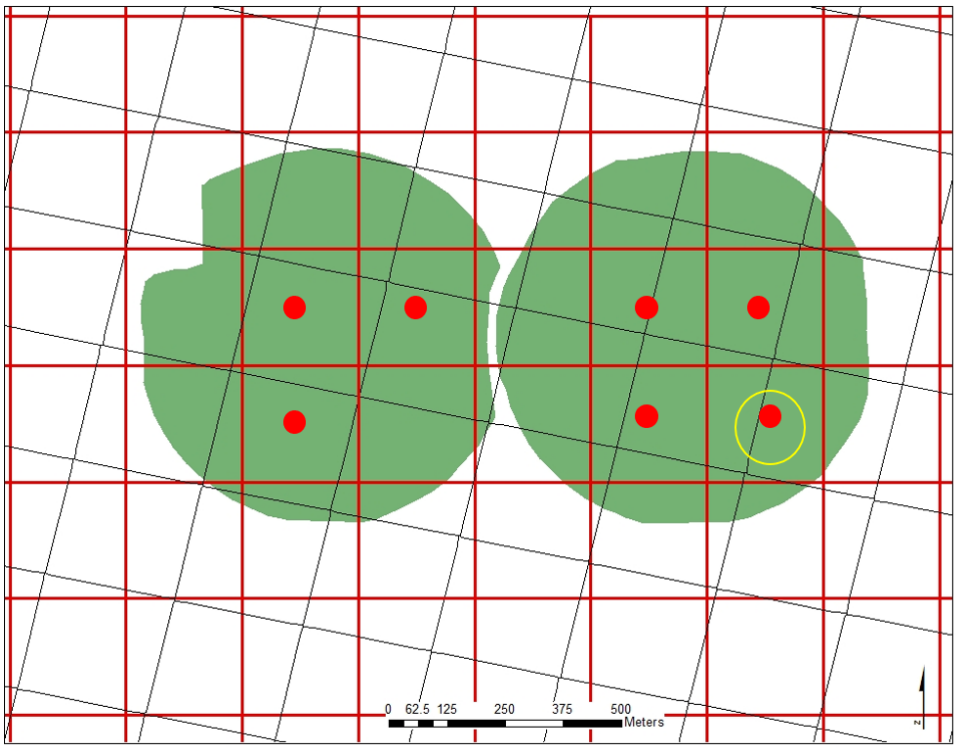

***Figure D.22**: Grid cells with contaminated pixels for MODIS image (fields US-Ne1 in left and US-Ne2 in right) from 07/24/12*

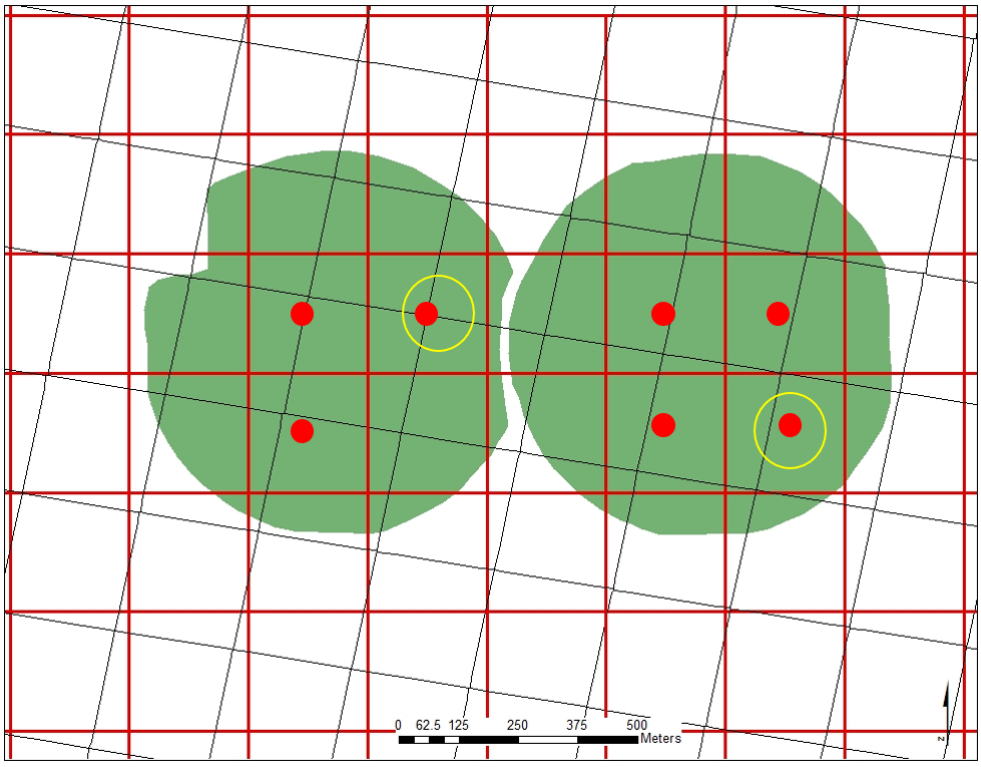

***Figure D.23**: Grid cells with contaminated pixels for MODIS image (fields US-Ne1 in left and US-Ne2 in right) from 07/26/12*

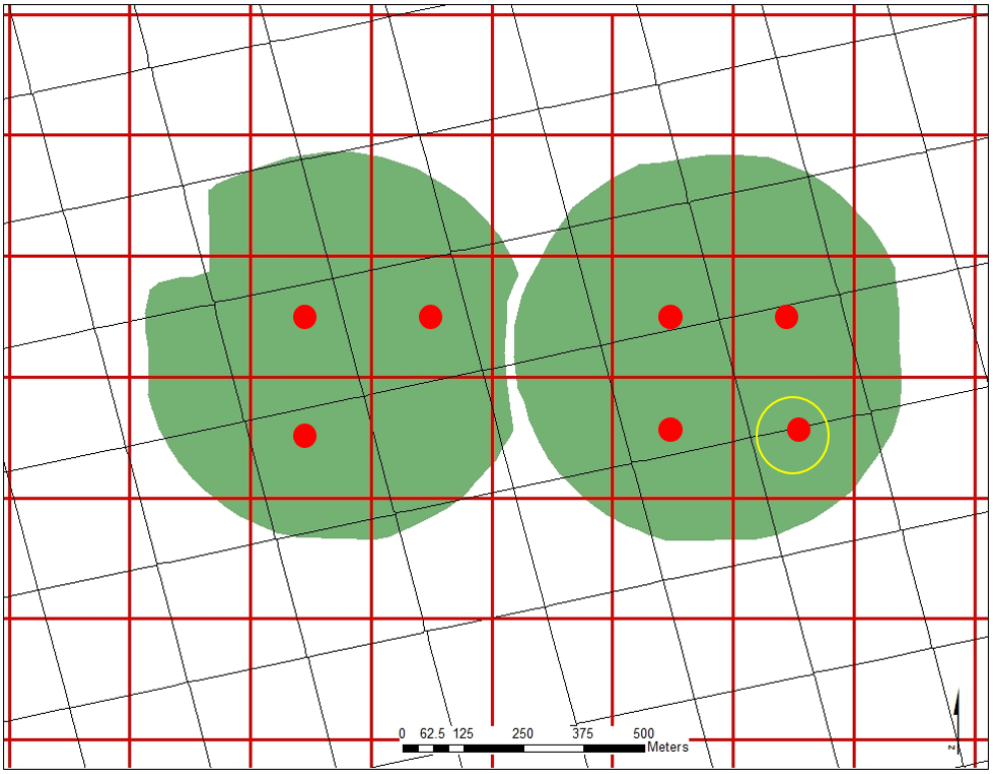

***Figure D.24**: Grid cells with contaminated pixels for MODIS image (fields US-Ne1 in left and US-Ne2 in right) from 07/29/12*

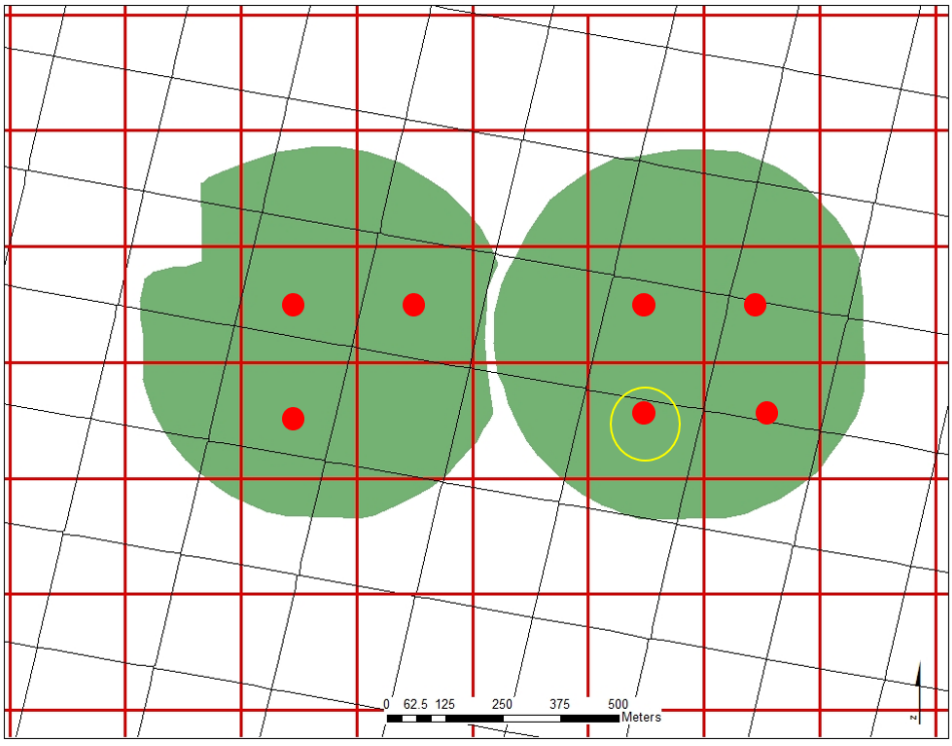

***Figure D.25**: Grid cells with contaminated pixels for MODIS image (fields US-Ne1 in left and US-Ne2 in right) from 08/02/12*

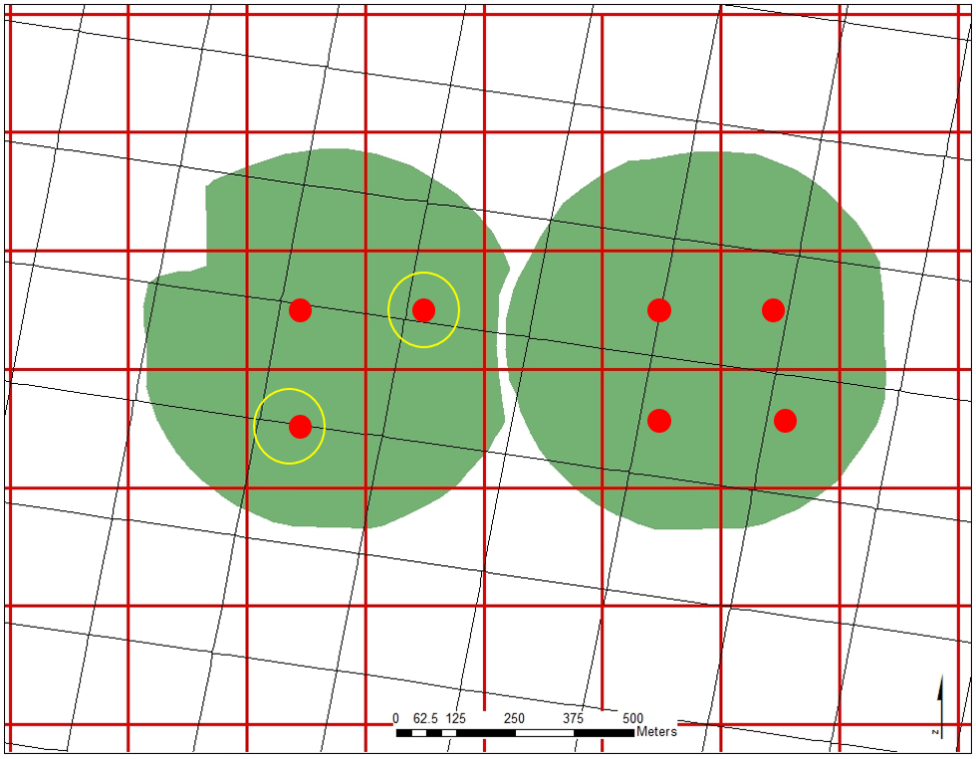

***Figure D.26**: Grid cells with contaminated pixels for MODIS image (fields US-Ne1 in left and US-Ne2 in right) from 08/04/12*

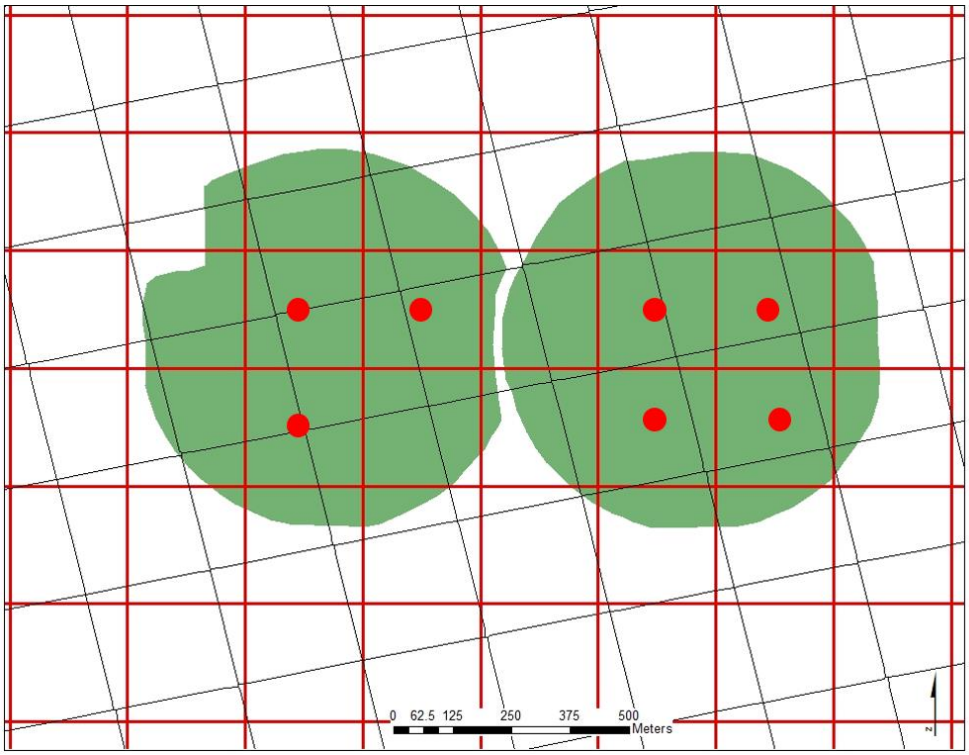

***Figure D.27**: Grid cells with contaminated pixels for MODIS image (fields US-Ne1 in left and US-Ne2 in right) from 08/05/12*

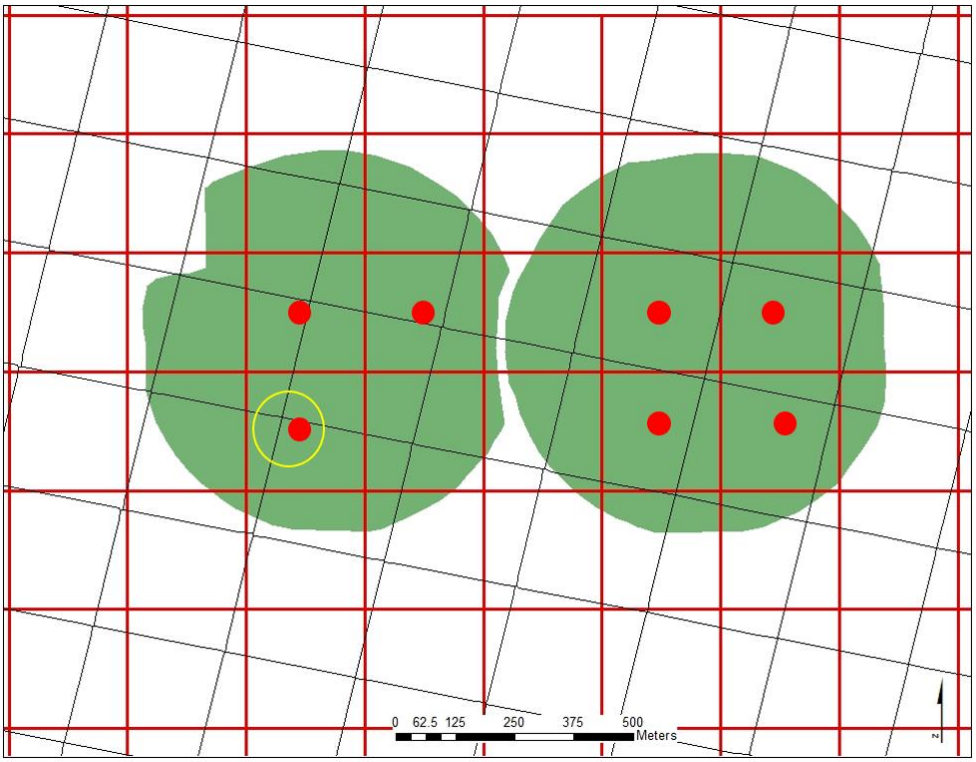

***Figure D.28**: Grid cells with contaminated pixels for MODIS image (fields US-Ne1 in left and US-Ne2 in right) from 08/09/12*

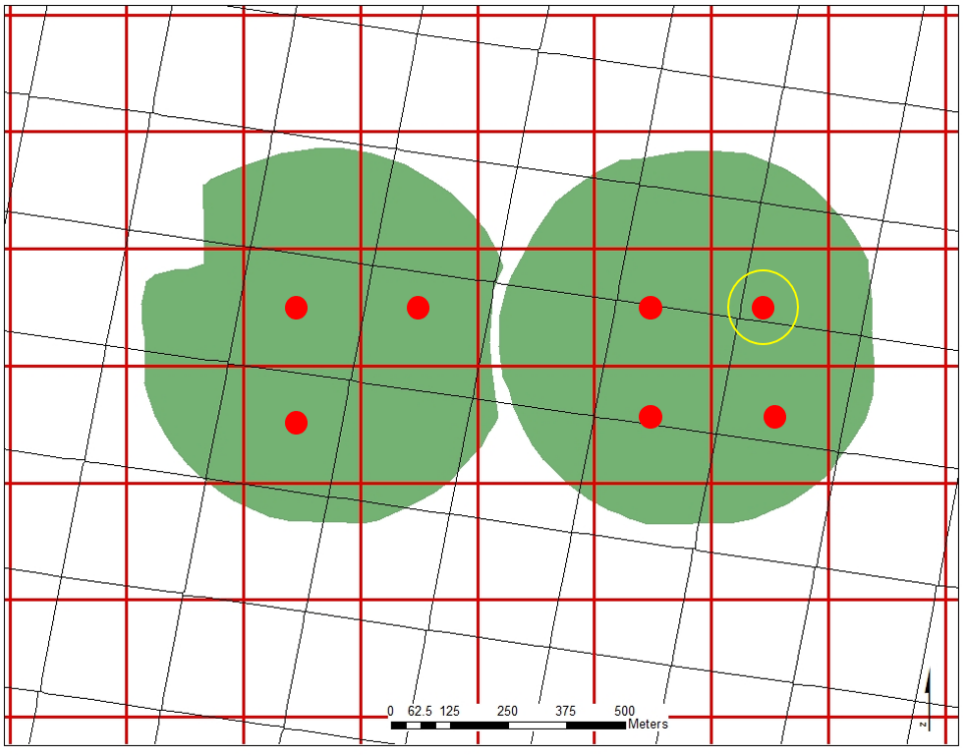

***Figure D.29**: Grid cells with contaminated pixels for MODIS image (fields US-Ne1 in left and US-Ne2 in right) from 08/20/12*

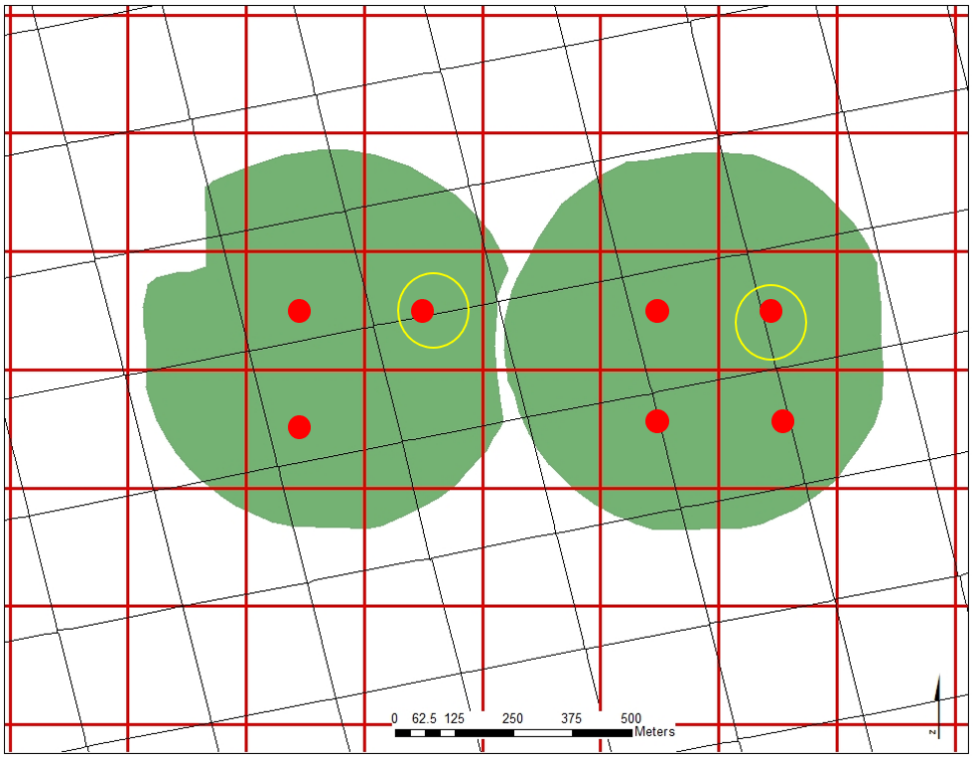

***Figure D.30**: Grid cells with contaminated pixels for MODIS image (fields US-Ne1 in left and US-Ne2 in right) from 08/21/12*

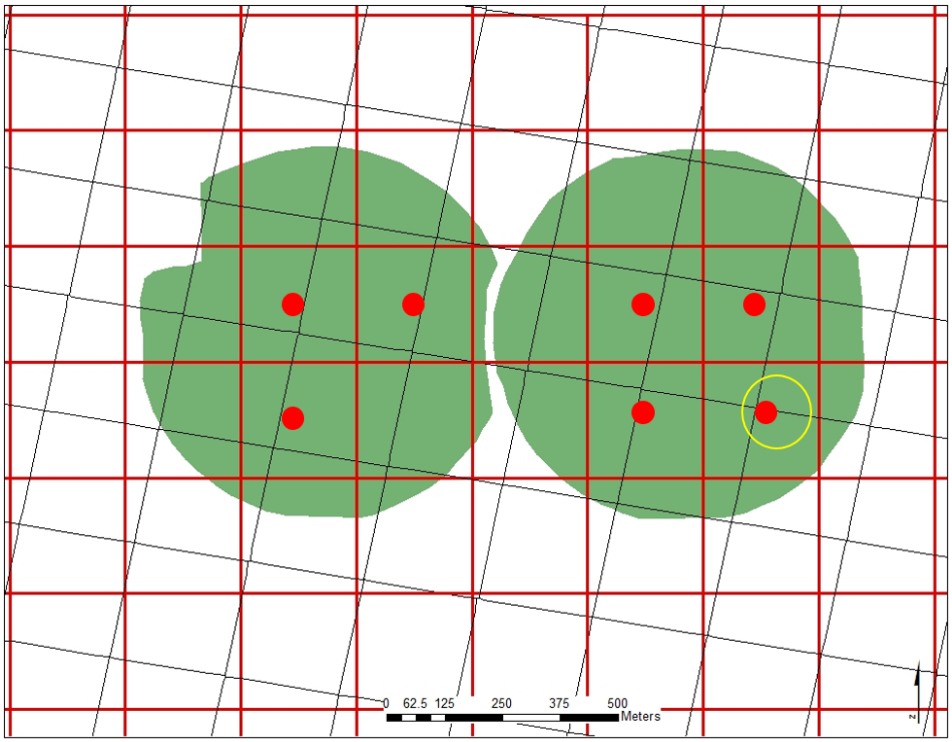

***Figure D.31**: Grid cells with contaminated pixels for MODIS image (fields US-Ne1 in left and US-Ne2 in right) from 08/27/12*

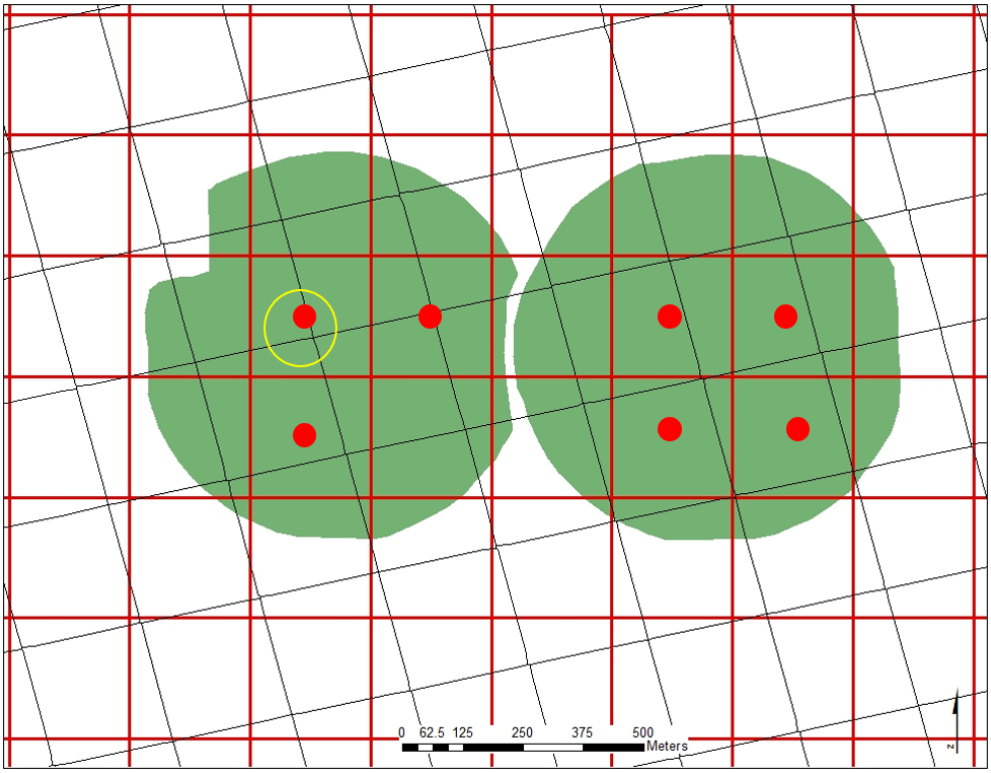

***Figure D.32**: Grid cells with contaminated pixels for MODIS image (fields US-Ne1 in left and US-Ne2 in right) from 08/30/12*

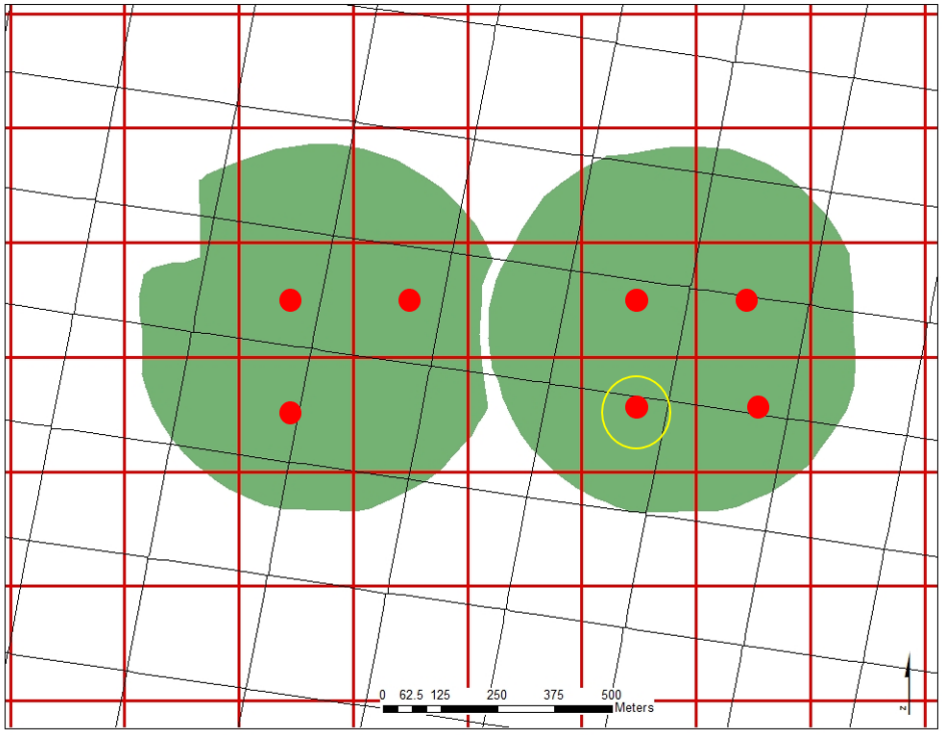

***Figure D.33**: Grid cells with contaminated pixels for MODIS image (fields US-Ne1 in left and US-Ne2 in right) from 09/05/12*

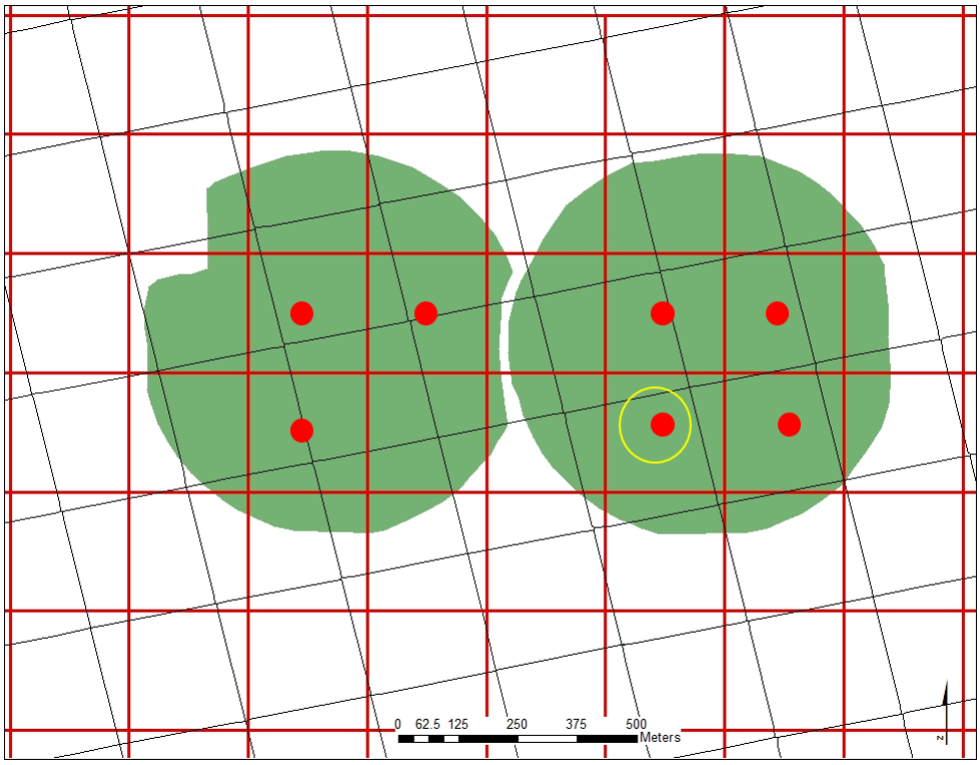

***Figure D.34**: Grid cells with contaminated pixels for MODIS image (fields US-Ne1 in left and US-Ne2 in right) from 09/06/12*

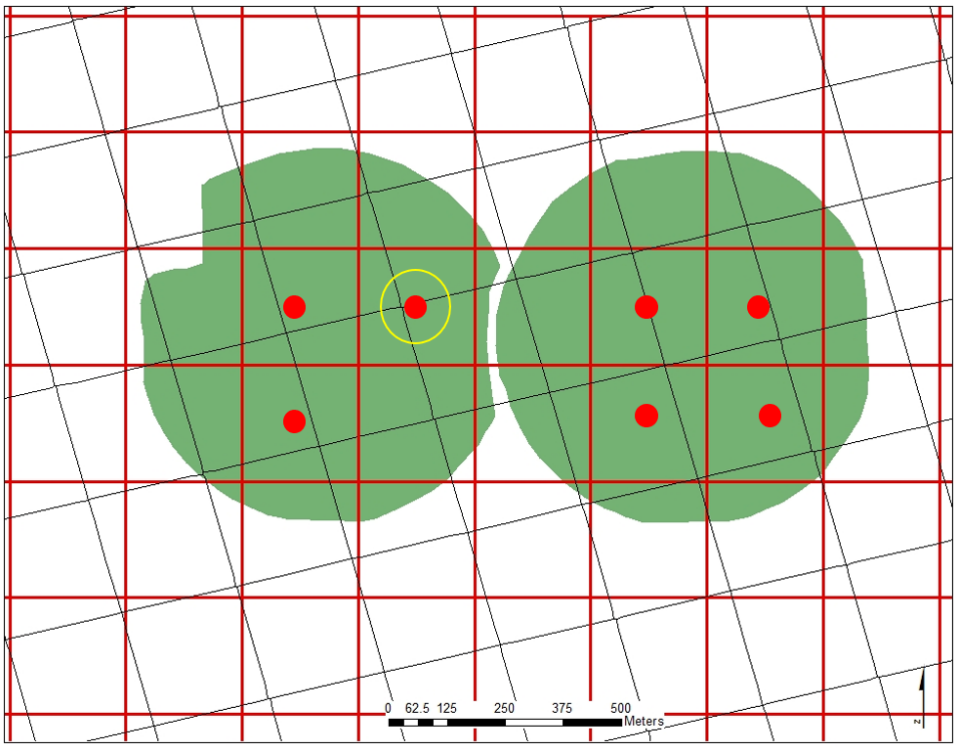

***Figure D.35**: Grid cells with contaminated pixels for MODIS image (fields US-Ne1 in left and US-Ne2 in right) from 09/08/12*

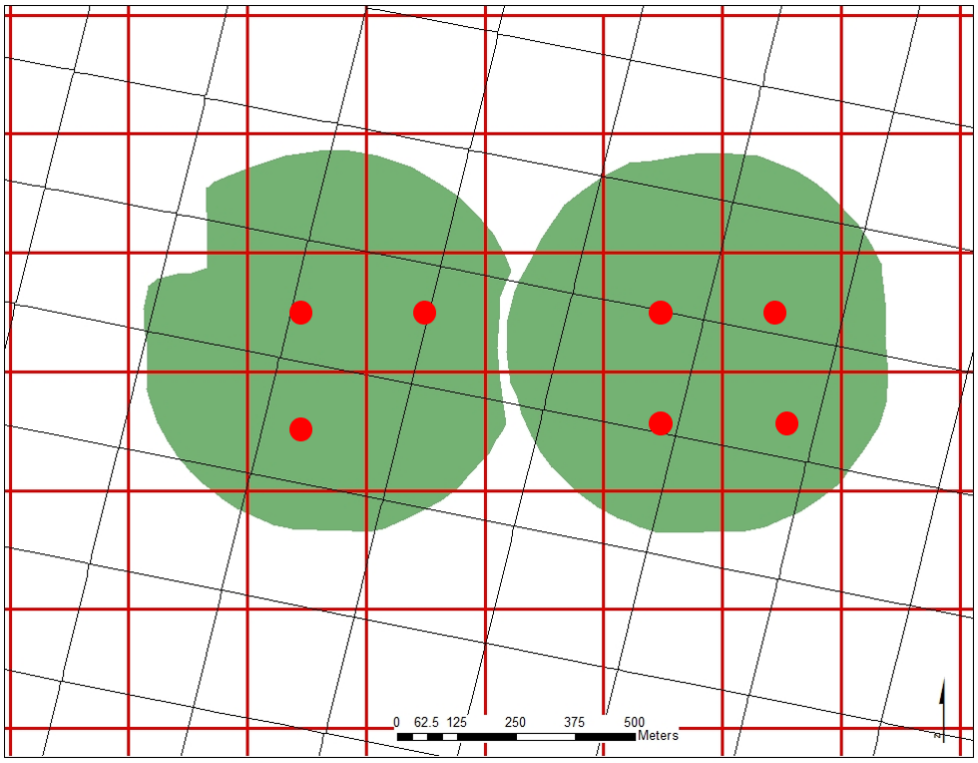

***Figure D.36**: Grid cells with contaminated pixels for MODIS image (fields US-Ne1 in left and US-Ne2 in right) from 09/10/12*

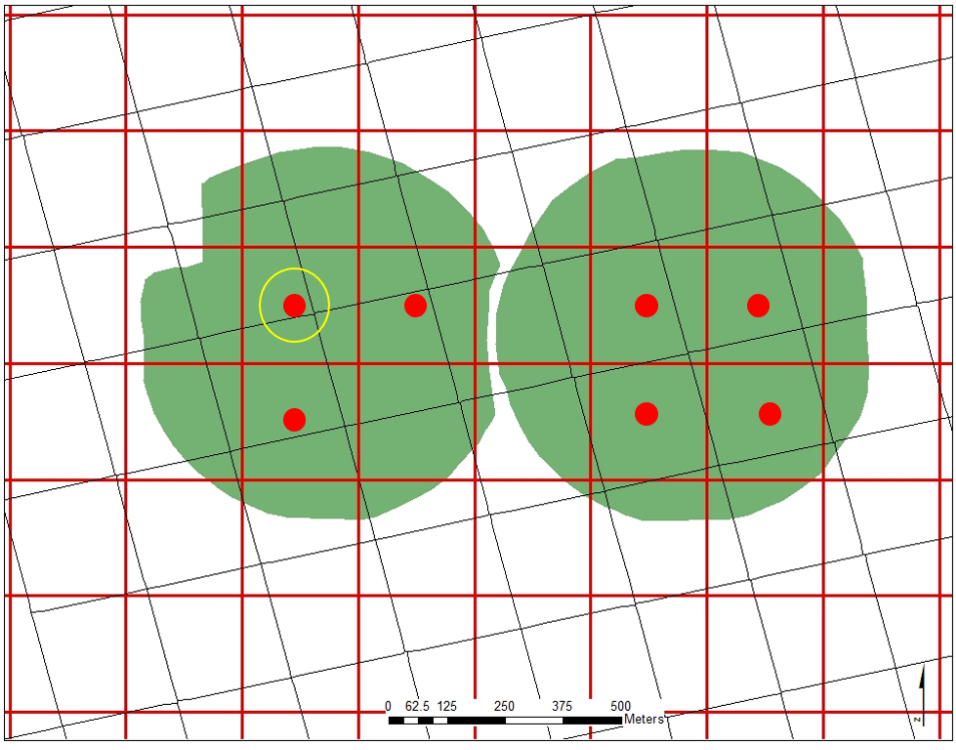

***Figure D.37**: Grid cells with contaminated pixels for MODIS image (fields US-Ne1 in left and US-Ne2 in right) from 09/15/12*

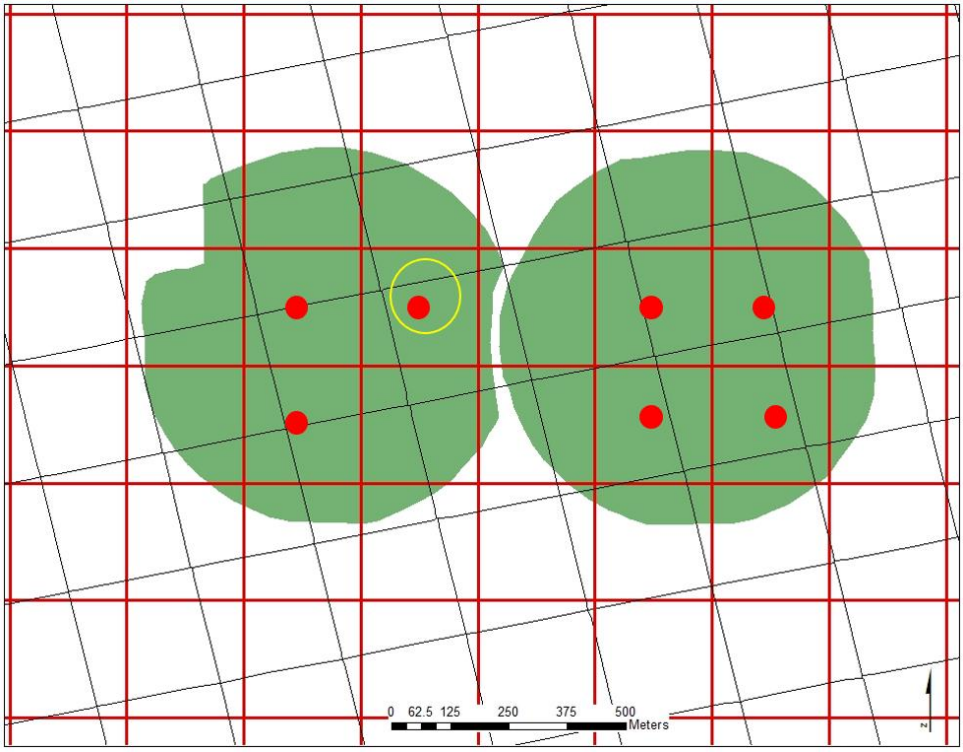

***Figure D.38**: Grid cells with contaminated pixels for MODIS image (fields US-Ne1 in left and US-Ne2 in right) from 09/22/12*

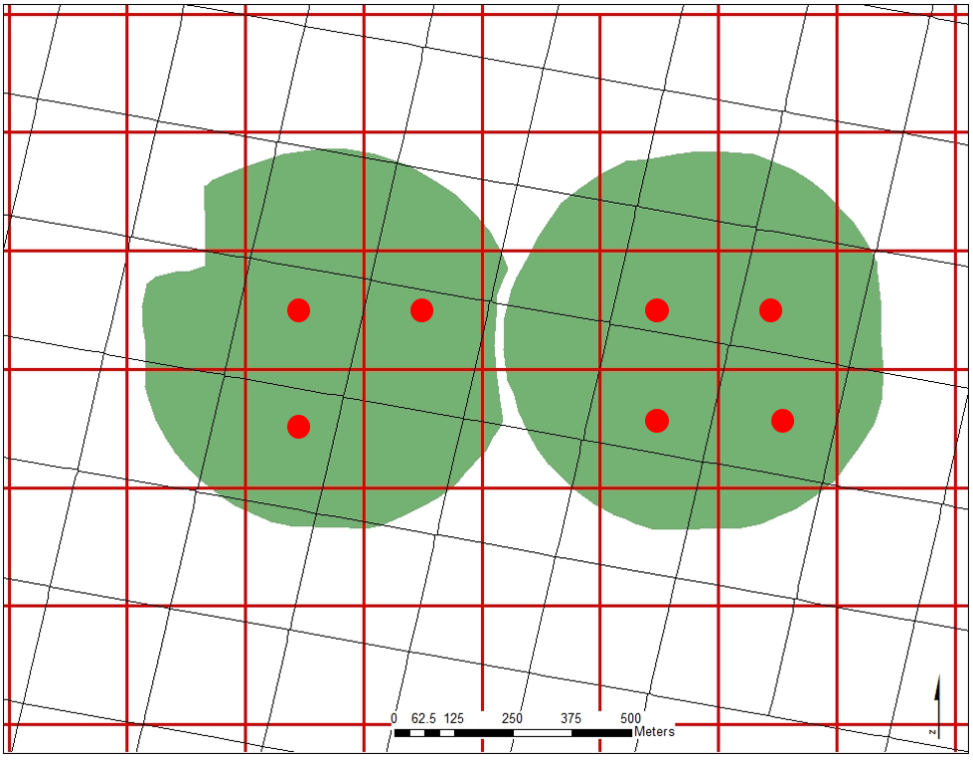

***Figure D.39**: Grid cells with contaminated pixels for MODIS image (fields US-Ne1 in left and US-Ne2 in right) from 10/21/12*

APPENDIX E: PYTHON SCRIPT (V 2.7) FOR REPROJECTING MODIS IMAGES WITH THE FOOTPRINT METHOD

```
# -*- coding: utf-8 -*-
"""
Created on Mon Nov  3 11:44:02 2014
    """

import os
import glob
from subprocess import call

def parse_hdf(gdal_dir, folder):
    """
    This is the script for reprojecting and converting modis hdf files.

    It will convert hdf files to 1km resolutioned Albers Equal Area projection
    tiff files. If you want to convert it to a different projection "command"
    should be changed. -t_srs is the target projection. Parameters can be
    accessed from the website "www.spatialreference.org"
    """

    ## Assign the downloaded modis products to the variables.
    mod11 = glob.glob(os.path.join(folder, "MOD02QKM*"))
    mask = glob.glob(os.path.join(folder, "*.shp"))[0]

    ## Assigning the different subdatasets to the variables.
    products = ['HDF4_EOS:EOS_SWATH:"%s"\
```

```
:MODIS_SWATH_Type_L1B:EV_250_RefSB' %(mod11[0])]

    ## Output names are here
    names = [os.path.splitext(mod11[0])[0] + "_EV_250_RefSB"]

    ## Loop through the products
    for i in range(len(products)):
        ## A special case here. Set no data value to -99 only for View_angle
        ## product. Otherwise it will be null

        if "View_angle" in names[i]:
            no_data = "-srcnodata -99"
        else:
            no_data = ""

        ## Grab the files and parse from the current directory
            command = '%s -of GTIFF --config GDAL_DATA "C:\OSGeo4W64\share\gdal" -crop_to_cutline -cutline %s -tr 10 10 -tps -s_srs "EPSG:4326" \
    -t_srs "+proj=utm +zone=14 +a=6378137 +b=6378135.99663591 +datum=WGS84 +units=m +no_defs" \
    -r near %s %s %s.tif' %(gdal_dir, mask, no_data, products[i], names[i])
        ## Call the command from terminal
        print command
            #call(command, shell = True)

## Call the function if it is standalone.
if __name__ == '__main__':

    ## Very important ##
    ## Change this directory to where your gdal api executables live
```

```
## For macs it is usually
##    /Library/Frameworks/GDAL.framework/Versions/x.x/Programs
## For Windows it is usually
##    C:\Python27\Lib\site-packages\osgeo
gdal_api_dir = "C:\\OSGeo4W64\\bin"
gdalwarp = os.path.join(gdal_api_dir, "gdalwarp.exe")

## Get the current directory (where script lives)
current_dir = os.path.dirname(os.path.realpath(__file__))
parse_hdf(gdalwarp, current_dir)
```

APPENDIX F: RESULTS OF FULL RANGE SENSITIVITY OF THE SOIL WATER BALANCE MODEL TO PRECIPITATION DATA

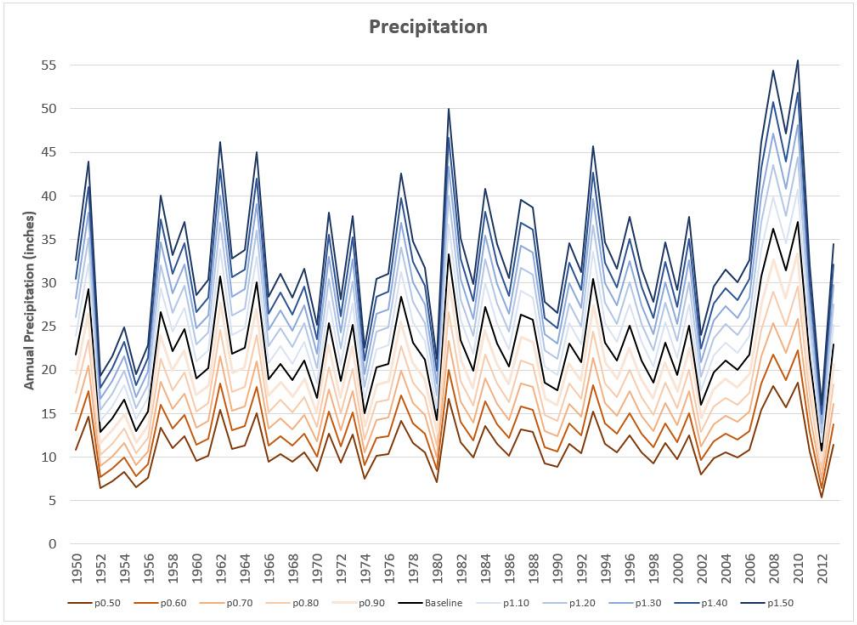

Figure F.1: *Annual baseline precipitation rate and multiplier rates from 1950 to 2013 for the Gothenburg weather station data*

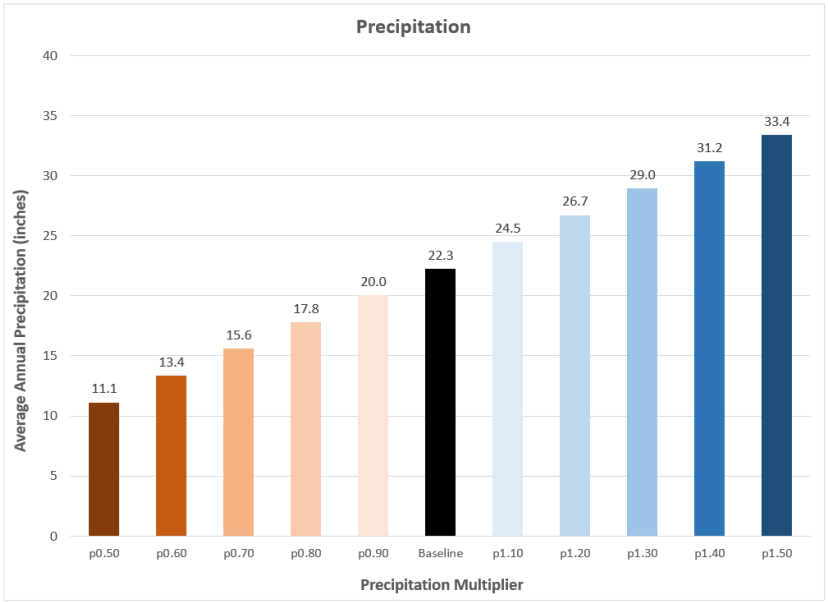

Figure F.2: *Average annual precipitation of baseline run and runs with multipliers applied*

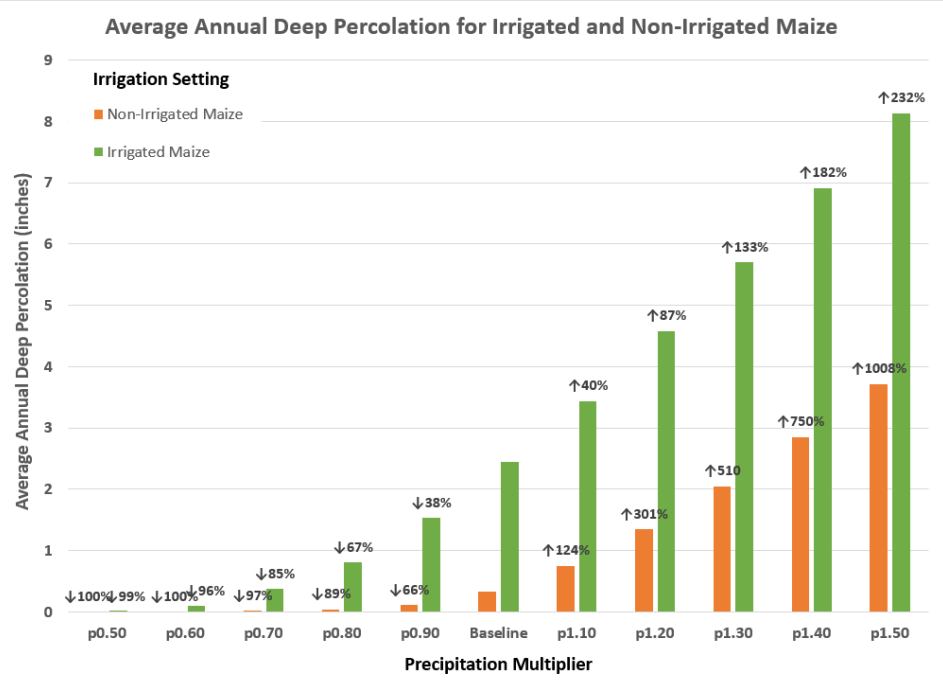

***Figure F.3**: Response of DP to a range of precipitation multipliers for irrigated and non-irrigated maize*

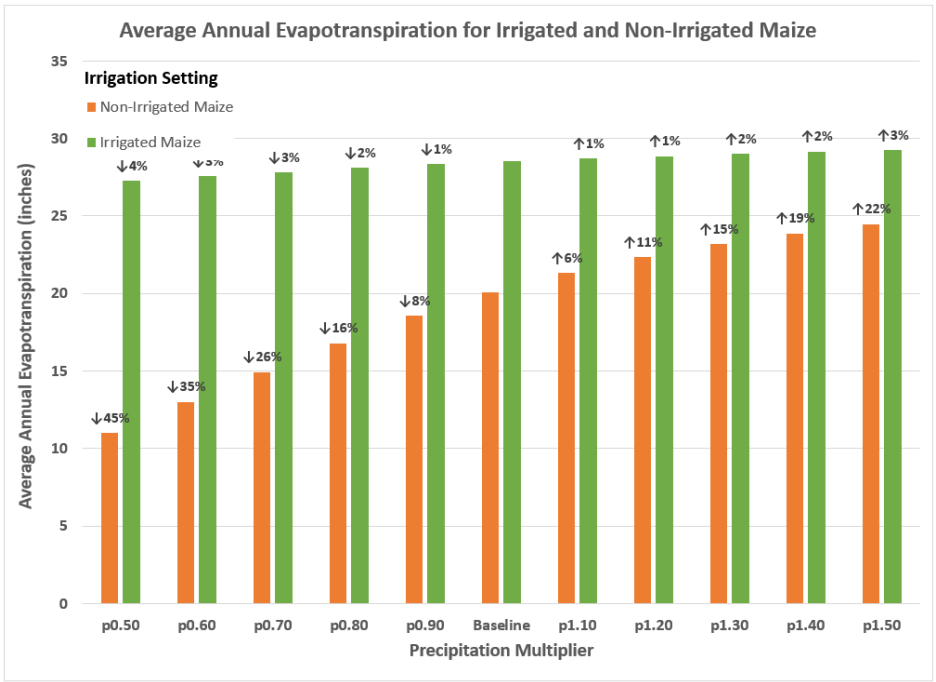

***Figure F.4**: Response of ET to precipitation multipliers for irrigated and non-irrigated maize*

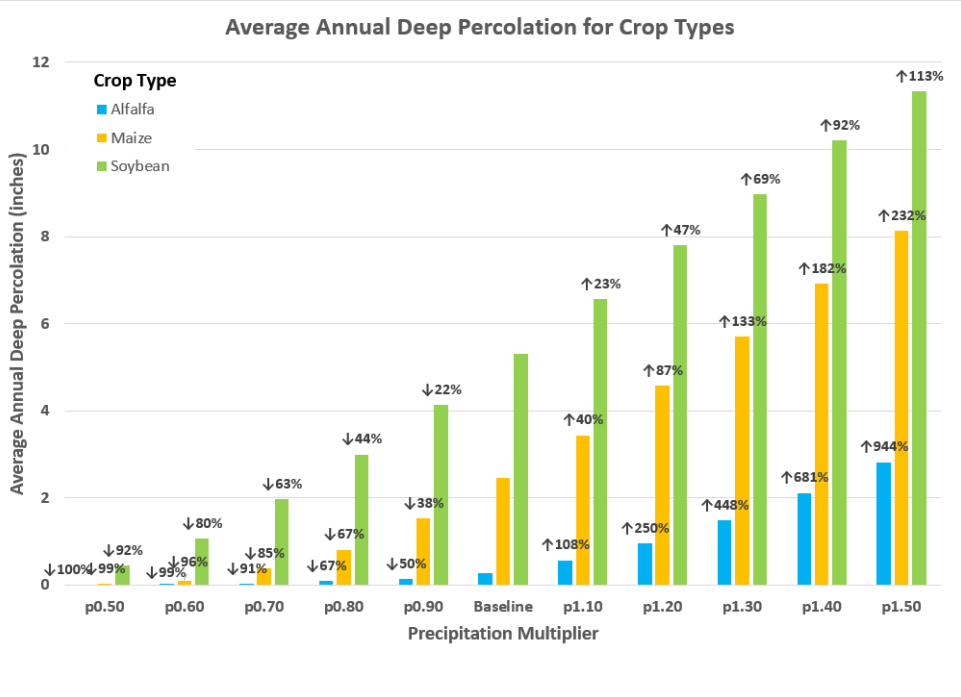

***Figure F.5**: Response of DP to precipitation multipliers for different crop types*

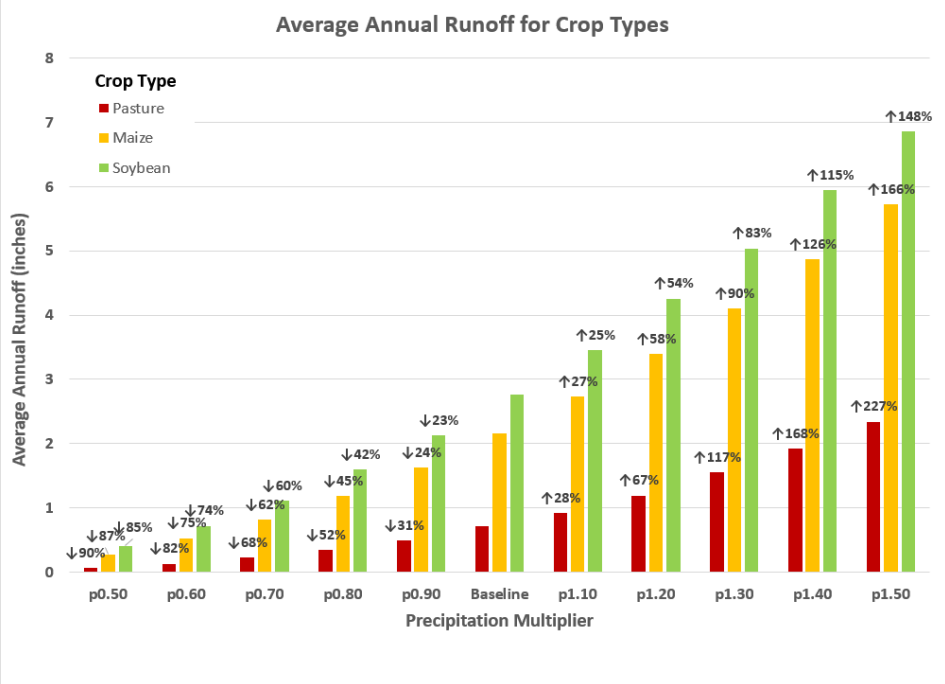

***Figure F.6**: Responses of RO to precipitation multipliers for different crop types*

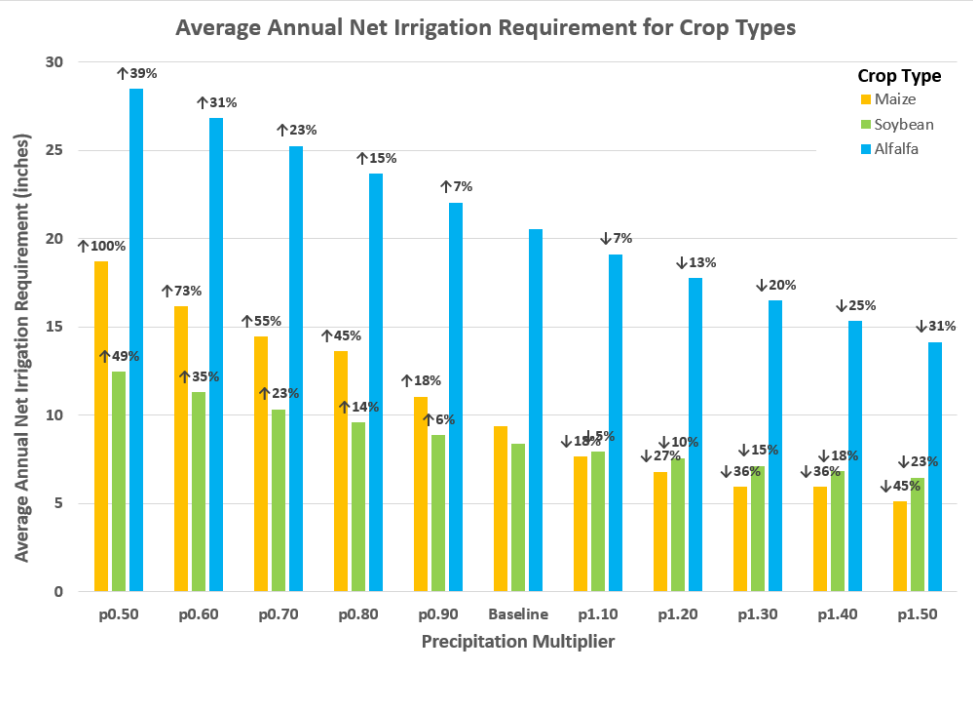

***Figure F.7**: Response of NIR to precipitation multipliers for different crop types*

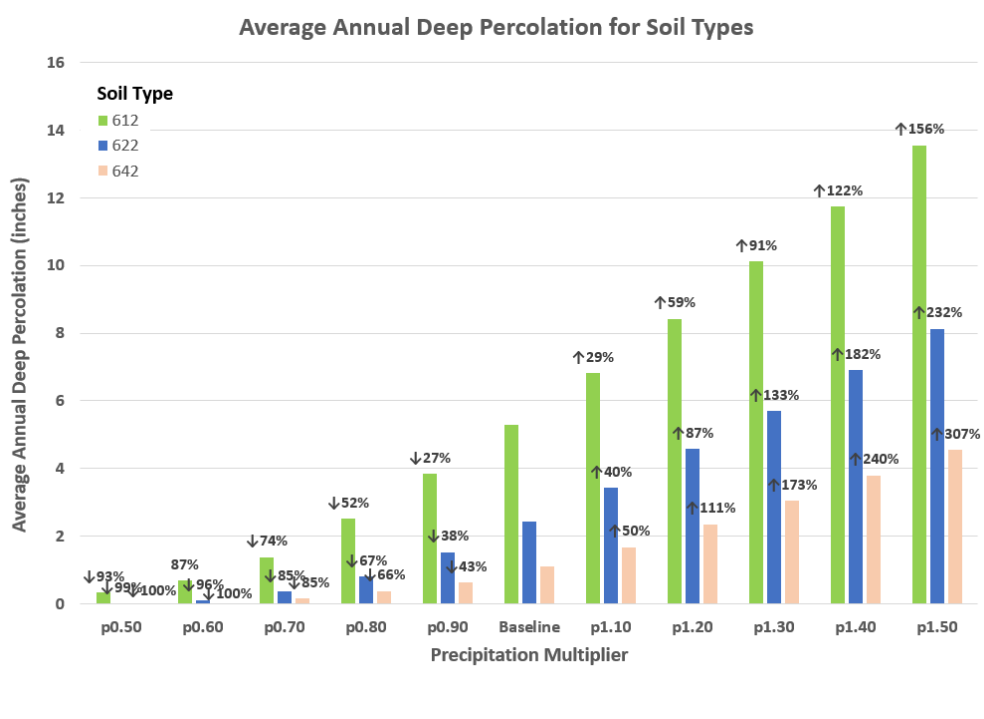

***Figure F.8**: Response of DP to changes in precipitation multipliers for soil types*

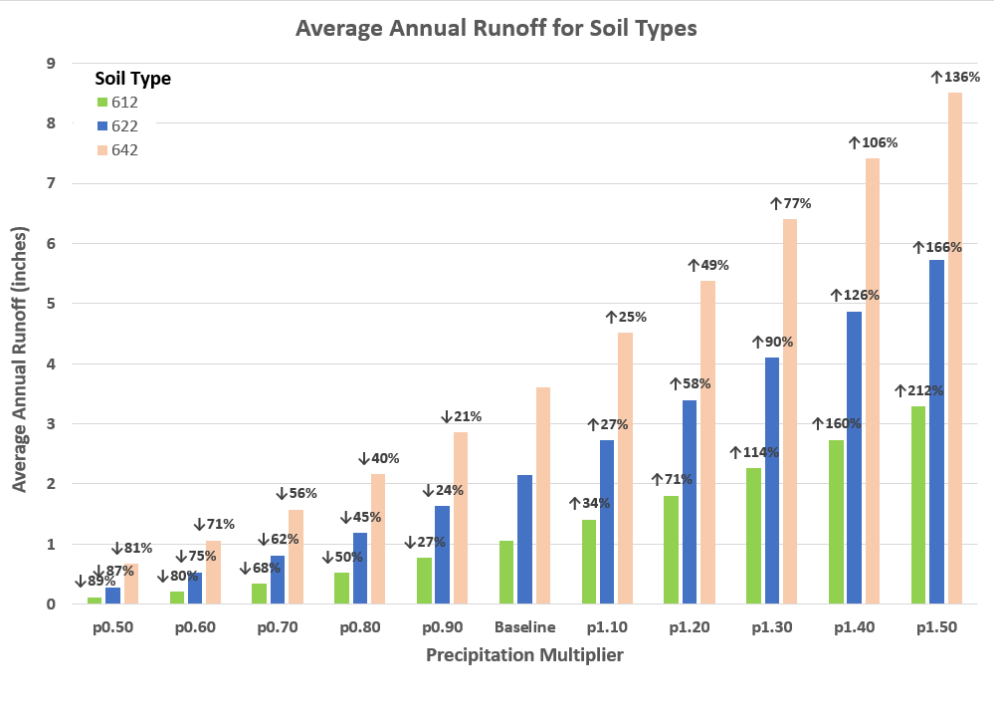

***Figure F.9**: Responses of RO to variations in the Precipitation multipliers for different soil types*

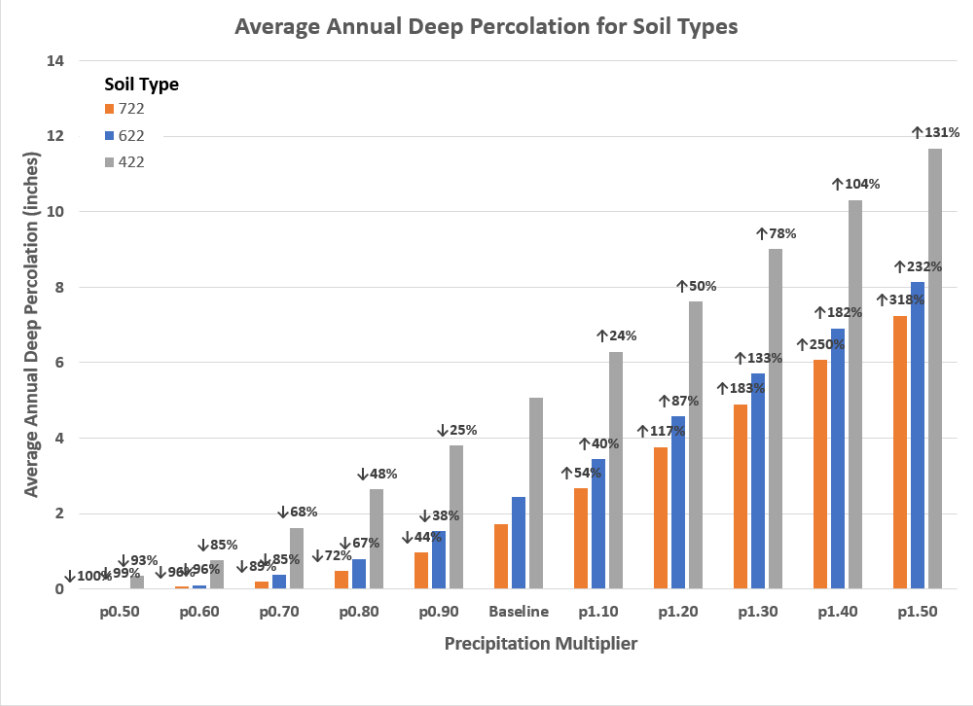

***Figure F.10**: Response of DP to varying multipliers of precipitation for soils with different Water Holding Capacity*

***Table F.1**: Response of hydrologic components in flux rates to variable precipitation multipliers*

Sensitivity Analysis Parameter	Hydrologic Component	p0.50 (in/yr)	p0.60 (in/yr)	p0.70 (in/yr)	p0.80 (in/yr)	p0.90 (in/yr)	Baseline (in/yr)	p1.10 (in/yr)	p1.20 (in/yr)	Rank
Irrigation Setting										
Non-Irrigated Maize	ET	11.02	13.01	14.93	16.78	18.55	20.07	**21.32**	**22.34**	16
Irrigated Maize	ET	27.27	27.56	27.80	28.09	28.34	28.52	**28.69**	**28.85**	18
Non-Irrigated Maize	DP	0.00	0.00	0.01	0.04	0.11	0.34	**0.75**	**1.34**	1
Irrigated Maize	DP	0.02	0.10	0.37	0.80	1.53	2.45	**3.44**	**4.58**	5
Crop Types										
Maize	DP	0.02	0.10	0.37	0.80	1.53	2.45	**3.44**	**4.58**	5
Soybeans	DP	0.44	1.05	1.97	2.99	4.12	5.31	**6.56**	**7.80**	13
Alfalfa	DP	0.00	0.00	0.02	0.09	0.14	0.27	**0.56**	**0.94**	2
Maize	RO	0.28	0.53	0.81	1.19	1.63	2.15	**2.73**	**3.39**	9
Soybean	RO	0.41	0.72	1.11	1.60	2.13	2.76	**3.46**	**4.26**	10
Pasture	RO	0.07	0.13	0.23	0.35	0.49	0.72	**0.92**	**1.19**	7
Maize	NIR	18.70	16.15	14.45	13.60	11.05	9.35	**7.65**	**6.80**	14
Soybean	NIR	12.46	11.29	10.33	9.58	8.87	8.37	**7.93**	**7.57**	17
Alfalfa	NIR	28.49	26.83	25.23	23.67	22.05	20.53	**19.11**	**17.77**	15
Soil Types										
Soil code 612	DP	0.35	0.68	1.38	2.51	3.85	5.29	**6.82**	**8.42**	8
Soil code 622	DP	0.02	0.10	0.37	0.80	1.53	2.45	**3.44**	**4.58**	5
Soil code 642	DP	0.00	0.00	0.17	0.38	0.63	1.12	**1.68**	**2.36**	4
Soil code 612	RO	0.12	0.21	0.34	0.52	0.77	1.05	**1.41**	**1.80**	6
Soil code 622	RO	0.28	0.53	0.81	1.19	1.63	2.15	**2.73**	**3.39**	9
Soil code 642	RO	0.67	1.06	1.57	2.16	2.86	3.61	**4.51**	**5.38**	12
Soil Water Holding Capitity										
Soil code 422	DP	0.35	0.77	1.62	2.63	3.80	5.06	**6.29**	**7.61**	11
Soil code 622	DP	0.02	0.10	0.37	0.80	1.53	2.45	**3.44**	**4.58**	5
Soil code 722	DP	0.00	0.06	0.20	0.48	0.97	1.73	**2.67**	**3.76**	3

***Table F.2**: Response of hydrologic components in percent change of flux rates to variable precipitation multipliers*

Sensitivity Analysis Parameter	Hydrologic Component	p0.50 (%)	p0.60 (%)	p0.70 (%)	p0.80 (%)	p0.90 (%)	Baseline (%)	p1.10 (%)	p1.20 (%)	p1.30 (%)	p1.40 (%)	p1.50 (%)	Rank
Irrigation Setting													
Non-Irrigated Maize	ET	-45	-35	-26	-16	-8	-	**6**	**11**	15	19	22	16
Irrigated Maize	ET	-4	-3	-3	-2	-1	-	**1**	**1**	2	2	3	18
Non-Irrigated Maize	DP	-100	-100	-97	-89	-66	-	**124**	**301**	510	750	1008	1
Irrigated Maize	DP	-99	-96	-85	-67	-38	-	**40**	**87**	133	182	232	5
Crop Types													
Maize	DP	-99	-96	-85	-67	-38	-	**40**	**87**	133	182	232	5
Soybeans	DP	-92	-80	-63	-44	-22	-	**23**	**47**	69	92	113	13
Alfalfa	DP	-100	-99	-91	-67	-50	-	**108**	**250**	448	681	944	2
Maize	RO	-87	-75	-62	-45	-24	-	**27**	**58**	90	126	166	9
Soybean	RO	-85	-74	-60	-42	-23	-	**25**	**54**	83	115	148	10
Pasture	RO	-90	-82	-68	-52	-31	-	**28**	**67**	117	168	227	7
Maize	NIR	100	73	55	45	18	-	**-18**	**-27**	-36	-36	-45	14
Soybean	NIR	49	35	23	14	6	-	**-5**	**-10**	-15	-18	-23	17
Alfalfa	NIR	39	31	23	15	7	-	**-7**	**-13**	-20	-25	-31	15
Soil Types													
Soil code 612	DP	-93	-87	-74	-52	-27	-	**29**	**59**	91	122	156	8
Soil code 622	DP	-99	-96	-85	-67	-38	-	**40**	**87**	133	182	232	5
Soil code 642	DP	-100	-100	-85	-66	-43	-	**50**	**111**	173	240	307	4
Soil code 612	RO	-89	-80	-68	-50	-27	-	**34**	**71**	114	160	212	6
Soil code 622	RO	-87	-75	-62	-45	-24	-	**27**	**58**	90	126	166	9
Soil code 642	RO	-81	-71	-56	-40	-21	-	**25**	**49**	77	106	136	12
Soil Water Holding Capitity													
Soil code 422	DP	-93	-85	-68	-48	-25	-	**24**	**50**	78	104	131	11
Soil code 622	DP	-99	-96	-85	-67	-38	-	**40**	**87**	133	182	232	5
Soil code 722	DP	-100	-96	-89	-72	-44	-	**54**	**117**	183	250	318	3

APPENDIX G: RESULTS OF FULL RANGE SENSITIVITY OF BASEFLOW OF RIVER SYSTEM TO PRECIPITATION DATA

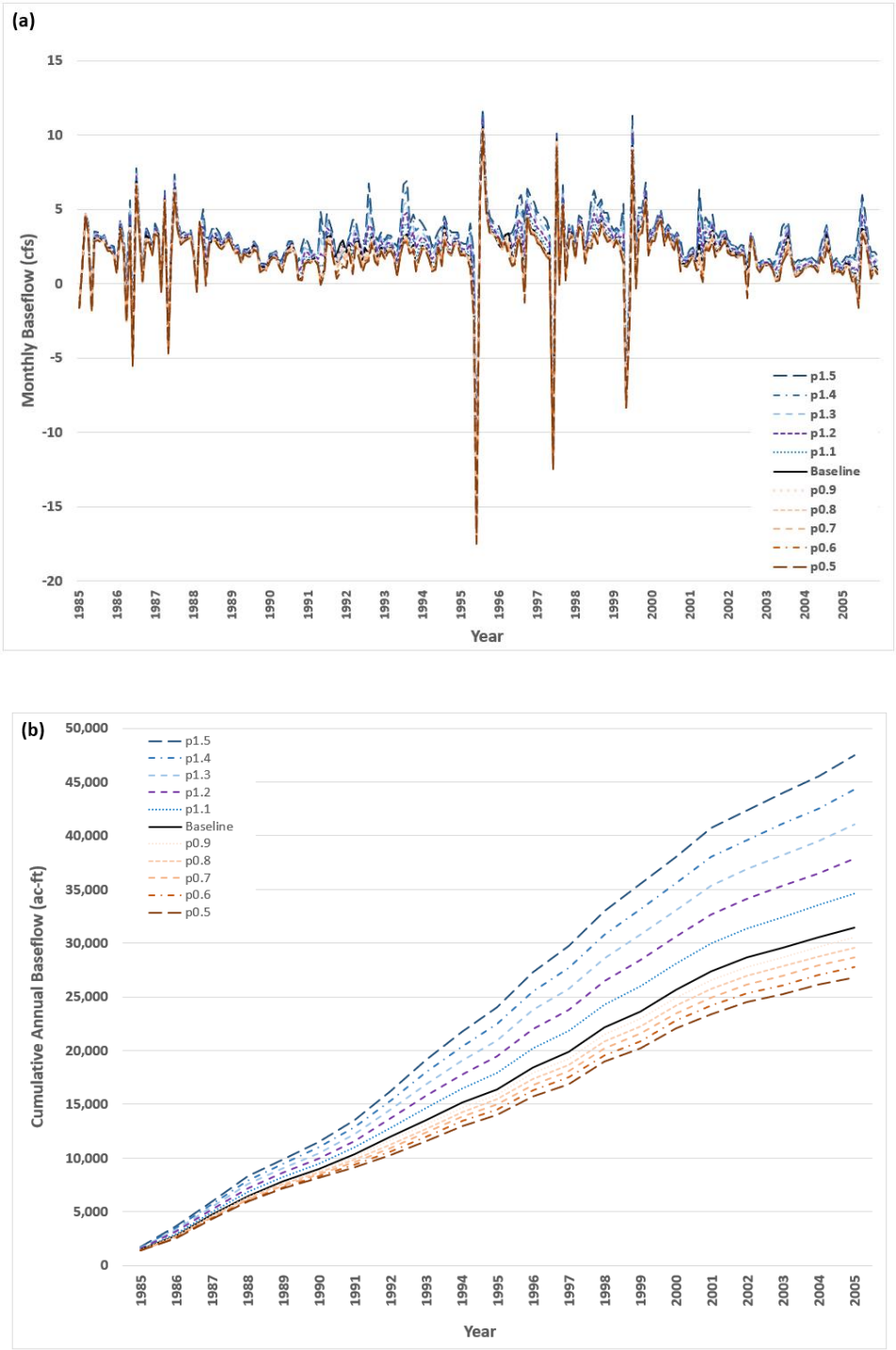

Figure G.1*: Baseflow comparison at the North Platte gaging station. (a) monthly baseflow and (b) cumulative annual baseflow*

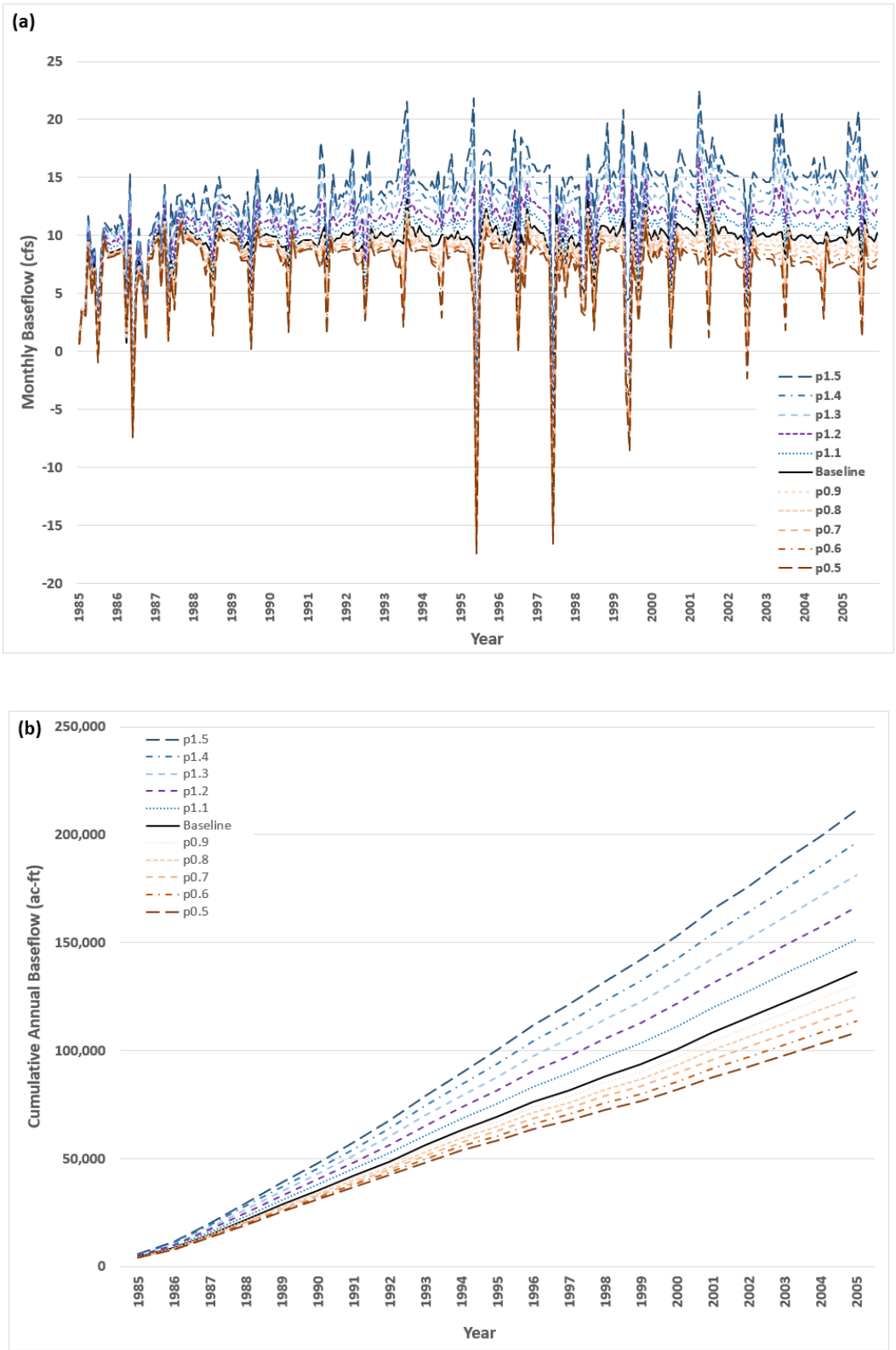

***Figure G.2**: Baseflow comparison at the Brady gaging station (a) monthly baseflow and (b) cumulative annual baseflow*

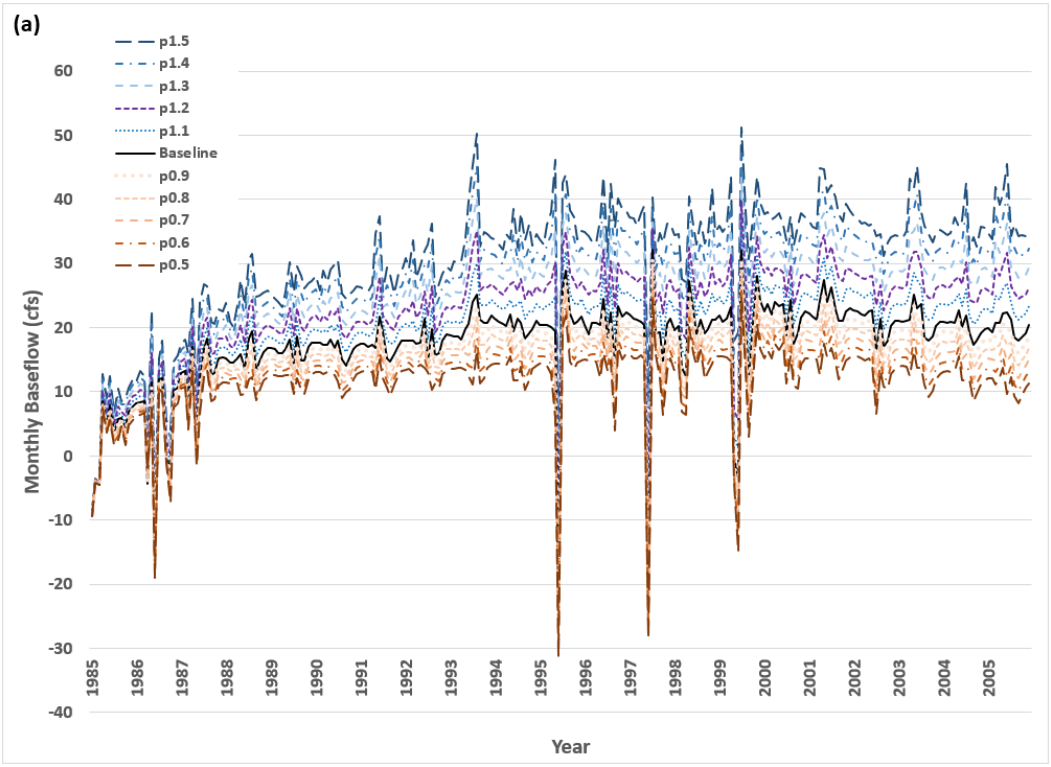

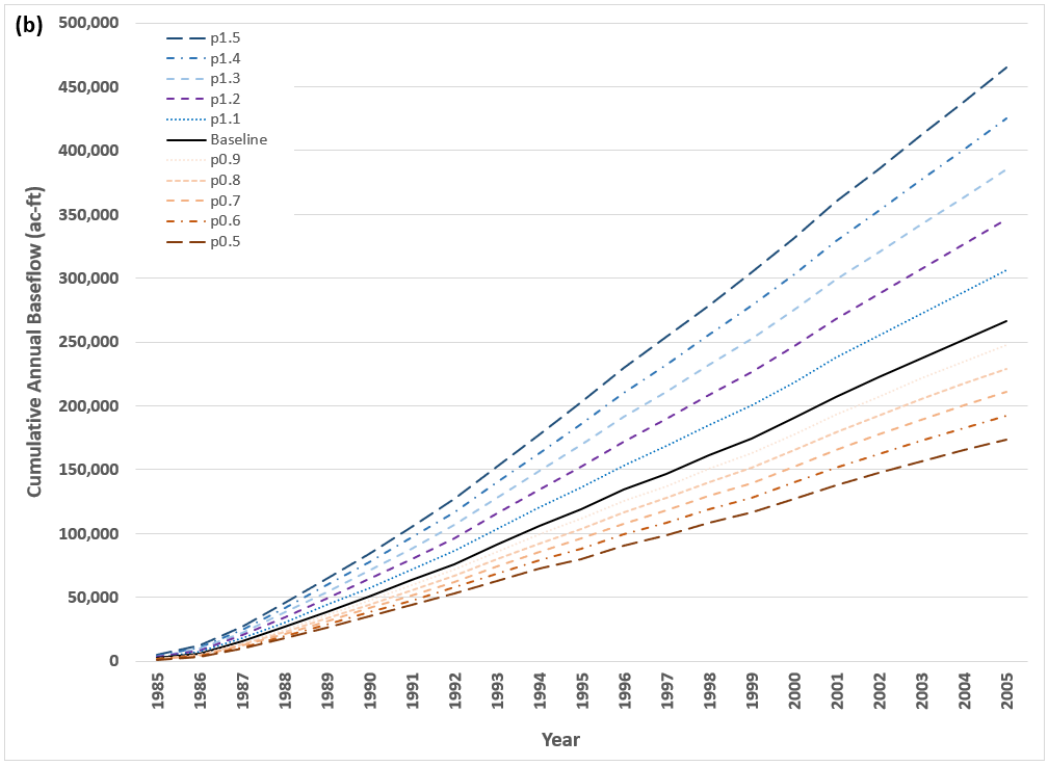

***Figure G.3**: Baseflow Comparison at the Cozad Gaging Station (a) monthly baseflow and (b) cumulative annual baseflow*

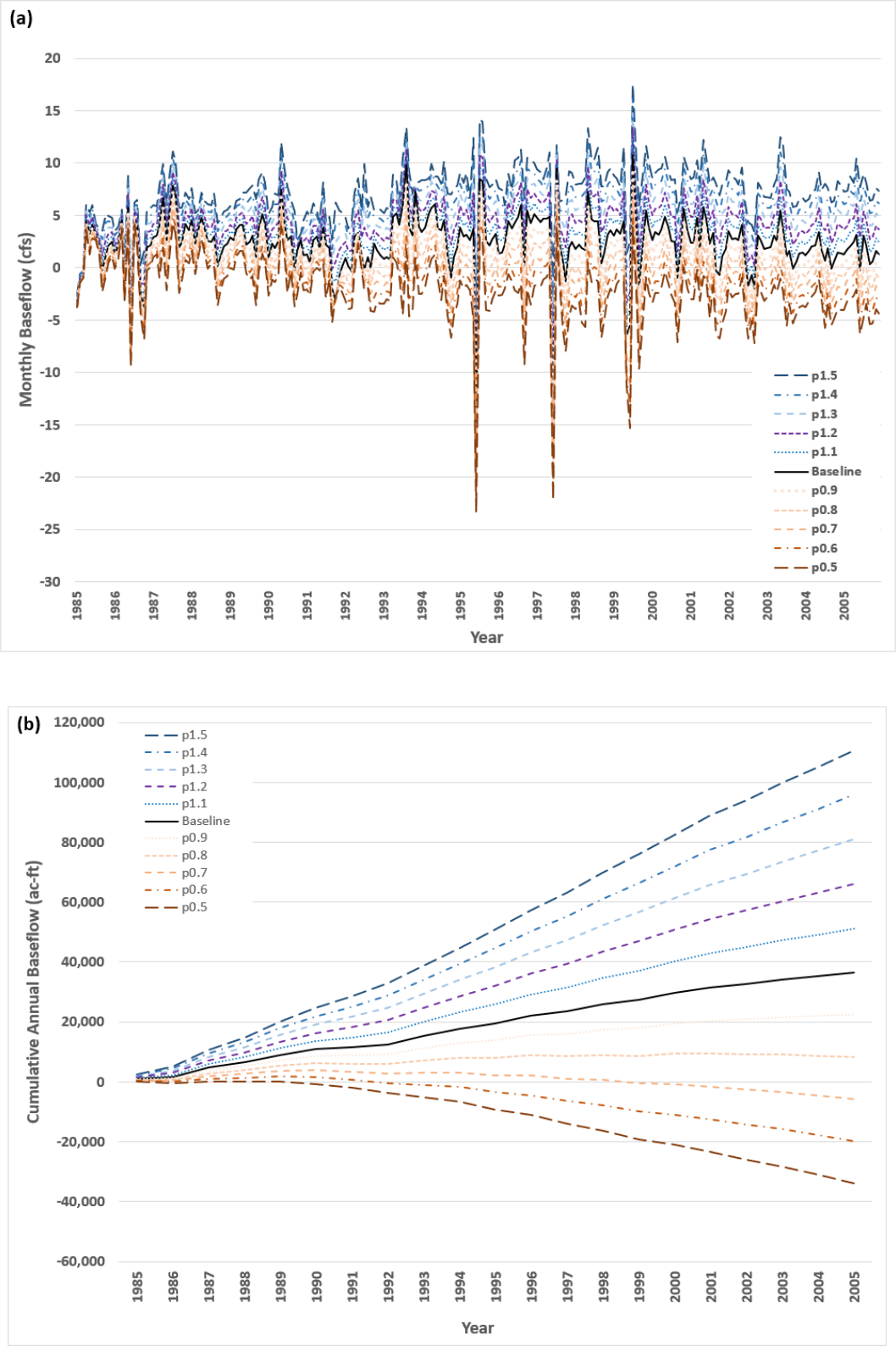

Figure G.4*: Baseflow comparison at the Overton gaging station (a) monthly baseflow and (b) cumulative annual baseflow*

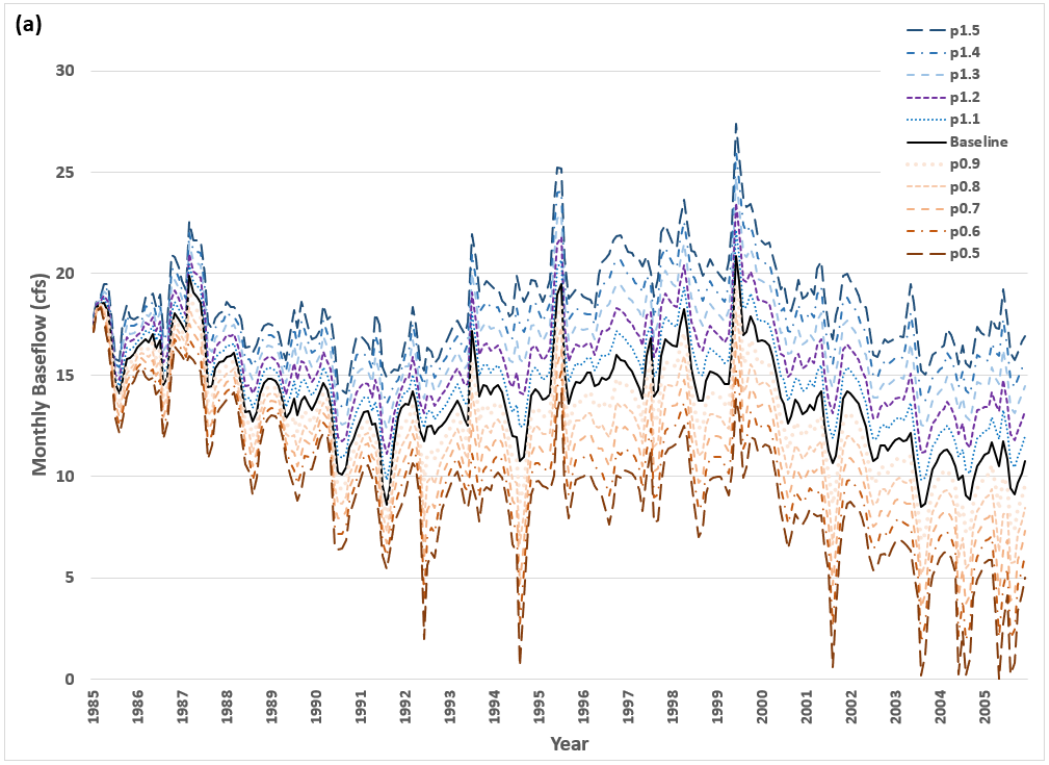

***Figure G.5**: Baseflow comparison at the Odessa gaging station (a) monthly baseflow and (b) cumulative annual baseflow*

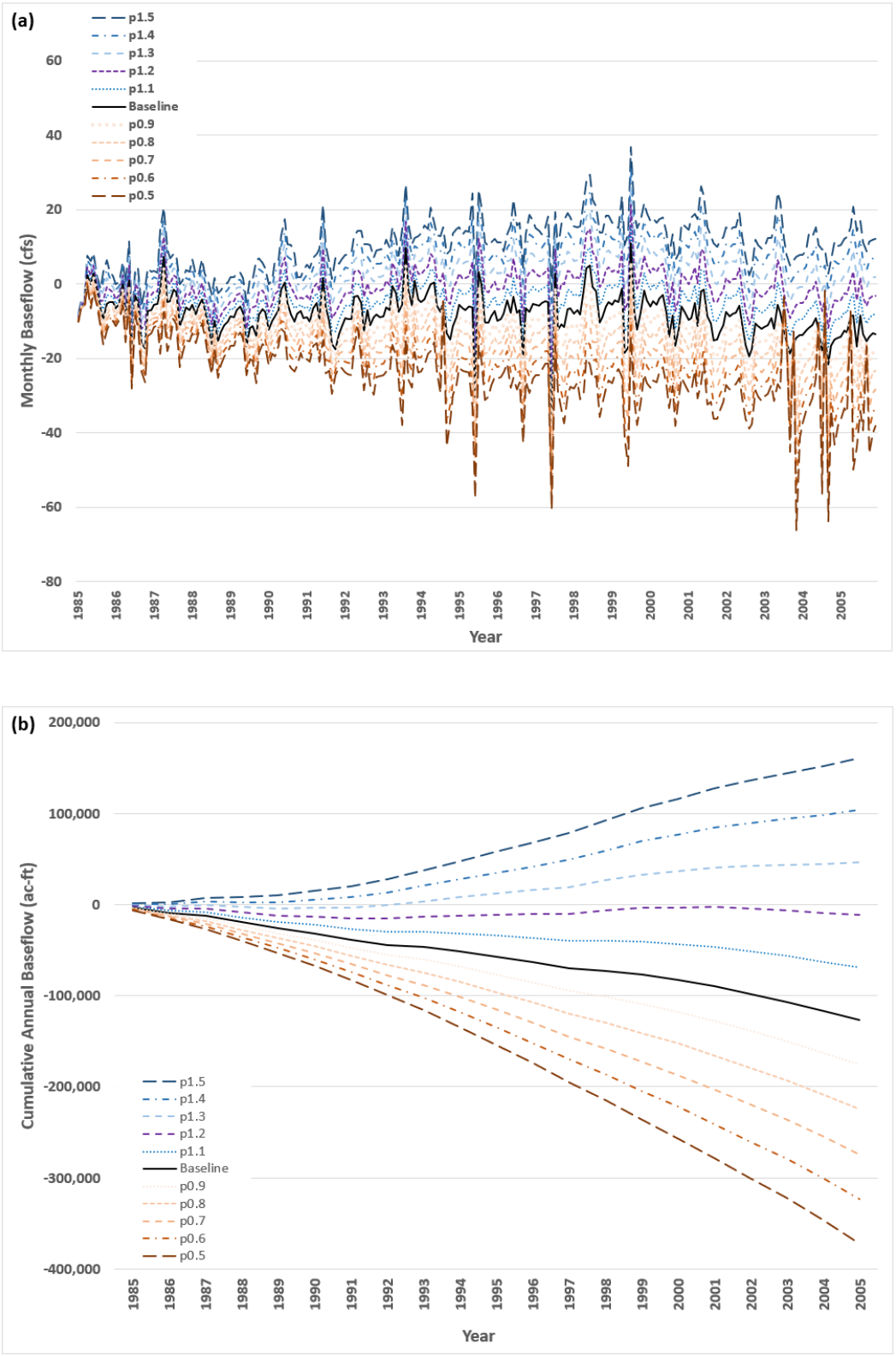

***Figure G.6**: Baseflow Comparison at the Grand Island Gaging Station (a) monthly baseflow and (b) cumulative annual baseflow*

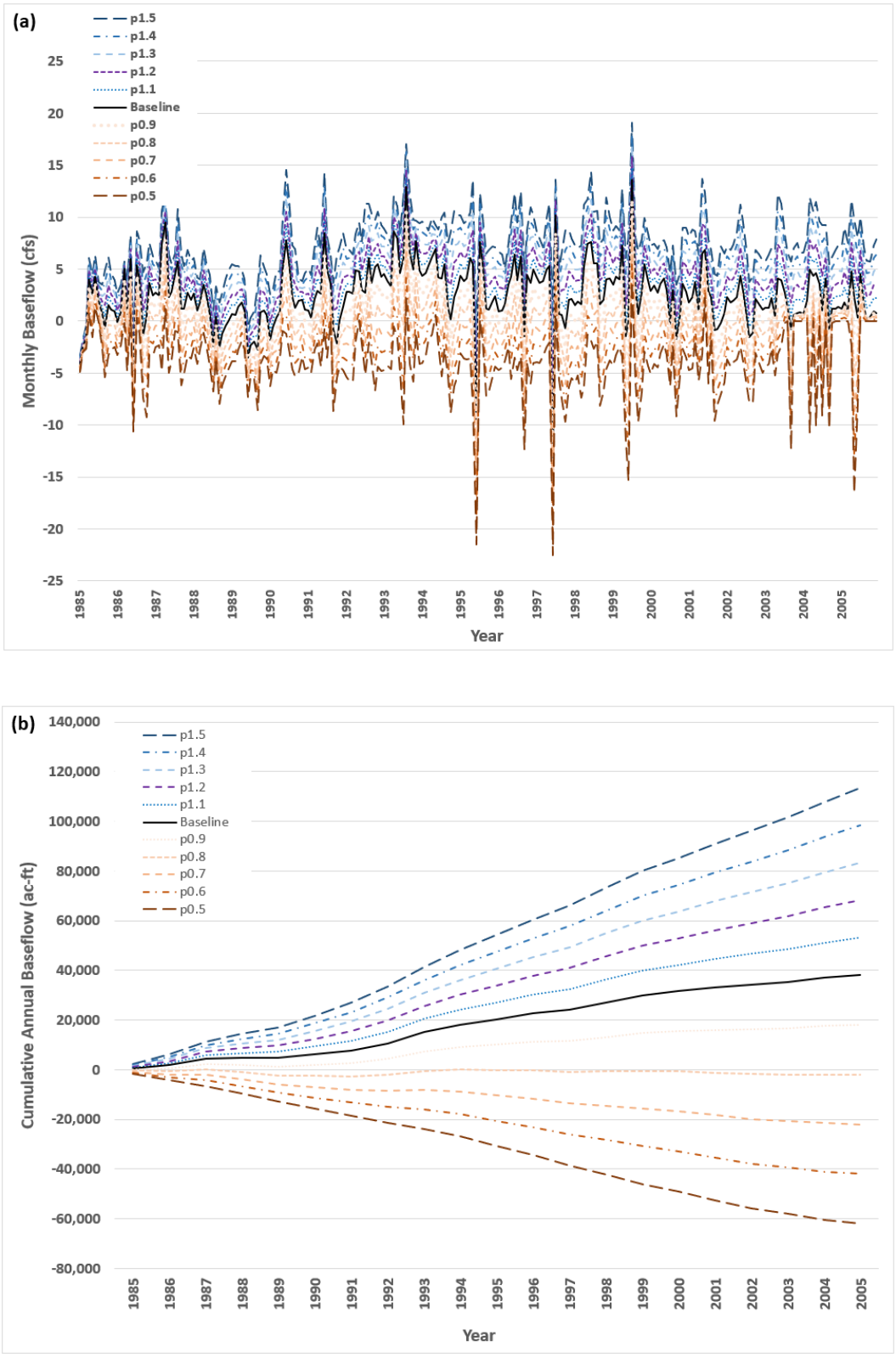

***Figure G.7**: Baseflow comparison at the Duncan gaging station (a) monthly baseflow and (b) cumulative annual baseflow*

In upstream gages, increases in precipitation rate have more influence on baseflow discharge than decreases in precipitation rates. At downstream gages the influences of increasing and decreasing precipitation rates are more comparable. The nature of the baseflow system at different locations of a river system can also be changed from a gaining to a losing system based on different rates of precipitation.

***Table G.1**: Response of model baseflow in annual average volume to variable precipitation multipliers at different gage locations*

Gage Station	p0.5	p.0.6	p.0.7	p.0.8	0.9	Baseline	p1.1	p1.2	p1.3	p1.4	p1.5
	(ac-ft/yr)	(ac-ft/yr)	(ac-ft/yr)	(ac-ft/yr)	(ac-ft/yr)	(ac-ft/yr)	(ac-ft/yr)	(ac-ft/yr)	(ac-ft/yr)	(ac-ft/yr)	(ac-ft/yr)
North Platte	1,277	1,321	1,365	1,409	1,453	1,497	1,650	1,803	1,955	2,108	2,261
Brady	5,151	5,420	5,690	5,959	6,228	6,498	7,211	7,924	8,637	9,350	10,062
Cozad	8,256	9,144	10,031	10,919	11,807	12,695	14,581	16,468	18,355	20,242	22,129
Overton	-1,608	-940	-273	395	1,063	1,731	2,439	3,148	3,856	4,564	5,273
Odessa	6,690	7,363	8,036	8,708	9,381	10,054	10,731	11,409	12,087	12,764	13,442
Grand Island	-17,728	-15,386	-13,045	-10,704	-8,363	-6,022	-3,281	-541	2,200	4,940	7,681
Duncan	-2,955	-1,999	-1,044	-88	867	1,823	2,541	3,258	3,976	4,693	5,410

***Table G.2**: Response of model baseflow in percent change to variable precipitation multipliers at different gage locations*

Gage Station	p0.5	p.0.6	p.0.7	p.0.8	0.9	Baseline	p1.1	p1.2	p1.3	p1.4	p1.5
	(%)	(%)	(%)	(%)	(%)	(%)	(%)	(%)	(%)	(%)	(%)
North Platte	-15	-12	-9	-6	-3	-	10	20	31	41	51
Brady	-21	-17	-12	-8	-4	-	11	22	33	44	55
Cozad	-35	-28	-21	-14	-7	-	15	30	45	59	74
Overton	-193	-154	-116	-77	-39	-	41	82	123	164	205
Odessa	-33	-27	-20	-13	-7	-	7	13	20	27	34
Grand Island	194	156	117	78	39	-	-46	-91	-137	-182	-228
Duncan	-262	-210	-157	-105	-52	-	39	79	118	157	197